# Development of Genetic Medicines for the Treatment and Prevention of Infectious Disease, Cancer, and Aging

by

Douglas Wilson Brown

A thesis submitted in partial fulfillment of the requirements for the degree of

Doctor of Philosophy

in
Cancer Sciences

Department of Oncology
University of Alberta

# Abstract

Gene therapy has potential to become the Holy Grail of modern medicine, however, its clinical success has been hindered due to the lack of a safe and effective nucleic acid delivery platform. The recent success of non-viral RNA delivery platforms has revitalized the field and spurred great interest in advancing these technologies to the clinic. In this thesis, I first describe the development and design of a novel non-viral nucleic acid delivery platform that utilizes a unique chimeric fusion protein to facilitate intracellular delivery of encapsulated cargo. I demonstrate that incorporation of this fusion protein into a lipid-based delivery platform enhances transgene expression and enables toxic components to be reduced, which significantly increases the tolerability relative to other clinically approved platforms. After establishing the feasibility of this nucleic acid delivery platform (called Fusogenix proteolipid vehicles or FAST-PLVs), I then explore various treatment indications in which gene therapy might provide some benefit. The first is development of a DNA-based vaccine against SARS-CoV-2, the virus that causes the disease known as COVID-19. We show that this vaccine can induce robust humoral immune responses, comparable to convalescent patients, and is able to protect hamsters from morbidity following viral challenge. Next, I examine the potential to create a genetic medicine for the treatment of one of the most complex genetic diseases, cancer. I first explore the consequence of p53 mutation on its own transcriptional regulation. I find that loss of p53 function is correlated with an upregulation in p53 transcriptional activity. Using this information, we designed a DNA-based suicide gene therapy, where the expression of a late-stage apoptotic protein is under control of the p53 promoter. I show that not only does this treatment selectively target cancer cells, but it also offers an effective means to attenuate tumor growth. Additionally, I demonstrate that the combination of this treatment with an immunotherapy is able to achieve tumor control in a poorly immunogenic, highly

metastatic tumor model. Finally, I explore the possibility of developing a genetic senolytic treatment to improve lifespan and prevent age-related organ function decline. To achieve this, we mimic the original transgenic mouse models that selectively eliminated senescent cells on the basis of their transcriptional activity. By generating a DNA-based suicide gene therapy where the expression of the same late-stage apoptotic protein is under control of the $p16^{Ink4a}$ promoter, we are able to selectively target and remove senescent cells. Combining this construct with the p53 promoter construct described above offers an effective means to improve lifespan in naturally aged mice possibly due to senescent cell elimination in the kidney. My work can help pave the way for the next generation of genetic medicines, as these Fusogenix proteolipid vehicles are currently the only known non-viral DNA delivery platform and our SARS-CoV-2 vaccine has begun phase II clinical trials. Additionally, this work may stimulate the development of new treatment strategies that target complex diseases based on their transcriptional activity.

# Preface

Chapter 2 of this thesis has been submitted for publication: Brown, D. W., *et al*., 2021, "Safe and Effective Delivery of Nucleic Acids Using Proteolipid Vehicles Formulated with Fusion-Associated Small Transmembrane Proteins." I was responsible for experimental design, data collection, in vitro and in vivo experimentation, as well as manuscript composition. Non-human primate experiments were performed at a CRO.

Chapter 3 of this thesis has been submitted for publication: Raturi, A., *et al*., 2021, "Rapid Prototyping and Immunogenicity of SARS-CoV-2 DNA Vaccine Candidates Formulated with the Fusion-Associated Small Transmembrane Protein Proteolipid Vehicle Delivery Platform." Due to the highly collaborative nature of this project, I was involved in experimental design, in vivo mouse work, as well as data collection and manuscript composition for relevant sections. Non-human primate study as well as hamster challenge study was performed at a CRO.

Chapter 4 of this thesis is in pre-submission. I was involved in experimental design, data collection, in vitro and in vivo experimentation, as well as manuscript composition.

Chapter 5 of this thesis is in pre-submission. I was involved in experimental design, data collection, in vitro and in vivo experimentation, as well as manuscript composition. SA-β-Gal staining on kidney tissue sections was done by our collaborator, M. Demaria.

All other work in this thesis is my original work.

# Acknowledgements

First and foremost, I would like to thank my supervisor, Dr. John Lewis. You helped me start my research career as a summer student back in 2015 and thankfully, disregarded how bad I was at research back then and took me on as your Ph. D student. Your support and guidance has been essential to my success. I still don't know how you were able to make time for me with how hectic your schedule is, but I am extremely thankful that you were always able to support me. It has been a pleasure to learn from you, as I have been exposed to things in the scientific world that would have not been possible elsewhere. You encouraged me to never give up and gave me the freedom to explore new experimental ideas. I truly believe this has made all the difference in my research career and I am very excited to see what the future will bring.

I would like to thank my Ph. D supervisory committee members, Dr. Afsaneh Lavasanifar and Dr. Michael Kolinsky. I am grateful you both were able to clear time out of your busy schedules to meet with me and go over experimental outlines. You have helped me approach my research from different perspectives, and though most of your questions stumped me at times, I am thankful you were able to push me to do better. I would also like to thank the members of my Ph. D examining committee, Dr. Lynne-Marie Postovit and Dr. David Murray. I don't know how you both were able to fit my candidacy exam into your schedule in the middle of grant writing season, but I don't think I would be here if you hadn't. Thank you for challenging me while still providing me with the guidance I would need to succeed in this program. Next, I would like to thank our collaborator Dr. Nadia Jahroudi and her graduate student Parnian Alavi. Your enthusiasm is unparalleled to anyone I've ever met. I'm so excited to see where this project takes us. I would also like to acknowledge support for my funding, FGSR, Prostate Cancer Canada, The Bird Dogs, NMIN, and Mitacs.

I would like to give a special thanks to my unofficial mentors, Dr. Arun Raturi and Dr. Desmond Pink. Desmond, you're the reason I was able to succeed in Dr. Lewis' lab in the first place. You taught me countless techniques and taught me how to think like a researcher. You gave me the freedom to explore my 'creative' process and helped chaperon me back to reality when that ultimately led to a dead end. Arun, you are without a doubt one of the most brilliant scientists I have ever met and how I was lucky enough to work alongside you is beyond me. Simply by being

around you and picking your brain has made me sound substantially smarter than I actually am. Without your support, I'm fairly certain I would still be struggling to transfect PC3 cells!

I am thankful to my former lab members, Lian and Deborah, for not only helping me with my animal experiments, but for teaching me everything I know about animal work. Maryam, I am indebted to you for taking on animal experiments with me, I don't think I would have ever gone home had you not joined the lab. Perrin, you have helped me immensely with all things writing and I cannot thank you enough for making it sound like I can write above a sixth-grade level. Suellen, you taught me everything about histology and you helped complete countless projects. Of course, I am eternally grateful to Liliya, Ping, Jenn, and Paola for always making themselves available to help make particles without a moment's notice. Thank you to Manoj and Natasha for your help with ELISA's through the years, who would have thought we'd end up specialized in this! Hector (and Liliya again), you have purified buckets of FAST protein and without you all our projects would unravel. Prakash and Rakesh thank you for taking on cloning and DNA purification, you have no idea how many headaches you both have saved all of us from. Thank you to Mike for making life in the lab fun and guiding every flow cytometry experiment I've ever conducted (obligatory comment: "AH _!"). Thank you, Konstantin, for all the help imaging. I must extend a special thanks on behalf of the entire lab to Katia for keeping the lab functional and keeping us from burning the place down. Thank you to everyone, past and present, for making those long nights and weekends in the lab enjoyable.

Finally, thank you to my parents for tolerating me for the past 30 years. Your endless support has made all the difference. Without your love and encouragement none of this would have been possible. I owe my deepest gratitude to my wife and best friend, Tia. You have flooded me with love and support throughout this entire experience. I know it wasn't easy dealing with my unpredictable schedule and random 'science thoughts,' but I never would have made it through grad school without you. I would also like to thank both of my dogs, I know neither of you can read, but it feels important to acknowledge you anyways.

# Table of Contents

## Contents

# List of Tables

# List of Figures

# List of Abbreviations

| | |
|---|---|
| **AAV** | Adeno-associated viral |
| **ACE2** | Angiotensin-converting enzyme 2 |
| **Ad** | Adenovirus |
| **Ad-p53** | Adenoviral WT p53 expression vector |
| **ADA** | Adenosine deaminase |
| **ALT** | Alanine Aminotransferase |
| **APC** | Antigen presenting cells |
| **ARF** | Alternative Reading Frame protein (p14ARF and p19ARF) |
| **ASO** | Antisense oligonucleotide |
| **AST** | Aspartate Aminotransferase |
| **ATM** | Ataxia–telangiectasia mutated |
| **BCL-2** | B-cell lymphoma 2 |
| **BTG2** | B-cell translocation gene 2 |
| **CARD** | Caspase activation and recruitment domains |
| **CARPA** | Complement activation-related pseudoallergy |
| **CDK** | Cyclin dependent kinase |
| **cGAS** | Cyclic GMP-AMP synthase |
| **CID** | Chemical inducer of dimerization |
| **CMV** | Cytomegalovirus |
| **CPK** | Creatine phosphokinase |
| **CPP** | Cell penetrating peptide |
| **CTL** | Cytotoxic T lymphocyte |
| **CTLA-4** | Cytotoxic T lymphocyte antigen-4 |
| **DDR** | DNA damage response |
| **DMG-PEG** | 1,2-dimyristoyl-*sn*-glycero-3-methoxypolyethylene glycol-2000 |
| **DNA** | Deoxyribonucleic acid |
| **DNMT1** | DNA methyltransferase 1 |
| **DODAP** | 1,2-dioleoyl-3-dimethylammonium-propane |
| **DODMA** | 1,2-dioleyloxy-3-dimethyla |
| **DOPE** | 2-dioleoyl-*sn*-glycero-3-phosphoethanolamine |
| **DOTAP** | 1,2-dioleoyl-3-trimethylammonium-propane |
| **DOTMA** | 1,2-di-O-octadecenyl-3-trimethylammonium propane |
| **DOX** | Doxorubicin |
| **ERK** | Extracellular signal-regulated kinase |
| **FAST** | Fusion-associated small transmembrane protein |
| **FDA** | Food and Drug Administration |
| **FLiPs** | Fusion-inducing lipid packing sensor |
| **FLuc** | Firefly luciferase |

| | |
|---|---|
| **FST** | Follistatin |
| **GAS** | Gastrocnemius |
| **GEPIA** | Gene Expression Profiling Interactive Analysis |
| **GFP** | Green fluorescent protein |
| **GOF** | Gain-of-Function |
| **HBP1** | HMG-Box Transcription Factor 1 |
| **HDAC** | Histone deacetylase |
| **HER2** | Human epidermal growth factor receptor 2 |
| **HIV** | Human immunodeficiency virus |
| **HSC** | Hematopoietic stem cells |
| **HUVEC** | Human umbilical vein endothelial cells |
| **iCasp9** | Inducible Caspase 9 |
| **IFN** | Interferon |
| **Ig** | Immunoglobulin |
| **IL** | Interleukin |
| **IM** | Intramuscular |
| **IP** | Intraperitoneal |
| **IT** | Intratumoral |
| **IV** | Intravenous |
| **LDH** | Lactate dehydrogenase |
| **LLOQ** | Lower limit of quantification |
| **LNP** | Lipid nanoparticle |
| **MAPK** | Mitogen-activated protein kinase |
| **MAVS** | Mitochondrial antiviral-signaling protein |
| **MC3** | DLin-MC3-DMA |
| **MDM2** | Mouse double minute homolog 2 |
| **MEK** | Mitogen-activated extracellular signal-regulated kinase |
| **MERS-CoV** | Middle East respiratory syndrome-related coronavirus |
| **MHC** | Major histocompatibility complex |
| **MLL1** | Myeloid/lymphoid or mixed-lineage leukemia 1 - methyltransferases |
| **MMP** | Matrix metalloproteinase |
| **mRNA** | Messenger RNA |
| **mup53** | Mutant p53 |
| **NF-κB** | Nuclear factor-kappa B |
| **NHP** | Non-human primates |
| **NSCLC** | Non-small cell lung cancer |
| **PAMP** | Pathogen-associated molecular patterns |
| **PDGF** | Platelet-derived growth factor |
| **PDGFR** | Platelet-derived growth factor receptor |
| **PD-L1** | Programmed cell death ligand 1 |
| **pDNA** | Plasmid DNA |

| | |
|---|---|
| **PEG** | Polyethylene glycol |
| **PKC** | Protein Kinase C |
| **PLV** | Proteolipid Vehicle |
| **pRb** | Retinoblastoma protein |
| **PRC2** | Polycomb-repressive complex 2 |
| **PRR** | Pattern-recognition receptor |
| **PTEN** | Phosphatase and Tensin Homolog |
| **RAPA** | Rapamycin |
| **RBD** | Receptor binding domain |
| **RIG-I** | Retinoic acid-inducible gene I |
| **RNA** | Ribonucleic acid |
| **RNAi** | RNA Interference |
| **ROS** | Reactive oxygen species |
| **SAHA** | Suberoylanilide hydroxamic acid |
| **SARS-CoV** | Severe acute respiratory syndrome-related coronavirus |
| **SASP** | Senescence-associated secretory phenotype |
| **SA-β-Gal** | Senescence associated β-galactosidase |
| **SC5b-9** | S protein bound C terminal complex |
| **SCID** | Severe combined immunodeficiency |
| **SFC** | Spot forming cells |
| **siRNA** | Short interfering RNA |
| **SMN** | Survival motor neuron 1 |
| **S-protein** | Spike protein |
| **STING** | Stimulator of interferon genes |
| **TAT** | transactivator of transcription |
| **TCR** | T cell receptor |
| **TLR** | Toll-like receptor |
| **TM** | Transmembrane |
| **TNF** | Tumor necrosis factor |
| **TP53TG3E** | TP53 target 3 family member E |
| **TTR** | Transthyretin |
| **TUNEL** | Terminal deoxynucleotidyl transferase dUTP nick end labeling |
| **VEGF** | Vascular Endothelial Growth Factor |
| **VSV** | Vesicular Stomatitis Virus |
| **WT** | Wild type |
| **ZNF223** | Zinc Finger Protein 223 |

# **Chapter 1:** Introduction

## Introduction

The global vaccination effort to halt the spread of COVID-19 in 2020 and 2021 has demonstrated the great value genetic medicines can have. The mRNA vaccines developed by Pfizer and Moderna, as well as the adenovirus vaccines developed by AstraZeneca and Janssen generated robust humoral responses and displayed excellent tolerability, with a relative ease of manufacturing compared to traditional vaccine approaches. Outside of the field of vaccination, gene therapy has potential to treat innumerable diseases ranging from monogenic disorders to cancer[1–3]. Despite the seemingly untapped potential of gene therapy, there are still many problems that must be addressed before it becomes more widely accepted in modern medicine. In particular, a lack of a safe and effective nucleic acid delivery platform has hindered the success of genetic medicines. Additionally, when utilized to target complex diseases, such as cancer, manipulation of a single gene may not produce the effects seen for monogenic disorders or vaccinations. This raises the question, what cargos can we deliver and how does treatment improve with the addition of gene therapy modalities?

In this thesis, I describe the optimization of a novel nucleic acid delivery platform, called Fusogenix Proteolipid Vehicles (FAST-PLVs), that combines the beneficial features of both viral and non-viral delivery vectors to generate a platform with high efficacy of transgene expression and high tolerability. Prior to this work, systemic delivery of DNA was restricted to viral vectors, therefore making this the first viable non-viral delivery vector suitable for plasmid DNA (pDNA) delivery. Using the pDNA delivery ability of FAST-PLVs, I then explored different treatment indications suitable for gene therapy, including vaccinology, cancer, and anti-aging. The research presented in this thesis not only presents a novel nucleic acid delivery vehicle, but also examines

different approaches to make gene therapy more selective, therefore increasing safety. The results presented here may act as a catalyst for the next phase of genetic medicines.

## 1.1 Gene Therapy

### 1.1.1. History of Gene Therapy

There are significant hurdles that genetic medicines must overcome to gain more broad applicability. The plasma membrane is a highly effective physical barrier that actively repels or sequesters exogenous macromolecules, such as negatively charged nucleic acids. This necessitates the use of a carrier vehicle, either viral or non-viral, to facilitate entry into the cytosol to exert the intended therapeutic effect. In 1990, the first successful transfer of genetic material into human cells was described. Tumor-infiltrating lymphocytes were isolated from patients with metastatic melanoma and transduced with a retroviral vector, following which, they were reintroduced into patients[4]. Though just a proof-of-concept experiment, this study served as the foundation for many of the modern genetic medicines utilized today, namely chimeric antigen receptor T-cell (CAR-T) therapy. It was also the beginning of viral nucleic acid delivery vehicles coming into the limelight. In 1995, utilizing a retroviral vector, researchers introduced the adenosine deaminase (ADA) gene into the T lymphocytes isolated from two children with severe combined immunodeficiency (SCID) born without a functional ADA gene. Treatment was able to increase circulating levels of CD3+ T lymphocytes and overall immune function over a period of four years with no significant safety concerns[5]. Nearly 20 years later, the ADA-SCID treatment, Strimvelis, became the first gene therapy product for *ex vivo* modification of human stem cells to receive regulatory approval[6]. Though revolutionary, these treatments involve isolating cells from a diseased patient, transducing them with a viral vector containing the gene of interest, and reintroducing the genetically modified

cells back into the patient's body. Modifying cellular gene expression systemically presents with its own unique set of problems.

### 1.1.2. Viral Gene Therapy Vectors

Viral vectors have dominated gene therapy efforts due to their high efficiency of gene expression, with adenoviral, retroviral/lentiviral, and adeno-associated viral (AAV) vectors leading the field[3,7]. The two subtypes of retroviruses, γ-retroviruses and lentiviruses contain an RNA genome that undergoes reverse transcription into DNA upon entry into a transduced cell. The new DNA genome is then integrated into the host cell therefore enabling durable gene expression for the life of the cell[8]. This makes retroviruses highly useful for *ex vivo* gene transfer in hematopoietic stem cells (HSCs)[9,10] and T cells[11,12]. Genetically altered cells can be reintroduced into patients and reverse gene deficiency in HSCs, or target cancer cells, respectively. Unfortunately, the risk of insertional mutagenesis has hindered the systemic use of retroviruses[13].

Adenoviral and AAV vectors have predominately been the chosen viral vectors for systemic gene therapy. These vectors have a DNA genome and possesses the ability to transduce quiescent cells, making them an ideal candidate for treatment of monogenic disorders[14]. However, initial studies examining the use of adenoviruses as gene therapy vectors were met with resistance after it was reported that serious and life-threatening side effects could occur[15], which has caused most approaches to shift to the use of safer AAV vectors[16,17]. The FDA approval of Glybera, an AAV vector designed to reverse lipoprotein lipase deficiency[18], strengthened the support for the use of AAV gene therapy vectors. Being a viral vector, adaptive immune responses prevent AAV vectors from being administered repeatedly, therefore requiring sustained gene expression from a single dose unless multiple AAV subtypes are utilized[17,19–21]. Additionally, preexisting neutralizing AAV antibodies can exist even without prior vector exposure further hindering gene expression[22–25]. This

being said, immune stimulation can come as advantageous in the field of vaccines, where robust T cell responses induced by the gene delivery vector can help facilitate long lasting immunity to the antigen[26]. Despite the improved safety profile, there are still some significant safety concerns that need to be addressed, particularly regarding immunogenicity. AAV vectors may trigger a cytotoxic T lymphocyte (CTL) response against transduced cells, which may lead to a loss of gene expression as well as toxicity development[27,28]. This has been demonstrated clinically, AAV9 mediated delivery of survival motor neuron 1 (SMN) gene via intravenous injection generated a CTL response being mounted against hepatocytes containing AAV9 capsid proteins resulting in elevated serum ALT levels[29]. Glucocorticoids were found to attenuate this increase, however, a follow-up study in non-human primates (NHP) and piglets found that administration of a similar dose of AAV9 delivering SMN resulted in severe liver toxicity in NHPs and neuronal toxicity in piglets; cautioning against high doses being used in the future[29]. There are also important manufacturing concerns surrounding AAV use. Inefficient AAV generation, challenging purification techniques, and high batch-to-batch variation have culminated in steep price tags for AAV-based drugs[17].

### 1.1.3. Non-Viral Gene Therapy Vectors

To overcome the limitations surrounding viral vectors, the focus in recent years has largely shifted to the development and optimization of the safer non-viral delivery vectors[30]. Non-viral delivery vectors are easier and cheaper to manufacture than viral vectors, allowing for rational design and large-scale testing of novel materials and formulations with nucleic acid delivery potential[31,32]. Of the various non-viral delivery vectors, lipid nanoparticles (LNPs) have demonstrated their success with the FDA approval of patisiran (Onpattro), an LNP-based RNA interference agent that inhibits transthyretin production[33,34]. Additionally, the success of the LNP-

based COVID-19 mRNA vaccines developed by Pfizer and Moderna have demonstrated the speed at which non-viral gene therapies can be implemented, while still meeting all required safety and efficacy targets[35,36]. LNPs are formulated with cationic or ionizable lipids that both neutralize the anionic charge of nucleic acids and facilitate endosomal escape of encapsulated nucleic acids through charge-mediated disruption of lipid bilayers[33,37–39]. The majority of contemporary LNPs utilize the ionizable lipid DLin-MC3-DMA (MC3) or one of its derivatives, which acquires positive charge in the acidic environment of the endosome. While ionizable lipids have substantially improved tolerability compared to cationic lipids[40], their mechanism of action potentiates apoptotic cell death, which translates to tolerability challenges after local delivery and dose-limiting liver toxicity following systemic delivery[41,42]. Additionally, interactions between LNPs and the immune system can have disastrous systemic effects and lead to secretion of proinflammatory cytokines like tumor necrosis factor alpha (TNF-α), interferon-gamma (IFN-γ), and interleukin-6 (IL-6)[43,44]. LNPs can also stimulate complement activation-related pseudoallergy (CARPA), a hypersensitivity reaction resulting in death in severe circumstances[45–47]. Regardless of the limitations surrounding LNPs and other non-viral delivery vectors, the relative safety and lack of humoral immune responses favor this platform for treatments requiring multiple doses.

Though non-viral vectors don't match the efficiency of viral gene transduction, the low systemic toxicity, low immunogenicity, and cost-effectiveness have made non-viral vectors an attractive candidate for future gene therapy approaches. Despite this, systemic delivery of DNA using non-viral vectors has seen little clinical success, and DNA delivery is still relatively restricted to viral platforms[3,7]. Size is one of the largest hurdles surrounding DNA delivery. Though number of base pairs has minimal impact on LNP size, larger DNA constructs have significantly lower gene expression than smaller constructs[48,49]. However, the large size of pDNA does require

higher molar ratios of cationic/ionizable components to neutralize its anionic charge and facilitate delivery relative to particles encapsulating mRNA and siRNA. Increasing the quantity of cationic components results in a corresponding increase in toxicity, preventing successful systemic delivery. Kulkarni *et al.*[50] demonstrated successful pDNA delivery *in vitro* and *in vivo* using a formulation primarily composed of the ionizable lipid, DLin-KC2-DMA; a structural analog of DLin-MC3-DMA. However, the *in vivo* delivery in this study was achieved via injection into the forelimb buds of chicken embryos rather than by systemic delivery.

### 1.1.4. Viral Fusion Proteins for Drug Delivery

Viral fusion proteins represent attractive candidates for drug delivery platform. Millions of years of evolution has resulted in viruses with sophisticated fusion proteins achieving high degrees of genetic transfer. Unfortunately, these complex multimeric proteins are difficult to purify and are highly immunogenic[51]. However, the discovery that the human immunodeficiency virus (HIV) transactivator of transcription (TAT) was able to cross the plasma membrane spurred significant research interest in developing and optimizing other similar cell penetrating peptides (CPPs) for clinical purposes[52,53]. CPPs synthesized with polyarginine have demonstrated superior cellular entry[54]. A small number of clinical trials have been conducted exploring the utility of CPP for drug delivery[55–58], however, there are some limitations that restrict their use, specifically for nucleic acid delivery. Polyarginine and other CPPs can be directly complexed with plasmid DNA and other nucleic acids to generate nanocomplexes with transfection capability. However, this strategy may generate nanocomplexes with sizes unsuitable for systemic gene therapy (>1000nm) and may also result in high cytotoxicity[59]. Saleh *et al.*[60] developed a method to generate a DNA vaccine against human papillomavirus using the CPP, MPG. These DNA-MPG nanocomplexes had a size ~200nm and were suitable for subcutaneous injection. Xiang *et al.*[61] developed a method to circumvent

these sizing restrictions to enable systemic delivery by incorporating an activatable octo-arginine CPP into LNPs encapsulating siRNA against PLK-1. They demonstrated enhanced endocytic entry and accumulation into prostate tumors resulting in attenuation of tumor growth. These studies demonstrate the potential feasibility of CPPs, however there are some concerns preventing their entry into the clinic. CPPs are subject to degradation[62] and likely aggregate with serum proteins, which would alter their functionality[63]. Structural modification of CPPs can lead to enhanced stability but may also result in a corresponding increase in manufacturing difficulty and introduce new toxicity[52]. Furthermore, there is the potential that CPPs might activate immunological responses, which may decrease their efficacy or increase systemic toxicity[64].

### 1.1.5. Fusion Associated Small Transmembrane Proteins

All enveloped viruses utilize elegant fusion proteins that fuse the viral envelope with cell membranes to facilitate efficient delivery of their genetic payload[51]. In contrast, the nonenveloped fusogenic orthoreoviruses encode a unique class of non-glycosylated fusion proteins known as fusion-associated small transmembrane (FAST) proteins. FAST proteins are not components of the virion, rather they are expressed in infected cells and are trafficked to the plasma membrane where they facilitate cell-cell (not virus-cell) fusion to promote virus dissemination via syncytium formation[65,66]. Being only ~100-200 amino acids in length, FAST proteins are the smallest known viral fusogens. They have a single transmembrane (TM) domain fixing the FAST protein in a $N_{exoplasmic}/C_{cytoplasmic}$ membrane topology that exposes an even smaller ectodomain (~19-40 residues) external to the plasma membrane and leaves an extended endodomain of ~40-140 residues in the cytoplasm[67–69]. Essential FAST protein structural motifs include diverse, myristoylated, ectodomain fusion peptides and endodomain polybasic and amphipathic helix motifs, which together with key features of the TM domain, remodel membranes from both sides

to promote membrane fusion[69–72]. FAST proteins lack specific receptor-binding activity, function at physiological pH, and act as a bona fide fusogens enabling them to fuse almost all cell types. Top *et al*.[73] demonstrated that incorporation of FAST protein into liposomes was able to induce liposome-cell fusion and facilitate intracellular delivery of the encapsulated, membrane impermeable, lactoferricin peptide. The unique ability of FAST proteins to stimulate liposome-cell membrane fusion provides encapsulated cargo direct access to the cytoplasm of the fused cell, effectively bypassing endocytosis. We postulate that incorporating FAST proteins into a non-viral lipid based nucleic acid delivery platform would enable us to reduce the dependence on toxic cationic components without compromising on delivery efficacy.

## 1.2. COVID-19, Immunology, and Vaccine Development

### 1.2.1. Immune Response to Viral Infection

Both the innate and adaptive immune responses function during viral infection. Due to their dependence on host cellular machinery for replication, cells have evolved multiple mechanisms to recognize and prevent viral infection. The innate immune system is mobilized in response to pathogen-associated molecular patterns (PAMPs) acting on pattern-recognition receptors (PRRs) that serve as the first line of defense to eliminate infected cells and prime the adaptive immune response. The most important PRRs for the purpose of this thesis are toll-like receptors (TLR), retinoic acid-inducible gene I (RIG-I) like receptors, and the intracellular DNA sensor cyclic GMP-AMP synthase (cGAS)[74]. TLRs are often the first activated PRRs due to their intracellular and surface localization. Important examples of TLRs include TLR9, TLR8, TLR7, and TLR3. TLR9 recognizes unmethylated CpG DNA motifs[75], TLR8 and TLR7 recognize single-stranded RNA[76,77], and TLR3 recognizes double-stranded RNA[78]. Stimulated TLRs primarily signal through nuclear factor-κ B (NF-κB), which facilitates a type I interferon (IFN) response[79]. Additionally,

activation of TLRs expressed on dendritic cells leads to increased expression of cytokines and chemokines, as well as costimulatory molecules (CD80 and CD86) and major histocompatibility complex (MHC) class molecules required for antigen presentation. TLR activated dendritic cells migrate to lymph nodes and function as antigen presenting cells (APCs) leading to activation of T lymphocytes – thus linking the innate and adaptive immune responses through TLR activation[80]. RIG-I like receptors are cytosolic DExD/H box RNA helicases often containing caspase activation and recruitment domains (CARDs) that are responsible for signal transduction[81]. RIG-I is activated in response to triphosphate groups found on the 5' end of RNA (typically only present in viral RNA)[82], 5' diphosphate RNA that is base-paired to form a blunt end[83], or in response to cytoplasmic mislocalized non-coding RNA, namely 5S ribosomal RNA pseudogene 141 [84,85]. RNA binding to RIG-I triggers a conformation change that enables the CARD to interact with the CARD present on the mitochondrial antiviral-signaling protein (MAVS), which signals to TANK-binding kinase 1 and IKK-ε, which activate interferon regulatory factor 3 and 7, as well as NF-κB to induce type I IFN expression[81]. Cytoplasmic DNA that lacks CpG motifs stimulates cGAS to produce cGMP and cAMP, which binds to and activates STING (stimulator of interferon genes) resulting in a type I IFN response[86]. The type I IFNs, IFN-α and IFN-β, restrict viral replication by inducing the expression of interferon-stimulated genes with profound antiviral functions. For example, increased PRR expression (RIG-I expression), enhanced nucleic acid degradation (via RNaseL expression), inhibition of viral transcription (expression of TRIM and Mx proteins), and inhibition of protein translation (expression of protein kinase R). IFN-α/β also prime T cells to initiate an antiviral adaptive immune response[87].

Adaptive immune responses to viruses serve to prevent reinfection and are thus the most important factor to consider for vaccine development. Activated APCs process viral antigens and

present these fragments via MHC molecules. MHC bound antigens are recognized by the T cell receptor (TCR) and together with costimulatory molecules and cytokines facilitate activation of T cells to enable recognition of virus infected cells. Typically, MHC class I stimulates CD8+ cytotoxic T cells and MHC class II stimulates CD4+ helper T cells. CD8+ T cells are primarily responsible for the elimination of infected cells and CD4+ T cells 'help' to stimulate an antibody response. B cells that internalize extracellular antigens increase expression of the costimulatory molecules, CD80 and CD86. These B cells then function as APCs and interact with CD4+ T cells leading to an interaction between CD40 expressed on the B cells surface and CD40 ligand expressed on the CD4+ T cell surface[88]. These T cell stimulated B cells undergo rapid proliferation and somatic hypermutation, leading to the production of antigen-specific antibodies that are localized to the B cell surface. B cells with surface expressed antigen-specific antibodies are then able recognize the antigen present on other APCs and are stimulated to mature into memory B cells or plasma cells via IL-21 produced by follicular helper T cells[89]. Viral antigens are then recognized by antibodies secreted by plasma cells, leading to antibody-specific elimination of viral particles or virus infected cells via cytotoxic CD8+ T cell mediated killing or complement recognition. As some viruses mediate down regulation of MHC class I molecules to avoid immune recognition, natural killer cells can eliminate cells via an antibody-independent mechanism that is inhibited by surface expression of MHC class I on non-infected cells[88].

### 1.2.2 COVID-19 Pandemic

In December of 2019, an unusual outbreak of pneumonia cases was documented in Wuhan, China. This pneumonia, called COVID-19, was caused by a novel beta-coronavirus, severe acute respiratory syndrome-related coronavirus 2 (SARS-CoV-2), with a high transmission rate and a staggering mortality rate; especially in patients with comorbidities[90–92]. The SARS-CoV-2 genome

sequence was reported shortly thereafter and indicated it bared a resemblance to other beta-coronaviruses, however, it had less than 25% similarity to the Spike (S) protein in other members of the family[93]. However, because of similarity to the SARS and Middle East respiratory syndrome-related (MERS) coronaviruses in this family, responsible for the pneumonia outbreaks in 2002 and 2012, respectively, the potential mechanism behind SARS-CoV-2 virulence was predominately known. The receptor binding domain (RBD) located on the S-protein binds to angiotensin-converting enzyme 2 (ACE2) expressed on alveolar epithelial cells, endothelial cells, macrophages, and monocytes to facilitate viral entry[93–96]. S-protein bound to ACE2 recruits the serine protease, TMPRSS2, which cleaves the S-protein at the S1/S2 and S2' sites to prime SARS-CoV-2 to fuse with the host cell[97]. The RBD is located on the S1 subunit and the S2 subunit can engage with the host cell membrane to facilitate fusion following cleavage[98,99]. Once endocytosed, the RNA genome either stimulates endosomal TLRs or is released and binds to cytosolic RNA sensors like RIG-I. These viral RNA sensors then activate NF-κB, which facilitates the expression of type I IFNs as well as other pro-inflammatory cytokines intended to curtail viral infection[100]. However, SARS-CoV-2 has evolved mechanisms to block the type I IFN response while simultaneously stimulating the secretion of high levels of chemokines and cytokines like IL-6, which can lead to the development of a deadly cytokine storm[101]. Only 21 months after the emergence the emergence of COVID-19, nearly 230 million people have contracted the disease and over 4.5 million have died from it (https://coronavirus.jhu.edu/map.html). These numbers continue to grow exponentially, primarily due to the emergence of multiple SARS-CoV-2 variants with enhanced transmission and a significant proportion of the global population that remains unvaccinated.

### 1.2.3 COVID-19 Pathophysiology

SARS-CoV-2 infected epithelial and endothelial cells may rapidly undergo apoptosis, resulting in vascular leak and a massive inflammatory response that exacerbates pulmonary symptoms characterizing the pathophysiology of COVID-19 [102]. A blunted type I IFN response as well as a cytokine storm characterized by elevated circulating levels of IL-6, TNF-α, IL-2R, and IL-10 is strongly associated with disease severity and mortality[103–105]. Infected ACE2 expressing monocytes may be stimulated by proinflammatory cytokines to differentiate into macrophages that can migrate into various tissues and contribute to viral propagation. Additionally, apoptotic bodies from infected cells may be phagocytosed by macrophages, leading to their infection and viral spread to distant tissues[100]. SARS-CoV-2 can also impact circulating lymphocyte populations, with severe cases presenting with a marked reduction in $CD4^+$ T cells, $CD8^+$ T cells, and total T lymphocytes. Additionally, IFN-γ production by $CD4^+$ T cells is reduced in severe cases, indicating a blunted Th1 immune response and inefficient T lymphocyte-mediated viral clearance[105]. Interestingly, the cardiovascular system and cardiovascular disease is strongly implicated in COVID-19 pathophysiology. SARS-CoV-2 internalization results in ACE2 shedding, decreasing the amount of angiotensin II that can be enzymatically converted to angiotensin I. This elevation in angiotensin II in the circulation results in vasoconstriction and increased inflammation, thus increasing thrombosis risk and aggravating cardiovascular disease[106].

### 1.2.4 Adaptive Immune Responses to COVID-19

Antibody responses are paramount for controlling pathogen infectivity. Patients that have recovered from SARS-CoV-2 infection present with high IgG and IgM titers directed against the S-protein as well as the nucleocapsid protein. Anti-S IgG antibodies display potent neutralizing capabilities, blocking its ability to bind ACE2 and infect cells[106]. Furthermore, T lymphocytes can recognize the S-protein, which causes activation and the production of IFN-γ[107]. The kinetics of

humoral and cellular immune responses to the original SARS-CoV give insight into SARS-CoV-2 infection and potential management strategies. Antibody titers steadily drop overtime[108], however, memory CD4 and CD8 T cells could be detected up to 17 years after infection, with the CD8 response being directed against the nucleocapsid and membrane proteins of SARS-CoV[107,109]. There is already evidence suggesting that antibody responses to SARS-CoV-2 may be short-lived, which has major implications for vaccine development[110]. Patients with mild symptoms display robust T cell responses relative to those with severe symptoms, even if antibody levels have dropped[111]. These findings indicate that vaccine approaches may be more successful if they are able to induce a robust memory T cell response rather than strictly focusing on short-term antibody production. This is of course unless the vaccine can facilitate a persistent B cell response, as proposed by Bachmann *et al.*[110].

### 1.2.5 COVID-19 Vaccine Strategies

If there is one positive that can be taken from the COVID-19 pandemic, it is the speed at which vaccines could be developed and deployed, which has saved countless lives. This is possible partially because traditional vaccine strategies were abandoned. These strategies typically involve identifying and developing attenuated viruses, purifying inactivated viruses, or purifying pathogenic peptides[112,113]. Most clinically utilized vaccines against COVID-19 are genetic medicines; they utilize nucleic acids (mRNA or DNA) encoding for the SARS-CoV-2 S-protein. Once injected, they rely on the patient's cellular machinery to synthesize the S-protein, which is then recognized by APCs and utilized to mount a humoral immune response to the S-protein antigen[114,115]. These vaccines have significant manufacturing advantages over conventional vaccines because nucleic acid sequences are easily manipulated without the need for post translation modifications, and therefore they can be developed at accelerated rates[116].

Moderna's mRNA-1273 vaccine as well as Pfizer/BioNTech's BNT162b2 vaccine are both mRNA-based, encapsulated within ionizable lipid based LNPs, and delivered via intramuscular injection. Both mRNA sequences include two proline substitutions that lock the expressed S-protein in the prefusion conformation, resulting in higher immunogenicity and neutralizing capacity[117–119]. In phase III clinical trials, these mRNA vaccines displayed excellent tolerability and 94-95% efficacy[35,36]. It is important to note that these trials were initiated prior to the wave of variants that overtook the original SARS-CoV-2 strain and therefore these efficacy rates are likely lower with the current variants[120,121]. The AstraZeneca ChAdOx1 nCoV-19 vaccine has a similar design to the mRNA vaccines, however, it uses an adenoviral vector to deliver DNA encoding the S-protein. The ChAdOx1 nCoV-19 DNA sequence encodes the full-length S-protein with a tissue plasminogen activator signal sequence upstream of the transgene, under control of the ubiquitous cytomegalovirus (CMV) promoter[122,123]. ChAdOx1 nCoV-19 efficacy was determined to be 62.1% with some adverse reactions being reported[124]. As expected, ChAdOx1 nCoV-19 has a lower neutralizing antibody titer against the new variants, but still provides protection from disease development[125].

The importance of a well-balanced T cell response following vaccination and SARS-CoV-2 exposure cannot be overstated. Studies examining potential vaccines for the original SARS-CoV found that inactivated virus vaccines induced a Th2 response following challenge, resulting in substantial lung pathology[126,127]. Conversely, $CD4^+$ T cells isolated from recovered COVID-19 patients display a classic Th1 response when stimulated with the S-protein. Most recovered patients also display a robust cytotoxic $CD8^+$ T cell response, however, the S-protein is not the dominant SARS-CoV-2 antigen recognized. Therefore, vaccines targeting only the S-protein may not produce a substantial $CD8^+$ T cell response, thus hindering the ability of the immune system

to clear SARS-CoV-2 infected cells[128]. Nevertheless, $CD4^+$ and $CD8^+$ T cells isolated from BNT162b1 (Pfizer's first-generation vaccine candidate) vaccinated patients both produced IFN-γ and IL-2, but not IL-4 when stimulated with the S-protein RBD antigen; consistent with a CTL and Th1 response[129]. Similarly, splenocytes isolated from mice vaccinated with mRNA-1273 displayed a balanced Th1/Th2 response, with $CD4^+$ T cells producing IFN-γ and IL-2 when stimulated with S1 and S2 peptide pools. However, $CD8^+$ T cells produced IFN-γ only when stimulated with S1 peptides[117]. These results indicate that it is possible to produce the desired immune response against SARS-CoV-2 following vaccination with S-protein based vaccines. It is still yet to be determined how long immunity will last and if additional booster doses will be required in the future.

## 1.3. Cancer and P53 Targeted Therapy

### 1.3.1. Cancer Treatment

Despite decades of research and rapidly advancing treatment modalities, cancer remains the second leading cause of premature death worldwide[130,131]. Cells are constantly exposed to exogenous stressors that can cause DNA mutations, such as ionizing radiation. Additionally, replication errors and defective DNA repair mechanisms can lead to a gradual accumulation of mutations over time, which can have disastrous consequences[132,133]. Multicellular organisms have evolved multiple tumor suppressive functions to prevent malignant transformation, such as cellular senescence and apoptosis. However, cancerous cells somehow seem to find numerous approaches to overcome these suppressive mechanisms. The Hanahan and Weinberg hallmarks of cancer illustrated some of these abilities, such as resistance to apoptotic stimuli, limitless proliferation, immune avoidance, constant mutation accumulation, metastasis, and many more[134,135]. These hallmarks are likely driven by natural selection because cells developing these characteristics

exhibit a survival and growth advantage that facilitates their propagation[136,137]. This also leads to difficulty in treatment, as cancer cells that adapt to resist cell death brought on by conventional genotoxic treatments like chemotherapy and radiation can divide and lead to new populations of treatment resistant progeny[138–140]. Taking all these factors into consideration, cancer can essentially be classed as a disease of dysfunction and chaotic cellular signaling, where almost everything that can go wrong will go wrong. This raises an important question; how do we treat chaos? One strategy has been developing precision treatments based on the unique gene signatures of individual cancers. Treatments targeting specific molecular targets have been utilized for many years with varying response rates depending on the target and cancer subtype[141,142]. In this section we will discuss one of the most elusive anti-cancer drug targets, tumor suppressor protein p53.

### 1.3.2. Tumor Protein P53

The tumor suppressor protein p53 has been deemed the 'guardian of the genome' due to its function in multiple anti-cancer pathways[143]. P53 is activated by a myriad of stresses, including but not limited to DNA damage, oxidative stress, oncogene activation, and cell cycle progression. Following exposure to these stresses, p53 is activated and functions as a transcription factor, leading to the expression of target genes that facilitate cell cycle arrest, DNA repair, senescence, and apoptosis. These include the cell cycle inhibitors p21 and 14-3-3σ, as well as the pro-apoptotic proteins Bax and NOXA[144]. In unstimulated cells p53 is normally kept at low levels through its interaction with the E3-ubiquitin ligase, mouse double minute homolog 2 (MDM2). The physical interaction between p53 and MDM2 prevents p53 from activating transcription, while MDM2-mediated ubiquitination of p53 signals it for proteasomal degradation[145,146]. A structurally homologous protein, MDMX/MDM4, has a similar role to MDM2 in negatively regulating p53 activity, except MDMX is not an E3 ubiquitin ligase and instead inhibits p53 transcriptional

activity by physical association[147,148]. Although, there is evidence that supports a model in which MDMX enhances the ability of MDM2 to ubiquitinate p53 [149].

Genotoxic stress has been found to activate p53, leading to its accumulation and transcription of p53-regulated genes[150–154]. Following DNA damage, the DNA damage response (DDR) pathway leads to activation of the ataxia–telangiectasia mutated (ATM) kinase, which phosphorylates Chk2. Both ATM and Chk2 phosphorylate p53 at Ser15 and Ser20, respectively, causing it to be released from MDM2 [155–157]. Phosphorylation of MDMX by Chk2 in response to ionizing radiation mediates an MDM2-dependent degradation[158,159]. MDMX phosphorylation by Chk1 in response to ultraviolet radiation results in MDMX nuclear export by enhancing binding to cytoplasmic 14-3-3γ [160]. In the case of oncogenic stimulation, cell cycle progression results in the activation of the cyclin dependent kinases, CDK4 and CDK6, which phosphorylate retinoblastoma protein (pRb) causing dissociation of the pRb-E2F complex. E2F, now free from inhibition, activates the transcription of multiple genes involved in the cell cycle, including ARF ($p14^{ARF}$ in humans and $p19^{ARF}$ in mice)[161]. ARF inhibits the ubiquitin ligase function of MDM2, thereby resulting in p53 accumulation[162]. Additionally, E2F can directly bind to p53 and block a nuclear export signal causing it to accumulate in the nucleus[163].

Since p53's critical role as a tumor suppressor was uncovered[164–168], there has been a significant research effort being directed to understanding the complexities of p53 signaling in cancer and in normal cell biology[169]. Despite this, the transcriptional regulation of p53 has been a relatively overlooked topic[170]. A handful of transcription factors have been found to directly bind to and regulate the p53 promoter. Positive regulators like Myc[171] and HoxA5 [172] are interesting as oncogenic Myc signaling is intricately linked to cancer progression[173] and HoxA5 appears to be an important tumor suppressor[174,175]. Understanding the regulation of p53 transcription in the context

of cancer is not a straightforward topic due to the complex interplay between transcription factors, epigenetic mechanisms, miRNAs, as well as the that impact mutant p53 (mup53) has on its own regulation[170].

### 1.3.3. P53 and Cancer

P53 is the most commonly mutated gene in cancer, with nearly 50% of all tumors displaying some form of mutation[176]. Even in the absence of a detectable mutation, some estimates predict that 80% of tumors have impaired p53 function, caused by factors such as epigenetic silencing or overexpression of a negative regulator like MDM2 [177,178]. The majority of p53 mutations are missense mutations that typically lead to accumulation of the mutant protein[179]. These missense mutations seem to be clustered into 'hotspots,' with ~25% of all mutations occurring at one of 6 codons within the DNA-binding domain of p53 [176,177]. These can be broken into two classes of mutations, DNA contact mutants (R248, R273) and p53 conformation mutants (R175, G245, R249, R282)[176,180]. The type of p53 mutation can have vastly different consequences on the cell, with these hotspot mutations being associated with p53 oncogenic gain of function (GOF). GOF mutations bestow mutant p53 (mup53) with novel tumor promoting capabilities not possessed by its wild type (WT) counterpart. If only one p53 allele is mutated a dominant negative (DN) effect may occur, where the mup53 can bind and sequester WT p53 thus blocking its normal function[179]. Additionally, the conformation mutation mup53$^{R175H}$ has been found to bind and sequester the tumor suppressors p73 and p63 [181], both of which facilitate expression of genes similar to p53 [182]. Expectedly, GOF mup53 plays a pivotal role in tumorigenesis and cancer progression. Mice possessing germline GOF mutations in one p53 allele develop unique tumors with high metastatic capacity when compared to p53$^{+/-}$ and p53$^{-/-}$ mice[183–185]. GOF mup53 has been demonstrated to affect multiple oncogenic signaling pathways, upregulating various stem cell markers in colorectal

cancer cells[186] and increasing human epidermal growth factor receptor 2 (HER2) expression in breast cancer cells[187]. In fact, mutation of p53 characterizes the progression of most forms of cancer[188–190].

P53 is implicated in virtually all the Hanahan and Weinberg "hallmarks of cancer." Activation of p53 in response to DNA damage, proliferation, and oxidative stress leads to cell cycle arrest and activation of apoptotic pathways[144]. P53 is intimately linked to cellular metabolism and functions to regulate nutrient availability and glycolysis[191,192]. In the context of tumor progression, WT p53 functions to prevent metastasis in part due to the expression of miRNAs that regulate the epithelial to mesenchymal transition[193,194]. This could possibly explain why most advanced cancers present with a mutation in p53 [189,190]. Inflammatory processes have an integral role in cancer progression. Inflammation is the bodies response to tissue damage, and it involves increased blood flow, secretion of proteins (cytokines, growth factors, enzymes), and the recruitment of immune cells to the affected area. These actions function to facilitate clearance of pathogenic material, remodel the extracellular matrix, as well as stimulate proliferation of fibroblasts, endothelial cells, and epithelial cells. In the context of cancer, immune cells accumulate at the site of neoplastic growth, due to immune recognition of cancerous cells and in response to cytokines released from cancer cells. These immune cells have a dual function, on the one hand they will attempt to eliminate the cancerous cells, but on the other hand the cytokines, growth factors, and enzymes they release are key factors in promoting tumor progression[195–197]. Obviously, p53 is activated in response to the proliferative signals brought on by inflammation, but the inflammatory response itself directly influences p53. Proinflammatory cytokines possess the ability to regulate p53 expression and accumulation[198,199]. The master regulator of inflammatory signals, NF-κB, is activated by various cytokines resulting in the transcription of anti-apoptotic

proteins, cytokines, and growth factors; all of which lead to enhanced tumorigenesis[200,201]. Despite the opposing functions of NF-κB and p53 on tumor progression, NF-κB has been found to directly bind to the p53 promoter and facilitate its expression, establishing a potential mechanism for negative regulation of tumorigenic inflammatory signals[202]. Clearly, the importance of p53 dysfunction in tumorigenesis cannot be overlooked. A handful of novel treatments are currently under development with the intention of targeting p53 and p53 signaling.

### 1.3.4. Restoring Endogenous P53 Signaling

Tumor suppressors evolved as a means to prevent malignant transformation, with oncogenic stimuli leading to their activation. As such, cancer cells are constantly activating the pathways that evolved to 'turn on' p53 signaling. However, with p53 function lost, they exist in a perpetual state of ineffective p53 activation. This led to the hypothesis that if normal p53 function were to be restored, cancer cells would be primed to arrest their growth and undergo apoptosis. Support for this method of treatment was strengthened following reports that replacement of WT p53 into p53-null cells lines resulted in arrested growth, increased apoptosis induction, and caused tumor regression *in vivo*[203,204]. P53 gene therapy was born in 1994 after Fujiwara, *et al.*[205] demonstrated that intratracheal administration of a retroviral vector expressing WT p53 suppressed the growth of established lung tumors *in vivo*. A small clinical trial was conducted in nine non-small cell lung cancer (NSCLC) patients and found that bronchoscopic administration of the retroviral-WT p53-vector suppressed tumor growth and increased the presence of the TUNEL apoptosis marker at follow-up[206]. A major limitation of this study was the use of the retroviral vector, which has significant safety concerns, mainly, the risk of insertional mutagenesis[13]. To overcome these issues, studies examining the use of an adenoviral WT p53 expression vector (Ad-p53) were conducted in multiple cancer subtypes and demonstrated similar effects – apoptosis induction and arrested

growth *in vitro* and *in vivo*, with genotoxic combination therapy resulting in a synergistic effect[207–209]. Clinical trials with this treatment have produced mixed results. Intratumoral injection of Ad-p53 in NSCLC patients resulted in a clinical response in 72% of patients[210], and intratumoral injection into patients with head and neck cancer resulted in a clinical response in 47% of patients[211]. These response rates could be strengthened by combining Ad-p53 treatment with radiation therapy[212,213]. Because of the encouraging response in patients with head and neck cancer, in 2003 China granted regulatory approval for the Ad-p53 treatment, making it the first gene therapy product ever approved[214]. Thousands of cancer patients have received some form of restorative p53 gene therapy with varying success rates. It appears restoring endogenous p53 activity via genetic means represents a safe method for controlling tumor growth, however, some form of genotoxic combination therapy seems to be necessary to produce meaningful response rates. Unfortunately, the addition of Ad-p53 often does not produce a survival benefit when compared to genotoxic treatment alone, which raises concerns about its potential use in the future[215]. The variation in response to Ad-p53 treatment could potentially be due to the presence of different p53 mutations. Wang *et al.*[216] found that restoring endogenous p53 function in mice harboring the $p53^{R172H}$ mutation (analogous to the R175H hot-spot mutation in humans) did not lead to tumor regression as it does in p53-null mice. Mutant $p53^{R172H}$ was demonstrated to bind to the restored WT p53 and exert a dominant negative effect that prevented the expression of pro-apoptotic proteins but not proteins involved in cell cycle arrest. Additionally, cancer cells with WT p53 would be largely unaffected by p53 restoration, as the p53 signaling network is still relatively intact[217,218]. These studies demonstrate the importance genetic profiling prior to implementing precision anti-cancer therapy, especially one as specific as restoring p53.

In the case of cancer cells with WT p53 that display overexpression of a negative regulator, there are several treatment modalities being explored for each indication. Perhaps the most promising and intensively studied are inhibitors of the MDM2-p53 interaction. The discovery that the small molecule nutlin-3a could bind to MDM2 and release p53 from its inhibition, resulting in apoptosis and hindered tumor growth *in vivo*[219], spurred the development of multiple small molecule MDM2 antagonists[220–224]. In patients with liposarcoma, the MDM2 antagonist, RG7112, was able to facilitate p53 accumulation and control tumor growth. However, 40% of patients presented with serious adverse events, primarily neutropenia and thrombocytopenia[225]. This is presumably due to increased apoptosis in hematopoietic progenitors in which the MDM2-p53 axis plays an essential role in differentiation[226]. Of the MDM2 antagonists currently in clinical trials, most compounds display similar results to RG7112 with the newer generation drugs demonstrating a slightly improved safety profile[225]. Due to the early clinical stages of these compounds, few have evaluated clinical responses to treatment and overall survival. One compound, MK-8242, tested in patients with liposarcoma resulted in a median progression free survival of 237 days. Unfortunately, due to the small cohort size a proper control was not included in this study and the authors compared their median progression free survival to that of another study that reported a median progression free survival of 126 days in patients with liposarcoma treated with a CDK4 inhibitor[227]. These studies indicate promise for development of MDM2 antagonists, however, larger double-blinded studies will be necessary before any meaningful conclusions can be made.

Targeting the MDMX-p53 interaction represents an alternative strategy for restoring p53 activity as it may result in fewer side effects than MDM2 antagonists. Hematopoietic stem cells recover from short term p53 restoration in mice lacking MDMX, presumably due to functional MDM2 retaining the ability to regulate p53 activity[228]. MDMX targeted treatments are still in

preclinical stages and a handful of promising compounds have been identified[229]. One of the most interesting MDMX inhibitors is an antisense oligonucleotide (ASO) directed against full length MDMX. Dewaele *et al.*[230] discovered that adult tissue lacked full length MDMX primarily due to inefficient splicing of Mdmx mRNA at exon 6, which does not occur in cancer cells. They designed a cancer-selective MDMX-ASO that targets the exon-intron boundary of exon 6 and leads to reduction in MDMX protein levels, impaired *in vitro* growth, increased apoptosis induction, as well as attenuated *in vivo* growth of both melanoma and large B cell lymphoma patient derived xenografts.

A relatively new approach for restoring WT p53 signaling involves targeting mutant forms of p53 and restoring their activity, primarily by reversing conformational changes acquired by mutation. The most clinically advanced compound, PRIMA-1, was able to preferentially inhibit the growth of tumor cell lines with the R273H DNA contact mutant or the R175H conformation mutant[231]. Upon entry into cancer cells, PRIMA-1 is converted to methylene quinuclidinone that covalently binds to the p53 core via alkylation of cysteine residues. This may prevent the formation of disulfide bonds that fix mup53 in an unfolded conformation or it may prevent aggregation of mup53, thus enabling the mup53 to bind DNA and activate the transcription of WT p53 genes[232]. Patients with acute myeloid leukemia or myelodysplastic syndromes with at least one p53 mutation that received the PRIMA-1 derivative, APR-246 (eprenetapopt), in combination with the first line therapy, azacytidine, displayed favorable response rates and a potentially increased survival when compared to previously published data on monotherapy with azacytidine alone, thus warranting future clinical examination[233]. Another compound, PK7088/PK083, targets p53 with a Y220C mutation, which is the ninth most common p53 mutation. PK7088 binds mup53 in a pocket created by the Y220C mutation and slows its denaturation[234]. This results in a restoration of the WT p53

conformation, nuclear accumulation of p53, and the expression of p53 dependent genes, which facilitate cell cycle arrest and apoptosis induction[234]. Other indirect methods of restoring the WT p53 conformation have also been discovered. The small molecule chetomin was identified in a high throughput screen and preferentially facilitated p53 gene expression and apoptosis induction in cell lines and tumors containing the R175H mutation. Interestingly, chetomin does not bind mup53 and instead increases the binding affinity of Hsp40 for mup53$^{R175H}$. Hsp40 bound to mup53$^{R175H}$ stabilizes the unfolded protein, restoring its function[235]. The preclinical results from these compounds are encouraging and indicate that we may soon have a tool belt full of p53 targeting drugs entering the clinic[236].

### 1.3.5. Inhibiting Oncogenic Gain of Function p53 Signaling

As if understanding endogenous p53 signaling was not complicated enough[169], even understanding p53 mutation is not a straightforward topic. Contrary to most tumor suppressor genes that undergo a loss-of-function following mutation, p53 can lose its endogenous function while simultaneously gaining novel tumor promoting capabilities. DNA contact mutants and conformational mutants alter the DNA binding domain, which can alter the DNA elements recognized by p53 and result in the expression of tumorigenic genes involved in apoptosis resistance, proliferation, angiogenesis, and metastasis[179]. Additionally, mup53 may associate with other oncogenic proteins and facilitate activation of their tumorigenic pathways[237].

In some cases, cancer cells possessing a GOF mutation in p53 are dependent on it for their survival as knock down of mup53 abrogates tumorigenic potential *in vitro* and *in vivo*[238,239]. In a proof-of-concept experiment, Alexandrova *et al.*[240] demonstrated that genetically ablating mup53$^{R248Q}$ slowed tumor growth and prolonged survival. The authors also demonstrated that Hsp90 is responsible for stabilization of mup53 and the addition of the Hsp90 inhibitor, ganetespib,

increased median survival in mice possessing either the R248Q or the R172H (R175H in humans) p53 mutant by 59% and 48%, respectively, while it had no effect on p53-null mice. Ganetespib mediated inhibition of Hsp90 results in selective degradation of mup53 that is accompanied by apoptosis induction, thus providing strong evidence that elimination of GOF mup53 represents a viable treatment option. Histone deacetylase inhibitors (HDACi) represent an alternative strategy to enhance mup53 degradation. The HDACi, suberoylanilide hydroxamic acid (SAHA), was found to inhibit HDAC6 and as a result Hsp90 remains acetylated at K294, which inhibits its chaperone activity. In turn, mup53 is released from Hsp90 and degraded resulting in apoptosis induction selectively in cancer cells harboring mup53 (IC50 values are >100X higher in cells with WT p53)[241]. Unfortunately, clinical trials with both ganetespib and SAHA have not been very promising. Patients in these trials were not selected based on their p53 status and therefore it is entirely possible that the efficacy of these two compounds can be significantly improved by altering the inclusion criteria[242,243].

Perhaps one of the more obvious strategies to inhibit GOF mup53 would be via knock down with siRNA. However, this may lead to inadvertent side effects due to p53 loss in healthy tissues. Martinez *et al.*[244] demonstrated that siRNAs can be designed to preferentially recognize single nucleotide changes in p53 mRNA by ensuring that the ninth nucleotide in the siRNA contained the mutated base pair. Recently, Ubby *et al.*[245] generated a panel of siRNAs targeting each GOF mup53 and used LNPs to deliver them to subcutaneous tumors, where they abrogated tumor growth. Though clearly still in its infancy, the preclinical data has indicated that eliminating mup53 can have potent anti-tumor effects.

### 1.3.6. Exploiting Dysfunctional p53 Signaling

Rather than trying to correct the problems brought on by p53 mutation, an alternative approach is to capitalize on it and utilize the dysfunction for treatment options. The earliest example of this is ONYX-015, a replication competent adenovirus that selectively infects and lyses cancer cells lacking functional p53. By removing the E1B gene that normally functions to inactivate p53 [246], the adenovirus would only be able to replicate in cells lacking p53 as cells with a functional copy of p53 would block viral replication by undergoing apoptosis or arresting their growth[247]. However, subsequent reports found that viral replication was not restricted to cells lacking p53, but rather it showed some preference for replicating in cancer cells with mup53 [248–251]. Unfortunately, ONYX-015 failed clinical trials as a monotherapy, because although it had a favorable safety profile, it demonstrated minimal antitumor efficacy[252,253]. However, ONYX-015 was able to sensitize cancer cells to chemotherapy[253–255], which reinvigorated interest in the treatment and eventually led to regulatory approval of a similar oncolytic virus (H101) in China[256].

GOF mutations in p53 can result in unique gene expression signatures relative to WT p53 possessing counterparts[179]. Because of this, mup53 may facilitate the expression of druggable genes offering a novel approach for targeting cancer. For example, mup53 can bind and sequester p73, which enables NF-Y to be released from p73 and facilitate the expression of platelet-derived growth factor receptor β (PDGFR-β). Consequentially, PDGFR-β then stimulates invasion and metastasis. However, this also enables the process to be blocked by adding PDGFR-β inhibitors like imatinib and crenolanib[257]. Mutant p53 has also been demonstrated to directly bind to NF-Y and recruit p300 in response to DNA damage, leading to expression of genes involved in cell cycle progression that would normally be inhibited in response to stress[258]. P300 is a histone acetyltransferase and is therefore a druggable target. In fact, several p300 (and CREB-binding protein) inhibitors are currently under development and clinical investigation for the treatment of

multiple cancer subtypes[259–261]. Mutation of p53 can also lead to substantial immune dysfunction, resulting in the secretion of tumorigenic cytokines that support cell growth and cancer progression[262]. However, missense mutations in p53 have recently been demonstrated to increase expression of programmed cell death ligand 1 (PD-L1) and can therefore be utilized to predict treatment responses to the anti-PD-L1 immune checkpoint inhibitor, nivolumab[263,264].

A different approach for targeting p53 dysfunction that is of particular interest to our group (and the subject of chapter 3 in this thesis), is targeting p53 transcriptional activation. Typically, p53 activation is thought of as accumulation of p53 protein due to decreased turnover by MDM2[155–157,162]. However, p53 transcription is induced by multiple oncogenic stimuli. For example, DNA damaging chemotherapeutic agents and ionizing radiation have been found to increase p53 transcription[150,151,154]. The DDR pathway leads to activation of Chk1 and Chk2 [265], both of which lead to the accumulation of p73 and E2F1 [266]. These two proteins have been found to directly bind to the p53 promoter and facilitate p53 transcription[150,151]. In turn, p53 functions to induce the transcription of p21, which facilitates downregulation of Chk1 thus stopping the DDR signaling[267]. Additionally, various oncogenes have been demonstrated to directly bind to the p53 promoter and facilitate its expression, for example, c-Myc[171] and NF-κB[268]. In most cases, p53 acts as a negative regulator of these oncogenes, inhibiting their activity as well as their transcriptional activation of the p53 promoter following induction[269,270]. As p53 is a master regulator of its own transcription, it is enticing to speculate about the impact that a loss of p53 function would have on the transcriptional activation state of p53. We hypothesize that loss of p53 in cancer cells would lead to a non-productive upregulation of p53 transcription due to a loss of p53-mediated negative feedback. The challenge becomes developing a treatment strategy that can capitalize on this

dysfunctional network. Fortunately, gene therapy offers a means to achieve this with the utilization of DNA based treatments.

## 1.4. Senescence and Anti-Aging

### 1.4.1. Cellular Senescence

For years, humans have viewed aging as an unrelenting, uncompromising, unstoppable natural process. Over the years, researchers have uncovered a small population of cells that contribute to the aging process. These cells, termed senescent cells, are aged cells that have undergone irreversible growth arrest and are responsible for organ function decline and disease development. Excitingly, elimination of senescent cells has been demonstrated to reduce age-related disease development and improve lifespan, leading to novel anti-aging treatments being uncovered[271,272].

To understand how to pharmacologically 'reverse' aging, it is necessary to first understand the molecular mechanisms driving cellular senescence. First described in 1964, the Hayflick limit defined the finite number of population doublings possible in human diploid cells[273]. This was later understood to be caused by telomere shortening. Following each genome replication, the telomeric DNA 'caps' (TTAGGG repeats) located on the 3' end of double stranded DNA are not fully replicated, therefore leading to progressively shorter telomeres after each cell division until DNA can no longer be replicated; resulting in senescence[274]. Despite its poor reputation, cellular senescence has a very important biological role, mainly tumor suppression. The same cellular stressors that lead to oncogenic transformation, like DNA damage and oncogene activation, also induce cellular senescence. Irreversible growth arrest serves as the tumor suppressive counterpart to limitless replication[275]. So, how does the cell signal senescence induction in response to stress? Through similar pathways involved in tumor suppression, mostly p53 and $p16^{Ink4a}$. As described

in Section 1.3 ii, DNA damage triggers the DDR pathway, which through activation of ATM and Chk2, leads to release of p53 from MDM2 and transcription of p53-target genes, the most important being p21 [155–157]. P21 functions as a ubiquitous CDK inhibitor, though it primarily inhibits the activity of CDK2, which halts the cell cycle at the G1/S phase[276,277]. Interestingly, shortened telomeres are recognized by the DDR as double-strand DNA breaks and thus result in p53/p21 mediated cell cycle arrest[278].

Like p53, understanding the regulation of $p16^{Ink4a}$ is not a straightforward topic due to the complex interplay between different pathways and stimuli. Mitogenic stimulation facilitates cell cycle progression via activation of CDK4/6, which phosphorylate pRb, causing E2F to be released and activate gene expression required for entry into S phase[161]. Cell cycle progression is blocked by $p16^{Ink4a}$ mediated inhibition of CDK4/6. As a result of CDK4/6 inhibition, pRb remains hypophosphorylated and sequesters E2F in the cytosol, preventing cell cycle progression. Cell cycle progression facilitates the activation of both p53 and $p16^{Ink4a}$ pathways. As mentioned previously, E2F causes ARF to be expressed, which releases p53 from MDM2-mediated inhibition[162]. E2F also facilitates transcription of DNA methyltransferase 1 (DNMT1), which normally functions to inhibit the $p16^{Ink4a}$ promoter. However, in the case of hyper-cell proliferation, as is the case for most oncogenes, production of reactive oxygen species (ROS) increases[279]. Increased ROS inhibits DNMT1 expression and reduces the activity of E2F. Low DNMT1 expression results in reduced H3K9 dimethylation in the $p16^{Ink4a}$ promoter resulting in increased $p16^{Ink4a}$ expression[280]. The DDR pathway also feeds into the $p16^{Ink4a}$ pathway by means of increased ROS production. DNA damage results in p21 activation, which signals through p38-MAPK (mitogen-activated protein kinase) to increase mitochondrial ROS production[281]. ROS either produced via the p21 pathway or via mitogenic signaling activates protein kinase C (PKC)-

δ [282] and in turn PKC-δ activates NADPH oxidase to produce more ROS. Expression of E2F regulated genes normally function to inhibit the PKC-δ/ROS feedback loop, however, activation of pRb via $p16^{Ink4a}$ mediated inhibition of CDK4/6 blocks E2F from activating this expression pathway. Thus, $p16^{Ink4a}$ activity maintains high levels of ROS production in senescent cells by sustaining the PKC-δ/ROS positive feedback loop[283], and ROS facilitates $p16^{Ink4a}$ expression by reducing DNMT1 expression[280]. DNA damage in the absence of oncogene activation can also result in ROS production, stimulating $p16^{Ink4a}$ transcription[280].

Oncogene activation has also been demonstrated to have a direct role in $p16^{Ink4a}$ expression. Activation of oncogenic RAS signaling stimulates MAPK-mediated phosphorylation of the Ets family of transcription factors[284]. Ets1 and Ets2 both directly bind and stimulate transcription from the $p16^{Ink4a}$ promoter, with Ets2 being involved in initiating $p16^{Ink4a}$ transcription and Ets1 maintaining expression in senescent cells[285]. RAS/MAPK signaling also leads to phosphorylation and accumulation of HMG box-containing protein 1 (HBP1)[286], which directly binds to the $p16^{Ink4a}$ promoter and stimulates its expression[287]. Furthermore, RAS is involved in the epigenetic regulation of the $p16^{Ink4a}$. RAS signaling facilitates recruitment of the H3K4 methyltransferase, MLL1, as well as the DDB1-CUL4-ROC1 complex to the $p16^{Ink4a}$ promoter; both of which are required for H3K4 trimethylation and activation of transcription[288]. Cumulative stress brought on by aging has been demonstrated to correlate with a global reduction of the histone methyltransferase, EZH2 [289]. This causes polycomb-repressive complex 2 (PRC2) to dissociate from the $p16^{Ink4a}$ promoter resulting in decreased H3K27 trimethylation and activation of $p16^{Ink4a}$ expression[290].

Cellular senescence is a coordinated effort between both the p53/p21 axis and the $p16^{Ink4a}$/pRb axis. As cells begin losing growth potential, p21 accumulates, but rapidly decreases

following senescence induction, concurrent with a rapid increase in $p16^{Ink4a}$ that persists for the life of the senescent cell. These findings therefore indicate that the initiation of senescence molecular programs is brought on by p53 and p21, while $p16^{Ink4a}$ is involved in maintaining senescence[291–294]. Therefore, increased expression of $p16^{Ink4a}$ is largely considered the most important marker of biological age[295].

### 1.4.2 Senescence and Health

With such an integral role in tumor suppression, it is difficult to imagine a problem with cellular senescence. However, senescence is a two-way street – as cell growth is halted, tissue dysfunction increases. This is largely mediated by the senescence-associated secretory phenotype (SASP) that is engaged in senescent cells. The SASP is a collection of proinflammatory cytokines and chemokines, growth factors, proteases, and extracellular matrix components[296]. These SASP factors influence the microenvironment by promoting inflammation, which ultimately decreases organ function. Additionally, growth factors and proinflammatory cytokines/chemokines can encourage tumorigenesis by facilitating proliferation, angiogenesis, and metastasis; thus, counteracting role of senescence in tumor suppression[296–300]. Not surprisingly, the DDR and oncogene signaling are also responsible for activating the expression of SASP components[301,302]. The SASP, like most senescent cell features, serves an important function in an acute setting. Initially, the SASP has an important tumor suppressive role. IL-6, IL-8, and GROα secretion have an autocrine effect and reinforce senescent growth arrest[303,304]. Additionally, SASP components like IL-1, TGF-β, VEGF, and CCL2 can function in a paracrine fashion, inducing senescence in neighboring cells via activation of $p16^{Ink4a}$ and p21 [305]. Inflammation is also acutely beneficial as increased recruitment of inflammatory cells can enable identification of cells expressing oncogenes and facilitate their removal, preventing malignant transformation[305,306]. However,

immune function declines as we age and therefore, rather than these senescent cells being eliminated, they persist and can enhance the tumorgenicity of surrounding cells influenced by their SASP[275].

Senescence induction and the SASP have a critical role in wound healing. Wound repair is a highly orchestrated effort between multiple cell types and multiple cellular programs, such as clot formation, re-vascularization, re-epithelialization, and matrix reorganization[307]. Senescent fibroblasts and senescent cells appear immediately following injury, and secrete VEGF and PDGF-AA, resulting in re-vascularization and myofibroblast differentiation, respectively[308]. Consequently, myofibroblasts stimulated by CCN1 undergo senescence to prevent excessive fibrosis following tissue repair[309]. Proteases facilitate breakdown of fibrotic scars and recruitment of immune cells to injured areas ultimately results in the clearance of senescent cells and reversal of fibrosis[310].

The distinction between acute and chronic senescence appears to be essential for understanding aging. As described above, senescence and the SASP acting in an acute fashion has an immediate and beneficial role in wound healing and tumor suppression. This is mostly due to the rapid elimination of senescent cells following completion of the intended biological process. However, as senescent cells are no longer cleared, they begin to accumulate and negatively influence the tissue microenvironment. Not surprisingly, senescent cells no longer fulfil their necessary biological function. For example, a senescent hepatocyte will no longer participate in metabolism and protein homeostasis. Though senescent hepatocytes (or other cell types) are not a problem in small numbers, the SASP can cause other hepatocytes to become senescent, contributing to organ function decline[311]. Additionally, the SASP can cause resident tissue stem cells to become dysfunctional, resulting in the pool to become exhausted, which reduces cell

turnover and tissue rejuvenation. Furthermore, degradation of the extracellular matrix, tissue fibrosis, and inflammation are all induced by SASP components and have a considerable negative effect on organ function[272]. Therefore, a single senescent cell can have a profound impact on tissue function, reaching far beyond its immediate loss of function.

Senescence has been implicated in numerous of diseases. Several senescent markers have been identified in the lungs from patients with idiopathic pulmonary fibrosis[312,313], and their expression can be induced by genetic or environmental factors[314]. Obesity and type 2 diabetes are also heavily influenced by cellular senescence[315]. Adipose tissue in obese patients can enter a chronic inflammatory state with increased cytokine secretion and immune cell infiltration, which contributes to insulin resistance[316]. Obesity is associated with increased p53 expression in adipose tissue, which facilitates senescence induction, leading to expression of proinflammatory SASP factors that exacerbate inflammation and contribute to further insulin resistance[317]. Insulin resistance is a precursor to type 2 diabetes due to a compensatory exhaustion of islet β-cells overproducing insulin[316]. As insulin production begins to decline, β-cells undergo senescence, presumably due to increased ROS production and p38-MAPK activation[318]. Frailty is perhaps the most common pathology associated with old age. Unsurprisingly, muscle satellite cells (resident stem cells) undergo senescence in a CCN1 and p38-MAPK dependent manner, resulting in decreased regeneration and sarcopenia[319–322].

### 1.4.3 Senolytics: Pharmacological Elimination of Senescent Cells

With senescence being implicated in nearly all aspects of aging and disease development, it is easy to hypothesize about the impact that senescent cell clearance could have on overall health. Targeted elimination of $p16^{Ink4a}$-expressing cells offers an effective means to selectively eliminate senescent cells. In both naturally aged mice and the rapidly aging $BubR1^{H/H}$ mouse model,

genetically modifying the animals to include a suicide gene under control of the $p16^{Ink4a}$ promoter was found to decrease the incidence rate of several senescence markers, improve organ function, and increase lifespan[323,324]. Not only did these experiments identify $p16^{Ink4a}$ as a critical factor in aging and tissue function decline, but they also demonstrated that senescent cells represent a viable therapeutic target to prevent or reverse age-related disease development. The first pharmacological agents found to eliminate senescent cells was a combination of two drugs, dasatinib and quercetin, that were identified by analyzing the RNA expression profile of senescent cells relative to non-senescent cells[325]. This drug cocktail decreases multiple markers of senescence, improves physical and organ function, and increases survival *in vivo*[325,326]. Dasatinib and quercetin have already undergone clinical testing. In patients with diabetic kidney disease, a single 3-day treatment cycle decreased circulating levels of the SASP markers IL-6, IL-1α, and MMP-2/9/12. Additionally, adipose and epidermis displayed lower $p16^{Ink4a}$ and p21 expression relative to baseline samples[327]. In patients with idiopathic pulmonary fibrosis, a 3-week treatment cycle of dasatinib and quercetin improved physical function, which was correlated to lower levels of several SASP markers[328].

Another class of senolytics targets the B-cell lymphoma 2 (BCL-2) family of anti-apoptotic proteins that are upregulated in senescent cells and serve to resist apoptotic stimuli, were identified from the same screen that led to the identification of dasatinib and quercetin[325]. ABT-737 and its orally bioavailable counterpart ABT-263, are BH3 mimetics that bind to BCL-2 proteins and prevent them from inhibiting the pro-apoptotic proteins, Bax, Bak, Bok[329,330]. Both compounds were found to selectively eliminate senescent cells. ABT-737 was found to eliminate senescent cells from the lungs and epidermis of irradiated mice and mice induced to increase p53 activation, respectively[331,332]. ABT-263 was also found to eliminate senescent hematopoietic stem cells and muscle stem cells, which enables the remaining stem cell populations to rejuvenate the population

and tissue function[333]. Though p53 is implicated in senescence induction, its pro-apoptotic functions suggest potential to overcome growth arrest. The MDM2 antagonist, nutlin-3a, was found to induce a reversible growth arrest relating to p53 activation. However, secretion and expression of several SASP markers (including IL-6, IL-8, IL-1A) was decreased and treated senescent cells were no longer able to enhance tumorigenesis[334]. Perhaps the most exciting p53 targeted senolytic is the FOXO4 D-Retro Inverso (FOXO4-DRI) peptide. FOXO4 is upregulated in senescent cells and functions to inhibit apoptosis by interacting with p53. By attaching a CPP to the FOXO4-DRI, the senolytic can be endocytosed and the FOXO4-DRI can interact with the binding domain of endogenous FOXO4 causing p53 to be released and activate apoptosis selectively in senescent cells. FOXO4-DRI treatment was found to ameliorate chemotoxicity *in vivo*, as well as restore physical and kidney function in a rapidly aging mouse model[335]. Targeting $p16^{Ink4a}$ expressing cells with pharmacological agents has proven not to be a straight-forward task, as there are currently no senolytics agents that can directly target this pathway. However, we hypothesize that mimicking the design of the original transgenic mouse models, where suicide gene expression was linked to the $p16^{Ink4a}$ promoter, with a DNA-based gene therapy will offer a means to directly eliminate $p16^{Ink4a}$ expressing cells.

### 1.5. Hypothesis and Aims

Given the immense potential that gene therapy holds, we sought to develop novel methods to deliver genetic medicines as well as novel approaches to treat multiple diseases. Viral and non-viral nucleic acid delivery vehicles have multiple strengths and weakness that impact their clinical success. In the first chapter of this thesis, we hypothesize that combining the positive aspects of viral and non-viral nucleic acid delivery platforms we will be able to generate a highly effective and safe nucleic acid delivery vehicle. I test whether this combination platform can be utilized to

deliver pDNA, a nucleic acid that is typically restricted to viral delivery platforms, and then compare its efficacy and safety to other clinically approved non-viral platforms. In the next chapter, we examine the applicability of this platform to treat disease. We developed a DNA-based COVID-19 vaccine that we hypothesize will be able to illicit robust immune responses comparable to other clinically approved vaccines, without some of the limitations that have hindered their implementation in developing nations. In the third chapter, I describe the development of a novel anti-cancer suicide gene therapy that relies on transcriptional activation of p53 to function. We hypothesize that p53 inactivation in cancer cells will lead to a loss of p53-mediated negative feedback, and therefore, p53 transcription will be highly upregulated relative to non-cancer cells. By incorporating the p53 promoter region in a plasmid DNA construct, we speculate that gene expression can selectively be induced in cancer cells. Finally, in the fourth chapter I use the same p53 suicide gene construct as well as an additional suicide gene construct that requires transcriptional activation of the $p16^{Ink4a}$ promoter to function to selectively target senescent cells. This approach is based on the groundbreaking study on senescent cell elimination where Baker *et al.*[323] generated a genetic mouse model where the $p16^{Ink4a}$ promoter drove the expression of an inducible suicide gene. Using this $p16^{Ink4a}$ promoter the authors were able to restrict the expression of the suicide gene to senescent cells. We hypothesize that a senolytic that requires the activation of the early and late senescence mediators, p53 and $p16^{Ink4a}$, respectively, would offer a means to eliminate senescent cells with minimal off-target effects. The research presented in this thesis not only describes a novel approach to deliver nucleic acids, but it also explores new ways to target genetic medicines to certain tissues. This knowledge can be utilized to develop new therapeutics or repurpose previously failed genetic medicines.

# **Chapter 2:** Safe and Effective Delivery of Nucleic Acids Using Proteolipid Vehicles Formulated with Fusion-Associated Small Transmembrane Proteins

# Safe and Effective Delivery of Nucleic Acids Using Proteolipid Vehicles Formulated with Fusion-Associated Small Transmembrane Proteins

Douglas W. Brown[1], Ping Wee[2], Prakash Bhandari[2], Manoj Parmar[2], Hector Vega[2], Liliya Grin[2], Deborah Sosnowski[1], Maryam Hejazi[1], Jennifer Gyoba[2], Jailal Ablack[3], Eileen K. Clancy[4], Desmond Pink[1], Jitendra Kumar[2], Paola Solis Ares[2], Suellen Lamb[1], Nichole McMullen[4], Duncan MacKenzie[4], Perrin H. Beatty[2], Henry Garcia[5], Matthew Scholz[5], Roy Duncan[2,4], Arun Raturi[1,2]*, and John D. Lewis[1,2,3,5,6]*

[1] Department of Oncology, University of Alberta, Edmonton, Alberta, Canada, T6G 2E1.
[2] Entos Pharmaceuticals, 10230 Jasper Avenue, Suite 4550, Edmonton, Alberta, Canada, T5J 4P6
[3] OncoSenX, 701 Fifth Ave, Suite 4200, Seattle, Washington 98104
[4] Department of Microbiology & Immunology, Dalhousie University, Halifax, Nova Scotia, Canada, B3H 4R2
[5] Oisin Biotechnologies, 701 Fifth Ave, Suite 4200, Seattle, Washington 98104
[6] Lead Contact: John D. Lewis.
*Correspondence to: John D. Lewis, University of Alberta, Katz Group Centre, 5-142, Edmonton, Canada. Phone: 780.492.6113, Email: jdlewis@ualberta.ca; and
Arun Raturi, Entos Pharmaceuticals, 4550-10230 Jasper Ave., Edmonton, AB T5Y 4P6. Email: arun.raturi@entospharma.com.

Figures (6) and Tables (1)

In Brief:
We developed a proteolipid vehicle formulated with viral fusion-associated small transmembrane proteins and well-tolerated lipids that demonstrated effective intracellular delivery and expression of messenger mRNA and plasmid DNA payloads, with broad biodistribution and low immunogenicity that was redosable over long periods.

**Abstract**

Genetic medicines hold great promise to treat a wide array of diseases, yet success in the clinic has been hindered by limitations in the tolerability, scalability, and immunogenicity of current delivery platforms. We sought to overcome these limitations by combining aspects from viral and non-viral platforms to develop a proteolipid vehicle (PLV) that incorporates fusion-associated small transmembrane (FAST) proteins from fusogenic orthoreoviruses into a well-tolerated lipid formulation using a scalable microfluidic mixing approach. We screened a library of FAST recombinants to identify a chimeric FAST protein with enhanced membrane fusion activity. A series of lipid formulations incorporating the chimeric FAST protein were optimized for high nucleic acid encapsulation, charge neutralization, and improved tolerability *in vitro* and *in vivo*. FAST-PLVs administered systemically in mouse and non-human primate models demonstrated broad biodistribution and significantly improved intracellular delivery and expression of messenger RNA (mRNA) and plasmid DNA (pDNA). At high local or systemic doses FAST-PLVs showed low immunogenicity and maintained activity upon repeat dosing over long periods. We utilized FAST-PLVs to deliver a pDNA follistatin gene therapy *in vivo* that increased circulating levels of follistatin, resulting in significantly increased muscle mass and grip strength. The activity and safety profile of FAST-PLVs make them a promising alternative platform for redosable gene therapies and genetic medicines.

Keywords: Encapsulation, FAST proteins, FAST-PLV, Gene therapy, Nucleic acid delivery, Proteolipid Vehicle, PLV, p14endo15, follistatin.

## 2.1. Introduction

The potential for genetic therapies to treat illness ranging from monogenic disease to cancer has resulted in over 2600 clinical trials and culminated in ten nucleic acid drugs receiving regulatory approval by the United States Food and Drug Administration (FDA) [336]. Despite this substantial research investment, gene therapy is still considered experimental by the FDA, with the primary limitation being the lack of a non-toxic and durable nucleic acid intracellular delivery platform [337]. The approval of alipogene tiparvovec (Glybera) to treat lipoprotein lipase deficiency in 2012 catalyzed an industry shift towards the use of adeno-associated virus (AAV) vectors [338,339]. Though safer than many traditional viral vectors, AAV use is limited by the existence of neutralizing antibodies with no prior AAV vector exposure [340–343]. Host immunogenic responses against the AAV vector can also inhibit gene transfer following repeat dosing unless multiple AAV serotypes are employed [344].

Non-viral delivery vectors such as lipid nanoparticles (LNPs) are traditionally used for RNA-based gene therapy approaches (siRNA, miRNA, mRNA) and have cost, manufacturing, and immunogenicity advantages over viral vectors [345–351]. The recent FDA approval of patisiran (Onpattro) has set the stage for more systemic non-viral nucleic acid therapies in the near future [352]. LNPs are formulated with cationic or ionizable lipids that neutralize the anionic charge of nucleic acids and facilitate the endosomal escape of encapsulated nucleic acids through charge-mediated lipid bilayer disruption[353–356]. Contemporary LNPs are formulated with ionizable lipids such as DLin-MC3-DMA (MC3), which become positively charged in the acidic endosomal compartment, facilitating endosomal escape. While ionizable lipids have substantially improved tolerability compared to cationic lipids, their mechanism of action potentiates apoptotic cell death,

which translates to tolerability challenges after local delivery and dose-limiting liver toxicity following systemic delivery[357–359].

Given the strengths and limitations of current viral and non-viral approaches, we sought to combine key features from each to potentiate effective intracellular delivery of nucleic acid payloads with low immunogenicity and high tolerability while allowing for cost-effective and scalable manufacturing. This was achieved through the development of a proteolipid vehicle (PLV) platform that incorporates an engineered viral fusion protein into a lipid-based formulation encapsulating a nucleic acid payload **(Figure 2.1A, B)**. All enveloped viruses utilize fusion proteins that fuse the viral envelope with cell membranes to effectively deliver their genetic payload into target cells[360]. These complex, glycosylated, and multimeric viral fusion proteins are highly immunogenic[360] and present significant challenges to purify. In contrast, a unique family of viral fusion proteins, the reovirus fusion-associated small transmembrane (FAST) proteins, are not subject to these constraints[361]. FAST proteins are the only examples of membrane fusion proteins encoded by nonenveloped viruses, and at ~100-200 residues in length are the smallest known viral fusogens. These non-glycosylated proteins are not components of the virion but are expressed inside virus-infected cells and traffic to the plasma membrane where they mediate cell-cell membrane fusion, generating multinucleated syncytia to promote cell-cell virus transmission[362]. FAST proteins function at physiological pH and do not require specific cell receptors, allowing them to fuse almost all cell types[363].

The FAST protein family comprises six structurally similar members named according to their molecular mass in Daltons (i.e., p10, p13, p14, p15, p16, and p22) and share no conserved sequence identity. All six known FAST proteins show a bipartite membrane topology with the single transmembrane (TM) domain connecting a minimal N-terminal ectodomain of ~19-40

residues to a longer C-terminal cytoplasmic endodomain[364]. Structural motifs contained within these domains and the rate and extent of syncytium formation vary considerably between family members [365]. FAST protein ectodomains typically have a myristate moiety on the penultimate N-terminal glycine and all contain diverse membrane-destabilizing fusion peptide motifs in their ectodomain (e.g., p14 proline-hinged loop, p15 type II polyproline helix)[366,367]. FAST protein endodomains all contain a juxtamembrane polybasic motif involved in protein trafficking[368], and a membrane-proximal membrane curvature sensor to drive pore formation[369]. Along with specific TM domain features[370,371], these motifs function in conjunction to remodel membranes and promote membrane fusion.

We previously showed in proof-of-concept experiments that p14 FAST protein-containing liposomes induce liposome-cell fusion and facilitate intracellular delivery of encapsulated membrane-impermeable cargo[363,372]. Here, we evaluated a panel of chimeric FAST protein constructs to identify a new high activity FAST protein chimera that was formulated into a PLV comprised of naturally occurring and well-tolerated lipids. We demonstrate that FAST-PLVs provide a novel nucleic acid delivery platform that mediates effective intracellular delivery of encapsulated mRNA and plasmid DNA (pDNA) *in vitro* and *in vivo* while maintaining excellent tolerability, low immunogenicity and favorable biodistribution in mouse and non-human primate models.

## 2.2. Results

### *2.2.1. Engineering of a FAST protein hybrid with enhanced fusion activity*

We exploited the modular nature of FAST proteins to determine whether a specific combination of motifs could be assembled into a recombinant FAST protein with enhanced

fusion activity, starting with the high activity p14 and p15 FAST proteins[365]. A chimeric p14 and p15 FAST protein library was generated where the ectodomain, TMD, or endodomain of p14 were substituted with the corresponding domain of p15, and the fusion activity of each construct was ranked using a syncytia formation assay (**Figure 2.1C**). Three of six chimeric proteins were fusion-dead while two maintained fusion activity comparable with the parental proteins. One candidate, p14endo15, had significantly higher activity than either p14 or p15 parent (**Figure 2.1D, E**). This chimera comprises the p14 ectodomain, which contains a myristoylated proline-hinged loop fusion peptide motif with robust membrane-destabilizing activity, connected via the p14 TM domain to the p15 endodomain, which contains an efficient amphipathic helix-kink-helix membrane curvature sensor. Based on these results, p14endo15 was selected for the optimization of novel PLV formulations for nucleic acid delivery (all references to FAST protein hereinafter are describing p14endo15).

### *2.2.2. Optimization of lipid/FAST protein formulations for nucleic acid delivery*

Conventional LNPs rely on endosomal escape for intracellular delivery, which results in limited nucleic acid release into the cytosol[347,354,373]. We hypothesized that incorporating p14endo15 into a lipid formulation would significantly improve the delivery of nucleic acids into the cytosol by promoting PLV-cell membrane fusion **(Figure 1A)**, while changing the formulation requirements to promote improved tolerability compared to conventional LNPs due to the need for lipids to only promote nucleic acid encapsulation through charge neutralization.

To this end, a panel of cationic and ionizable lipids was evaluated for their toxicity on human fibroblasts (WI-38), including cationic lipids 1,2-di-O-octadecenyl-3-trimethylammonium propane (DOTMA) and 1,2-dioleoyl-3-trimethylammonium-propane (DOTAP), as well as the

ionizable lipids 1,2-dioleoyl-3-dimethylammonium-propane (DODAP), DLin-MC3-DMA (MC3), and 1,2-dioleyloxy-3-dimethylaminopropane (DODMA). Of these, DODAP had the most favorable tolerability, with DOTAP showing slightly higher toxicity **(Supplementary Figure 2.1A)**. These lipids were utilized in a PLV formulation to promote nucleic acid encapsulation through charge neutralization. The optimal molar ratio of DODAP to pDNA was assessed by measuring the delivery and subsequent expression of DNA-encoded firefly luciferase (pDNA-FLuc) in retinal pigmented epithelial (ARPE-19) cells. A ratio of 5:1 ionizable lipid DODAP to pDNA resulted in maximal expression **(Supplementary Figure 2.1B)**.

A pDNA payload was then used to create a panel of more than 40 lipid formulations combining cationic lipid (DOTAP), ionizable lipid (DODAP), helper lipid (2-dioleoyl-*sn*-glycero-3-phosphoethanolamine; DOPE), and PEGylated lipid (1,2-dimyristoyl-*sn*-glycero-3-methoxypolyethylene glycol-2000; DMG-PEG) at different ratios in an effort to balance intracellular delivery and activity with tolerability. The most promising of these based on encapsulation and sizing (designated 28M, 33T, 37N and 41N) were produced using a microfluidic platform at the following lipid molar ratios (cationic/ionizable/helper/PEGylated): 28M (24:42:30:4), 33T (42:24:30:4), 37N (6:60:30:4) and 41N (0:66:30:4)[374–376]. To assess the contribution of FAST protein to their delivery efficiency, pDNA-FLuc was encapsulated in each formulation with or without p14endo15 FAST protein and the resulting size, polydispersion index (PDI), and zeta potential was determined **(Supplementary Table 2.1)**. All PLV formulations were found to be < 80 nm in diameter with a PDI < 0.3, indicating monodispersity.

The potency and cytotoxicity of these formulations were assessed in kidney epithelial (Vero) cells. Overall, formulation 41N showed the most favorable tolerability **(Supplementary Figure 2.1C)** and was slightly less potent than formulation 37N **(Supplementary Figure 2.1D)**.

While formulation 37N showed roughly 3-times higher potency, it was > 6-times more toxic than 41N. Formulation 33T was far more toxic than the other formulations and omitted from further analysis, while 28M was similar in tolerability to 37N with significantly lower potency. A direct comparison of the potency vs. tolerability (weighted equally) indicated that formulation 41N scored higher than 37N, which in turn scored significantly higher than 28M and 33T **(Supplementary Figure 2.1E)**. The tolerability results obtained with FAST-PLV formulations in Vero cells were confirmed *in vivo* by intravenous injection of mice with an 8 mg/kg dose of pDNA-FLuc, using pro-inflammatory cytokine responses (TNF-α, IL-6, IFN-γ, IL-1β, CXCL1, IL-10, IL-5) as an indicator of immunotoxicity[377]. Mice injected with FAST-PLV formulation 41N induced the lowest levels of pro-inflammatory cytokines, comparable to those in the PBS-injected control mice **(Supplementary Figure 2.1F-I)**. Formulation 37N induced modest, but consistently higher, increases in several cytokines compared to 41N, while formulation 28M induced significant elevations in all cytokine levels **(Supplementary Figure 2.1F-I)**. These *in vivo* tolerability results mirror those observed in Vero cells. A direct comparison of the efficacy of 41N and 37N PLVs containing pDNA-FLuc was then performed in immune-competent animals through the intramuscular route. In contrast to the *in vitro* potency, it was found that 41N PLVs significantly outperformed 37N, by a factor of almost 10 (**Supplementary Figure 2.1M, N**). This is likely attributable to lower localized toxicity and immune stimulation which facilitated an improvement in pDNA delivery. Based on all these results, PLV formulation 41N was selected for further development and optimization.

The size and structure of the 41N pDNA FAST-PLV was assessed by transmission electron microscopy (TEM) and atomic force microscopy (AFM). TEM revealed uniform spherical structures made of an outer lipid bilayer and a negatively stained inner core (**Figure 2.2A**). AFM

showed uniform spherical structures with an approximate size distribution of 66.3±15.3 nm (**Figures 2.2B, C**), in agreement with the dynamic light scattering (DLS) measurements **(Supplementary Table 2.1)**. The potency of 41N pDNA-GFP PLV formulated with and without FAST protein and with varying ratios of ionizable lipid to pDNA-GFP was evaluated in a panel of cultured and primary cell lines. In all cell lines tested, FAST-containing formulations showed significantly improved potency as measured by GFP expression **(Figure 2.2D)**, which was maximal at a 5:1 ratio of ionizable lipid to pDNA **(Figure 2.2E)**. Based on this, the optimized FAST-PLV formulation was finalized using the 41N lipid formulation (DODAP, DOPE, and DMG-PEG lipids in a molar ratio of 66:30:4) and a 5:1 molar ratio of DODAP to pDNA.

To establish a suitable reference point, we compared the potency and tolerability of FAST-PLVs to the cationic lipid formulation Lipofectamine 2000 and a conventional LNP formulation composed of DLin-MC3-DMA (MC3-LNPs) in human umbilical vein endothelial cells (HUVEC) and human fibroblasts (IMR-90)[357]. FAST-PLVs containing pDNA-FLuc were significantly less toxic than Lipofectamine 2000, with comparable tolerability to MC3-LNPs **(Figure 2.2F)**. However, FAST-PLVs demonstrated significantly higher expression of pDNA-FLuc than MC3-LNPs **(Figure 2.2G)**.

The delivery of mRNA in the 41N PLV formulation with and without FAST protein was then assessed using a range of molar ratios of DODAP to mRNA. The highest expression of mRNA-FLuc in WI-38 cells was found at a DODAP:mRNA ratio of 3:1, and the incorporation of FAST protein significantly enhanced potency in every case **(Figure 2.2H)**. Similar results were also seen with the delivery of mRNA-mCherry into human primary endothelial cells (HUVEC) using 41N PLVs **(Figure 2.2I)**. The ability of FAST-PLVs to deliver multiple mRNAs to the same cell was demonstrated by co-expression of mRNA-mCherry and mRNA-eGFP in cells treated with

PLVs containing a 1:1 molar ratio of each mRNA at a combined 12 nM dose **(Figure 2.2J)**. Furthermore, FAST-PLVs formulated with a mixture of pDNA-GFP and mRNA-mCherry payload at a 1:6 molar ratio demonstrated expression of both reporters in cells at a combined 7 nM dose **(Figure 2.2K)**. Thus, the optimized 41N FAST-PLV formulation is suitable for encapsulation and intracellular delivery of pDNA and/or mRNA to cultured and primary cells with high potency and low toxicity compared to conventional LNPs.

### *2.2.3. Systemic in vivo delivery of pDNA and mRNA via FAST-PLVs*

Safe and effective systemic delivery of DNA is a significant challenge, with many platforms exhibiting low tolerability *in vivo* leading to host immune stimulation and liver toxicity[373,378,379]. We evaluated the *in vivo* biodistribution, potency and tolerability of FAST-PLVs compared to the conventional MC3-LNP lipid formulation over a dose range of 0.5 mg/kg to 80 mg/kg DNA. We set out to uncover suitable MC3-LNP dose for comparison, however, we found that systemic intravenous administration of MC3-LNPs encapsulating pDNA-FLuc at doses higher than 1 mg/kg resulted in unexpected mortality or significant morbidity of mice within 48 hours of injection that warranted veterinary directed euthanasia. These studies uncovered a 0.5 mg/kg maximum tolerated dose for systemic administration of MC3-LNPs encapsulating pDNA that was selected moving forward. Conversely, pDNA encapsulating FAST-PLVs were well tolerated at doses > 60 mg/kg **(Supplementary Table 2.2)**. Post-mortem analysis of MC3-LNP treated mice at 1 and 5 mg/kg revealed significant liver toxicity that was readily apparent upon gross visual examination **(Figure 2.3A)**, with histological analysis indicating liver damage characterized by hemorrhage **(Figure 2.3B)**. In contrast, mice treated with FAST-PLVs at doses up to 20 mg/kg dose showed no signs of liver pathology by gross visual or histological examination **(Figures 2.3A,**

**B)**. Cytokine responses in mice were also examined as an immune indicator of toxicity following intravenous injection of FAST-PLVs administered at 5 mg/kg and 20 mg/kg pDNA doses or MC3-LNPs administered at a 0.5 mg/kg dose pDNA, a typical dose for systemic delivery of mRNA[357]. Mice receiving either dose of FAST-PLVs encapsulating pDNA-FLuc showed no significant increase in any of the examined cytokines while all cytokines, particularly IL-6, TNF-α, and IL-5, were significantly elevated in mice treated with the MC3-LNPs **(Figures 2.3C-I)**.

Whole-body luminescence imaging was used to evaluate the *in vivo* delivery capability of FAST-PLVs. Results showed a dose-dependent increase in FLuc expression between the 5 and 20 mg/kg FAST-PLV doses, with the 5 mg/kg dose of FAST-PLVs generating comparable signals to the 0.5 mg/kg dose of MC3-LNPs **(Figure 2.3J, K)**, while *ex vivo* bioluminescence showed 5 mg/kg FAST-PLVs generated comparable FLuc signals in multiple organs to 0.5 mg/kg MC3-LNPs (**Figure 2.3L**). The durability of *in vivo* pDNA expression was also assessed in immune-competent mice by whole-body luminescence imaging over 365 days after systemic administration of 20 mg/kg pDNA-FLuc FAST-PLVs. A strong and widespread whole-body luminescence signal was observed in the first two days that decreased to a steady state maintained for greater than twenty weeks, with expression continuing through one year after administration **(Figure 2.3M and Supplementary Figure 2.2)**. Immunohistochemistry of the lungs, liver, and spleen of animals 63 days after injection demonstrated widespread expression of FLuc in each tissue examined **(Figure 2.3M)**.

Next, we assessed the ability of FAST-PLVs to deliver mRNA *in vivo*. Incorporation of FAST protein into mRNA-FLuc PLVs resulted in significantly increased expression following intramuscular injection (**Figure 2.4A**). Widespread whole-body luminescence was observed four hours after intravenous injection with FAST-PLVs encapsulating mRNA-FLuc at a dose of 2

mg/kg **(Figure 2.4B),** and *ex vivo* luminescence imaging confirmed luciferase expression in a wide array of organs, including the lungs, liver, spleen, kidneys, and brain **(Figure 2.4C)**. We then examined the ability of FAST-PLVs to deliver therapeutic mRNA cargos. Delivery of LNPs encapsulating human erythropoietin (EPO) encoding mRNA is currently being investigated by multiple research groups as a potential anemia treatment modality[347,351,359,380]. We assessed circulating EPO levels in mice following intravenous injection with FAST-PLV encapsulating 0.5 or 1.25 mg/kg mRNA-EPO, as well as intramuscular injection with FAST-PLVs encapsulating 0.3 mg/kg mRNA-EPO. 8 hours after injection we observed a large spike in serum EPO levels following systemic FAST-PLV injection reaching 7000 pg/ml and 13000 pg/ml in mice injected with the low and high dose mRNA-EPO, respectively. Surprisingly, intramuscular injection with only 0.3 mg/kg mRNA-EPO resulted in a detectable serum EPO concentration just under 2000 pg/ml 8 hours following injection. Circulating EPO levels returned to near baseline levels 48 hours after injection for low systemic dose and intramuscularly injected mice, and 72 hours for high systemic dose mice (**Figure 2.4D**). Overall, systemic *in vivo* administration of FAST-PLVs encapsulating either pDNA or mRNA showed durable, dose-dependent expression and biodistribution to a wide array of organs with no significant increase in liver or immune-toxicity at doses significantly higher than can be achieved with conventional LNPs.

### *2.2.4. Repeat dosing of FAST-PLVs through intramuscular or systemic route.*

Administered biologic drugs such as monoclonal antibodies or viral gene therapy vectors elicit an adaptive immune response in the form of anti-drug or anti-vector antibodies that can interfere with or neutralize the effect of the drug, restricting their use in applications that require repeat dosing[341,342,381]. Given the incorporation of a novel virus-derived fusion protein in our

FAST-PLV platform, we sought to determine if FAST-PLVs generate an immune response capable of reducing their *in vivo* efficiency upon repeated administration intramuscularly or intravenously. To that end, FAST-PLVs encapsulating mRNA-FLuc were administered at 0.3 mg/kg via intramuscular injection **(Figure 2.4E-G)** or 1.2 mg/kg intravenously **(Figure 2.4H-J)** once per month for six months. Significant expression of luciferase was seen after each intramuscular injection **(Figure 2.4E)**, with a slight increase in expression observed over each injection, likely attributable to residual expression from the previous doses accumulating over time **(Figure 2.4F, G)**. When FAST-PLVs were repeatedly administered intravenously, no significant change in total luminescence intensity was observed over time **(Figure 2.4H-J).** Antibodies against FAST protein were quantified in the serum of these mice one month after the fifth and final FAST-PLV administration using indirect ELISA with a lower limit of quantification (LLOQ) of 50 ng/mL. After intramuscular administration, two of the four animals had no detectable anti-FAST antibody level and two had levels just above the LLOD at 221.6±40.6 and 173.5±36.3 ng/mL. Of the three mice repeatedly administered FAST-PLVs intravenously, one had no detectable anti-FAST antibody while two had levels of 335.2±5.1 and 453.7±71.1 ng/mL (**Figure 2.4K**). Interestingly, high titers of anti-FLuc antibodies were detected in all intravenously repeat-dosed animals and two out of four intramuscular repeat-dosed animals **(Figure 2.4L)**, which may help to explain the variability in luciferase expression distribution following systemic repeat doses **(Figure 2.4H)**. To determine whether the detected levels anti-FAST antibodies have neutralizing activity, the activity of pDNA-GFP PLVs in the presence of serum from repeatedly dosed and control mice was assessed in an *in vitro* transfection assay. No reduction in GFP expression was observed when serum treated FAST-PLVs were used to transfect 3T3 cells *in vitro* **(Figure 2.4M)**, indicating no neutralizing activity. Overall, repeat dosing of FAST-PLVs by intramuscular or

intravenous administration produced consistent reporter expression, was well tolerated, and did not stimulate adverse immune responses.

### 2.2.5. *FAST-PLVs safely and effectively deliver pDNA in non-human primates with broad biodistribution to tissues*

The safety, tolerability and biodistribution of FAST-PLVs at various doses following systemic administration was further examined in African green monkeys (*Chlorocebus sabaeus*). The biodistribution of pDNA-GFP cargo delivered by intravenous administration in FAST-PLV at a 1 mg/kg dose of pDNA was quantified in 30 tissues using a quantitative PCR approach two days after administration. Significant levels of pDNA were detected in all organs tested, with the highest levels detected in the lungs, spleen, gall bladder, and bone marrow. Of particular interest was the fact that liver ranked sixth for pDNA accumulation, which, unlike conventional LNP, suggests that extrahepatic pDNA delivery can be achieved **(Figure 2.5A)**. Tolerability was similarly evaluated following intravenous dosing with FAST-PLVs at 1 and 6 mg/kg pDNA doses. No significant abnormalities were observed in any organs assessed **(Figure 2.5B)**, and no treatment-related changes were noted in any organs tested **(Table 2.1)**. Some findings were reported in all animals in the aged, feral African green monkey cohort used for the study. For example, the mononuclear cell infiltrates observed in the livers of all animals, as well as the vacuolation and hydropic degeneration (consistent with increased hepatocellular glycogen) were within normal variability for African green monkeys. Additionally, the periportal hemosiderin and pigmented macrophages detected are typical of prior parasite migration tracks – consistent with the use of wild-caught animals[382,383]. Circulating levels of alanine transaminase (ALT) and aspartate transaminase (AST) remained within the normal range for the duration of the study

**(Figure 2.5C, D)**. Creatine phosphokinase (CPK) and lactate dehydrogenase (LDH) levels were elevated immediately following infusion but decreased to within expected ranges by 21 days post infusion. All other clinical chemistry parameters remained within the normal range for the study duration **(Supplementary Table 2.3)**. A transient elevation in systemic pro-inflammatory cytokines was observed 1-4 hours after FAST-PLV infusion that returned to baseline levels 12-72 hours post-infusion **(Figure 2.5E-G and Supplementary Table 2.4)**. A similar pattern was observed on chemokine secretion after FAST-PLV infusion, with chemokines returning to baseline values 72 hours after infusion **(Supplementary Table 2.5)**. Elevations in cytokine and chemokines were not dose-dependent, suggesting factors related to the intravenous infusion, such as local inflammation, might be the principle contributing factor. Complement activation-related pseudoallergy (CARPA), which can cause potentially dangerous hypersensitivity reactions in response to intravenous injection of lipid-containing entities[384,385], was also assessed. Serum levels of S protein bound C terminal complex (SC5b-9) did not increase significantly following FAST-PLV infusion (**Figure 2.5H**), while serum levels of C4d were elevated approximately 3-fold by the 1 mg/kg dose but were unaffected by the 6 mg/kg dose (**Figure 2.5I**). The lack of a dose dependent response indicates that it is unlikely the administration of FAST-PLVs is contributing to this elevation. (**Figure 2.5H, I**).

The presence of anti-FAST antibodies was also assessed in these animals at 25 days post-administration of 6 mg/kg pDNA FAST-PLVs. Anti-FAST antibodies were detected in one of the three monkeys at a level of 144.72±13.5 ng/mL. To determine whether the detected levels anti-FAST antibodies have neutralizing activity, the activity of pDNA-GFP PLVs in the presence of serum from repeatedly dosed and control animals was assessed, and no reduction in GFP expression was observed when serum treated FAST-PLVs were used to transfect 3T3 cells *in vitro*

**(Supplementary Figure 2.3)**. Taken together, these data indicate that FAST-PLVs are safe and well-tolerated in non-human primates, with broad biodistribution and evidence for significant delivery to extrahepatic organs.

### *2.2.6. Therapeutic activity of FAST-PLV follistatin gene therapy.*

To determine the ability of FAST-PLVs to deliver pDNA encoding a therapeutic cargo, we developed a gene therapy approach to elevate expression of the protein follistatin (FST). FST facilitates hypertrophy of skeletal muscle by exhibiting an antagonistic effect on myostatin – a member of the Transforming Growth Factor-β family that inhibits muscle growth[386]. AAV gene delivery vectors have been used to evaluate FST gene therapy as a potential treatment for muscle wasting disorders[387,388]. We sought to determine if delivery of pDNA encoding the FST-344 splice variant in FAST-PLV would be a viable alternative to AAV-based therapies. When pDNA-CMV-FST FAST-PLVs were incubated with C2C12 mouse myoblasts, robust FST expression relative was observed (**Figure 2.6A**). FST expression correlated with an increase in Akt and mTOR phosphorylation 24 and 48 hours after addition of pDNA-CMV-FST FAST-PLV (**Figure 2.6A**)[389]. FST in the growth media also increased in a time-dependent manner, with levels reaching 10,000 pg/ml 72 hours after addition of pDNA-CMV-FST FAST-PLV (**Figure 2.6B**).

Next, we examined the ability of systemically administered pDNA FAST PLVs using two different promoters to drive FST expression *in vivo*. As FST is primarily produced in the liver, we evaluated expression when driven by the liver promoter, transthyretin (TTR), compared to the ubiquitous CMV promoter[390]. Intravenous administration of 10 mg/kg of either pDNA-CMV-FST or pDNA-TTR-FST FAST PLVs in mice resulted in a significant spike in serum FST concentration one day after injection, with levels returning to near baseline level 3-7 days following

administration. Animals receiving pDNA-CMV-FST PLVs reached a one-day peak serum FST concentration of 1700 pg/ml, while animals receiving pDNA-TTR-FST FAST PLVs had a peak FST serum concentration of 2300 pg/ml (**Figure 2.6C**). After fifteen weeks, administration with either FST FAST-PLV gene therapy resulted in animals displaying a fuller frame and musculature, while PBS injected control animals appeared thinner with protruding pelvic and vertebral bones (**Figure 2.6D**). Mice receiving pDNA-TTR-FST FAST PLV after fifteen weeks had significantly higher body weight compared to PBS control mice (**Figure 2.6E, F**). This observed increase in body weight was consistent with significant increases in grip strength in these animals (**Figure 2.6G, H**).

We also examined the relative impact of local and systemic administration of the FAST-PLV FST gene therapy. Mice were administered pDNA-CMV-FST FAST-PLV locally by single intramuscular injection of 5 mg/kg in the left gastrocnemius (GAS) muscle or systemically at 10 mg/kg. Relative to mice administered PBS control, intramuscular administration into the left GAS muscle resulted in a significant increase in hind limb grip strength (**Figure 2.6I**). Gross dissection indicated that localized FST administration and expression resulted in a significant increase in the GAS size and weight relative to the contralateral non-injected GAS (**Figure 2.6J, K**), and a significant increase in the cross-sectional muscle fiber area of the injected GAS relative to the non-injected GAS as shown by WGA staining (**Figure 2.6J, L**). Subsequent to systemic intravenous administration of 10 mg/kg pDNA-CMV-FST, a significant increase in hind limb grip strength was observed (**Figure 2.6M**). Gross dissection revealed a significant increase in hindlimb muscle size and GAS weight (**Figure 2.6N, O**). Relative to control animals, WGA staining of GAS demonstrated a significant increase in cross-sectional muscle fiber area (**Figure 2.6N, P**). These

data demonstrate that FAST-PLVs, administered locally or systemically, can effectively deliver a therapeutic pDNA payload to generate localized or body-wide effects.

## 2.3. Discussion

Proteo-lipid vehicles formulated with FAST proteins represent an effective and redosable nucleic acid delivery platform that enables broad biodistribution with high tolerability compared to conventional non-viral approaches. The discovery of a novel and highly active chimeric FAST fusogen, p14endo15, has enabled the re-imagining of the conventional lipid nanoparticle formulation to remove cholesterol, utilize alternative ionizable lipids, and to select an optimal ratio of ionizable, helper, and PEGylated lipids to achieve these characteristics **(Figure 1)**. The superior fusion activity of p14endo15 is likely mediated by the efficient p14 ectodomain fusion peptide and myristate moiety facilitating lipid mixing with the target cell membrane, followed by the p15 endodomain fusion-inducing lipid packing sensor (FLiPs) motif partitioning into the PLV membrane to promote pore formation and liposome-cell fusion activity[366,369].

Systemic *in vivo* administration of pDNA FAST-PLVs resulted in durable, dose-dependent expression of target proteins in a wide array of organs with no detectable tissue or immune toxicity, even at doses orders of magnitude higher than the maximum tolerated dose of conventional (clinically approved) LNP formulations. Conventional LNPs accumulate preferentially in the liver when administered systemically, mediated by ApoE binding to the LNP surface. This behavior has driven the clinical development of liver targeting siRNA based LNP drugs[352,391,392,] while limiting their broader application. Extrahepatic nucleic acid delivery is particularly important for indications such as cancer, which requires broad biodistribution to achieve sufficient uptake[339]. Like conventional LNPs, most AAV serotypes tend to preferentially target the liver, except in the case of AAV9 that can target neurons, albeit with a lower efficiency of gene transfer[393,394]. This creates problems for other conditions, as gene transfer may require local AAV delivery that is not possible for all conditions[395]. Additionally, cells with a high turnover rate will quickly dilute the

transgene and due to immunogenic responses, the vector cannot be utilized again[396–399]. This creates problems for development of genetic medicines targeting disseminated cancer. Based on our NHP biodistribution data that demonstrates quite extensive extrahepatic delivery of pDNA, we anticipate that FAST-PLVs will have substantial clinical utility in the treatment of advanced cancer. Several factors could contribute to the favorable *in vivo* biodistribution profile of FAST-PLVs compared to AAV and conventional LNPs. For example, the ~60 nm size of FAST-PLVs is advantageous for bypassing major uptake organs like the liver and spleen[400], and the absence of cholesterol from the 41N FAST PLV lipid formulation (cholesterol is a major driver of liver uptake of LNPs) could aid in delivery to extrahepatic organs[401].

The ability of FAST-PLVs administered locally or systemically to deliver pDNA encoding FST-344, and for gene delivery to effect quantifiable changes in muscle tissue similar to previous reports with AAV, demonstrates the potential clinical utility of this non-viral platform[402–404]. Again, the low immunogenicity of FAST-PLVs is beneficial for this type of gene therapy. Where AAV essentially requires lifelong gene expression with a single dose, FAST-PLV administration can be adjusted to fit each patient need. This also enables treatment to be stopped and started as needed. Our results also indicate that therapeutic gene expression following systemic FAST-PLV administration can be targeted to specific tissue types by altering the pDNA promoter, which can be utilized in the future to prevent off-target effects.

The successful *in vivo* delivery of pDNA using FAST-PLVs described herein represents a promising step forward for development of non-viral gene therapy approaches as DNA delivery has typically been restricted to viral platforms[339,373]. Additionally, FAST-PLVs were able to deliver mRNA to a wide array of extrahepatic organs. Typically, non-viral delivery vectors, such as LNPs, are only suitable for RNA-based gene therapy approaches due to challenges

encapsulating large molecules like DNA[373]. Because of its large size, pDNA requires higher molar ratios of cationic components to neutralize its anionic charge and facilitate delivery relative to particles encapsulating mRNA and siRNA. Increasing the amount of cationic components results in a corresponding increase in toxicity, preventing successful systemic delivery. FAST-PLVs represent one of the first non-viral nucleic acid delivery vehicles that can encapsulate pDNA and mRNA and is able to deliver both nucleic acids to the same cell.

Initial gene therapy trials using adenovirus vectors reported serious and life-threatening adverse events, instigating the shift to AAV vectors[338,405,406]. While promising results have been obtained with AAV vectors, their small cargo capacity and anti-AAV immune responses limits their use[342,406–408]. The large cargo capacity of FAST-PLVs indicate a potential for development of CRISPR/Cas9 gene editing technologies[407,409]. Successful gene editing requires delivery of both Cas9 protein and a guide RNA (gRNA) to the target cell. Cas9 transgenes are approximately 4.2 kb, which puts them at the upper end of AAV packing capacity[410]. To overcome this limitation, multiple AAV vectors are often required to deliver the Cas9 and gRNA separately[411], or a combination of LNPs and AAVs can be utilized[412]. Additionally, modifications can be made to the Cas9 structure that enable the gRNA and Cas9 sequences to be included in the same AAV genome[408]. On the other hand, utilizing FAST-PLVs would enable both Cas9 and gRNA sequences to be included on a single pDNA. Alternatively, Cas9 and gRNA could be co-encapsulated into the same PLV, which would enable the use of either pDNA or mRNA, or a combination of both.

The recent development, manufacture, and production of the highly effective LNP-formulated mRNA vaccines against SARS-CoV-2 that causes COVID-19 have validated the LNP platform and shown the potential of nucleic acid for vaccines and therapeutics[413–417]. However, the potential for nanoparticle encapsulated DNA vaccines has been overlooked primarily due to the

high toxicity associated with cationic lipids, necessitating use of physical methods like electroporation to deliver the DNA vaccine[418–422]. Our findings suggest that FAST-PLVs could also be used to deliver mRNA or DNA vaccines, avoiding the immunogenicity and toxicity seen with cationic LNP delivery platforms and the necrosis and widespread tissue damage observed with electroporation[418,423–426].

In summary, we present a novel approach to achieve systemic nucleic acid delivery by combining the fusion-inducing activities of FAST proteins with the improved safety and scalability of lipid-based non-viral delivery vectors. Given the small size of FAST-PLVs, as well as their efficacy, low immunogenicity, high tolerability, and the ability to reach extrahepatic tissues, we anticipate that FAST-PLVs will have substantial clinical utility, enabling the development of low-cost genetic medicines in the near future.

## 2.4. Methods

*Materials*

The following lipids were purchased from NOF Co. (Tokyo, Japan): 1,2-di-O-octadecenyl-3-trimethylammonium propane (DOTMA), 1,2-dioleoyl-3-dimethylammonium-propane (DODAP), 1,2-Dioleyloxy-3-dimethylaminopropane (DODMA), 1,2-dimyristoyl-*sn*-glycero-3-methoxypolyethylene glycol-2000 (DMG-PEG). 2-dioleoyl-*sn*-glycero-3-phosphoethanolamine (DOPE) and 1,2-dioleoyl-3-trimethylammonium-propane (DOTAP) were purchased from Avanti Polar Lipids (Alabaster, United States). DLin-MC3-DMA (MC3) was purchased from Precision Bio Laboratories (Edmonton, Canada). Plasmid DNA (pDNA) with the cytomegalovirus (CMV) promoter driving the DNA-encoded inserts, green fluorescent protein (GFP), and firefly luciferase (FLuc) was cloned into the p10 plasmid vector produced by Entos Pharmaceuticals (Edmonton, Canada). These pDNA preps were expanded and purified by Precision Bio Laboratories. pDNA encoding the follistatin 344 splice variant under the transthyretin (TTR) and CMV promoters was cloned into the NTC Nanoplasmid and produced by Nature Technology Company (Lincoln, United States). CleanCap mRNA with mRNA-encoded inserts; monomeric red fluorescent protein (mCherry), enhanced green fluorescent protein (eGFP), and firefly luciferase (FLuc) was purchased from TriLink Biotechnologies (San Diego, United States). Lipofectamine 2000 and CyQUANT LDH Cytotoxicity Assay was purchased from Thermo Fisher Scientific (Edmonton, Canada). Harris modified hematoxylin was purchased from Fisher Scientific (Ottawa, Canada). Eosin Y and resazurin were purchased from Millipore Sigma (Oakville, Canada). Anti-Firefly Luciferase antibody (ab181640) and anti-GAPDH antibody (ab8245) were purchased from Abcam (Cambridge, United Kingdom). Rabbit polyclonal p14endo15 antibody was produced by New England Peptide (Gardner, United States), using the target sequence Ac-

PSNFVNHAPGEAIVTGLEKGADKVAGTC-Amide. Goat anti-follistatin antibody (AF669) was purchased from R&D systems (Minneapolis, United States). Phospho-Akt Ser473 (4069), pan-Akt (2920), phosphor-mTOR Ser2448 (2971), and mTOR (2972) antibodies were purchased from Cell Signaling Technology (Danvers, United States).

*Cells and Culturing*

Quail fibrosarcoma (QM5) cells were cultured in Medium 199 with 3% fetal bovine serum (FBS; Sigma) and 0.5% penicillin/streptomycin (Thermo Fisher Scientific, Edmonton, Canada). Human hepatocellular carcinoma cells (HEP3B), human non-small cell lung cancer cells (NCI-H1299), human lung fibroblast cells (IMR-90 and WI-38), mouse embryo fibroblast cells (3T3), VERO CCL-81 cells (*Cercopithecus aethiops* epithelial kidney cells), and mouse myoblasts (C2C12) were purchased from ATCC (Manassas, VA) and cultured in high glucose-DMEM with 10% FBS and 1% penicillin/streptomycin. Human retinal pigmented epithelium cells (ARPE-19) were a gift from Dr. Ian MacDonald (University of Alberta) and were cultured in DMEM/F12 with 10% FBS and 1% penicillin/streptomycin. Human umbilical vein endothelial cells (HUVEC) were a gift from Dr. Allan Murray (University of Alberta) and were cultured in EGM-2 BulletKit (Lonza, Cat No. CC-3162). Sprague-Dawley Rat Primary Hepatocytes were purchased from Cell Biologics and were cultured in Complete Hepatocyte Medium Kit from Cell Biologics (Cat No. M1365). Primary rat astrocytes were purchased from Cell Applications Inc. (San Diego, United States) and cultured in rat astrocyte growth medium (Cat No. R821-500). Mammalian adherent cells were grown in tissue-culture treated 75 $cm^2$ flasks (VWR 10062-860) until cells were 80% confluent or nutrients in the media are depleted in a 37°C incubator with humidified atmosphere of 5% $CO_2$ (Nuaire NU-5510). *Spodoptera frugiperda* pupal ovarian tissue (Sf9) cells were stepwise cultured

at 25C to $2x10^6$ – $4x10^6$ cells/mL from 25 mL to 100 mL and finally into a 2 L wave bioreactor. The Trypan Blue assay was used to check for cell viability.

*Purification of FAST Proteins*

The Sf9 cells were lysed, and supernatant was clarified by 0.2 µm filtration. The FAST proteins were purified from the supernatant using an AKTA affinity purification column, followed by dialysis and cationic exchange purification (AKTA). Protein samples were quality control analyzed by SDS-PAGE and Western blot; functional validation was done via syncytia formation assay.

*Western Blot*

Cells were lysed in ice-cold Pierce RIPA buffer (Thermo Scientific, Cat. No. 89900). Protein amount was determined using Pierce BCA protein assay (Thermo Scientific, Cat. No. 23225). Equal amounts of total protein from each lysate were loaded onto Mini-PROTEAN 4-20% Gradient TGX precast gels (BIO-RAD, Cat. No. 456-1095). Separated protein was transferred to nitrocellulose membranes (BIO-RAD, Cat. No. 1620112). Membranes were blocked with fluorescent western blocking buffer (Rockland, Cat. No. MB-070) for 1 hour at room temperature. Primary antibodies were diluted 1:1000 in blocking buffer and added to the membranes overnight at 4˚C with shaking. Goat anti-rabbit Alexa Fluor 680 (Thermo Scientific, Cat. No. A27042), donkey anti-goat Alexa Fluor 680 (Thermo Scientific, Cat. No. A-21084), or goat anti-mouse Alexa Fluor 750 (Thermo Scientific, Cat. No. A-21084) were diluted 1:10000 in blocking buffer and added for 1 hour at room temperature in the dark. Membranes were visualized on the LI-COR Odyssey.

*Syncytia Formation and Inhibition*

QM5 quail fibrosarcoma cells were seeded at a density of $3.5x10^5$ in twelve well cluster plates in Medium 199 containing 10% FBS and cultured overnight before transfecting with Lipofectamine 2000 and 1 µg of pcDNA3 plasmid expressing either p14, p14endo15, or p15 per manufacturer's instructions. Cells were fixed in 3.7% formaldehyde in HBSS at the indicated intervals post-transfection and stained with Hoechst 33342 and WGA-Alexa 647 per manufacturer's instructions. Images (n=5) of each condition were captured on a Zeiss Axio Observer A1 inverted microscope at predetermined coordinates within the well (n=3). Syncytia were then manually identified with syncytial and total nuclei quantified using FIJI imaging software.

*Lipid Formulations*

The lipid formulations designated as 28M, 33T, 37N and 41N were made by combining the cationic lipid (DOTAP), ionizable lipid (DODAP), helper lipid (DOPE) and PEGylated lipid (DMG-PEG2000) in the following lipid molar ratios: 28M (24:42:30:4), 33T (42:24:30:4), 37N (6:60:30:4) and 41N (0:66:30:4). The lipids were heated in a 37°C water bath for 1 min, vortexed for 10 seconds each, then combined and vortexed for 10 seconds. The combined lipid mixture was dehydrated in a rotavapor at 60 rpm for 2 hours, under vacuum, then rehydrated with 14 mL 100% ethanol, and sonicated (Branson 2510 Sonicator) at 37°C, set to sonication of 60. The lipid formulation was aliquoted in 500 µL batches and stored at -20°C. MC3-LNP formulation was composed of DLin-MC3-DMA/DSPC/Cholesterol/PEG-lipid with the molar ratio 50:10:38.5:1.5[345].

*Nucleic Acid Quantification*

Nucleic acid concentration and purity was measured via absorbance at 260 nm and 280 nm using the Nanodrop method according to the manufacturer's instructions (Nanodrop 2000 Spectrophotometer, Thermo Scientific, Edmonton, Canada).

*FAST-PLV Construction*

The FAST-PLVs were made with lipid formulation 41N unless otherwise stated. The NanoAssemblr Benchtop microfluidics mixing instrument (Precision NanoSystems, Vancouver, BC, NIT0013, and NA-1.5-88, respectively) was used to mix the organic and aqueous solutions and make the PLVs. The organic solution consisted of lipid formulation. The aqueous solution consisted of nucleic acid cargo, 5 nM FAST (p14endo15) protein, and 10 mM acetate buffer (pH 4.0). The Benchtop NanoAssemblr running protocol consisted of a total flow rate of 12 mL/min and a 3:1 aqueous to organic flow rate ratio. PLVs were dialyzed in 8000 MWCO dialysis tubing (BioDesign, D102) clipped at one end. The loaded tubing was rinsed with 5 mL of double distilled water and dialyzed in 500 mL of Dialysis Buffer (ENT1844) with gentle stirring (60 rpm) at ambient temperature for 1 hour and was repeated twice with fresh Dialysis Buffer. PLVs were concentrated using a 100 kDa Ultra filter (Amicon, UFC810096) according to the manufacturer's instructions. PLVs were filter sterilized through 0.2 µm Acrodisc Supor filters (Amicon, UFC910008)

*In Vitro Transfection*

Cells were counted using a hemocytometer, and 3,000-5,000 cells were seeded to 96-well or 20,000-40,000 cells to 48-well tissue-culture treated plates and left overnight. The cells were

transfected with 10-2000 ng of pDNA encapsulated in FAST-PLVs, MC3-LNPs, or Lipofectamine 2000 for 96-well plate (300µl cell culture media final) and 1000 ng for 48-well plates (1000µl cell culture media final). Lipofectamine 2000 was prepared according to manufacture instructions. The optimal transfection time for mRNA is 24-48 hours and 72-96 hours for pDNA. A luciferase reporter assay was used to measure expression levels of FLuc in different cell lines. Cell culture media was removed from cells growing in a 96-well plate, and cells washed with 1x PBS. A 50-microliter aliquot of reporter lysis buffer (Promega E397A) was added to the cells. The cells were mixed and incubated at room temperature for 10-20 mins. D-luciferin (150µg/mL, GOLDBIO, LUCK-100) was dissolved in 100mM Tris-HCl (pH 7.8), 5mM $MgCl_2$, 2mM EDTA, 4mM DTT, 250µM acetyl-CoA, and 150µM ATP[427]. The luciferin substrate (100 µL) of was added to each well immediately before measurement. Luminescence was measured via the FLUOSTAR Omega fluorometer using the MARS data analysis software for analysis. Green fluorescent protein (GFP) or mCherry expressing cells were processed for flow cytometry analysis. The cells were trypsinized and resuspended in 400 µL (per well of 48 well plate) of FACS buffer, then transferred to a 5 mL flow cytometry tube (SARSTEDT 75X 12 mm PS Cat. no. 55.1579) and analyzed with a BD LSRFortessa X20 SORP. Mean fluorescence intensity (MFI) presented on the Fluorophore$^+$ population unless otherwise stated.

*PLVs Characteristics and Encapsulation Efficiency*

PLVs made by NanoAssemblr Benchtop were diluted 1:50 to 1:20,000, depending on concentration, with twice 0.2 µm syringe-filtered PBS buffer. Particle size, polydispersity index (PDI), and zeta potential was measured on final samples using the Malvern Zetasizer Range and a Universal 'Dip' Cell Kit (Malvern, ZEN1002) following the manufacturer's instructions. The

nucleic acid encapsulation efficiency was calculated using a modified Quant-IT PicoGreen dsDNA assay with the following modifications to the assay protocol (Thermo Fisher Scientific, Edmonton, Canada). PLVs were mixed 1:1 with TE + Triton (2%) to obtain the Total DNA Concentration, or with TE alone to obtain the Unencapsulated DNA Concentration. The DNA standards were also diluted in TE + Triton (2%), and samples were and incubated at 37°C for 10 min, then diluted a final time with TE + Triton (1%) or TE alone, plated in a black 96 well flat-bottomed plate, and measured with a FLUOstar Omega plate reader (BMG Labtech, 415-1147). Encapsulation efficiency was calculated by using the following equation:

$$Encapsulation\ Efficiency = \frac{Total\ DNA\ Concentration - Unencapsulated\ DNA\ Concentration}{Total\ DNA\ Concentration} \times 100$$

*Atomic Force Microscopy*

Final FAST-PLVs encapsulating pDNA were evaluated by Atomic Force Microscopy (AFM, Bruker Dimension Edge) for visual validation of the measured particle size. The PLVs were diluted with 0.1 μm filtered PBS to 0.1 μg/mL. An aliquot (2 μL) of the diluted sample solutions was immediately spread on a clean glass slide. The sample was dried at ambient temperature (25 °C) for 5 min and any excess aqueous solution was removed with filter paper. The sample was dried for another 15 minutes before imaging at a scan speed of 1 Hz. Tapping mode was carried out using a Ted Pella Tap300 cantilever with a quoted spring constant of 20–75 N/m. 2 D and 3 D images of different zones were examined due to the limitation of small, scanned areas by AFM. Height, Phase and Amplitude mode was used for image analysis using Gwyddion software.

*Transmission Electron Microscopy*

Final FAST-PLVs encapsulating pDNA were evaluated by transmission electron microscopy. 5µL aliquots of thousand-fold diluted FAST-PLVs, were placed on 300 mesh carbon-coated copper grids for an hour to dry on the surface, followed by two washes with 0.1µm filtered water. After removal of excess liquid, samples were negatively stained using 0.1µm filtered 1% uranyl acetate. The dried samples were examined in a JEOL JEM-ARM200CF S/TEM electron microscope.

*Viability Assay with Alamar Blue*

Cell cultures in a 96 well plates were treated with test compounds at indicated concentrations. After 24-96 hours, a 1/10 volume of Alamar blue solution (440 µM Resazurin; Sigma R7017 5GM) was added to the cells in culture medium and incubated for 2-4 hours at 37°C 5% $CO_2$. The Omega Fluostar (BMG LabTech) plate reader was used to measure the fluorescence (excitation wavelength of 540 nm and emission at 590 nm) of the treated cells. Cell viability was calculated using the following formula:

$$Viability = \frac{Treated\ Absorbance - Media\ Background\ Absorbance}{Vehicle\ Absorbance - Media\ Background\ Absorbance}$$

*Lactate Dehydrogenase (LDH) Cytotoxicity Assay*

VERO cells were seeded into 96 well plates, and the CyQUANT LDH Cytotoxicity Assay was conducted to determine the toxicity of different lipid formulations following manufacturers' instructions. In brief, pDNA-FLuc was encapsulated within each lipid formulation (28M, 33T, 37N, and 41N) and added to cells at a pDNA concentration of 1.5 nM. Twenty-four hours after pDNA addition, 50 µL of cell culture media was collected for LDH absorbance. Cytotoxicity was calculated using the following equation:

$$\%Cytotoxicity = \frac{Lipid\ Treated\ LDH\ Activity - Vehicle\ LDH\ Activity}{Maximum\ LDH\ Activity - Vehicle\ LDH\ Activity} \times 100$$

*Mouse Studies*

All animal studies were carried out according to the guidelines of the Canadian Council on Animal Care (CCAC) and approved by the University of Alberta Animal Care and Use Committee. *In vivo* studies were done using 25 to 35 g body weight, male and female C57BL/6 (Charles River Laboratories, Saint-Constant, Canada). Animals were group-housed in IVCs under SPF conditions, with constant temperature and humidity with lighting on a fixed light/dark cycle (12-hours/12-hours). Intravenous injection occurred via the lateral tail vein with 200 µL of the test agent. Intramuscular injection occurred in the semitendinosus and semimembranosus muscle of the hind limb with 50 µL of the test agent. Blood was collected via the lateral tail vein or cardiac puncture at indicated time points into serum collection tubes (Sarstedt, Montreal, Canada). Hindlimb grip strength was measured in quintuplicate using a T-bar attachment on the BIOSEB grip strength meter (Panlab, Cat. No. BSBIOGS3BS 76-1066).

*Whole Body and Ex Vivo Bioluminescence*

At indicated time points after the injection of the FAST-PLVs, mice were injected intraperitoneally with 0.25 mL D-luciferin (30 mg/mL in PBS) and allowed to recover for 5 minutes. The mice were then anesthetized in a ventilated anesthesia chamber with 2% isoflurane in oxygen and imaged ~10 min after D-luciferin injection with an *in vivo* imaging system (In Vivo Xtreme, Bruker, Montreal, Canada). All images are taken with a non-injected control mouse to serve as a reference point to determine the lower threshold of each image. Grouped experiments are presented with the upper threshold being held consistent between time points; however, the lower threshold is set

based on the signal of the non-injected control mouse at the point when it no longer shows any signal. Quantification of the luminescent signal was done using Bruker Molecular Imaging Software. A manual ROI was drawn to encompass the entire area of each mouse. The sum intensity (photons/second) from the non-injected control mouse was subtracted from the sum intensity from each experimental mouse to normalize different timepoints and control for background signal drift on each image. For *ex vivo* images, major organs were paired with those from a non-injected control mouse. 30 mg/ml D-Luciferin was mixed at a 1:1 ratio with the *in vitro* 150µg/mL D-Luciferin described above and added to the organs immediately before imaging. Non-injected control mouse organs were included with each set as a reference point to determine the lower threshold.

*Non-Human Primate Studies*

All in-life NHP procedures were carried out by Virscio, Inc, under the guidance of the Institutional Animal Care and Use Committee (IACUC) of the St. Kitts Biomedical Research Foundation (SKBRF), St Kitts, West Indies. SKBRF research facility is fully accredited by the Association for Assessment and Accreditation of Laboratory Animal Care International (AAALAC International). African green monkeys (*Chlorocebus sabaeus*) are an invasive species on the island of St. Kitts and were procured locally using approved practices with IACUC oversight. Animals were housed in well-ventilated outdoor enclosures for the duration of the study. PLVs were infused into the saphenous or cephalic vein at a rate of 2 mL/min. Blood was collected via femoral or saphenous vein phlebotomy following overnight fasting under ketamine/xylazine anesthesia. Blood was transferred to Vacutainer serum collection tubes without clot activators (BD Medical, New Jersey, United States) for 1 hour at room temperature to allow clotting followed by centrifugation at 3000

rpm for 10 minutes at 4˚C. At scheduled sacrifice, animals were sedated with ketamine and xylazine (8 mg/kg and 1.6 mg/kg respectively, IM) and euthanized with sodium pentobarbital (25-30 mg/kg IV). Upon loss of corneal reflex, transcardial perfusion was performed with chilled, heparinized 0.9% saline, and the brain and spinal cord were removed. Following perfusion, a gross necropsy was conducted. All abnormal findings were recorded, and associated tissues were collected and post-fixed in formalin for histopathology. Serum samples were sent to Antech Diagnostics (Los Angeles, CA) for clinical chemistry evaluation.

*Biodistribution of pDNA in excised tissues*

Adult green monkeys (*Chlorocebus sabaeus*) were intravenously infused with 1 mg/kg pDNA encapsulated within FAST-PLVs and sacrificed two days later. DNA was isolated using the DNeasy Blood & Tissue Kit (Qiagen, Toronto, Canada) protocol following the manufacturer's instructions. Cells were centrifuged for 5 min at 300 x g, the pellet resuspended in 200 µL PBS, and 20 µL proteinase K was added plus 200 µL Buffer AL (without added ethanol). The mixture was vortexed and incubated at 56°C in a Thermomixer (Labnet International, Inc, Edison, NJ) for 10 min. The levels of pDNA in excised tissues were measured using a PCR assay with primers specific to the pDNA backbone. A standard curve was generated using known amounts of pDNA and used to quantify the amount present in each tissue.

*Meso Scale Discovery*

The Mesoscale Discovery QuickPlex SQ 120 (MSD, Rockville, MD) was used with mouse and non-human primate samples as per the manufacturer's instructions. The data was analyzed with MSD Workbench 4.0 software, following the software protocol. The Meso Scale Discovery V-

PLEX NHP cytokine 24-Plex Kit (MSD, Rockville, MD) was used to quantitatively determine serum concentrations of 24 proinflammatory cytokines, including IFN-γ, IL-1β, IL-5, IL-6, IL-7, IL-8, IL-10, IL12/IL23 p40 Subunit, IL-15, IL-16, IL17A, CXCL1, GM-CSF, TNF-α, TNF-β, VEGF, IP10, Eotaxin, MCP-1, MCP-4, MDC, MIP-1α, MIP-1β, and TARC. The Meso Scale Discovery V-PLEX Proinflammatory Panel 1 mouse kit was used to quantitatively determine serum concentrations of 10 proinflammatory cytokines: IFN-γ, IL-1β, IL-2, IL-4, IL-5, IL-6, IL-10, IL-12p70, CXCL1 (KC/GRO), and TNF-α.

*Anti-Drug Antibody Titer: Indirect electrochemiluminescence immunoassay (ECLIA) for p14endo15 and FLuc*

Recombinant firefly luciferase protein (NBP1-48355, Novus Biologicals, Centennial, United States) or purified p14endo15 protein was coated on the standard binding plate (Meso Scale Discovery; MSD, Rockville, United States) at one µg/mL for one hour at ambient temperature with shaking. The plate was washed three times with 0.05% Tween-20 in PBS followed by the addition of Blocker A (blocking buffer, MSD). After 30 min of incubation, the plate was rewashed with PBS-T. Serially diluted p14endo15 antibody and luciferase antibody standards were prepared in Blocker A. Mouse, and nonhuman primate serum samples were diluted 1:100 in Blocker A. The antibody standards and diluted mouse serum samples were loaded to plates and incubated for one hour at ambient temperature with shaking. The plate was washed again with PBS-T followed by the addition of 1 µg/mL sulfo-tag anti-rabbit or anti-goat secondary antibody in standards (Meso Scale Discovery; MSD, Rockville, United States), and one µg/mL sulfo-tag anti-mouse secondary antibody in mouse serum samples (Meso Scale Discovery; MSD, Rockville, United States). Read buffer (Meso Scale Discovery; MSD, Rockville, United States) was added to the plate after

washing with PBS-T, and the plate was read in MESO QuickPlex SQ 120 (Meso Scale Discovery; MSD, Rockville, United States).

*MicroVue Complement C3a C4d and SC5b-9 Enzyme Immunoassay*

The levels of fragments of complement components such as C3a, C4d, and SC5b-9 in NHP serum were measured to determine whether PLVs activated the complement system (C3, C4 and C5). After PLVs were administered, blood was collected at 0.5, 1.0, 1.5, and 12 hours and the sera were immediately extracted. One hundred μL of serum was used to determine the levels of C3a, C4d, and SC5b-9 using QUIDEL MicroVue complement C3a/C4d/SC5b-9 Plus EIA kits (Quidel A032 XUS, San Diego, CA) according to manufacturer's instructions, including the high and low controls. A sample of serum taken before PLV administration was used to determine baseline levels of C3a, C4d, and SC5b-9. According to the manufacturer's instructions, the FLUOstar Omega microplate reader was used to measure the optical density of the samples.

*Follistatin ELISA*

Serum and media follistatin levels were quantified using human follistatin ELISA kit (PeproTech, Cat. No. 900-K299) with slight modification to adapt it to the MSD system. Capture FST antibody was coated on MSD standard binding plate at one μg/ml overnight at room temperature with shaking. The plate was washed three times with 0.05% Tween-20 in PBS followed by the addition of Blocker A (blocking buffer, MSD). After 1 hour of incubation, the plate was rewashed with PBS-T. Serially diluted Follistatin standard was prepared in Blocker A with 10% mouse serum. Mouse serum samples were prepared in Blocker A with a 1:10 dilution. The serum samples and follistatin standards were incubated overnight at 4˚C with shaking. The plate was rewashed with

PBS-T and biotinylated follistatin detection antibody was added at a concentration of 1 µg/ml for 2 hours at room temperature with shaking. The plate was washed three times with PBS-T followed by the addition of 1 µg/mL sulfo-tag streptavidin (Meso Scale Discovery; MSD, Rockville, United States) for 1 hour at room temperature. The plate was washed with PBS-T three times, then Read buffer (Meso Scale Discovery; MSD, Rockville, United States) was added to the plate then analyzed with the MESO QuickPlex SQ 120 (Meso Scale Discovery; MSD, Rockville, United States).

*Human Erythropoietin (EPO) ELISA*

Serum EPO levels were quantified using the U-PLEX Human EPO Assay kit developed my Meso Scale Discovery (Cat. No. K151VXK-2), following manufacturer's instructions. Briefly, plates are coated with biotinylated capture antibody prior to sample and standard administration. Samples are incubated on plate for 1 hour at room temperature, following which detection antibody is added for 1 hour. MSD GOLD Read Buffer B (Meso Scale Discovery; MSD, Rockville, United States) was added to the plate and then it was analyzed with the MESO QuickPlex SQ 120 (Meso Scale Discovery; MSD, Rockville, United States).

*Histology: Immunohistochemistry and H&E staining*

Major organs, including the heart, liver, spleen, lungs, and kidneys, were collected, formalin-fixed, and paraffin-embedded. 4-6 µm sections were generated. Sections were dewaxed in xylene and rehydrated using graded ethanol to water washes. Samples for H&E staining were stained in hematoxylin for 8 minutes, briefly differentiated in acid alcohol, and blued with Scott's Tap Water (pH 8). Slides were then stained in acidified eosin for 30 seconds, and dehydrated, cleared, and

then mounted. Whole slide images were generated using Panoramic SCAN (3D Histech, Budapest, Hungary) and reviewed by a certified DVM pathologist (Greenfield Pathology Services, Greenfield, United States) to evaluate the organ-specific toxicity. Heat-induced antigen retrieval for IHC samples was conducted by immersing rehydrated slides in 10mM sodium citrate (pH 6) and heating until boiling occurred. Slides were blocked in 10% normal rabbit serum (Cat. No. 869019-M, Sigma, Oakville, Canada) with 1% bovine serum albumin (BSA, Cat. No. A9418, Sigma, Oakville, Canada) in TBS with 0.1% Tween-20 for one hour at ambient temperature. Anti-firefly luciferase antibody was diluted at 1:1000 in blocking buffer and incubated on slide overnight. Endogenous peroxidase was blocked with 3% $H_2O_2$ in PBS. HRP conjugated rabbit anti-goat secondary antibody (ab97100, Abcam, Cambridge, United Kingdom) was diluted to 1:200 in 1% BSA TBS with 0.1% Tween-20 and added to slides for 1 hour at ambient temperature. Samples were stained with EnVision FLEX DAB + Chromogen (GV82511-2, Agilent Dako, Santa Clara, United States) for 20 minutes. The reaction was stopped by rinsing in $H_2O$. Slides were counterstained with hematoxylin and dehydrated, cleared, and then mounted. Gastrocnemius utilized for determining muscle fiber area were flash-frozen in O.C.T. Compound (Fisher Scientific, Cat. No. 23-730-571) and sectioned using a cryostat. Ten µm sections were warmed to room temperature and fixed with 3.7% formaldehyde for 15 minutes. Cells were washed three times with PBS. Sections were covered with 5 µg/ml wheat germ agglutinin Alexa Fluor-488 (Thermo Scientific, Cat. No. W11261) for 10 minutes at room temperature. Cells were washed three times with PBS and mounted using ProLong Gold antifade reagent (Thermo Scientific, Cat. No. P36930). Sections were visualized using EVOS fl inverted microscope (Advanced Microscopy Group, Bothell, United States) and 7-15 images were taken per section. Cross sectional muscle fiber area was determined using MyoVision software[428].

*Statistical analysis*

A two-tailed Student's *t*-test or a one-way analysis of variance (ANOVA) was performed when comparing two groups or more than two groups, respectively. Statistical analysis was performed using Microsoft Excel and Prism 7.0 (GraphPad). Data are expressed as means ± s.d. The difference was considered significant if $P < 0.05$ ($*P < 0.05$, $**P < 0.01$, $***P < 0.001$, $****P < 0.0001$ unless otherwise indicated).

**Acknowledgments**

This research was supported by an operating grant to John D. Lewis from the Canadian Institutes of Health Research (CIHR), in partnership with the Institute of Aging: Research Nova Scotia, reference number VR1-172710. Dr. Lewis holds the Frank and Carla Sojonky Chair in Prostate Cancer Research funded by the Alberta Cancer Foundation. Roy Duncan's laboratory was funded by the CIHR and the Natural Sciences and Engineering Research Council of Canada (NSERC). Douglas W. Brown was funded by fellowships from Prostate Cancer Canada and Mitacs. Eileen K. Clancy was funded by scholarships from the Nova Scotia Health Research Foundation (NSHRF) and the Cancer Research Training Program (CRTP) and with funding from the Dalhousie Medical Research Foundation (DMRF). We thank Abul Kalam Azad for isolating and sub-culturing HUVEC and Katia Carmine-Simmen for her technical support.

**Author Contributions**

DWB, AR, and JDL designed the study. RD, EKC, DP, NM, and DM constructed and screened the FAST protein recombinants. AR, PW, PB, MP, HV, LG, JG and PSA optimized the FAST-

PLV system. DWB, DS, MH, and SL performed the mice studies. AR, PW, PB, MP, HG, and JA performed the NHP studies. DWB, AR, PHB, RD, MS, and JDL wrote the manuscript with input from all authors.

## Declaration of Interests

None declared

**Table 2.1. Tissue pathology from the nonhuman primate study of FAST-PLV carrying plasmid DNA at two separate doses; 1 and 6 mg/kg.**

| Organ | Feature | 1 mg/kg | 6 mg/kg |
|---|---|---|---|
| **Lung** | Alveolar Macrophages | 0 (3/3) | 1 (2/3), 2 (1/3) |
| **Liver** | Mononuclear Cell Infiltration | 1 (3/3) | 1 (3/3) |
| | Sinusoidal Leukocytes | 0 (3/3) | 0 (3/3) |
| | Vacuolation | 0 (3/3) | 0 (3/3) |
| | Biliary Hyperplasia | 0 (3/3) | 0 (3/3) |
| | Periportal Hemosiderin | 0 (2/3), 1 (1/3) | 0 (3/3) |
| **Spleen** | Congestion | 0 (1/3), 2 (1/3), 3 (1/3) | 0 (3/3) |
| | Decreased Cellularity, Red Pulp | 0 (2/3), 3 (1/3) | 0 (3/3) |
| **Heart** | Mononuclear Cell Infiltration | 0 (3/3) | 0 (3/3) |
| | Fibrosis | 0 (3/3) | 0 (3/3) |
| **Kidney** | Glomerulopathy | 0 (3/3) | 0 (3/3) |

All pathological findings are scored on a scale from 0 to 5: 0 = No Visible Lesions, 1 = Minimal, 2 = Mild, 3 = Moderate, 4 = Marked, 5 = Severe.
The first number denotes the grade of lesion being reported; the second number in brackets denotes the number of subjects with the finding/total number of subjects evaluated.

## 2.5. Figures

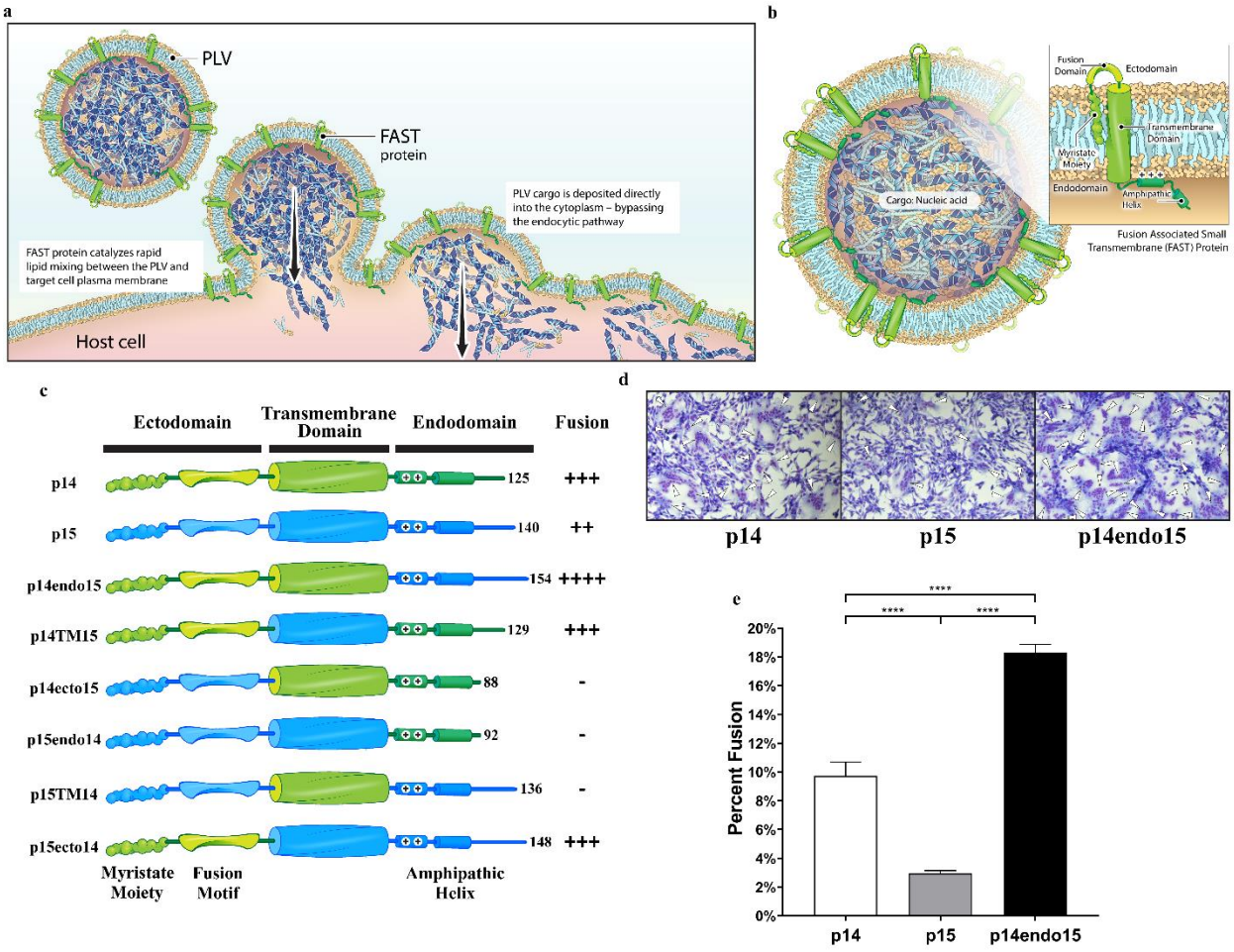
a
PLV
FAST protein
PLV cargo is deposited directly into the cytoplasm – bypassing the endocytic pathway
FAST protein catalyzes rapid lipid mixing between the PLV and target cell plasma membrane
Host cell
b
Cargo: Nucleic acid
Fusion Domain
Ectodomain
Transmembrane Domain
Myristate Moiety
Endodomain
Amphipathic Helix
Fusion Associated Small Transmembrane (FAST) Protein
c
Ectodomain
Transmembrane Domain
Endodomain
Fusion
p14 125 +++
p15 140 ++
p14endo15 154 ++++
p14TM15 129 +++
p14ecto15 88 -
p15endo14 92 -
p15TM14 136 -
p15ecto14 148 +++
Myristate Moiety
Fusion Motif
Amphipathic Helix
d
p14
p15
p14endo15
e
Percent Fusion
20%
18%
16%
14%
12%
10%
8%
6%
4%
2%
0%
****
****
****
p14
p15
p14endo15

**Figure 2.1: Engineering p14endo15 proteolipid vehicles (FAST-PLVs).**
(A) FAST-PLVs demonstrating nucleic acid encapsulation, fusion between the FAST-PLV and plasma membrane, and cargo delivery directly into cytosol.
(B) Schematic showing the topology of a generic FAST protein in the PLV membrane and key structural motifs present in the ecto- and endodomains.
(C) Arrangement of the ectodomain, transmembrane (TM) domain, and endodomain fusion modules of the parental p14 and p15 FAST proteins and various chimeric constructs. Color scheme depicts the wildtype source of each fusion module (p14, green; p15, blue). The locations of the N-terminal myristylation site and adjacent fusion peptide motif in the ectodomain, and the endodomain polybasic motif (++) and adjacent amphipathic helix are indicated. Chimeras were named with the FAST protein contributing two domains as the backbone followed by the inserted domain name abbreviation and FAST protein identity. Numbers indicate the number of residues in each protein. Syncytium formation of the various constructs was scored on a 4+ scale with '-' indicating no syncytium formation.
(D) Representative images of Giemsa stained QM5 cells transfected with pcDNA3 expressing either p14, p15, or p14endo15 captured at 13 hours post-transfection. Arrows indicate syncytial nuclei.
(E) Quantification of syncytium formation expressed as a percentage of syncytial nuclei over total nuclei. Data are represented as mean ± standard deviation. One-way ANOVA and Tukey's multiple comparisons test. ****$P<0.0001$.

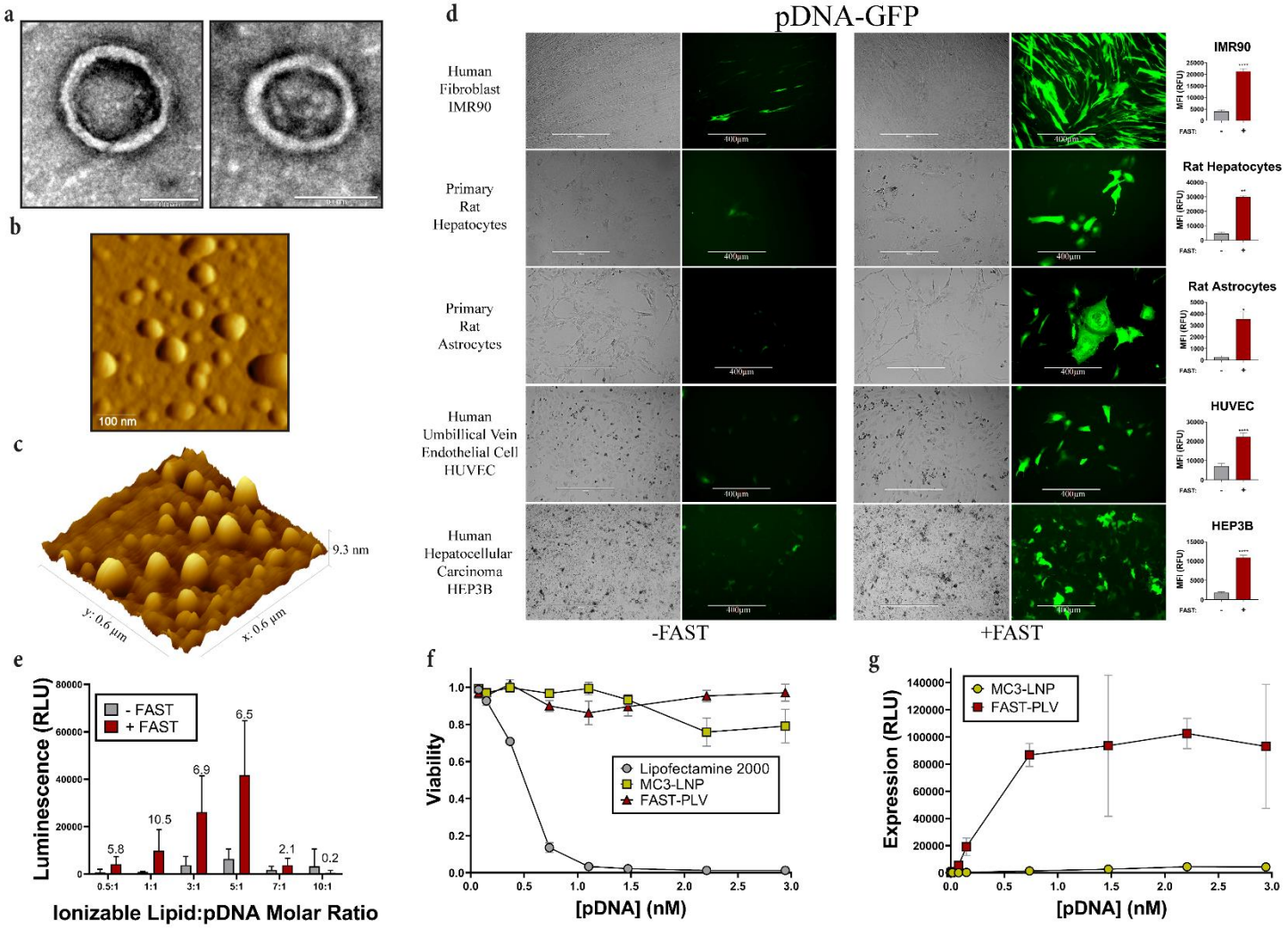
a
b
100 nm
c
9.3 nm
y: 0.6 µm
x: 0.6 µm
d
pDNA-GFP
Human Fibroblast IMR90
Primary Rat Hepatocytes
Primary Rat Astrocytes
Human Umbilical Vein Endothelial Cell HUVEC
Human Hepatocellular Carcinoma HEP3B
IMR90
Rat Hepatocytes
Rat Astrocytes
HUVEC
HEP3B
MFI (RFU)
FAST: - +
-FAST
+FAST
e
Luminescence (RLU)
- FAST
+ FAST
5.8
10.5
6.9
6.5
2.1
0.2
0.5:1 1:1 3:1 5:1 7:1 10:1
Ionizable Lipid:pDNA Molar Ratio
f
Viability
Lipofectamine 2000
MC3-LNP
FAST-PLV
[pDNA] (nM)
g
Expression (RLU)
MC3-LNP
FAST-PLV
[pDNA] (nM)
h
Luminescence (RLU)
- FAST
+ FAST
0.25:1 0.5:1 1:1 2:1 3:1 5:1 7:1 10:1
Ionizable Lipid:mRNA Molar Ratio
i
mRNA-mCherry
-FAST
+ FAST
HUVEC
Median Fluorescence Intensity (RFU)
****
FAST: - +
j
HEP3B Cells
mRNA-eGFP + mRNA-mCherry
mRNA-mCherry
mRNA-eGFP
mRNA-eGFP mRNA-mCherry
mRNA-eGFP
mRNA-mCherry
Bright Field
k
HEP3B Cells
pDNA-GFP + mRNA-mCherry
mRNA-mCherry
pDNA-GFP
pDNA-GFP mRNA-mCherry
pDNA-GFP
mRNA-mCherry
Bright Field

**Figure 2.2: *In vitro* validation of FAST-PLVs.**
(A) Transmission electron microscope images of optimized lipid formulation 41N containing p14endo15 encapsulating pDNA.
(B-C) Atomic force microscopy used to assess the (B) 2D and (C) 3D structure of optimized lipid formulation 41N with p14endo15 encapsulating pDNA.
(D) Optimized lipid formulation 41N with (right) and without (left) FAST protein (p14endo15) was used to encapsulate pDNA-GFP and 0.9 nM was incubated with IMR-90, primary rat hepatocytes, primary rat astrocytes, HUVECs, and HEP3B cells for 96 hours before fluorescence images were taken, and flow cytometry was conducted. Mean fluorescence intensity (MFI) is presented for the $GFP^+$ fraction for all cell types except for rat astrocytes, where it is presented for the total cell population due to low transfection efficiency in the (–) FAST group.
(E) Ability of FAST protein to reduce the amount of ionizable lipid and improve expression from pDNA-FLuc *in vitro*. ARPE-19 cells were incubated with pDNA-FLuc encapsulated within optimized lipid formulation 41N with and without FAST protein at different ionizable lipid:pDNA molar ratios for 96 hours before luminescence was determined.
(F) Cell viability of HUVEC treated with varying amounts of pDNA encapsulated in Lipofectamine 2000, MC3-LNPs, and FAST-PLVs.
(G) Expression of pDNA-FLuc in IMR-90 cells delivered by MC3-LNPs or FAST-PLVs.
(H) *In vitro* expression of mRNA-FLuc encapsulated within optimized lipid formulation 41N at multiple ionizable lipid:mRNA molar ratios made with and without FAST protein 48 hours after addition to WI38 cells. Data are represented as the mean ± standard deviation.
(I) Optimized lipid formulation 41N with and without FAST protein was used to encapsulated mRNA-mCherry at the optimal 3:1 molar ratio and incubated with HUVEC for 48 hours before fluorescence images were taken, and flow cytometry was conducted. Median fluorescent intensity is presented for the total cell population due to low transfection efficiency in the -FAST group.
(J) Ability of FAST-PLVs to deliver two different mRNA molecules to the same cell. HEP3B cells were incubated with FAST-PLVs encapsulating mRNA-eGFP and mRNA-mCherry (1:1 molar ratio) for 48 hours before fluorescence images were taken, and flow cytometry was conducted.
(K) Ability of FAST-PLVs to delivery both pDNA-GFP and mRNA-mCherry to the same cell. HEP3B cells were incubated with FAST-PLVs encapsulating pDNA-GFP and mRNA-mCherry (1:6 molar ratio) for 72 hours before fluorescence images were taken, and flow cytometry was conducted.

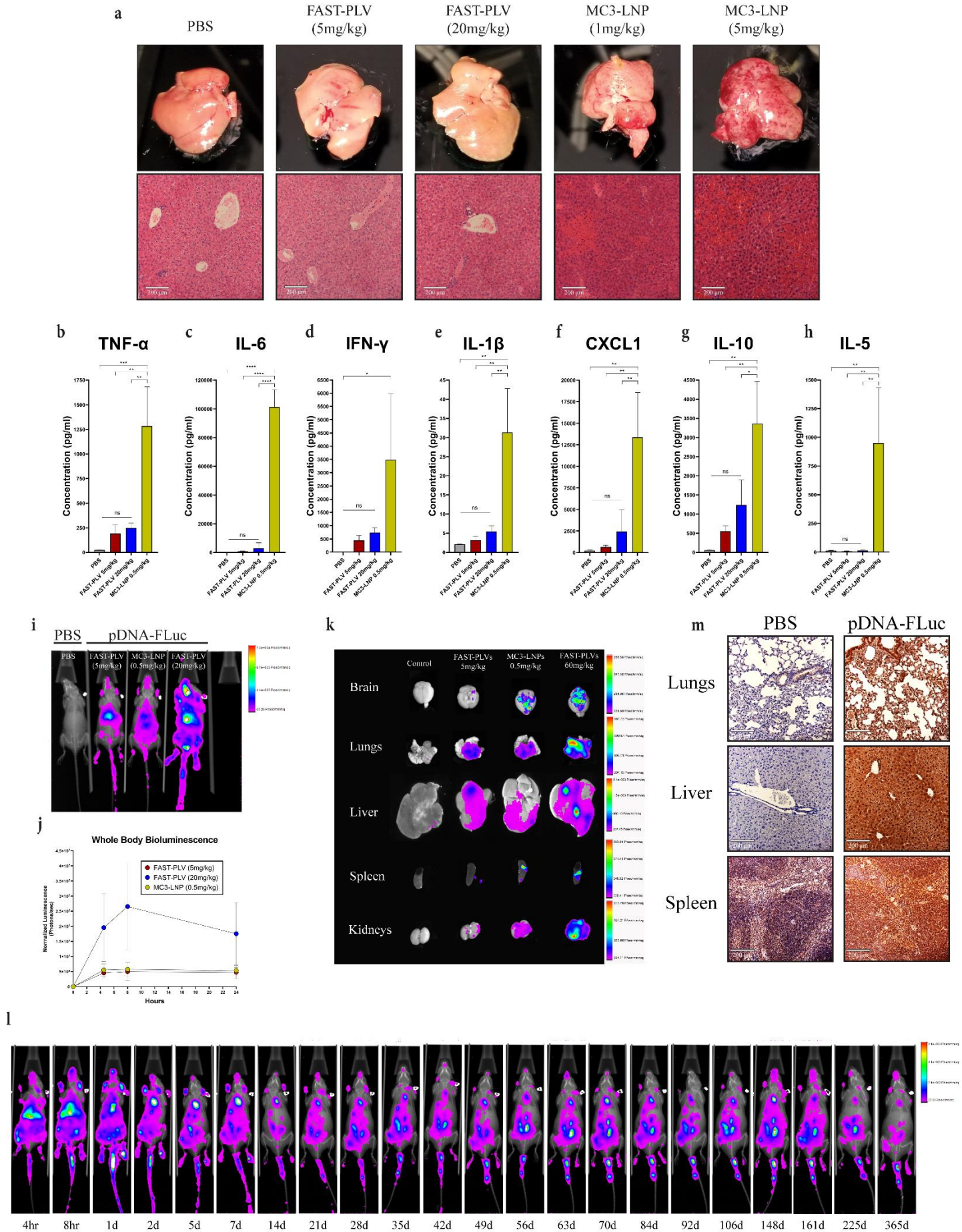
a
PBS
FAST-PLV (5mg/kg)
FAST-PLV (20mg/kg)
MC3-LNP (1mg/kg)
MC3-LNP (5mg/kg)
b
TNF-α
c
IL-6
d
IFN-γ
e
IL-1β
f
CXCL1
g
IL-10
h
IL-5
Concentration (pg/ml)
PBS
FAST-PLV 5mg/kg
FAST-PLV 20mg/kg
MC3-LNP 0.5mg/kg
ns
i
PBS
pDNA-FLuc
PBS
FAST-PLV (5mg/kg)
MC3-LNP (0.5mg/kg)
FAST-PLV (20mg/kg)
j
Whole Body Bioluminescence
FAST-PLV (5mg/kg)
FAST-PLV (20mg/kg)
MC3-LNP (0.5mg/kg)
Normalized Luminescence (Photons/sec)
Hours
k
Control
FAST-PLVs 5mg/kg
MC3-LNPs 0.5mg/kg
FAST-PLVs 60mg/kg
Brain
Lungs
Liver
Spleen
Kidneys
m
PBS
pDNA-FLuc
Lungs
Liver
Spleen
l
4hr
8hr
1d
2d
5d
7d
14d
21d
28d
35d
42d
49d
56d
63d
70d
84d
92d
106d
148d
161d
225d
365d

**Figure 2.3: Delivery of pDNA by FAST-PLVs in mice.**
(A) Post-mortem liver images and hematoxylin and eosin staining of liver sections from mice injected with multiple doses of FAST-PLVs or MC3-LNPs encapsulating pDNA-FLuc (magnification = 10X).
(B)-(H) Blood samples were collected from mice 24 hours after injection with PBS, MC3-LNPs, or FAST-PLVs encapsulating pDNA-FLuc and Meso Scale Discovery V-PLEX was used to determine serum concentrations of pro-inflammatory cytokines: (B) TNF-α, (C) IL-6, (D), IFN-γ, (E) IL-1β, (F) CXCL1, (G) IL-10, (H) IL-5. Data are represented as mean ± standard deviation, *n*=3 biologically independent mice per group, one-way ANOVA and Tukey's multiple comparisons test, *P < 0.05, **P < 0.01, ***P < 0.001, ****P<0.0001, ns, not significant.
(I) Whole body bioluminescent imaging of mice 24 hours after injection with pDNA-FLuc encapsulated within MC3-LNPs or FAST-PLVs. Mice injected intravenously with pDNA-FLuc encapsulated within MC3-LNPs received 0.5 mg/kg pDNA-FLuc, mice injected with FAST-PLVs encapsulating pDNA-FLuc received either 5 mg/kg or 20 mg/kg pDNA-FLuc.
(J) Quantification of whole-body luminescence from mice in panel I (*n*=3 biologically independent mice per group).
(K) *Ex vivo* organ bioluminescence from mice injected intravenously with pDNA-FLuc encapsulated within MC3-LNPs (0.5 mg/kg) or FAST-PLVs (5 mg/kg or 60 mg/kg).
(L) Whole-body bioluminescence of mice injected intravenously with FAST-PLVs encapsulating 20 mg/kg pDNA-FLuc and monitored for one year. Quantification of luminescent signal presented in Figure S2.
(M) Immunohistochemistry staining for FLuc 63 days after intravenous injection with FAST-PLVs encapsulating 20 mg/kg pDNA-FLuc (magnification = 10X). TNF-α, tumor necrosis factor alpha; IFN-γ, interferon-gamma; CXCL1, chemokine (C-X-C motif) ligand 1.

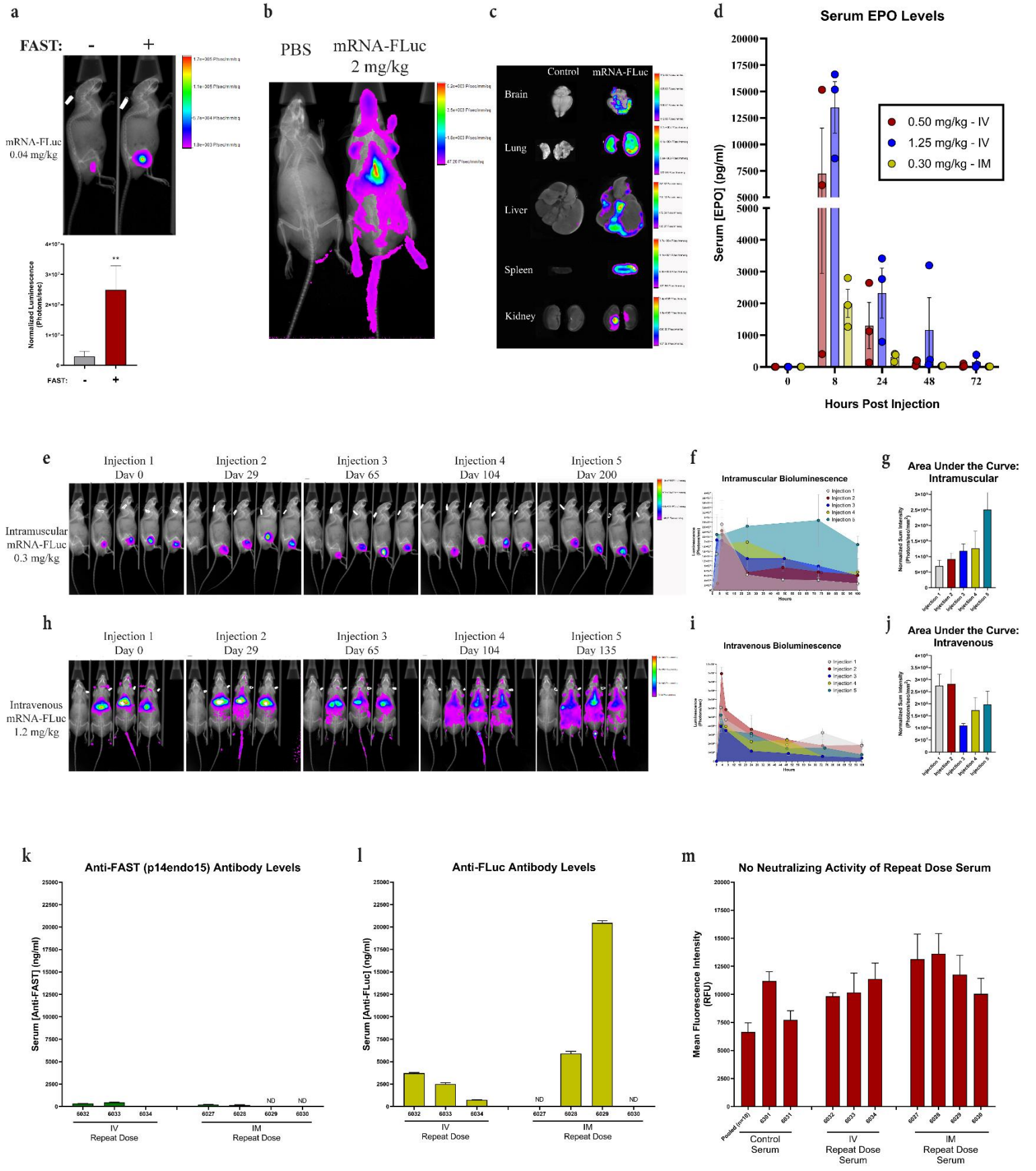
a
FAST: - +
mRNA-FLuc
0.04 mg/kg
Normalized Luminescence (Photons/sec)
FAST: - +
b
PBS
mRNA-FLuc
2 mg/kg
c
Control
mRNA-FLuc
Brain
Lung
Liver
Spleen
Kidney
d
Serum EPO Levels
Serum [EPO] (pg/ml)
0.50 mg/kg - IV
1.25 mg/kg - IV
0.30 mg/kg - IM
Hours Post Injection
e
Injection 1 Day 0
Injection 2 Day 29
Injection 3 Day 65
Injection 4 Day 104
Injection 5 Day 200
Intramuscular mRNA-FLuc 0.3 mg/kg
f
Intramuscular Bioluminescence
g
Area Under the Curve: Intramuscular
h
Injection 1 Day 0
Injection 2 Day 29
Injection 3 Day 65
Injection 4 Day 104
Injection 5 Day 135
Intravenous mRNA-FLuc 1.2 mg/kg
i
Intravenous Bioluminescence
j
Area Under the Curve: Intravenous
k
Anti-FAST (p14endo15) Antibody Levels
Serum [Anti-FAST] (ng/ml)
ND
IV Repeat Dose
IM Repeat Dose
l
Anti-FLuc Antibody Levels
Serum [Anti-FLuc] (ng/ml)
ND
IV Repeat Dose
IM Repeat Dose
m
No Neutralizing Activity of Repeat Dose Serum
Mean Fluorescence Intensity (RFU)
Pooled (n=10)
Control Serum
IV Repeat Dose Serum
IM Repeat Dose Serum

**Figure 2.4: Delivery of mRNA by FAST-PLVs in mice.**
(A) Incorporation of FAST protein into 41N lipid formulation improves the in vivo expression of mRNA-FLuc following intramuscular injection. Quantification of the bioluminescent signal from panel A. Data are represented as mean ± standard deviation, *n*=3 biologically independent mice per group. Unpaired t-test, **P<0.01
(B) Whole-body bioluminescent of mice 4 hours after intravenous injection of FAST-PLVs encapsulating 2 mg/kg mRNA-FLuc.
(C) *Ex vivo* organ bioluminescence of mice 4 hours after intravenous injection with FAST-PLVs encapsulating 2 mg/kg mRNA-FLuc.
(D) Serum EPO concentrations following intravenous or intramuscular injection with FAST-PLVs encapsulating mRNA-EPO. *n*=3 biologically independent mice per group.
(E) Mice repeatedly dosed intramuscularly with 0.3 mg/kg mRNA-FLuc encapsulated within FAST-PLVs, once a month for six months.
(F) Quantification of whole-body bioluminescence from mice in panel E for 100 hours following injection.
(G) Area under the curve calculated on time course shown in panels E and F
(H) Mice repeatedly dosed intravenously with 1.2 mg/kg mRNA-FLuc encapsulated in FAST-PLVs, once a month for six months.
(I) Quantification of whole-body bioluminescence from mice in panel H for 100 hours following injection.
(J) Area under the curve calculated on the time course shown in panels H and I.
(K) Serum collected from mice dosed repeatedly intramuscularly or intravenously was assessed for anti-FAST antibody levels via ELISA.
(L) Serum collected from repeatedly intramuscularly and intravenously dosed mice was assessed for anti-FLuc antibody levels via ELISA.
(M) Serum from repeatedly dosed mice was incubated with FAST-PLVs encapsulating pDNA-GFP prior to addition to 3T3 cells. Flow cytometry was conducted 96 hours after addition and mean fluorescence intensity of the $GFP^+$ population is presented. Pooled serum is a combination of equivalent volumes of serum from 10 separate animals with varying degrees of hemolysis to control for matrix interference.

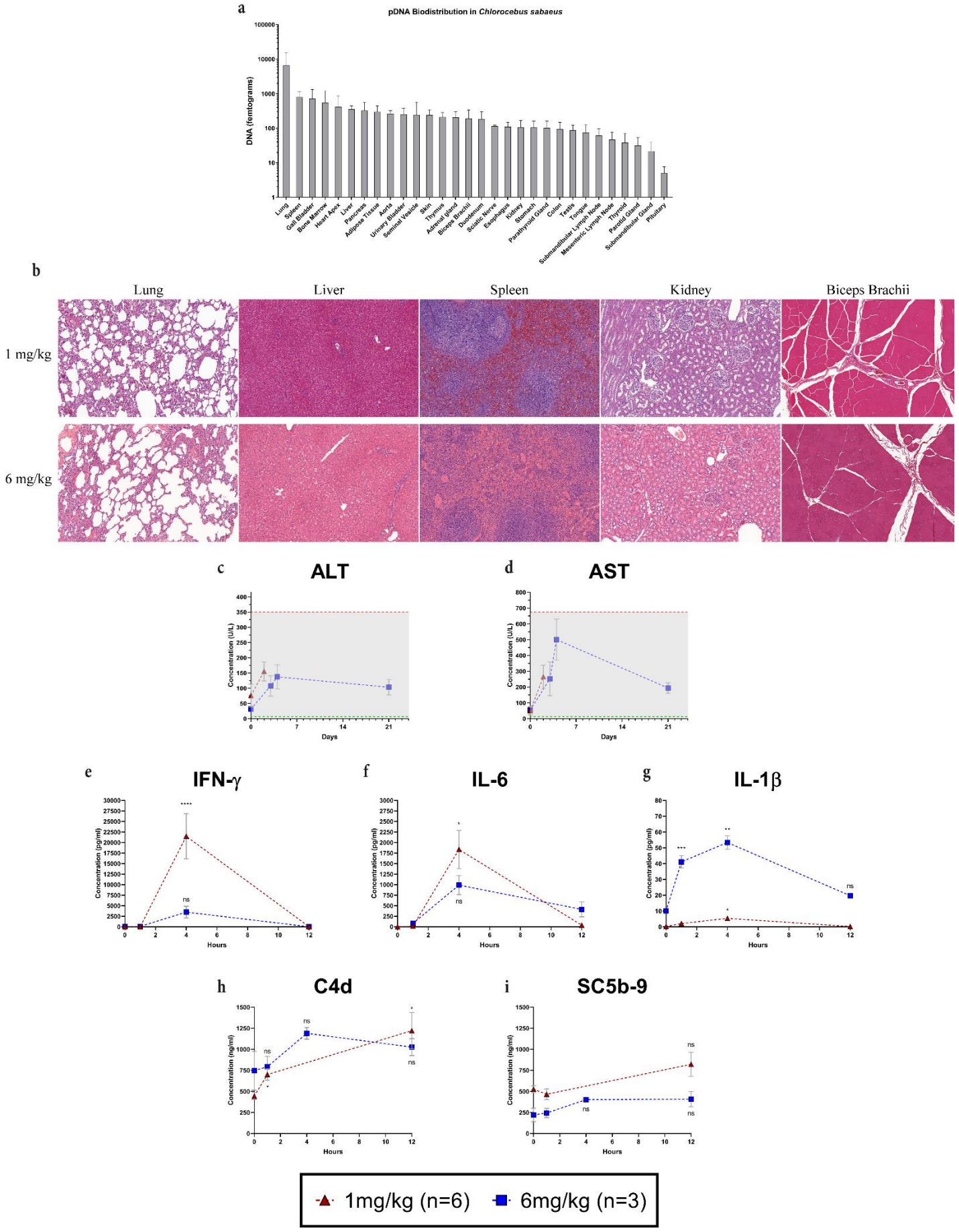
a
pDNA Biodistribution in Chlorocebus sabaeus
DNA (femtograms)
Lung
Spleen
Gall Bladder
Bone Marrow
Heart Apex
Liver
Pancreas
Adipose Tissue
Aorta
Urinary Bladder
Seminal Vesicle
Skin
Thymus
Adrenal gland
Biceps Brachii
Duodenum
Sciatic Nerve
Esophagus
Kidney
Stomach
Parathyroid Gland
Colon
Testis
Tongue
Submandibular Lymph Node
Mesenteric Lymph Node
Thyroid
Parotid Gland
Submandibular Gland
Pituitary
b
Lung
Liver
Spleen
Kidney
Biceps Brachii
1 mg/kg
6 mg/kg
c
ALT
Concentration (U/L)
Days
d
AST
Concentration (U/L)
Days
e
IFN-γ
Concentration (pg/ml)
Hours
f
IL-6
Concentration (pg/ml)
Hours
g
IL-1β
Concentration (pg/ml)
Hours
h
C4d
Concentration (ng/ml)
Hours
i
SC5b-9
Concentration (ng/ml)
Hours
1mg/kg (n=6)
6mg/kg (n=3)

**Figure 2.5: Validation of FAST-PLVs safety in non-human primates.**
(A) Adult green monkeys (*Chlorocebus sabaeus*) were intravenously infused with FAST-PLVs encapsulating 1 mg/kg pDNA-GFP at a rate of 2 mL/min. Two days after infusion, the amount of pDNA was quantified in 30 tissues using a quantitative PCR approach with primers specific to the pDNA backbone.
(B) Representative images of tissues stained with hematoxylin and eosin one day after intravenous infusion with FAST-PLVs encapsulating 1 or 6 mg/kg pDNA-GFP (magnification = 10X).
(C)-(D) Blood samples were collected from test subjects injected with FAST-PLVs encapsulating two doses of pDNA at indicated time points was used to determine the serum concentrations of the clinical chemistry parameters (C) ALT and (D) AST. Shaded area indicates normal parameter range.
(E)-(G) Blood samples were collected from test subjects injected with FAST-PLVs encapsulating two doses of pDNA at indicated time points and Meso Scale Discovery V-PLEX was used to determine serum concentrations of pro-inflammatory cytokines: (E) IFN-γ, (F) IL-6, (G) IL-1β.
(H)-(I), Blood samples were collected from test subjects injected with FAST-PLVs encapsulating two doses of pDNA at indicated time points and serum concentrations of the CARPA mediators, (H) C4d, and (I) SC5b-9, were determined via ELISA assay. ALT, alanine aminotransferase; AST, aspartate aminotransferase; IFN-γ, interferon-gamma.

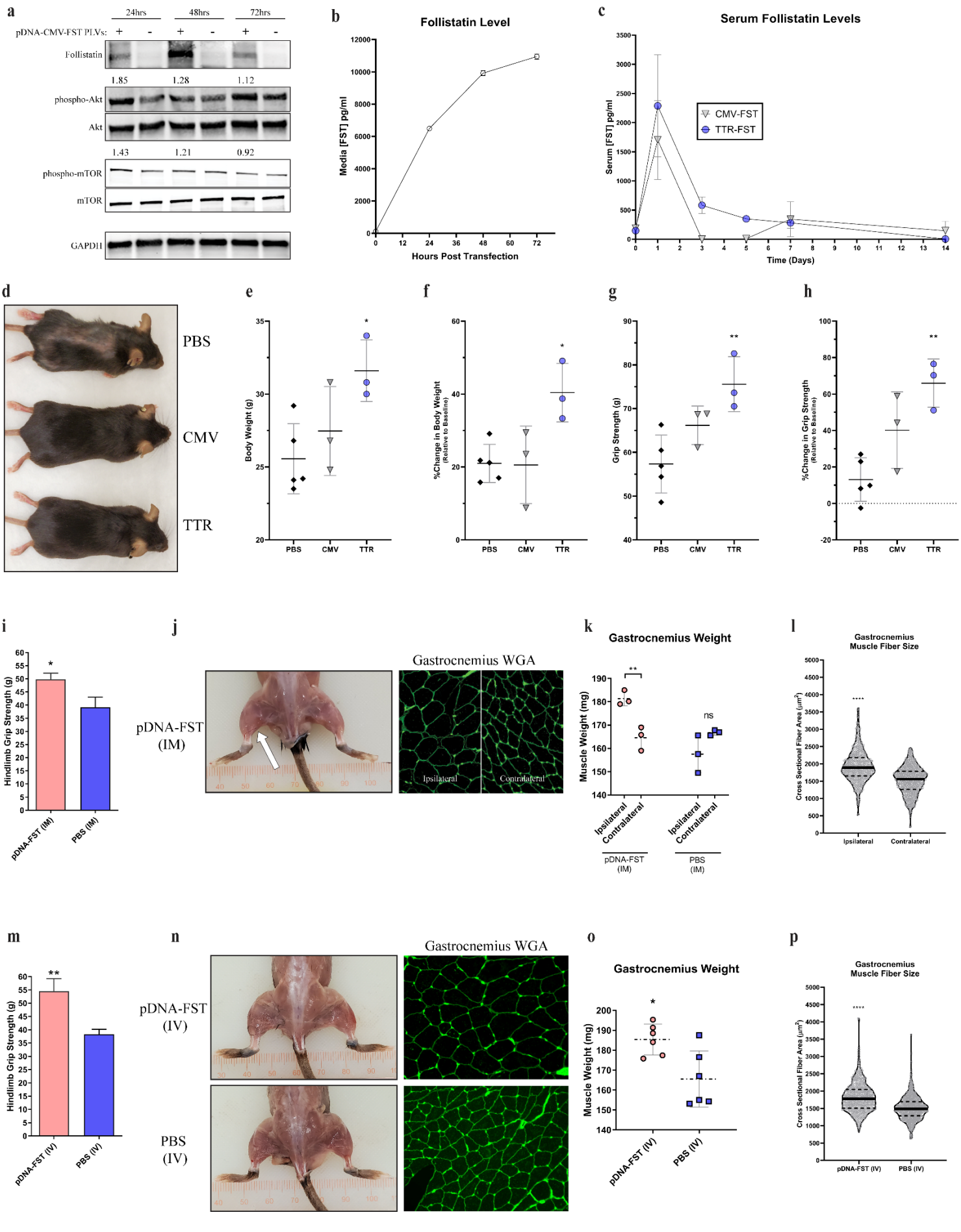
a
24hrs
48hrs
72hrs
pDNA-CMV-FST PLVs: + - + - + -
Follistatin
1.85
1.28
1.12
phospho-Akt
Akt
1.43
1.21
0.92
phospho-mTOR
mTOR
GAPDH
b
Follistatin Level
Media [FST] pg/ml
Hours Post Transfection
c
Serum Follistatin Levels
Serum [FST] pg/ml
CMV-FST
TTR-FST
Time (Days)
d
PBS
CMV
TTR
e
Body Weight (g)
PBS
CMV
TTR
f
%Change in Body Weight
(Relative to Baseline)
g
Grip Strength (g)
h
%Change in Grip Strength
(Relative to Baseline)
i
Hindlimb Grip Strength (g)
pDNA-FST (IM)
PBS (IM)
j
pDNA-FST
(IM)
Gastrocnemius WGA
Ipsilateral
Contralateral
k
Gastrocnemius Weight
Muscle Weight (mg)
ns
Ipsilateral
Contralateral
pDNA-FST
(IM)
PBS
(IM)
l
Gastrocnemius
Muscle Fiber Size
Cross Sectional Fiber Area (μm²)
Ipsilateral
Contralateral
m
Hindlimb Grip Strength (g)
pDNA-FST (IV)
PBS (IV)
n
pDNA-FST
(IV)
PBS
(IV)
Gastrocnemius WGA
o
Gastrocnemius Weight
Muscle Weight (mg)
pDNA-FST (IV)
PBS (IV)
p
Gastrocnemius
Muscle Fiber Size
Cross Sectional Fiber Area (μm²)
pDNA-FST (IV)
PBS (IV)

**Figure 2.6: Delivery of pDNA encoding follistatin using FAST-PLVs.**
(A) FAST-PLVs were used to encapsulate pDNA-CMV-FST (+) or pDNA-CMV-GFP (-) and added to C2C12 mouse myoblasts. Western blot was conducted to examine expression of FST as well as phosphorylation of Akt and mTOR. Numbers above phosphorylated bands represent fold increase relative to pDNA-CMV-GFP treated C2C12 lysates.
(B) Media concentration of FST following FAST-PLV addition to C2C12 mouse myoblasts determined via ELISA.
(C) Serum levels of FST following intravenous injection of C57Bl/6 mice with FAST-PLVs encapsulating 10 mg/kg pDNA-CMV-FST or pDNA-TTR-FST determined via ELISA ($n$=3 biologically independent mice per group).
(D) Representative animals from each group 15 weeks following intravenous injection with PBS or FAST-PLVs encapsulating 10 mg/kg pDNA-CMV-FST or pDNA-TTR-FST. Note, hair loss in PBS mouse is likely unrelated to treatment as all cage mates presented with the same condition.
(E) Body weight of mice 15 weeks following intravenous injection with PBS or FAST-PLVs encapsulating 10 mg/kg pDNA-CMV-FST or pDNA-TTR-FST. One-way ANOVA and Dunnett's multiple comparisons test, *P<0.05.
(F) Body weight measurements from panel (E) were normalized to the initial body weight taken immediately prior to injection. One-way ANOVA and Dunnett's multiple comparisons test, *P<0.05.
(G) Hindlimb grip strength of mice 15 weeks following intravenous injection with PBS or FAST-PLVs encapsulating 10 mg/kg pDNA-CMV-FST or pDNA-TTR-FST. One-way ANOVA and Dunnett's multiple comparisons test, **P<0.01.
(H) Grip strength measurements from panel (G) were normalized to the initial grip strength reading taken immediately prior to injection. One-way ANOVA and Dunnett's multiple comparisons test, **P < 0.01.
(I) Hindlimb grip strength of mice injected intramuscularly into the left GAS with PBS or 5 mg/kg pDNA-CMV-FST 46 weeks after injection. Unpaired t-test, *P<0.05.
(J) Gross dissection of mice 46 weeks after intramuscular injection with 5 mg/kg pDNA-CMV-FST into the left GAS (indicated with arrow) with representative WGA-488 stained GAS sections.
(K) Ipsilateral and contralateral GAS weight 46 weeks after intramuscular injection with pDNA-CMV-FST or PBS. Unpaired t-test, **P<0.01.
(L) Ipsilateral and contralateral GAS from pDNA-CMV-FST intramuscularly injected mice was stained with WGA-488 and cross-sectional muscle fiber area was determined using MyoVision Software. Unpaired t-test, ****P<0.0001
(M) Hindlimb grip strength of mice injected intravenously with 10 mg/kg pDNA-CMV-FST 46 weeks after injection. Unpaired t-test, **P<0.01.
(N) Gross dissection of mice 46 weeks after intravenous injection with PBS or 10 mg/kg pDNA-CMV-FST with representative images of GAS WGA-488 staining.
(O) GAS weight 46 weeks after intravenous injection with pDNA-CMV-FST or PBS. Unpaired t-test, *P<0.05.
(P) Cross-sectional muscle fiber area of WGA-488 stained GAS from intravenously injected pDNA-CMV-FST or PBS mice was determined using MyoVision Software. Unpaired t-test, ****P<0.0001. FST, follistatin; GFP, green fluorescent protein; GAS, gastrocnemius muscle; WGA-488, wheat germ agglutinin Alexa Fluor 488; CMV, cytomegalovirus; TTR, transthyretin.

## 2.6. Supplementary Material

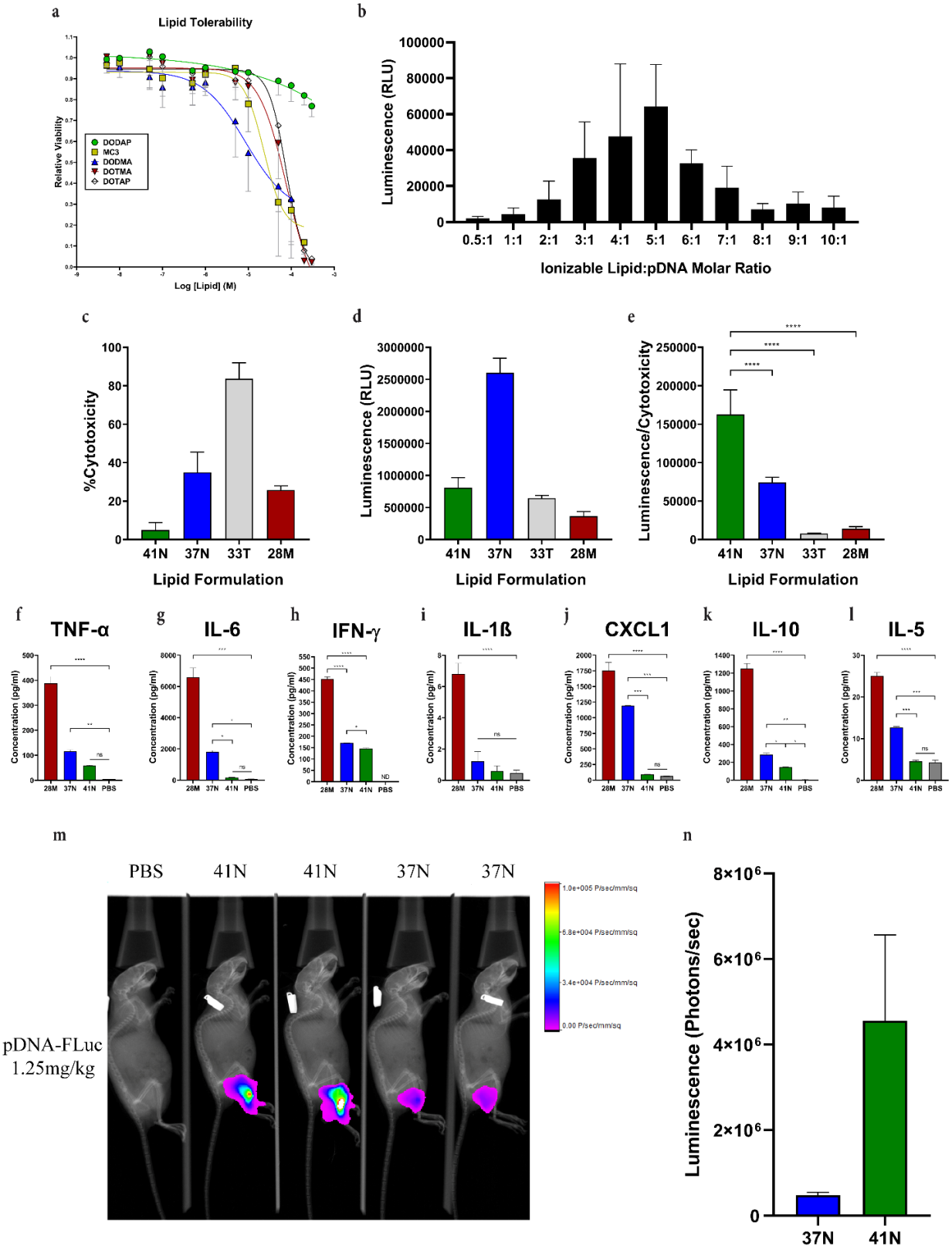

**Supplementary Figure 2.1: Optimizing lipid formulation for FAST-PLVs.**
(A) Tolerability comparison of 3 ionizable (DODAP, DLin-MC3-DMA, DODMA) and 2 cationic (DOTMA, DOTAP) lipids determined via Alamar Blue, 72 hours after their addition to WI-38 cells.
(B) Effect of different ionizable lipid:pDNA molar ratios on the *in vitro* expression of pDNA-FLuc in ARPE-19 cells 96 hours after addition.
(C)-(E) Comparison of the toxicity and efficacy of four lipid formulations (41N, 37N, 33T, 28M), formulated with FAST protein delivering 1.5 nM pDNA-FLuc to VERO cells. (C) LDH assay used to determine cytotoxicity 24 hours after pDNA-FLuc addition. (D) Luminescence determined 72 hours after pDNA-FLuc addition. (E) Expression as a function of cytotoxicity. Data are represented as the mean ± standard deviation. One-way ANOVA, Tukey's multiple comparisons, ****P<0.0001.
(F)-(L) Blood samples were collected from mice 24 hours after intravenous injection with each PLV lipid formulation encapsulating 8 mg/kg pDNA-FLuc and Meso Scale Discovery V-PLEX was used to determine serum concentrations of pro-inflammatory cytokines: (F) TNF-α, (G) IL-6, (H) IFN-γ, (I) IL-1β, (J) CXCL1, (K) IL-10, (L) IL-5. One-way ANOVA and Tukey's multiple comparisons test, *P < 0.05, **P < 0.01, ***P < 0.001, ****P<0.0001.
(M) Whole-body bioluminescence of mice injected intramuscularly FAST-PLVs encapsulating 1.25 mg/kg pDNA-FLuc, manufactured with lipid formulation 41N or lipid formulation 37N.
(N) Quantification of the bioluminescent signal in panel M (*n*=2 biologically independent mice per group).

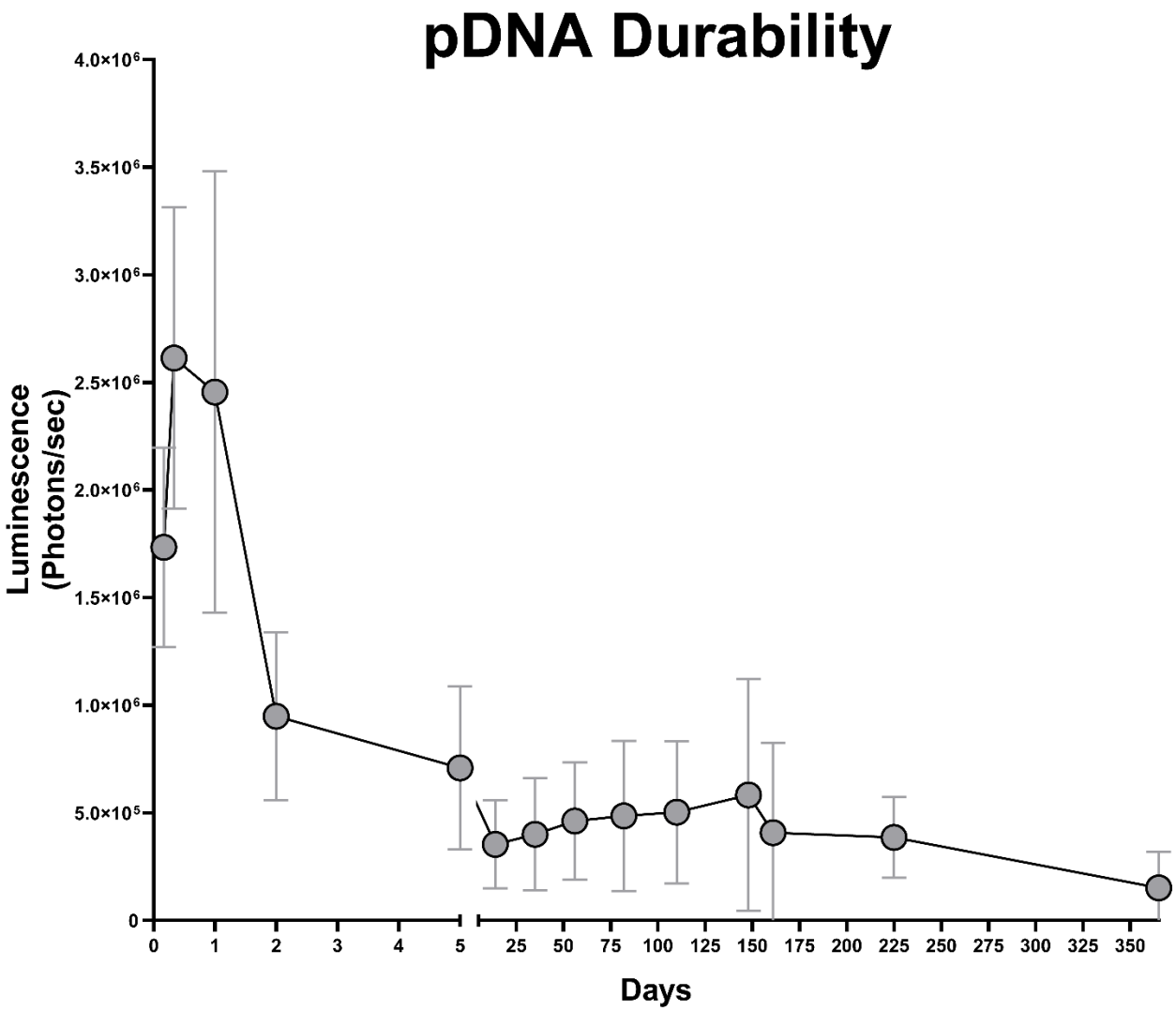


**Supplementary Figure 2.2: Durability of pDNA transgene expression.**
Quantification of whole-body bioluminescent signal from mice in Figure 3L intravenously injected with FAST-PLVs encapsulating 20 mg/kg pDNA-FLuc. Each point from day 7 onwards represents a rolling average, where the measurements from three weeks were averaged to control for fluctuations in luminescent capture overtime. Data are represented as the mean ± standard deviation, *n*=3 biologically independent animals.

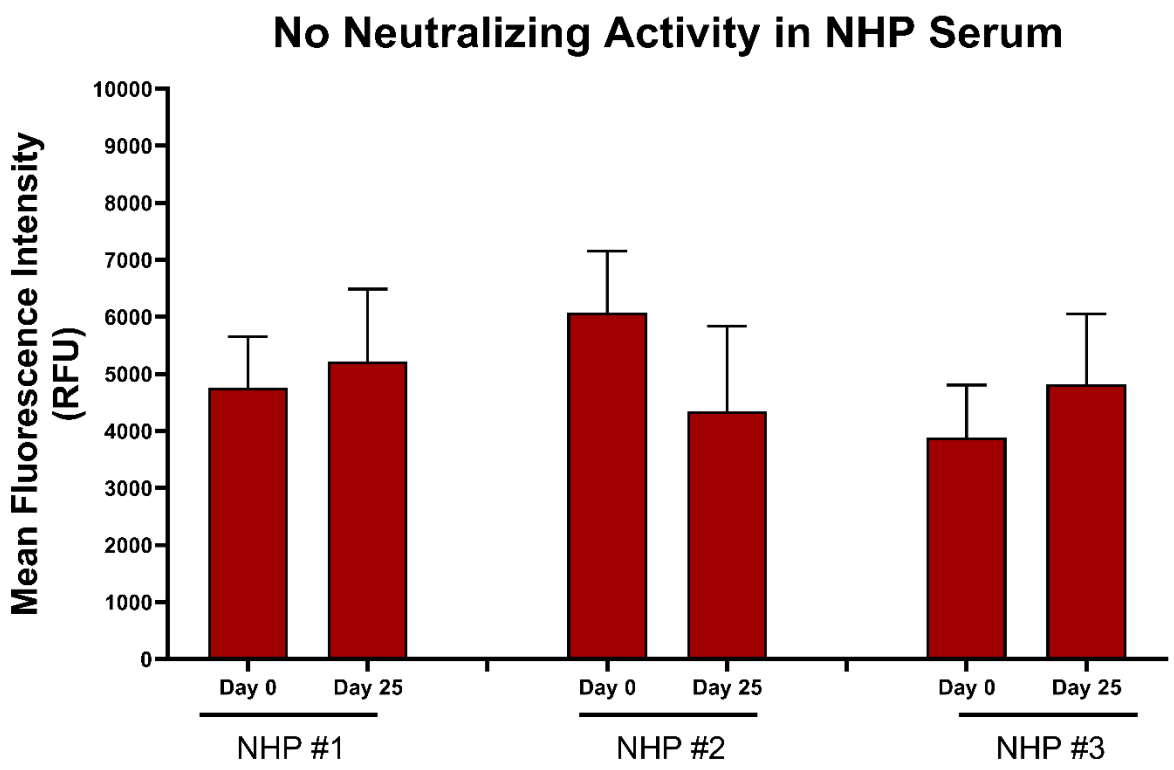


**Supplementary Figure 2.3: Immunogenicity of FAST-PLVs in nonhuman primates.**
Serum collected from nonhuman primates prior to FAST-PLV administration and 25 days after administration was incubated with FAST-PLVs encapsulating pDNA-GFP prior to addition to 3T3 cells. Flow cytometry was conducted 96 hours after addition and mean fluorescence intensity of the $GFP^+$ population is presented.

**Supplementary Table 2.1. Physical characteristics of lipid formulations with and without p14endo15 chimeric FAST protein.**

| Formulation | Mean Size (nm) | Polydispersity Index | Zeta Potential (mV) |
|---|---|---|---|
| **28M** | 62.2 ± 6.9 | 0.1525 ± 0.0058 | +0.560 ± 0.920 |
| **28M + p14endo15** | 52.7 ± 8.3 | 0.1865 ± 0.0064 | +1.738 ± 0.167 |
| **33T** | 51.9 ± 3.0 | 0.2211 ± 0.0389 | +0.429 ± 0.166 |
| **33T + p14endo15** | 59.3 ± 5.0 | 0.1606 ± 0.0079 | +0.645 ± 0.746 |
| **37N** | 75.8 ± 16.6 | 0.1730 ± 0.0044 | +0.886 ± 0.588 |
| **37N + p14endo15** | 52.4 ± 6.4 | 0.1740 ± 0.0159 | +6.442 ± 2.905 |
| **41N** | 47.3 ± 6.2 | 0.2000 ± 0.0183 | -10.550 ± 0.573 |
| **41N + p14endo15** | 61.7 ± 11.7 | 0.1570 ± 0.0072 | -7.174 ± 1.631 |

**Supplementary Table 2.2. The tolerability and survivability of mice injected with a range of dose concentrations of FAST-PLVs encapsulating pDNA versus MC3-LNP encapsulating pDNA.**

ND = not determined.

| | p14endo15-PLV | | MC3-LNP | |
|---|---|---|---|---|
| **Dose (mg/kg)** | **Total Mice Injected** | **Surviving Mice** | **Total Mice Injected** | **Surviving Mice** |
| **0.5** | ND | | 3 | 3 |
| **1** | 3 | 3 | 3 | 1 |
| **5** | 3 | 3 | 3 | 0 |
| **8** | 3 | 3 | 3 | 0 |
| **20** | 3 | 3 | ND | |
| **60** | 3 | 3 | ND | |
| **80** | 3 | 2 | ND | |

**Supplementary Table 2.3. Clinical chemistry composition in non-human primates.**

| Parameter | Normal Range | Units | PLV Dose (mg/kg) | Time Post Infusion (Days) | | | | | |
|---|---|---|---|---|---|---|---|---|---|
| | | | | 0 | 2 | 3 | 4 | 14 | 21 |
| **Blood urea nitrogen (BUN)** | 6.3 - 31.3 | mg/dL | 1 | 18.67 ± 5.03 | 16.33 ± 0.58 | | | | |
| | | | 6 | 18.33 ± 2.52 | | 20.33 ± 1.15 | 29.33 ± 2.31 | | 23.00 ± 2.65 |
| **Creatinine** | 0.3 - 1.3 | mg/dL | 1 | 0.80 ± 0.10 | 0.80 ± 0.10 | | | | |
| | | | 6 | 0.77 ± 0.06 | | 0.93 ± 0.15 | 1.03 ± 0.06 | | 0.77 ± 0.06 |
| **Glucose** | 32.5 - 199.1 | mg/dL | 1 | 109.67 ± 37.31 | 185.33 ± 17.62 | | | | |
| | | | 6 | 165.00 ± 69.35 | | 144.00 ± 41.07 | 124.33 ± 6.03 | | 203.00 ± 38.94 |
| **Sodium (Na)** | 141.7 - 154.8 | mmol/ L | 1 | 150.33 ± 3.21 | 147.00 ± 2.65 | | | | |
| | | | 6 | 147.67 ± 4.73 | | 147.00 ± 1.00 | 145.67 ± 0.58 | | 147.67 ± 2.31 |
| **Potassium (K)** | 2.6 - 5.4 | mmol/ L | 1 | 3.97 ± 0.15 | 3.6 ± 0.36 | | | | |
| | | | 6 | 3.93 ± 0.38 | | 3.67 ± 0.12 | 3.70 ± 0.10 | | 4.40 ± 0.20 |
| **Chloride (Cl)** | 100.6 - 112.5 | mmol/ L | 1 | 108.67 ± 2.08 | 107 ± 1.73 | | | | |
| | | | 6 | 105.67 ± 3.06 | | 104.67 ± 1.53 | 104.00 ± 1.00 | | 102.00 ± 1.73 |
| **Alkaline phosphatase (ALP)** | 25 - 360.5 | U/L | 1 | 117.00 ± 81.43 | 106.67 ± 53.98 | | | | |
| | | | 6 | 103.33 ± 21.22 | | 108.33 ± 42.34 | 102.67 ± 41.86 | | 108.67 ± 47.72 |
| **Total bilirubin** | 0.1 - 1.2 | mg/dL | 1 | 0.20 ± 0.10 | 0.40 ± 0.20 | | | | |
| | | | 6 | 0.20 ± 0.00 | | 0.33 ± 0.15 | 0.40 ± 0.10 | | 0.30 ± 0.00 |
| **Lactate dehydrogenase (LDH)** | 53.5 - 622.5 | U/L | 1 | 442.00 ± 404.73 | 798.00 ± 213.42 | | | | |
| | | | 6 | 309.67 ± 182.15 | | 1022.33 ± 970.50 | 2394.00 ± 1511.01 | | 698.67 ± 51.54 |
| **Creatine phosphokinase (CPK)** | 193 - 4843.1 | U/L | 1 | 1545.33 ± 1750.30 | 22717.00 ± 9336.12 | | | | |
| | | | 6 | 2214.33 ± 2616.93 | | 18988.33 ± 17330.98 | 47630.33 ± 25298.93 | | 14367.33 ± 5572.00 |
| **Gamma glutamyl transferase (GGT)** | 3.6 - 96.7 | U/L | 1 | 32 ± 16.70 | 41.67 ± 15.01 | | | | |
| | | | 6 | 43.00 ± 23.90 | | 44.00 ± 16.52 | 42.00 ± 15.13 | | 53.00 ± 13.86 |
| **Total protein** | 5.8 - 8.3 | g/dL | 1 | 5.40 ± 0.72 | 6.00 ± 0.44 | | | | |
| | | | 6 | 6.57 ± 1.24 | | 6.80 ± 0.35 | 6.67 ± 0.40 | | 6.87 ± 0.29 |
| **Albumin** | 3.4 - 5.6 | g/dL | 1 | 3.60 ± 0.60 | 3.83 ± 0.49 | | | | |
| | | | 6 | 4.17 ± 0.72 | | 4.27 ± 0.15 | 4.27 ± 0.21 | | 4.20 ± 0.10 |
| **Globulin** | 1.4 - 3.8 | g/dL | 1 | 1.80 ± 0.20 | 2.17 ± 0.12 | | | | |
| | | | 6 | 2.40 ± 0.53 | | 2.53 ± 0.21 | 2.40 ± 0.20 | | 2.67 ± 0.31 |
| **Albumin/ Globulin ratio** | 0.8 - 2.7 | Ratio | 1 | 2.00 ± 0.29 | 1.78 ± 0.30 | | | | |
| | | | 6 | 1.75 ± 0.13 | | 1.69 ± 0.10 | 1.78 ± 0.07 | | 1.59 ± 0.20 |
| **Calcium (Ca)** | 8.1 - 10.3 | mg/dL | 1 | 8.80 ± 0.26 | 8.73 ± 0.58 | | | | |
| | | | 6 | 9.33 ± 0.92 | | 9.23 ± 0.06 | 9.57 ± 0.51 | | 9.90 ± 0.35 |
| **Phosphorus** | 2.0 - 8.0 | mg/dL | 1 | 3.83 ± 1.84 | 5.93 ± 1.36 | | | | |
| | | | 6 | 5.47 ± 1.56 | | 4.93 ± 0.55 | 4.17 ± 0.70 | | 4.73 ± 1.10 |
| **Cholesterol** | 88.4 - 176.2 | mg/dL | 1 | 102.00 ± 8.19 | 91.67 ± 20.31 | | | | |
| | | | 6 | 117.33 ± 21.46 | | 152.67 ± 29.96 | 152.33 ± 34.02 | | 160.67 ± 16.29 |
| **Triglycerides** | 1.9 - 105.9 | mg/dL | 1 | 37.33 ± 11.37 | 64.00 ± 10.15 | | | | |

| | | | | | | | | | |
|---|---|---|---|---|---|---|---|---|---|
| | | | 6 | 40.33 ± 2.52 | | 34.67 ± 9.29 | 52.33 ± 3.51 | | 69.00 ± 39.28 |
| **Glutamate dehydrogenase (GDH)** | 3 - 42 | U/L | 1 | 36.67 ± 16.80 | 101.33 ± 40.5 | | | | |
| | | | 6 | 13.33 ± 5.13 | | 20.67 ± 11.50 | 17.33 ± 6.35 | | 35.33 ± 25.17 |

**Supplementary Table 2.4. Cytokine composition in non-human primates.**

| Cytokine | PLV | Time Post Infusion (Hours) | | | | |
|---|---|---|---|---|---|---|
| (pg/ml) | Dose (mg/kg) | 0 | 1 | 4 | 12 | 72 |
| **IL-2** | 1 | 0.03 ± 0.04 | 0.14 ± 0.08 | 1.57 ± 2.28 | 0.86 ± 0.96 | |
| | 6 | 14.65 ± 8.83 | 19.25 ± 1.63 | 24.21 ± 2.39 | 27.87 ± 12.92 | |
| **IL-7** | 1 | 7.14 ± 1.95 | 8.37 ± 2.9 | 13.64 ± 3.32 | 6.91 ± 5.03 | |
| | 6 | 7.39 ± 4.84 | 11.05 ± 6.74 | 12.27 ± 6.58 | 10.97 ± 5.00 | 7.33 ± 4.29 |
| **IL-8** | 1 | 290.72 ± 209.25 | 1055.34 ± 496.87 | 4683.95 ± 595.93 | 36.73 ± 37.68 | |
| | 6 | 841.14 ± 272.64 | 824.87 ± 231.92 | 2289.71 ± 121.99 | 1111.65 ± 264.04 | |
| **IL-10** | 1 | 0.03 ± 0.02 | 0.27 ± 0.10 | 0.12 ± 0.18 | 0.09 ± 0.12 | |
| **IL-12/ IL-23 p40** | 1 | 79.06 ± 30.17 | 92.07 ± 34.65 | 350.18 ± 134.45 | 69.53 ± 61.60 | |
| | 6 | 50.53 ± 69.79 | 79.15 ± 101.08 | 188.98 ± 251.27 | 92.37 ± 98.84 | 21.76 ± 22.09 |
| **IL-15** | 1 | 1.76 ± 0.29 | 2.55 ± 0.41 | 4.83 ± 0.86 | 12.03 ± 9.51 | |
| | 6 | 2.49 ± 1.33 | 3.20 ± 1.16 | 3.99 ± 1.01 | 27.64 ± 6.49 | 4.07 ± 0.97 |
| **IL-16** | 1 | 13.63 ± 4.93 | 618.94 ± 191.11 | 462.00 ± 146.09 | 140.90 ± 140.30 | |
| | 6 | 16.80 ± 12.70 | 597.54 ± 435.03 | 558.90 ± 351.72 | 170.96 ± 93.84 | 12.17 ± 5.19 |
| **IL-17A** | 1 | 13.85 ± 10.42 | 18.08 ± 13.83 | 65.79 ± 24.91 | 6.60 ± 6.28 | |
| | 6 | 8.57 ± 4.14 | 11.90 ± 7.09 | 26.53 ± 15.53 | 15.62 ± 7.63 | 9.54 ± 6.18 |
| **GM-CSF** | 1 | 0.06 ± 0.09 | 1.59 ± 0.66 | 3.36 ± 1.63 | 0.22 ± 0.22 | |
| | 6 | 0.04 ± 0.07 | 0.73 ± 0.39 | 1.76 ± 0.86 | 0.13 ± 0.13 | |
| **TNF-β** | 1 | 0.15 ± 0.13 | 0.40 ± 0.10 | 3.71 ± 2.92 | 5.93 ± 12.56 | |
| | 6 | 0.09 ± 0.09 | 0.14 ± 0.09 | 1.52 ± 0.92 | 0.54 ± 0.34 | 0.09 ± 0.08 |
| **VEGF** | 1 | 4.02 ± 3.60 | 0.52 ± 0.65 | 1.64 ± 1.91 | 15.83 ± 15.09 | |
| | 6 | 2.81 ± 1.44 | 3.53 ± 1.27 | 3.30 ± 3.11 | 12.99 ± 8.52 | 5.42 ± 4.94 |

**Supplementary Table 2.5. Chemokine composition in non-human primates.**

| Chemokine | PLV | Time Post Infusion (Hours) | | | | |
|---|---|---|---|---|---|---|
| (pg/ml) | Dose (mg/kg) | 0 | 1 | 4 | 12 | 72 |
| **Eotaxin** | 1 | 48.57 ± 19.03 | 185.08 ± 95.42 | 136.19 ± 36.84 | 108.67 | |
| **IP-10** | 1 | 222.87 ± 66.18 | 1098.04 ± 507.82 | 31159.32 ± 35453.74 | 16783.25 ± 16881.47 | |
| | 6 | 393.91 ± 83.67 | 653.69 ± 26.56 | 1315.36 ± 469.99 | 619.63 ± 130.70 | 186.64 ± 35.93 |
| **MCP-1** | 1 | 138.83 ± 35.70 | 378.24 ± 142.42 | 4695.52 ± 180.44 | 4581.40 ± 125.88 | |
| | 6 | 1.86 ± 0.34 | 2.66 ± 0.84 | 5.61 ± 2.79 | 3.33 ± 1.00 | 2.15 ± 0.85 |
| **MCP-4** | 1 | 6.93 ± 2.24 | 11.93 ± 5.51 | 67.15 ± 34.60 | 103.76 ± 49.91 | |
| | 6 | 3.70 ± 2.74 | 5.57 ± 1.26 | 6.00 ± 4.49 | 24.00 ± 1.54 | 3.76 ± 3.70 |
| **MDC** | 1 | 35.70 ± 10.99 | 53.79 ± 14.52 | 240.44 ± 103.96 | 109.95 ± 77.27 | |
| | 6 | 4.08 ± 1.10 | 5.61 ± 0.70 | 57.67 ± 14.78 | 20.63 ± 6.13 | 3.85 ± 0.33 |
| **MIP-1α** | 1 | 13.97 ± 12.78 | 228.60 ± 27.16 | 458.31 ± 108.78 | 89.19 ± 21.23 | |
| | 6 | 8.43 ± 1.80 | 9.94 ± 2.18 | 11.81 ± 1.97 | 73.60 ± 24.04 | 11.89 ± 2.12 |
| **MIP-1β** | 1 | 24.09 ± 3.91 | 1299.62 ± 148.57 | 1574.58 ± 267.97 | 426.80 ± 95.93 | |
| **TARC** | 1 | 7.60 ± 2.56 | 9.58 ± 2.56 | 13.34 ± 1.86 | 3.52 ± 0.69 | |
| | 6 | 35.20 ± 14.40 | 54.33 ± 16.03 | 64.05 ± 8.34 | 53.85 ± 9.07 | 32.51 ± 16.26 |

# **Chapter 3:** Rapid Prototyping and Immunogenicity of SARS-CoV-2 DNA Vaccine Candidates Formulated with the Fusion-Associated Small Transmembrane Protein Proteolipid Vehicle Delivery Platform

**Rapid Prototyping and Immunogenicity of SARS-CoV-2 DNA Vaccine Candidates Formulated with the Fusion-Associated Small Transmembrane Protein Proteolipid Vehicle Delivery Platform**

Arun Raturi[1,2,&], Jailal Ablack[3,&], Ping Wee[1,2], Prakash Bhanduri[1,2], Douglas W Brown[4], Manoj Parmar[1,2], Maryam Hejazi[4], Nichole McMullen[5], Liliya Grin[1,2], Hector Vega[1,2], Jennifer Gyoba[1,2], Henry Garcia[6], Natasha Govindasamy[1,2], Jitendra Kumar[1,2], Paola Solis Ares[1,2], Chandra McAllister[1,2], Katia Carmine-Simmon[4], Perrin H Beatty[1,2], Adam Nelson[5], Brent Johnston[5], Eric S Pringle[5], Craig McCormick[5], Mary Foley[5], Magen Ellen Francis[7,8], Brian Abel[2], Alyson Kelvin[7,8], Roy Duncan[5], John D Lewis[1,2,3,4,6,9]*

[1] Entos Pharmaceuticals, 4550 - 10230 Jasper Avenue, Edmonton, Alberta, Canada, T5J 4P6
[2] Aegis Life, 3033 Science Park Road, San Diego, California, 92121
[3] OncoSenX, 701 Fifth Ave, Suite 4200, Seattle, Washington 98104
[4] Department of Oncology, University of Alberta, Edmonton, Alberta, Canada, T6G 2E1
[5] Department of Microbiology & Immunology, Dalhousie University, Halifax, Nova Scotia, Canada, B3H 4R2
[6] Oisin Biotechnologies, 701 Fifth Ave, Suite 4200, Seattle, Washington 98104
[7] Vaccine and Infectious Disease Organization VIDO, University of Saskatchewan, Saskatoon, Saskatchewan, Canada, S7N 5E3.
[8] Department of Biochemistry, Microbiology, and Immunology, University of Saskatchewan, Saskatoon, Saskatchewan, Canada, S7N 5E3.
[9] Lead Contact: John D. Lewis.
[&]Authors contributed equally.
*Correspondence: John D. Lewis. University of Alberta, Katz Group Centre, 5-142, Edmonton, Canada. Phone: 780.492.6113, Fax: 780-492-8160, Email: jdlewis@ualberta.ca

Figures (7) and Tables (0).

**Subject Areas:** Vaccine development, Infectious diseases

**In Brief:** A DNA vaccine candidate encoding SARS-CoV-2 Spike protein and genetic adjuvants stimulated potent cellular and humoral immunity against SARS-CoV-2 and was protective in a hamster challenge model.

**Abstract**

Ending the COVID-19 pandemic requires a global vaccination effort leveraging scalable, globally deployable vaccine platforms that are also rapidly adaptable to emerging variants. DNA-based vaccines can satisfy these criteria, but inefficient intracellular DNA delivery has limited their development and efficacy. Here we report rapid prototyping of DNA vaccine candidates utilizing an intracellular delivery platform where plasmid DNA vaccines are encapsulated in proteolipid vehicles (PLVs) formulated with a fusion-associated small transmembrane (FAST) protein and well-tolerated lipids. Rapid prototyping of SARS-CoV2 vaccine candidates identified full-length SARS-CoV-2 Spike protein combined with two genetic adjuvants (CpG motifs, RIG-I agonist, termed NP-S-CpG-RIGI) could elicit both Spike neutralizing humoral responses in mice and non-human primates comparable to COVID-19 convalescent patients, and Spike-specific T cell responses including functional cytotoxic T lymphocyte responses. A single dose of NP-S-CpG-RIGI protects hamsters from morbidity following SARS-CoV-2 challenge. The FAST-PLV vaccine platform is ideally suited to develop countermeasures against emerging infections.

**Keywords:** CD8+ T cells, cytotoxic T lymphocytes, FAST proteins, genetic adjuvants, neutralizing antibodies, plasmid DNA vaccine, proteolipid vehicle, neutralizing antibodies, SARS-CoV-2, Spike protein

## 3.1. Introduction

Several features of nucleic acid vaccines have propelled mRNA vaccines to the forefront of COVID-19 vaccination efforts, including rapid prototyping of vaccine candidates for improved immune responses and protection from emerging variants, the absence of an infectious agent delivery system, and the ease of nucleic acid vaccine manufacturing[415,417,424,429–433] Nucleic acid vaccine payloads must be decoded intracellularly to yield antigens that elicit a host immune response[434]. The value of mRNA-based vaccines to prevent COVID-19 has been clearly demonstrated, but the requirement for cold-storage hinders their use in lower middle-income countries[423]. By contrast, the inherent stability of DNA allows DNA vaccines to be stored and transported at normal refrigeration temperatures. DNA vaccines are relatively inexpensive to manufacture at scale and can be programmed with multiple antigens and/or immunostimulatory factors on the same molecule[434,435]. In addition, cytoplasmic DNA activates innate immune responses leading to IFN production through the cGAS-STING pathway, and cytokine production through the AIM2 inflammasome pathway[436]. Recently, DNA vaccines have been shown to generate both innate cytokine signaling and antigen-specific B and T cell responses via the STING pathway but independent of the cGAS sensor *in vivo*, indicating the presence of a redundant DNA sensor[437]. For these reasons, DNA-based vaccines may be ideally suited for rapid prototyping and global deployment.

DNA vaccines are safe in animals and humans and generate balanced cellular and humoral immune responses in non-human primates (NHPs) [438–442]. These vaccines are effective and licensed for animal use but not yet approved for use in humans[443–447] . Recently, Zydus Cadila has applied for emergency use approval of its three-dose COVID-19 vaccine, ZyCoV-D, that showed

efficacy of 66.6% in an interim study, and if approved, will be the worlds' first DNA vaccine for humans[448].

Inefficient intracellular plasmid delivery has been a major barrier limiting the clinical application of DNA vaccines to date. Intracellular DNA vaccine delivery has traditionally relied on viral vectors, cationic lipid nanoparticles (LNPs) or electroporation[354,434]. However, these methods each suffer from notable limitations; the immunogenicity of adenovirus- and adeno-associated virus (AAV)-based vectors limits their repeated administration, cationic lipid nanoparticles can generate immunogenic toxicity and acute proinflammatory cytokine secretion, and electroporation requires a device to deliver an electric charge at the injection site[358,449,450]. These limitations prompted our development of FAST-PLVs as a DNA vaccine delivery platform. FAST-PLVs are a fusogenic proteolipid vehicle (PLV) based on well-tolerated lipids and a recombinant fusion-associated small transmembrane (FAST) protein that catalyzes fusion between the PLV membrane and cell membrane to promote intracellular DNA delivery[361,362,451]. FAST-PLVs demonstrated low toxicity and improved intracellular delivery of both mRNA and plasmid DNA in mouse and non-human primate models with no diminished transgene expression following repeat injections[451]. The utility of this delivery platform was also demonstrated in a gene therapy mouse model for muscle wasting disorders, showing increased hindlimb muscle size and grip strength. We leveraged the efficacy and highly favorable safety profile of FAST-PLVs as a DNA delivery platform to develop a DNA-based COVID-19 vaccine[362,364,366,367,369,370,452,453] (**Figure 3.1A**). Rapid prototyping of multiple antigen candidates, including full-length SARS-CoV-2 Spike (S), receptor binding domain (RBD), and secreted RBD (sRBD) configurations, plus two genetically encoded adjuvants (CpG motifs and a RIGI agonist) on a Nanoplasmid (NP) backbone, identified a preferred vaccine candidate; NP-S-CpG-RIGI. This vaccine stimulated spike-specific

humoral and cellular immunity manifested by neutralizing antibody titers and a functional cytotoxic T cell response, and importantly protected against SARS-CoV-2 in a hamster challenge study. Based on these preclinical results, NP-S-CpG-RIGI recently advanced to human clinical trials.

## 3.2. Results

### *3.2.1. Prototyping of DNA Vaccine Candidates with the FAST-PLV Platform for Intracellular Delivery.*

A mammalian codon-optimized DNA sequence encoding the entire open reading frame (ORF) of Wuhan SARS-CoV-2 Spike glycoprotein was synthesized based on the published amino acid sequence (QHD43416; **Figure 3.1B**) [454]. Similarly, DNA encoding the RBD and sRBD fused to the Kappa light chain signal peptide were synthesized as additional SARS-CoV-2 antigen candidates (**Figure 3.1B**). These antigens were cloned into two different plasmid backbones and the plasmid DNAs were formulated in the FAST-PLV delivery platform and added directly to the media of 293T cells[451]. We compared the expression of wild type SARS-CoV-2 Spike from both a Nanoplasmid backbone and our optimized p10 backbone[451]. The Nanoplasmid backbone is small, non-immunogenic, and capable of potent expression of encoded gene products[455]. Expression of Spike protein from the Nanoplasmid backbone far exceeded that of the p10 backbone at the same dose of DNA (**Figure 3.1C**); expression was dose-dependent, and full-length Spike was efficiently post-translationally processed to S1/S2 fragments (**Figure 3.1D**). Expression of sRBD from the Nanoplasmid was also readily detected (**Figure 3.1E**). Therefore, the FAST-PLV platform is sufficient for intracellular delivery, robust expression, and proper post-translational processing of plasmid DNA encoded Spike antigens.

The FAST-PLV platform leverages the ease and flexibility of recombinant DNA manipulation by enabling efficient intracellular delivery of plasmid DNAs. Five prototype vaccine candidates were generated encoding either full length SARS-CoV-2 Spike, RBD, or sRBD, and adjuvants. NP-S-CpG-RIGI encodes Spike on a Nanoplasmid backbone with two genetic adjuvants; an RNA Pol III driven retinoic acid-inducible gene 1 (RIG-I) double-stranded RNA agonist element, eRNA41H, and CpG motifs included in the 3'-UTR of the Spike mRNA transcribed by a pol II promoter[456]. NP-S-RIGI encodes Spike on the Nanoplasmid backbone with the RIG-I agonist genetic adjuvant only. A full-length Spike gene in our optimized p10 plasmid backbone, denoted p10-S, lacks all encoded genetic adjuvants. Similarly, p10-RBD encodes the RBD from the SARS-CoV-2 Spike protein, and p10-sRBD encodes a secreted RBD on the optimized p10 backbone without genetic adjuvants (**Figure 3.1B**). Immunogenicity of these five DNA vaccine prototypes formulated into FAST-PLVs were assessed in mouse models.

### *3.2.2. FAST-PLV Vaccine Candidates Encoding both Spike and Genetic Adjuvants Induce Humoral Immunity in Mice.*

To assess the ability of the different vaccine candidates to induce an anti-Spike neutralizing titer, mice were immunized intramuscularly with each candidate using a prime (day 0)-boost (day 14) regimen. At seven days post-boost (day 21), an indirect electro-chemiluminescence immunoassay (ECLIA) was used to measure the binding of anti-Spike IgG to recombinant SARS-CoV-2 Spike protein, reported as the fold change from control (vehicle) treated animals. NP-S-CpG-RIGI elicited dose-dependent anti-Spike antibody responses that were approximately two- to three-fold as great as those induced by NP-S-RIGI lacking the CpG RNA element or the other vaccine candidates, with the 250 ug dose inducing the greatest response (**Figure 3.2A**). The

enhancing effect of the encoded RNA CpG adjuvant on anti-Spike antibody production was most noticeable following the second dose (**Figure 3.2B**), and although a trend was observed, no significant difference was detected upon boosting with the adjuvant, RIGI, alone. Neither increasing the dose of the other candidates nor co-formulating them with CpG DNA oligonucleotides achieved responses greater than NP-S-CpG-RIGI (**Figure 3.2A**). Addition of the IgG signal peptide to generate secreted RBD (p10-sRBD) improved antibody production, yielding equivalent responses as p10-RBD, but at lower DNA doses that were not improved by co-formulation with CpG DNA (**Figure 3.2A**). Consistent with the specific antibody responses, both NP-based Spike vaccines dramatically increased the frequency of splenic $CD19^+$ B cells following the second dose (**Figure 3.2C**). Thus, NP-S-CpG-RIGI and NP-S-RIGI elicited the strongest humoral immune responses of the candidates tested, including expansion of B cells in the spleen following re-exposure to SARS-CoV-2 Spike protein, with the addition of two genetic adjuvants generating the most robust antibody responses.

### *3.2.3. Vaccine Candidates Encoding Spike Protein and Genetic Adjuvants Induce Robust Neutralizing Antibody Responses in Mice*

To assess the functionality of the humoral responses generated by our vaccine candidates in mice, we employed a pseudovirus neutralization assay (pVNT) using luciferase-expressing lentivirus pseudotyped with SARS-CoV-2 Spike to infect permissive 293T-ACE2 cells (Figure 3A). Serum containing neutralizing antibodies (nAb) against SARS-CoV-2 blocked infection of the pseudotyped lentivirus, resulting in a dose-dependent decrease in luciferase signal. Consistent with total IgG responses, NP-S-CpG-RIGI at a 25 μg DNA dose induced robust neutralizing activity, which was approximately twice the dilution factor of serum required to attain an $IC_{50}$ from

high-responding SARS-CoV2 convalescent patients (**Figure 3.3B, Supplementary Figure 3.1**). Even though p10-RBD- and p10-sRBD-immunized mice generated low anti-Spike IgG titers (**Figure 3.2A**), their serum neutralizing activities were nevertheless, equivalent to the 25 ug dose of NP-S-CpG-RIGI (**Figure 3.3B, Supplementary Figure 3.1**).

The neutralizing activity induced by NP-S-CpG-RIGI peaked at a dose of 25 μg, generating an effect similar to that observed in high-responding convalescent serum samples, and greater than observed at 100 and 250 μg doses (**Figure 3.3C**). Similar results were obtained using an assay with SARS-CoV-2 Spike pseudotyped Vesicular Stomatitis Virus (VSV) expressing GFP (**Supplementary Figure 3.2**). Mock and control-treated pseudotyped VSV readily infected permissive cells while VSV-GFP lacking both the VSV G receptor binding protein and the SARS-CoV-2 Spike protein (VSVΔG) was incapable of efficient infection, confirming that infection is Spike-mediated (**Supplementary Figure 3.2B**). Pre-treatment with serum from NP-S-CpG-RIGI immunized animals inhibited infection of pseudotyped VSV-GFP at levels comparable to those obtained using convalescent patients (**Supplementary Figure 3.2C, D**). Therefore, two different pseudovirus neutralization assays demonstrated that immunization with the NP-S-CpG-RIGI candidate elicits a functional neutralizing antibody response that has comparable neutralizing activity to serum derived from convalescent patients.

### *3.2.4. Vaccine Candidates Encoding Spike Protein and Genetic Adjuvants Elicit a Robust Cellular Immune Response.*

To assess T cell responses elicited by the DNA vaccine candidates, mice were immunized intramuscularly with a 25 μg dose of the candidates following the same prime-boost protocol used to elicit humoral responses. At 21 days post-immunization (7 days following the booster), the

frequency of IFN-γ spot forming cells (SFC) per million splenocytes was quantified by an enzyme-linked immune absorbent spot (ELISpot) assay following *ex vivo* stimulation with overlapping peptide pools (15mers overlapping by 11 amino acids) spanning the entire SARS-CoV-2 Spike protein ORF. NP-S-CpG-RIGI vaccination stimulated a robust T cell response indicated by increased frequencies of T cells expressing IFN-γ, reaching a frequency greater than 170 SFCs/million splenocytes at day 21 (**Figure 3.4A**). NP-S-RIGI and p10-sRBD also elicited a significant increase in the frequency of IFN-γ SFCs compared to control immunized mice (Figure 4A). There was no detectable difference in the responses to p10-Spike and p10-RBD compared to control immunized mice, and the addition of co-formulated CpG to the p10-RBD did not improve the response.

Compared to control, NP-S-CpG-RIGI immunization also increased the frequency of activated CD69+CD8+ T cells following stimulation with SARS-CoV-2 Spike protein (Figure 4B). Consistent with robust immune cell activation, NP-S-CpG-RIGI induced a 4-fold increase in the frequency of blasting lymphocytes in the spleen, and significant splenomegaly compared to controls 7 days after each immunization (**Figure 3.4C, D, E**). Features characteristic of lymphoid hyperplasia, including increased size and number of follicles in the spleens and draining lymph nodes was observed at day 8 post-immunization of mice with NP-S-CpG-RIGI (**Figure 3.4F, G**).

Cytotoxic T lymphocytes (CTLs) are an important effector T cell type. Once activated and fully licensed, CTLs target and kill virus-infected cells presenting viral epitopes (peptides) in the context of major histocompatibility complex I (MHC-I) (**Figure 3.5A**). To confirm that $CD8^+$ T cells activated by NP-S-CpG-RIGI had the capacity to kill relevant target cells, we established a syngeneic target cell line using B16 melanoma cells from C57BL/6 mice stably expressing SARS-CoV-2 Spike protein (**Figure 3.5B**). Splenocytes from NP-S-CpG-RIGI immunized mice showed

increased, dose-dependent killing of these co-cultured syngeneic target cells compared to splenocytes from control mice (**Figure 3.5C, D**). Together these findings indicate that NP-S-CpG-RIGI elicits a largely spike-specific T cell immune responses that includes a Spike-specific CTL response with the capacity to functionally kill virally infected target cells.

### *3.2.5. NP-S-CpG-RIGI was Well Tolerated and Induces Robust Neutralizing Activity in Non-Human Primates*

To assess the safety of the NP-S-CpG-RIGI vaccine candidate and its ability to induce anti-Spike neutralizing activity in a translational preclinical model, adult African green monkeys (*Chlorocebus sabaeus*) were immunized intramuscularly with the full human dose of 250 µg NP-S-CpG-RIGI plasmid DNA formulated in FAST-PLV or with saline as a control (**Figure 3.6A**). NHPs were separated into 3 groups and received either (i) saline alone (Control), (ii) one dose of 250 µg NP-S-CpG-RIGI at day 0 (Single Dose), or (iii) two doses of 250 µg NP-S-CpG-RIGI at days 0 and 28 (Two Doses) (**Figure 3.6A**). Sera obtained from NHPs at baseline and at weekly intervals were assessed for their capacity to neutralize SARS-CoV-2 Spike using the earlier described pVNT system (**Figure 3.3A**). Both one- and two-dose groups demonstrated effective and comparable neutralization of SARS-CoV-2 Spike pseudotyped lentivirus, which increased greatly with time post-vaccination (**Figure 3.6B**), and after 42 days, demonstrated similar neutralization to convalescent human sera, whereas sera from control animals demonstrated no neutralization capacity (**Figure 3.6C**). Local tolerance to the intramuscular administration of NP-S-CpG-RIGI plasmid DNA vaccine was evaluated using the Draize Measurement, which captures the manifestation and severity of both erythema and edema at the site of the injection, to generate a Primary Dermal Irritation Index[457]. No detectable differences were observed in the primary

dermal irritation index between control animals and either of the 2 dose groups indicating that the repeat dosing (full human dose, IM) in NHP is well tolerated (**Figure 3.6D**). Thus, a single dose of PLV formulated NP-S-CpG-RIGI plasmid DNA vaccine was well tolerated and sufficient to generate a neutralizing immune response in NHP.

### *3.2.6. NP-S-CpG-RIGI protects Hamsters from SARS-CoV-2 Infection in a Challenge Model.*

To evaluate the protective efficacy of NP-S-CpG-RIGI encapsulated in FAST-PLVs as a COVID-19 vaccine we used a SARS-CoV-2 challenge model in Golden Syrian Hamsters. Golden Syrian Hamsters were vaccinated 42 days before challenge (priming) with either PLV formulated NP-S-CpG-RIGI or PLV formulated empty vector encoding only the genetic adjuvants (NP-CpG-RIGI). Twenty-one days before challenge, a second dose of NP-S-CpG-RIGI was given to the two-dose group (boosting). Control animals were also given a second dose of NP-CpG-RIGI at Day -21 (**Figure 3.7A**). Anti-Spike antibody titers were shown to persist to Day -1 prior to challenge (**Figure 3.7B**). Animals were challenged intranasally with a sublethal dose of SARS-CoV-2 (Day 0) and followed for 14 days (**Figure 3.7A**). The two-dose NP-S-CpG-RIGI group showed significantly reduced weight loss as early as Day 1 post-challenge and through to the peak weight loss at Day 7 (**Figure 3.7C**). Although a single dose of NP-S-CpG-RIGI did not significantly decrease weight loss over the first six days, these animals recovered significantly faster, and were indistinguishable from the two-dose group at Day 8 post-challenge, with both vaccinated groups showing significantly faster body weight recovery compared to control vaccinated animals (**Figure 3.7C, D**). While no changes to viral loads in nasal washes or lungs were detected by qRT-PCR at three days post-challenge (**Figure 3.7E and Supplementary Figure 3.3A, B**), the

proinflammatory factors, CXCL10 and IL-6, were reduced 2-fold in nasal turbinates in the single-dose group and almost 10-fold in the two-dose group (**Figure 3.7F-H**). Both groups of vaccinated animals had reduced viral loads in nasal washes 7 and 14-days post-challenge compared to control as determined by qRT-PCR (**Figure 3.7E**). Vaccinated animals showed reduced IL-6 and IFN-γ in nasal turbinates 7 days post-challenge with no detectable difference between single- and two-dose groups (**Figure 3.7G, H**). NP-S-CpG-RIGI vaccinated animals that received two doses had undetectable viral loads in the lungs seven days post-challenge, and viral loads in the lungs of both vaccinated groups at day 14 were decreased by 2-3 logs, to near background levels (**Figure 3.7I and Supplementary Figure 3.3C, D**). Inflammatory cytokine expression in the lung was also deceased in both vaccinated animal groups. Both CXCL10 and IL-6 showed decreases in the lung on day 3 with a greater effect observed with 2 doses for CXCL10, (**Figure 3.7J, K**) but no detectable difference between single- and two-dose groups on day 7, and this was resolved by day 14 in all animals, consistent with IL-6 levels (**Figure 3.7J, K**). IFN-γ expression in the lung was decreased in the two-dose group on day 3 and in both groups on day 7 compared to the control and remained significantly lower than the controls till day 14 (**Figure 3.7L**). Thus, vaccination with FAST-PLVs encapsulating NP-S-CpG-RIGI stimulates a protective immune response that decreases animal morbidity, reduces tissue inflammation, and leads to decreased viral shedding and more rapid viral clearance from the lungs in the hamster challenge model.

## 3.3. Discussion

The devastating COVID-19 pandemic has led to greater than 4 million deaths worldwide, caused by the novel coronavirus, SARS-CoV-2 (https://coronavirus.jhu.edu/map.html). Approximately 4.8 billion doses of COVID-19 vaccines have been administered, enough to fully

vaccinate 23.8% of the global population, however there is still an enormous number of unvaccinated individuals and reduced vaccine-induced efficacy against the emerging SARS-CoV-2 variants. To combat this global health crisis, new and improved vaccine strategies that can lead to rapid vaccine development, scaling up, and stable deployment in the field, are critical. Nucleic acid vaccines, particularly mRNA vaccines, employing novel delivery modalities have emerged and gained a foothold in COVID-19 vaccination programs, however DNA-based vaccines and particularly efficient delivery of DNA vaccines has lagged, until now. Plasmid DNA has long been considered an ideal vaccine platform[458]. DNA vaccines are stable, scalable, and possess potentially unlimited coding capacity. However, the inherent barriers to intracellular delivery of the DNA payload have hindered success in the plasmid DNA vaccine space. Additionally, DNA vaccine delivery platforms to date have suffered from inherent challenges such as vector immunogenicity limiting repeated administration, dose-limiting LNP-induced toxicity, and the requirement for drug delivery devices such as electroporation[358,449,450]. Here we report the design and immunogenicity of a plasmid DNA vaccine encoding SARS-CoV-2 Spike protein, NP-S-CpG-RIGI formulated with the FAST-PLV platform, that elicits a protective immune response against SARS-CoV-2 as a potential platform to countermeasure the ongoing, global COVID-19 pandemic. Our data indicates that a single-dose of NP-S-CpG-RIGI was protective in the hamster SARS-CoV-2 challenge model as demonstrated by reduced weight loss during infection, reduced viral shedding and burden in the lungs, as well as a reduced proinflammatory response in the airways. Furthermore, vaccination with a single dose of NP-S-CpG-RIGI produced neutralizing antibodies in the NHP model, and the full human dose was well tolerated with no detectable injection site manifestations. These features are in stark contrast to most of the conventional DNA vaccine delivery platforms used to date. The FAST-PLV platform and antigen encoding plasmid DNA

payload strategy employed for these SARS-CoV-2 vaccine candidates could also be widely applied to other viruses in the near future with great potential impact on newly emerging pandemics.

Zydus Cadila has recently applied for emergency use approval of its three-dose COVID-19 vaccine (3mg/ dose), ZyCoV-D, administered with the PharmaJet® Tropis® Needle-free device, which will be the worlds' first human DNA vaccine to enter the marketplace, and this will have great impact on driving further development and innovation in the DNA-based vaccine space. Furthermore, INOVIO is entering into a Phase 3 study with its DNA-based vaccine candidate, INO-4800, which is administered intradermally as a 2mg dose in a two-dose regimen, followed by electroporation with their proprietary hand-held CELLECTRA® device. Entos and Aegis Life are currently completing a Phase 1 clinical trial of its DNA encoded Spike Covigenix VAX-001 vaccine [459], which was administered intramuscularly at either 0.1mg or 0.25mg doses in a two-dose regimen, and is expected to start a Phase 2 study shortly with the same doses, but comparing one- and two-dose regimens. Of note, the Covigenix VAX-001 vaccine is intracellularly delivered through Fusogenix proteolipid vehicles without the need for electroporation at doses that are between 8-30 times lower than the other DNA vaccines progressing through the pipeline.

Studies with convalescent patient sera show that SARS-CoV-2 elicits a robust but potentially short to medium-lived humoral antibody response followed by more durable cell-mediated $CD4^+$ and $CD8^+$ responses across all levels of disease severity[460,461]. SARS-CoV-2 memory T cells have also been detected in blood samples stored before the COVID-19 pandemic, indicating an effect of cross-reactivity between the common cold-causing coronaviruses and SARS-CoV-2[461–463]. SARS-CoV-2 Spike protein-encoding nucleic acid vaccines that elicit a neutralizing antibody response and a $CD8^+$ T cell-based response are predicted to provide longer-

lasting immunity[416,429,430,432]. Our DNA vaccine candidate NP-S-CpG-RIGI elicits a robust T cell response and demonstrates Spike-specific $CD8^+$ T cell-mediated killing of Spike-expressing target cells. The potent CTL response likely plays a key role in the control of viral shedding and viral load in hamsters following challenge, as well as mediating a key effector mechanism against reinfection events. We speculate that the enhanced CTL response induced by NP-S-CpG-RIGI is due to direct intracellular delivery of the DNA payload encoding the antigen and two genetic adjuvants, CpG and RIGI, on the same DNA molecule. Furthermore, this is in addition to the response induced by recognition of the plasmid DNA payload by the STING and AIM2 pathways. Adjuvants such as CpG and RIGI enhance adaptive immunity through innate signaling[464]; thus all cells expressing antigen will also express the adjuvants mobilizing innate immune cells to help shape the adaptive response.

We cannot preclude the possibility that the robust cell-mediated response is an inherent property of the full-length wildtype Spike protein itself. However, since we observed enhanced antibody, neutralizing antibody, and T cell responses from the Spike candidate with CpG-RIGI but no cell-mediated immune response without CpG-RIGI, it seems evident that the genetically encoded adjuvants enhanced cell-mediated immunity. This effect has been seen in human vaccine trials with encoded adjuvants; oligonucleotide CpG added to a hepatitis B vaccine induced a higher and more rapid antibody response, and long-term seroprotection in HIV infected adults, compared to the vaccine administered without CpG[465–467]. A neutralizing antibody response is certainly critical for protection against SARS-CoV-2 infection, but in synergy with a potent cellular immune response, will have a greater likelihood of providing long-term immunity. Early evidence in patients undergoing B cell-depleting cancer therapies indicates that cell-mediated immunity is sufficient to reduce COVID-19 disease severity[468]. Our findings showing FAST-PLV delivery of

a Spike, CpG and RIGI encoded DNA vaccine generated a potent and orchestrated $CD8^+$ T cell response, suggests that this vaccine candidate might be effective at reducing COVID-19 disease severity in humans. The vast majority of neutralizing antibodies against SARS-CoV-2 target the RBD of the Spike protein, the region where most mutations have arisen in the emerging variants of concern that may circumvent neutralizing antibodies against the Wuhan strain[469]. Our findings demonstrate that an optimized combination of antigen, adjuvant, and dose, induces a robust SARS-CoV-2-specific cell-mediated response and neutralizing antibodies, with the potential to confer strong immunity against COVID-19 infection and/ or disease. As aforementioned, we are currently testing NP-S-CPG-RIGI for safety and immunogenicity in a Phase 1 clinical trial[459].

A single dose of NP-S-CpG-RIGI was sufficient to meet or exceed the predicted threshold pVNT $IC_{50}$ values shown to be protective in NHPs[416,431,470,471], and this appears promising for translation into the clinic, especially when combined with the induction of a robust anti-spike T cell response. Notably, the FAST-PLV delivery system is immunogenic and protective in the hamster SARS-CoV-2 challenge model with 20-50 times less plasmid DNA per dose[431] compared with conventional strategies for delivering DNA-based vaccines such as electroporation,

We adapted the FAST-PLV delivery system as a plasmid DNA vaccine platform capable of stimulating a protective immune response consistent with other nucleic acid vaccines targeting SARS-CoV-2 Spike, ideally with a single dose[451]. However, in contrast to conventional nucleic acid vaccine strategies, our approach yields an inexpensive, rapidly scalable platform that is not constrained by cold-chain processes; ideally suited for rapid prototyping and global distribution of countermeasures against emerging pathogens[434].

## 3.4. Methods

*DNA Vaccine Expression Plasmids*

The NTC9385R Nanoplasmid expression plasmid contains a bacterial backbone comprising a 140 bp RNA-based sucrose selectable antibiotic-free marker (RNA-OUT) and a 300 bp R6K origin. Nanoplasmids NTC9385R-eRNA41H and NTC9385R-eRNA41H-CpG RNA are derivatives that co-express RNA adjuvants with the DNA encoded antigen[456]. The D type CpG RNA sequence is 5'GGTGCATCGATGCAGGGGGG 3'. The RIGI agonist sequence is 5'AAAACAGGTCCTCCCCATACTCTTTCATTGTACACACCGCAAGCTCGACAATCAT CGGATTGAAGCATTGTCGCACACATCTTCCACACAGGATCAGTACCTGCTTTCGCTT TT 3'. Nanoplasmid uses the chimeric CMV promoter to drive transgene expression, with a rabbit beta-globin intron and splice enhancer for efficient RNA export. Rabbit beta-globin polyA signal was used for mRNA transcriptional termination and polyadenylation. Nanoplasmids were manufactured by the Nature Technology Corporation (Lincoln, NE). NP-S-CpG-RIGI comprised the Nanoplasmid NTC9395R-eRNA41H-CpG RNA plasmid with the 3822 bp human codon-optimized SARS-CoV-2 Spike gene (synthesized by Integrated DNA Technology; Iowa, USA) cloned in using *Sal*I and *Bgl*II restriction sites. NP-S-RIGI comprised the Nanoplasmid NTC9385R-eRNA41H backbone with the 3822 bp human codon-optimized SARS-CoV-2 Spike gene insert. p10-S, p10-RBD, and p10-sRBD candidates used the optimized p10 backbone[472] with no encoded RIG-I agonist or CpG sequences. p10-S carried the same Spike gene that was cloned into NP-S-CpG-RIGI and NP-S-RIGI. p10-RBD had the 243 bp RBD sequence from the SARS-CoV-2 Spike gene as the DNA encoded antigen. p10-sRBD carried the RBD sequence fused to the 60 bp sized murine Ig Kappa-chain signal peptide sequence to create a secreted RBD.

*DNA Vaccine Formulation*

To manufacture the FAST-PLV DNA vaccines, the antigen-encoded plasmid DNA species were encapsulated within FAST-PLVs as payload. Plasmid DNA was diluted in 10 mM sodium acetate buffer (pH 4.0) containing 5 nM FAST protein. Separately, the PLV lipid components were dissolved in ethanol. Mixing the DNA-protein fraction with the lipid fraction was performed in the NanoAssemblr Benchtop microfluidics instrument (Precision Nanosystems Inc, Vancouver, BC) at a 3:1 ratio and a flow rate of 12 mL/min. Formulations were dialyzed in 8000 MWCO dialysis membranes (product code 12757486, BioDesign, Carmel, New York) against phosphate-buffered saline (pH 7.4) for 3 hours with three buffer changes, then concentrated using Amicon ultracentrifuge filters (EMD Millipore, Burlington, Massachusetts) before passage through a 0.22 µm filter (GSWP04700, EMD Millipore). The resulting FAST-PLV DNA vaccine candidates were stored at 4ºC until used.

*PLV Characteristics and Encapsulation Efficiency*

PLVs made by NanoAssemblr Benchtop were diluted 1:50 to 1:20,000, depending on concentration, with twice 0.2 µm syringe-filtered PBS buffer. Particle size, polydispersity index (PDI), and zeta potential were measured on final samples using the Malvern Zetasizer Range and a Universal 'Dip' Cell Kit (ZEN1002, Malvern) following the manufacturer's instructions. A modified Quant-IT PicoGreen dsDNA assay (P7589, Thermo Fisher Scientific, Edmonton, Canada) was used according to the Assay Kit instructions to calculate the nucleic acid encapsulation efficiency, with the following modifications. PLVs were mixed 1:1 with TE plus Triton (2%) to obtain the Total DNA Concentration, or with TE alone to obtain the Unencapsulated DNA Concentration. The DNA standards were also diluted in TE plus Triton (2%), then together with the samples were incubated at 37°C for 10 min, then diluted a final time with TE plus Triton (1%) or TE alone, plated in a black 96 well flat-bottomed plate, and measured with a FLUOstar

Omega plate reader (415-1147, BMG Labtech). Encapsulation efficiency was calculated by using the following equation:

$$Encapsulation\ Efficiency = \frac{Total\ DNA\ Concentration - Unencapsulated\ DNA\ Concentration}{Total\ DNA\ Concentration} \times 100$$

*Western Blot Analysis*

Cell lysates from HEK293T cells (CRC-3216 ATCC) transfected with Nanoplasmid or the p10 backbone encoding Spike or secreted RBD, or with PLVs carrying SARS-CoV-2 Nucleocapsid as a control, were analyzed via Western blot. Thirty micrograms of cell lysate were loaded per lane and electrophoresed through a 4-20% gradient gel, then transferred to 0.22µm nitrocellulose at 80V for one hour at 4˚C. The nitrocellulose blot was blocked using fluorescent blocking buffer (MB-070, Rockland Immunochemicals, Limerick, United States) or 1% BSA for one hour at ambient temperature then probed with either a 1:2000 dilution of rabbit anti-spike (Catalogue No. 3223, ProSci Antibodies) or mouse anti- Spike RBD (MAB10540, R&D Systems) overnight followed by 1:10000 dilution HRP-conjugated anti-mouse (HAF018, R&D Systems) or Goat anti-rabbit Alexa Fluor 750 (A-21039, Thermo Fisher Scientific) IgG secondary antibody for one hour. Primary mouse anti-alpha tubulin (MAB9344, R&D Systems) or mouse anti-alpha smooth muscle actin (MAB1420, R&D Systems) antibodies were also used as loading controls.

*Rodent Experiments: Ethics and Study Design*

All rodent studies were carried out according to the Canadian Council on Animal Care (CCAC) guidelines and approved by the University of Alberta Animal Care and Use Committee. *In vivo* studies were done using 8-20 weeks old, 25 to 35 g body weight, male and female C57BL/6 mice

(Charles River Laboratories, Saint-Constant, QC, Canada). The mice were group-housed in IVCs under SPF conditions, with constant temperature and humidity and with lighting on a fixed light/dark cycle (12-hours/12-hours). Mice were immunized intramuscularly in the musculus tibialis with 50µl of the test agent unless otherwise stated. Baseline blood was collected via tail vein before immunization. Blood was collected again 14 days after initial immunization, immediately before booster administration. Twenty-one days after immunization, mice were euthanized, and terminal blood was collected via cardiac puncture.

*Non-Human Primate Experiments: Ethics and Study Design*

All in-life NHP procedures were carried out by Virscio, Inc, under the guidance of the Institutional Animal Care and Use Committee (IACUC) of the St. Kitts Biomedical Research Foundation (SKBRF), St Kitts, West Indies. SKBRF research facility is fully accredited by the Association for Assessment and Accreditation of Laboratory Animal Care International (AAALAC International). African green monkeys (*Chlorocebus sabaeus*) are an invasive species on the island of St. Kitts and were procured locally using approved practices with IACUC oversight. Groups of 6 animals (3 male and 3 female) per group were enrolled. For all immunization and blood collection procedures, animals were anesthetized with ketamine/xylazine (8.0 mg/kg ketamine (Fort Dodge)/1.6 mg/kg xylazine (Lloyd Lab)) as a sterile, mixed cocktail. General well-being was assessed before, during, and after sedation. All animals were single housed. Baseline plasma was collected immediately prior to intramuscular immunization in the deltoid muscle with the full human dose 250 µg NP-S-CpG-RIGI plasmid DNA formulated in FAST-PLV in 0.5ml sterile PBS or saline control. Blood draws were collected weekly for 6 weeks and stored at -80°C until analysis.

Individual dose sites were scored according to the Draize system (Table 3) with assessments performed daily post-dosing. On procedure days, animals were sedated with ketamine and xylazine (8 mg/kg:1.6 mg/kg IM), removed from their cages, and injection site assessed. The classification of the irritancy was obtained by adding the average erythema and edema scores for each assessment and dividing by the number of evaluations. The resulting primary dermal irritation index (PDII) score was classified as follows: PDII <0.5 = no irritation; 0.5-2.0 = slightly irritating; 2.1-5.0 = moderately irritating; >5.0 = severely irritating.

*Anti-Spike Antibody Indirect ELISA*

Recombinant SARS-CoV-2 S1 Protein (RPO1262, ABclonal, Wuhan, China) was coated on the standard binding plate (Meso Scale Discovery; MSD, Rockville, MD) at 1 μg/mL for 1 h at ambient temperature with shaking. The plate was washed three times with 0.05% Tween-20 in PBS (PBS-T) followed by the addition of Blocker A blocking buffer (R93AA-2, Meso Scale Discovery). After 30 min of incubation, the plate was re-washed with PBS-T. DNA vaccine candidate-immunized mouse serum samples were diluted 1:100 in Blocker A blocking buffer. The plate was rewashed with PBS-T followed by the addition of 1 μg/mL Sulfo-tag Anti-Mouse Secondary Antibody (R32AC-1, Meso Scale Discovery, Rockville, MD). Read Buffer (R92TG-2, Meso Scale Discovery, Rockville, MD) was added to the plate after washing with PBS-T, and the plate was read using the MESO QuickPlex SQ 120 (Meso Scale Discovery; MSD, Rockville, MD). Fold change in anti-Spike IgG was calculated for each animal relative to untreated animals in the same experiment.

*Preparation of VSV-Spike and Lentivirus-Spike Pseudotyped Virus*

Neutralizing antibody responses were assessed using either a vesicular stomatitis virus (VSV) encoding GFP but lacking the VSV G protein and pseudotyped with the SARS-CoV-2 Spike protein, or Spike-pseudotyped lentivirus encoding luciferase. To generate the Spike-pseudotyped VSV, 293T cells were transfected with plasmid pMD2.G (pMD2.G was a gift from Didier Trono (Addgene plasmid # 12259; http://n2t.net/addgene:12259 ; RRID:Addgene_12259) expressing the VSV-G protein and 24 h later infected with VSV-ΔG-GFP[473]. The supernatant from cells containing VSV was harvested at 24 h post-transduction, clarified by centrifugation at 500 x g for 5 min, and aliquots stored at -80ºC. This virus was used to infect 293T cells transfected the previous day with pcDNA3 expressing a codon-optimized version of the SARS-CoV-2 Spike protein (accession # QHD43416.1) with a truncated cytoplasmic tail missing the C-terminal 19 amino acids (pcDNA3-Spike-ΔC19). Virus inoculum was removed after 1 h at 37ºC, cells were washed twice with PBS, incubated in growth medium for 24 h, and the supernatant removed and clarified by centrifugation at 500 x g for 5 min before freezing the stock aliquots at -80ºC. The Spike-pseudotyped VSV virion stocks were subsequently used for pseudotyped antibody neutralization assays.

To generate spike pseudotyped lentivirus, 293T cells were transfected with pSPAX2 (pSPAX2 was a gift from Didier Trono (Addgene plasmid # 12260; http://n2t.net/addgene:12260; RRID: Addgene 12260)), a lentiviral vector encoding Luc2 (based on pLJM1-EGFP, a gift from David Sabatini (Addgene plasmid # 19319; http://n2t.net/addgene:19319; RRID: Addgene_19319), and pcDNA3-Spike-ΔC19. After 48 h, the supernatant was removed, filtered at 0.45 µm, aliquoted, and stored at -80 ºC.

*Pseudotyped Virus Antibody Neutralization Assay*

Mouse serum from vaccinated animals and convalescent serum from SARS-CoV-2 infected patients, previously heat-inactivated at 56ºC for 30 min and stored at -80ºC, was serially diluted in serum-free media (1:5, 1:10.1:30, 1:80, 1:150 for pseduotyped VSV and 1:12.5-1:1280 for pseudotyped lentivirus) and 50ul aliquots mixed with 50 ul of Spike-pseudotyped VSV or lentivirus. VSV-antibody mixtures were incubated at 37ºC for 1 h, added to ACE2-expressing Vero E6 cells (African green monkey kidney epithelial cells, ATCC CRL-1586) for 1 h at 37ºC; then the virus inoculum was removed, cells were washed with PBS, and incubated in growth medium for 10 h at 37ºC. Cell monolayers were imaged at 200X using an EVOS model cell imaging system (ThermoFisher Scientific, Waltham, MA), and the number of fluorescent cells in 3 random fields from each well quantified using ImageJ software. Lentivirus-antibody mixtures were incubated at 37ºC for 1 h on ACE2-expressing 293A cells (ThermoFisher Scientific #R705). The cells were lysed after 24h using reporter lysis buffer (Promega #E4030) and stored at -80 ºC. Luciferase activity was measured using the luciferase assay system (Promega #E1501) on a FLUOstar Omega plate reader (415-1147, BMG Labtech).

*Interferon-Gamma ELISpot*

Spleens from immunized animals were dissociated into single-cell suspensions using Spleen Dissociation Kit (130-095-926, Miltenyi Biotec, CA) following the manufacturer's protocol. Single-cell suspensions were counted and resuspended at 2 x$10^6$ cells/ml for use in the ELISpot assay. Mouse IFN-γ ELISpot assays were performed using the Mouse IFN-γ ELISpot Kit (EL485, R&D Systems, Minneapolis, MN) according to the manufacturer's directions. Briefly, 96-well ELISpot plates pre-coated with capture antibody were hydrated with complete media for 2 hours. Mouse splenocytes were plated at 2.0x$10^5$ per well and stimulated at 37˚C for 18 hours with

PepMix™ SARS-Cov-2 Spike peptide pools (PM-WCPV-S-1, JPT, Berlin, Germany) at a final concentration of 1.5nM. PepMix™ peptide pools consist of 15-mer peptides overlapping by 11 amino acids spanning the entire ORF of SARS-COV-2 Spike divided into two peptide sub-pools. Unstimulated cells served as control. Splenocytes were removed after incubation, and plates were stained with detection antibody for 2 hours at ambient temperature, following which Streptavidin-AP was added for an additional 2 hours. BCIP/NBT substrate (ab7468, Abcam) was added for 1 hour at room temperature. Plates were washed 4X between each staining procedure. Plates were dried for 2 days following BCIP/NBT addition then spots were scanned and quantified using the ImmunoSpot S6 MACRO Analyzer (CTL, Cleveland, United States). Assays were performed in duplicate (for each donor mouse). To calculate Spot-Forming Cells (SFC) per million ± SEM for each donor animal mean spot counts were summed for each peptide sub-pool. Control unstimulated splenocytes were subtracted from the representative SARS-CoV-2 Spike-stimulated splenocyte sample for each donor spleen.

*Flow Cytometry Analysis and Immune Phenotyping*

Spleen and lymph nodes were isolated and dispersed into single-cell suspensions using mechanical dispersion through 70 µm wire mesh. Red blood cells were lysed using ammonium chloride buffer, followed by a wash with PBS with 2% FBS/PBS. Lymphoid and myeloid populations were examined by flow cytometry. The following antibodies were used: fluorescein isothiocyanate-labeled TCRβ (clone H57-597, Biolegend, Cat # 109206); Peridinin-chlorophyll-protein Complex: CY5.5 conjugate-labeled TCRβ (clone H57-597, eBioscience, Cat# 45-5961-82), CD8α (clone 53-6.7, Biolegend, Cat# 100734); Phycoerythrin: Cy-7 tandem conjugate-labeled CXCR5 (clone L138D7, eBioscience, Cat# 145515); Allophycocyanin-labelled CD62L (clone MEL-14,

Biolegend, Cat#104412); Allophycocyanin-efluor 780-labelled CD69 (clone H1.2F3, eBiosciences, Cat#47-0691-82). Analysis was performed using a three-laser FACSCelesta and Flowjo software (BD Biosciences).

*CTL Killing Assay*

Splenocytes were isolated from vaccinated and control mice and co-cultured at a 50:1 ratio with B16-F10 cells stably expressing Sars-CoV-2 Spike protein for 18hrs at 37°C, 5% CO2 in Dulbecco's Modified Eagle's Medium (DMEM) (Corning, Cat# 10-013-CV) supplemented with 10% fetal bovine serum (FBS)(Gibco, Cat# 12484028), 100 units/mL of Penicillin (Hyclone, Cat# 16777-164), and 100µg/mL of Streptomycin (Hyclone, Cat# 16777-164). B16-F10 cells were washed twice and resuspended in Annexin V binding buffer (Biolegend, Cat# 422201). B16-F10 cells were stained with Allophycocyanin-labeled annexin V (BioLegend, Cat# 640941) and 7-amino-actinomycin D (BioLegend, Cat# 420404) for 15 mins at RT and examined by flow cytometry using a three-laser FACSCelesta.

*Histology*

Spleens and lymph nodes isolated from immunized and control animals were weighed then formalin fixed, and paraffin embedded. 4-6 µm sections were generated. Sections were dewaxed in xylene and rehydrated using graded ethanol to water washes. Sections were stained in Harris Modified Hematoxylin (SH30-4D, Fisher Chemical) for 8 minutes, briefly differentiated in acid alcohol and blued with Scott's Tap Water (pH 8). Slides were then stained in acidified eosin for 30 seconds and dehydrated, cleared, and then mounted. Whole slide images were generated using

Panoramic SCAN (3D Histech, Budapest, Hungary) and reviewed by a certified veterinary pathologist for pathology and immune cell proliferation.

*SARS-CoV-2 Challenge Study in Hamsters Vaccinated with NP-S-CpG-RIGI*

A SARS-Cov2 challenge model in Golden Syrian Hamsters was performed by the Vaccine and Infectious Disease Organization (VIDO) at the University of Saskatchewan. Thirty-six male hamsters were purchased from Charles River Laboratories, Inc. The age of the hamsters at first vaccination was approximately 7-8 weeks. Animals were micro-chipped and randomly assigned to one of 3 groups (n=12/group). The FAST-PLV vaccines were administered intramuscularly (100 µL in each flank). Animals were immunized on Day -42 and animals receiving two-dose regimens were given a second dose on day -21. Hamsters were challenged i.n. with 2x10^5 TCID50 units (50 µL/nare total dose volume=100 µL) of SARS-CoV-2/Canada/ON/VIDO-01/2020/Vero'76/p.2 (Seq. available at GISAID – EPI_ISL_413015) on Day 0. The same virus stocks were used for challenge and for subsequent assays. Clinical signs, body weights, and body temperature of animals were measured. Animals were observed daily for general health conditions throughout the study period. Animals were euthanized as follows: 3 per Group 3 days post-challenge, 3 per group 7 days post-challenge and 6 per group 14 days post-challenge. At necropsy blood, lung tissues, and nasal turbinates, were collected for assessment of lesions, viral RNA load, infectious virus quantification, virus neutralization assay, and ELISA.

*Assessment of viral load by qRT-PCR*

Extraction of RNA from nasal washes was performed using Qiagen reagents (QIAamp Viral RNA Mini Kit Cat No. 52906) following the manufacturers protocol. Extraction of RNA from lung lobes

and nasal turbinates was completed using approximately 100 µg of tissue. The tissues were homogenized in 600 µL of lysis buffer (RLT Qiagen) with a sterile stainless-steel bead in the TissueLyserII (Qiagen) for 6 min, at 30Hz. The solution was centrifuged at 5000 x g for 5 min. Supernatant was transferred to a fresh tube containing 600 µL of 70% ethanol, and the tube was incubated at room temperature for 10 min. Viral RNA was then purified using Qiagen RNeasy Mini Kit (Cat No 74106) and eluted with 50 µL elution buffer.

*Viral qRT-PCR reaction*

The qRT-PCR assays were performed on isolated RNA from samples of nasal washes, lung tissues and nasal turbinates using the following SARS-CoV-2 primer-probe combination: Forward Primer (Fwd) 5'-ACAGGTACGTTAATAGTTAATAGCGT-3', Reverse Primer (Rev) 5'- ATATTGCAGCAGTACGCACACA-3', Labelled Probe 5'-ACACTAGCCATCCTTACTGCGCTTCG-3'.

*Determination of infectious virus by cell culture $TCID_{50}$*

Assays to examine biological samples for infectious virus were performed on those samples with a positive qRT-PCR reaction. The assays were conducted in 96-well plates using Vero'76 cells (ATCC CRL-1587). $TCID_{50}$ was determined by microscopic observation of the cytopathogenic effect (CPE) of cells.

*Hamster anti-Spike antibody determination by enzyme-linked immunosorbent assay (ELISA)*

ELISA assays were performed on serum samples. Plates were coated with SARS-CoV-2 S1 protein antigen at a concentration of 1 µg/mL. Recombinant SARS-CoV-2 S1 protein was

produced at VIDO. Plates were blocked with 5% non-fat skim milk powder in PBS containing 0.05% Tween 20. Fourfold dilutions of serum were used. Goat anti-Hamster IgG HRP from ThermoFisher (PA1-29626) was used as the secondary antibody at 1:7000. Plates were developed with OPD peroxidase substrate (0.5 mg/ml) (Thermo Scientific Pierce 34006). The reaction was stopped with 2.5 M sulfuric acid and absorbance was measured at 490 nm. Throughout the assay, plates were washed with PBS containing 0.05% Tween 20. The assay was performed in duplicate. The titers were reported as the end point of the dilutions.

*Cytokine Expression in Hamster Tissues by qRT-PCR*

Changes in tissue cytokine expression following challenge were determined by qRT-PCR as described previously[474].

*Statistical analyses*

The statistics were calculated using GraphPad Prism 5.0 program. Statistical differences between the control and experimental groups were analysed using one-way ANOVA and Dunnet's multiple comparison test and were considered significant for $p< 0.05$. Non-parametric comparisons were performed using the Mann-Whitney test, $p<0.05$ was considered significant.

**Author Contributions**

AR, JA, AK, RD, and JDL designed the study. EP, NM, AN, MF, MR, CM, and BJ performed mice studies, pseudotyped neutralization and flow cytometry assays. AR, PW, PB, MP, HV, LG, and JG developed the FAST-PLV DNA vaccine candidates and performed tissue culture and MSD analyses. MP and NM performed Western blot analyses. DWB and MH performed mice studies.

HG analysed the H&E pathology data. AR, MP, JA, EP, NM, AN, RD, BA and JDL analysed the data. AR, JA, DWB, PHB, RD, BA and JDL contributed original ideas and wrote the manuscript with input from all authors.

**Acknowledgements**

Supported by an operating grant to JDL from the Canadian Institutes of Health Research (CIHR), in partnership with the Institute of Aging and Research Nova Scotia (reference number VR1-172710), and by operating grants to RD from the CIHR and the Natural Sciences and Engineering Research Council of Canada (NSERC). JDL holds the Frank and Carla Sojonky Chair in Prostate Cancer Research at the University of Alberta, supported by the Alberta Cancer Foundation. RD holds the Killam Chair in Virology at Dalhousie University. DWB was funded by fellowships from Prostate Cancer Canada and Mitacs. ESP was funded by postdoctoral fellowships from Mitacs and the Dalhousie Medical Research Foundation. AN was funded by a Mitacs Industrial Studentship MH was funded by a Mitacs Industrial Postdoctoral Fellowships. We thank Chris Richardson for providing the Spike protein construct used for Spike expression and purification.

**Declaration of Interests**

Roy Duncan is a co-founder of Entos Pharmaceuticals and a member of its scientific advisory board.

## 3.5. Figures

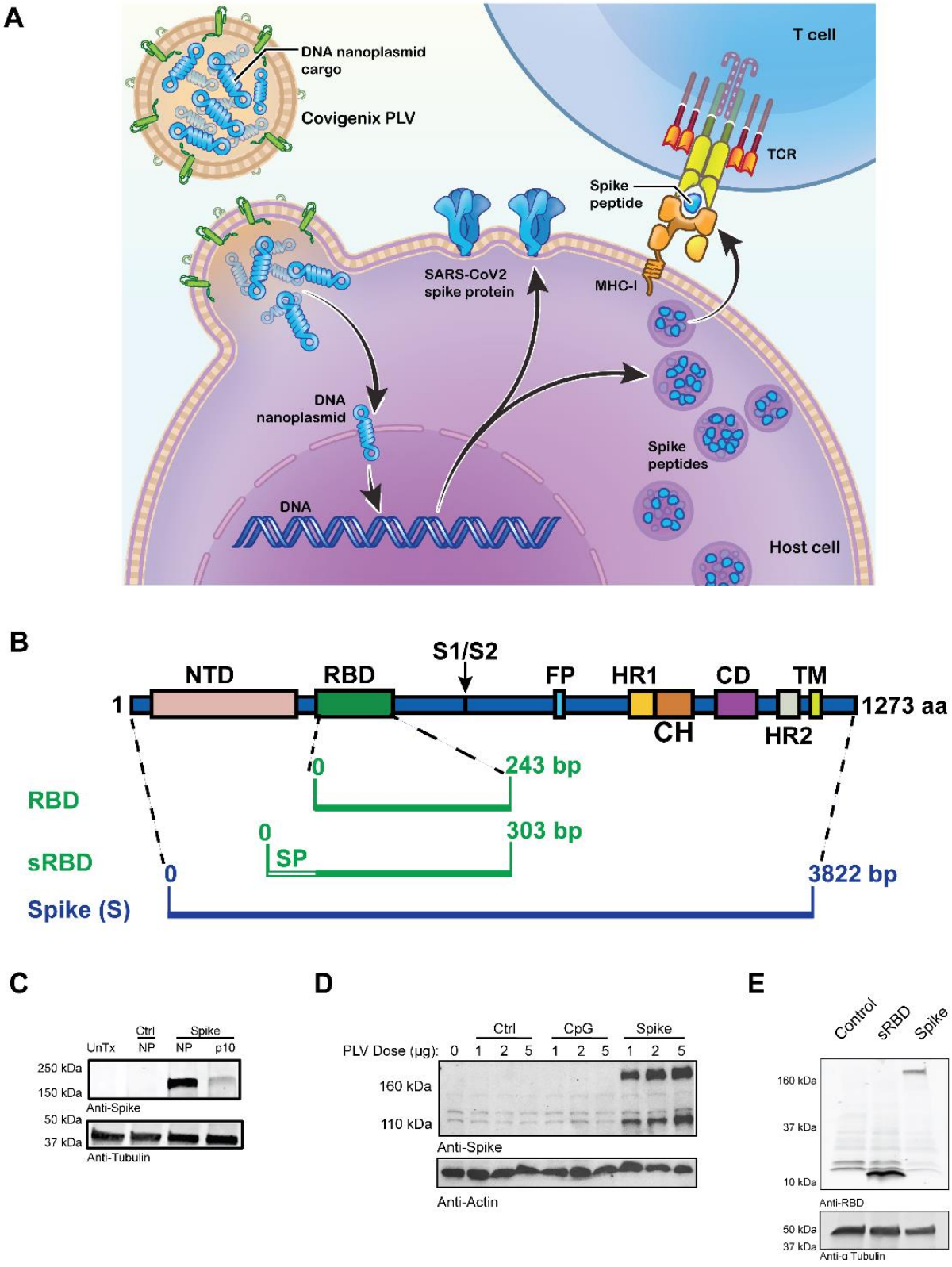
A
DNA nanoplasmid cargo
Covigenix PLV
T cell
TCR
Spike peptide
SARS-CoV2 spike protein
MHC-I
DNA nanoplasmid
DNA
Spike peptides
Host cell
B
NTD
RBD
S1/S2
FP
HR1
CD
TM
1
1273 aa
CH
HR2
0
243 bp
RBD
0
303 bp
SP
sRBD
0
3822 bp
Spike (S)
C
Ctrl
Spike
UnTx
NP
NP
p10
250 kDa
150 kDa
Anti-Spike
50 kDa
37 kDa
Anti-Tubulin
D
Ctrl
CpG
Spike
PLV Dose (µg): 0 1 2 5 1 2 5 1 2 5
160 kDa
110 kDa
Anti-Spike
Anti-Actin
E
Control
sRBD
Spike
160 kDa
37 kDa
10 kDa
Anti-RBD
50 kDa
37 kDa
Anti-α Tubulin

**Figure 3.1. A Novel FAST-PLV Platform for Intracellular Delivery of Plasmid DNA vaccines *in vivo*.**

A) Illustration of FAST-PLV DNA vaccine fusing with host cell plasma membrane to deliver the DNA vaccine payload directly into the host cell cytoplasm. The DNA encoded antigens are expressed and post-translationally processed for stimulation of the host humoral and cell mediated immune responses.

B) Schematic representation of the 1273 amino acid residue SARS-CoV-2 Spike glycoprotein including location of the N-terminal domain (NTD), receptor binding domain (RBD), furin protease cleavage site (S1/S2), fusion peptide (FP), heptad repeat 1 (HR1), central helix (CH), connector domain (CD), heptad repeat 2 (HR2), and transmembrane domain (TM). DNA encoded antigens are shown below; receptor binding domain (RBD) 243 base pairs, secreted RBD (sRBD) with 5' fused IgG heavy chain signal peptide sequence (SP) 303 base pairs, Full length Spike (Spike) 3822 base pairs.

C) Western blot analysis of 293T cell extracts, untransfected (UnTx), or transiently transfected with empty Nanoplasmid vector (Ctrl NP), Nanoplasmid encoding Spike (Spike NP), or p10 backbone encoding Spike (Spike p10) using SARS-CoV-2 Spike rabbit mAb (upper) and alpha-tubulin mouse mAb (lower).

D) Western blot of 293T cell lysates from cells transfected with 0, 1, 2 and 5 ug of PLVs carrying various plasmid DNA encoded antigens; control (Ctrl) lanes are SARS-CoV-2 Nucleocapsid, CpG lanes are SARS-CoV-2 Nucleocapsid + CpG, Spike lanes are SARS-CoV-2 full length Spike. The primary antibodies used were RBD mouse mAb (upper) and alpha-actin mouse mAb (lower).

E) Western blot analysis of secreted Receptor Binding Domain from 293T cell extracts from cells transfected with either empty p10 vector, p10 backbone encoding sRBD or p10 encoding full length Spike. The primary antibodies used were SARS-CoV-2 Spike RBD mouse mAb (upper) and alpha-tubulin mouse mAb (lower).

A

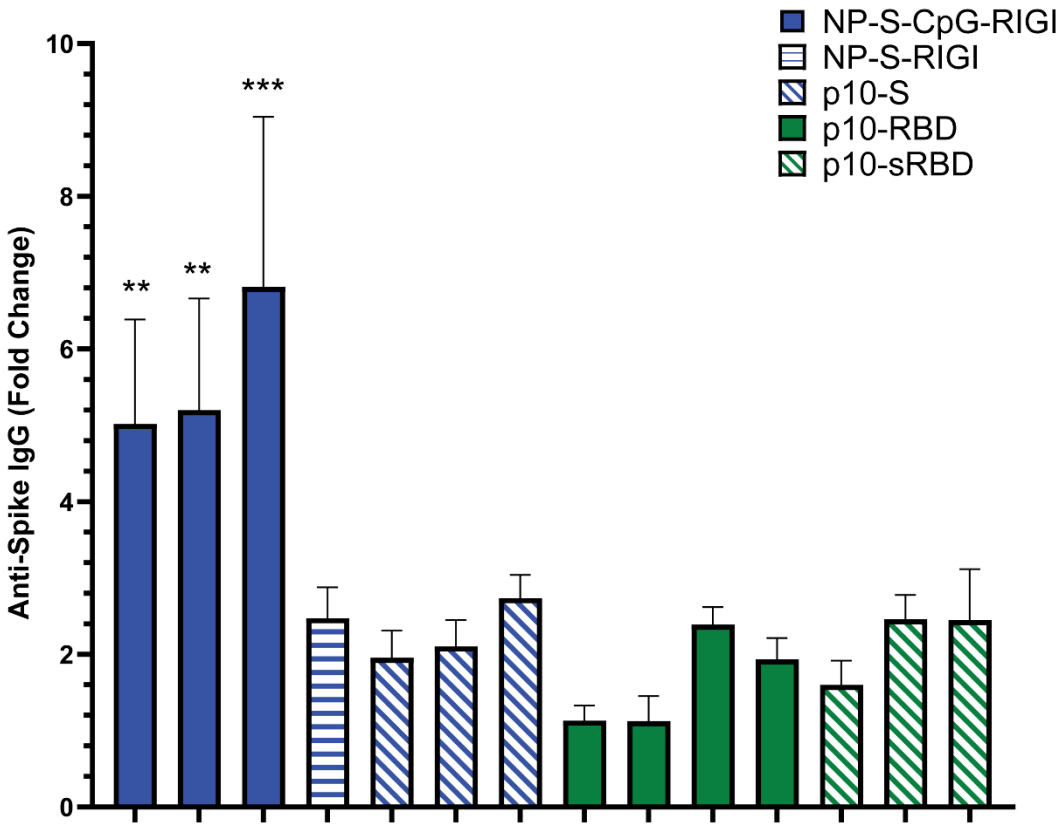


| Antigen | Spike | Spike | Spike | Spike | Spike | Spike | Spike | RBD | RBD | RBD | RBD | sRBD | sRBD | sRBD |
|---|---|---|---|---|---|---|---|---|---|---|---|---|---|---|
| Backbone | NP | NP | NP | NP | p10 | p10 | p10 | p10 | p10 | p10 | p10 | p10 | p10 | p10 |
| CpG RNA | + | + | + | - | - | - | - | - | - | - | - | - | - | - |
| RIG-I | + | + | + | + | - | - | - | - | - | - | - | - | - | - |
| CPG DNA | - | - | - | - | - | - | + | - | + | - | + | + | - | + |
| Dose (μg) | 25 | 100 | 250 | 25 | 25 | 100 | 100 | 25 | 25 | 100 | 100 | 5 | 25 | 25 |

B

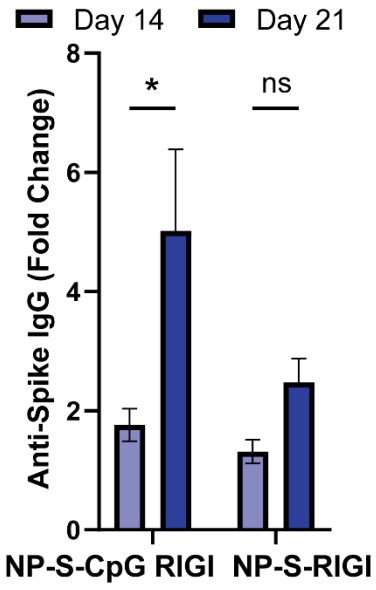


C

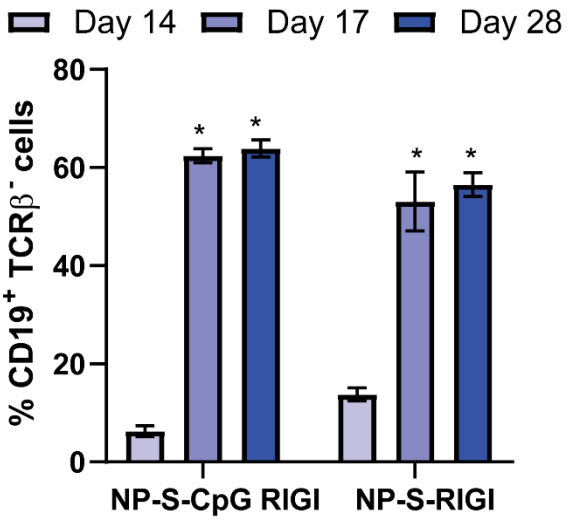

**Figure 3.2. FAST-PLV Vaccine Candidates Encoding both Spike and Genetic Adjuvants Induce Robust Humoral Immunity in Mice.**

Mice were immunized intramuscularly (IM) on day 1 (prime) and day 14 (booster) with either a 25 μg or 100 μg dose of DNA vaccine candidates comprised of either the Nanoplasmid (NP) or p10 DNA plasmid, with or without the CpG and RIG-I adjuvants formulated as PLVs.

A) The fold change in anti-Spike antibodies from vaccinated animals versus control animals was measured from serum by indirect electro-chemiluminescence immunoassay (ECLIA), 21 days after initial dose (7 days post-boost). NP-S-CpG-RIGI, NP-S-RIGI, p10-S correspond to DNA plasmids encoding full length Spike, p10-RBD encoded the RBD of the Spike protein, and p10-sRBD encoded sRBD.

B) Anti-Spike antibody production by candidates NP-S-CpG-RIGI and NP-S-RIGI 14 days following the initial 25 μg dose and 7 days following the second 25 μg dose.

C) Percent $CD19^{+}$ TCR-$\beta^{-}$ cells at Days 14, 17 and 28 in splenocytes isolated from mice immunized with candidates NP-S-CpG-RIGI and NP-S-RIGI. Data are represented as mean ± SEM, $n$=3 mice per group. One-way ANOVA and Dunnet's multiple comparisons test, *$P$<0.05, **$P$<0.01, ***$P$<0.001.

A

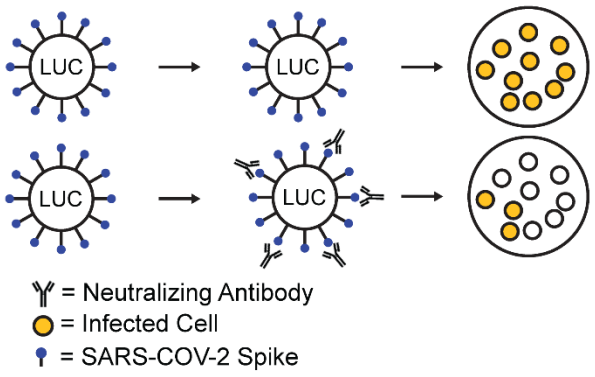


B

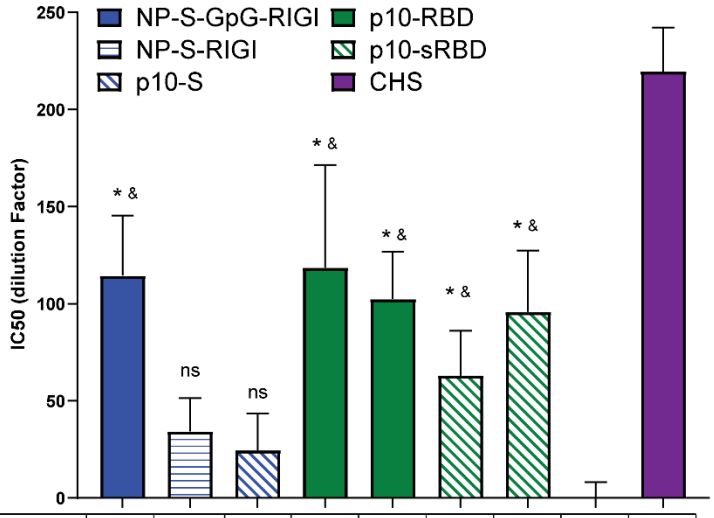


| Antigen | Spike | Spike | Spike | RBD | RBD | sRBD | sRBD | Ctrl | CHS |
|---|---|---|---|---|---|---|---|---|---|
| Backbone | NP | NP | p10 | p10 | p10 | p10 | p10 | - | - |
| CpG RNA | + | - | - | - | - | - | - | - | - |
| RIG-I | + | + | - | - | - | - | - | - | - |
| CpG DNA | - | - | - | - | + | - | + | + | - |
| Dose (µg) | 25 | 25 | 25 | 25 | 25 | 25 | 25 | 25 | - |

C

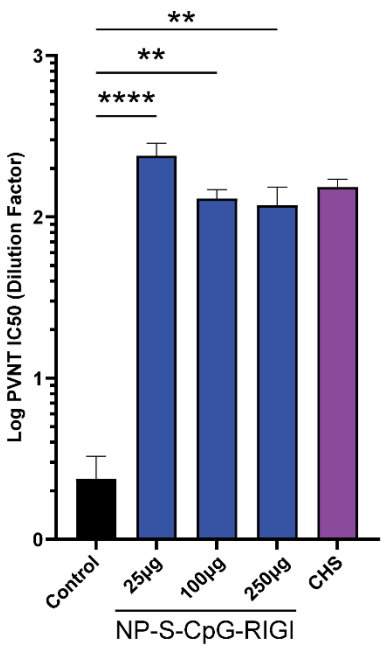

**Figure 3.3. Vaccine Candidates Encoding Spike and Genetic Adjuvants Induce Robust Neutralizing Antibody Responses in Mice.**

A) Neutralizing antibody titer was determined by incubating sera from immunized animals with lentivirus-expressing firefly luciferase (FLuc) pseudotyped with SARS-CoV-2 Spike protein. Followed by addition of the lentivirus to permissive 293T-ACE2 cells. Luminescence was used as a metric for viral infectivity.

B) Neutralizing antibody response in serum isolated from immunized animals 21 days after first dose *n*=3 mice per group. Control animals (Ctrl) were immunized with PBS (vehicle). For comparison convalescent human serum (CHS) samples were tested in parallel (n=19). A SARS-CoV-2 negative human serum sample was used as a control for human samples. Serum samples were serially diluted and incubated with Spike protein pseudotyped lentivirus-FLuc prior to addition to 293T-ACE2 cells. The resulting luminescence values obtained 24 hours post infection were fit to a curve to determine the $IC_{50}$ dilution factor. Data are represented as mean ± SEM, one-way ANOVA and Dunnet's multiple comparisons test, **P*<0.05 relative to control "&" denotes *P*>0.05 compared to CHS.

C) $IC_{50}$ values from animals immunized with two doses of either 25µg (n=6), 100 µg (n=3) or 250 µg (n=3) of NP-S-CpG-RIGI or convalescent human serum.

A

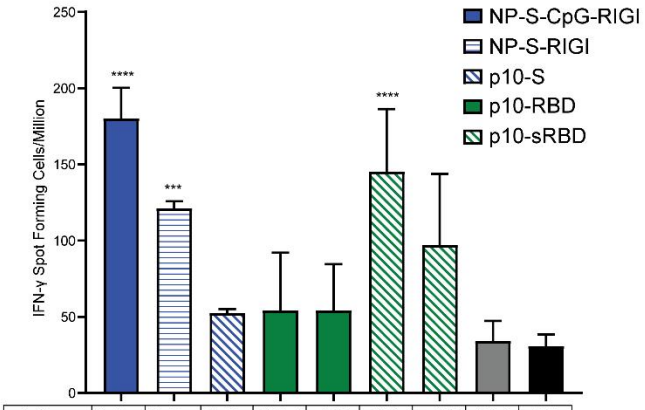


| Antigen | Spike | Spike | Spike | RBD | RBD | sRBD | sRBD | Ctrl | Ctrl |
|---|---|---|---|---|---|---|---|---|---|
| Backbone | NP | NP | p10 | p10 | p10 | p10 | p10 | - | - |
| CpG RNA | + | - | - | - | - | - | - | - | - |
| RIG-I | + | + | - | - | - | - | - | - | - |
| CPG DNA | - | - | - | - | + | - | + | + | - |
| Dose (μg) | 25 | 25 | 25 | 25 | 25 | 25 | 25 | - | - |

B

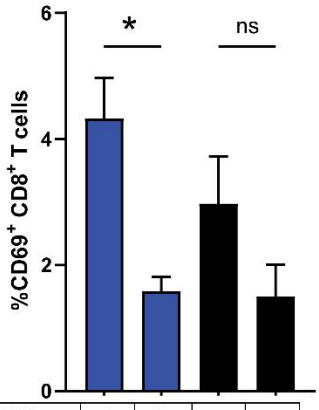


| NP-S-CpG-RIGI | + | + | - | - |
|---|---|---|---|---|
| Dose (μg) | 100 | 100 | 0 | 0 |
| Spike Peptide Stimulation | + | - | + | - |

C

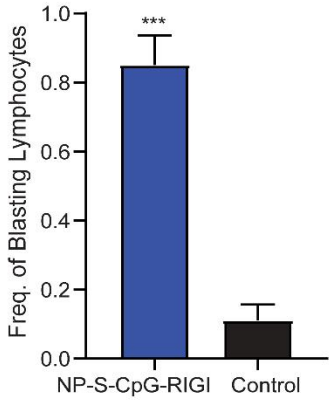


D

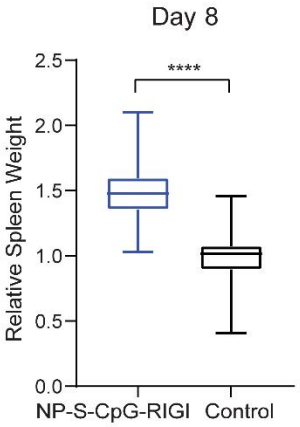


E

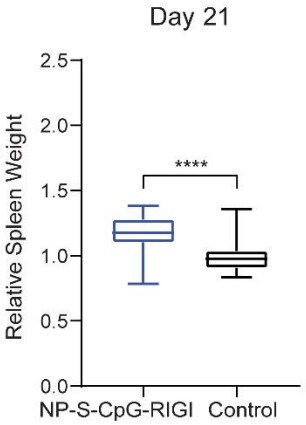


F

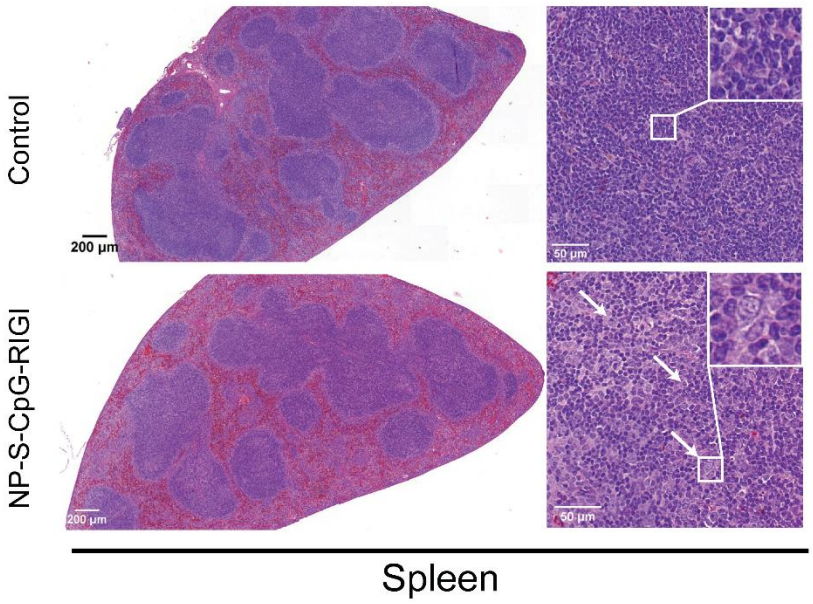


G

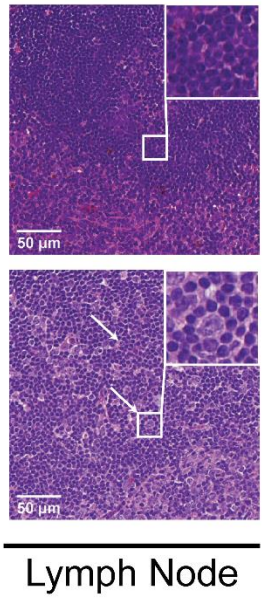

**Figure 3.4. Vaccine candidates Encoding Spike and Genetic Adjuvants Elicit a Robust Cellular Immune Response in Mice.**

A) IFN-γ ELISpot assay conducted on splenocytes isolated from immunized and control mice. At 21 days post immunization (7 days following the booster), the mouse splenocytes were stimulated *ex vivo* with overlapping peptides spanning the entire SARS-CoV-2 Spike protein open reading frame (ORF). IFN-γ producing cells were measured by enumerating the antigen specific spot forming cells per million splenocytes (SFC/million). Mean SFC per million ± SEM is depicted *n*=3 mice per group, one-way ANOVA and Dunnett's multiple comparisons test, ***P<0.001, ****P<0.0001.

B) Immunophenotyping of CD8+ populations from splenocytes isolated at day 28 (14 post-boost) from NP-S-CpG-RIGI immunized and control mice that were stimulated with SARS-CoV-2 spike peptides. Proportion of activated CD69+ CD8+ T cells. Mean frequency of CD69+ CD8+ T cells ±SEM is depicted. Means were compared using one-way ANOVA and Dunnett's multiple comparisons test, *P<0.05.

C) The frequency of blasting lymphocytes per area was determined by enumerating cells with a blasting phenotype from H&E-stained sections of spleen 8 days post infection. Mean frequency ± SEM is depicted. Means were compared by student's T test, *** denotes P<0.001.

D) Evidence of splenomegaly was quantified by organ weight 8 days post immunization. Mean spleen weight relative to control treated animals 8 days post immunization. Means compared by Student's T test **** denotes P<0.0001.

E) As in (D) 21 days after immunization.

F) Representative H&E staining in spleens from control and NP-S-CpG-RIGI immunized mice 8 days after dosing.

G) as in F, from draining lymph node.

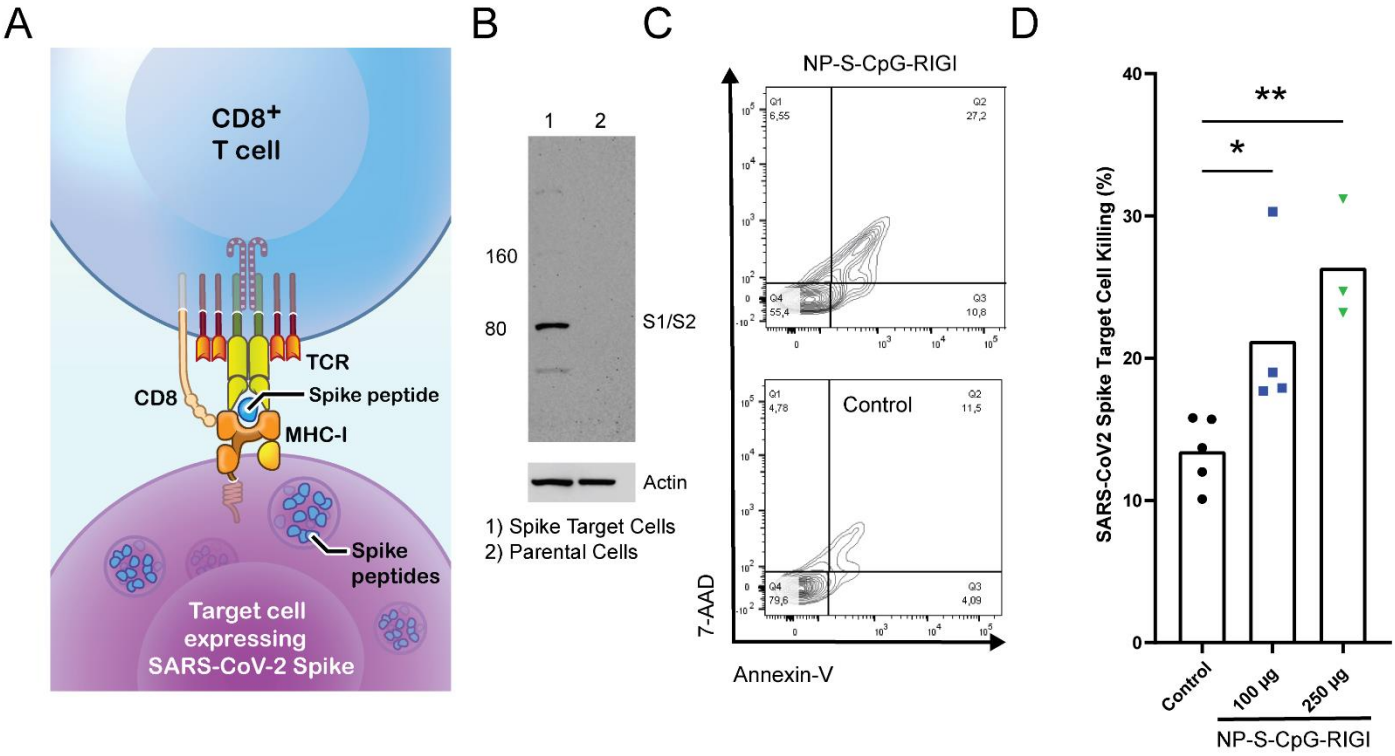


**Figure 3.5. NP-S-CpG-RIGI Generates a Spike-Specific Cytotoxic T Lymphocyte Response.**
A) Activated $CD8^+$ T cells recognize SARS-CoV-2 infected cells by binding of the T cell receptor (TCR) to MHC-I presented SARS-CoV-2 antigens.
B) Western blot showing that B16F10 melanoma cells were induced to stably express SARS-CoV-2 Spike protein.
C) B16F10-Spike cells were cultured with splenocytes isolated from NP-S-CpG-RIGI immunized and control mice. Annexin V and 7-AAD flow cytometry used to confirm apoptosis induction in B16F10 cells.
D) Percentage of dead target cells represented as the Annexin $V^+/7\text{-}AAD^+$ population, gated on B16F10-Spike cells. Target cell killing for each splenocyte donor (n=3 per group) is depicted. One-way ANNOVA and Dunnett's posttest were used to compare treatments, $*P < 0.05$, **P<0.01.

A

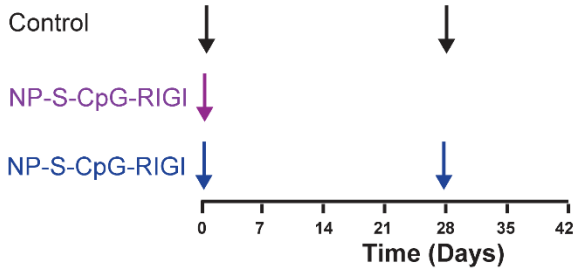
Control
NP-S-CpG-RIGI
NP-S-CpG-RIGI
0
7
14
21
28
35
42
Time (Days)

B

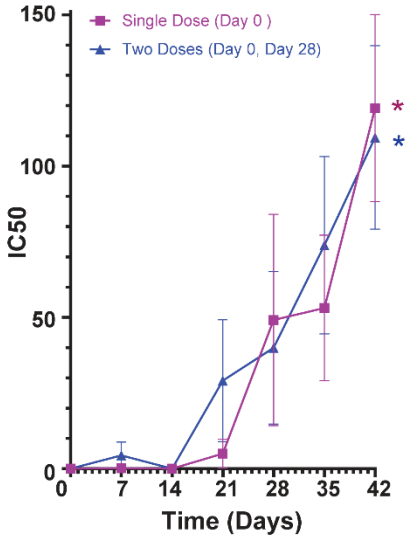
Single Dose (Day 0 )
Two Doses (Day 0, Day 28)
IC50
150
100
50
0
0
7
14
21
28
35
42
Time (Days)
*
*

C

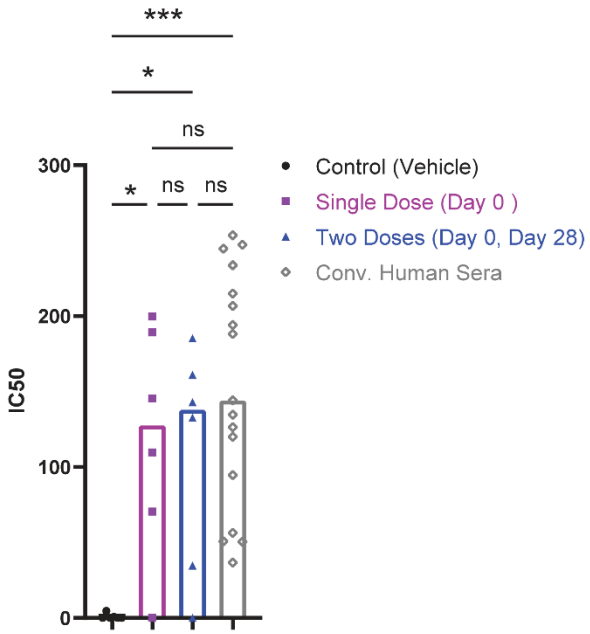
***
*
ns
*
ns
ns
IC50
300
200
100
0
Control (Vehicle)
Single Dose (Day 0 )
Two Doses (Day 0, Day 28)
Conv. Human Sera

D

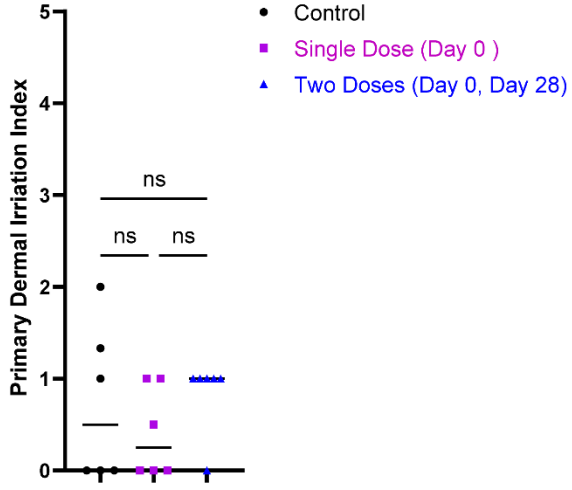
Primary Dermal Irriation Index
5
4
3
2
1
0
ns
ns
ns
Control
Single Dose (Day 0 )
Two Doses (Day 0, Day 28)

**Figure 3.6. NP-S-CpG-RIGI is Immunogenic and Well Tolerated in Non-Human Primates**
A) Groups of 6 NHPs (n= 6 per group 3 male and 3 female) received either saline alone (Control), one 250 μg dose of NP-S-CpG-RIGI (IM) on day 0 (Single Dose), or two 250 μg doses of NP-S-CpG-RIGI (IM) at days 0 and 28 (Two Doses). Weekly serum samples were collected for analysis for 6 weeks.
B) $IC_{50}$ values from serum (days 0, 7, 14, 21, 28, 35 and 42) obtained from NHPs (n=6 per group) immunized as described in (A). Data are represented as mean±SEM, *denotes $P<0.05$ by two-way ANNOVA compared to baseline (Day 0).
C) Day 42 $IC_{50}$ neutralizing titers for each animal compared to convalescent human serum. "ns" denotes P>0.05, *denotes $P<0.05$, *** denotes P<0.001 by one-way ANNOVA and Tukey's multiple comparison test.
D) Injection site irritation as measured by Primary Dermal Irritation Index. Erythema and edema at the site of injection for each animal was used to generate PDII. Animals with no observable edema or erythema were assigned a value of 0. "ns" denotes P>0.05 by one-way ANNOVA and Tukey's multiple comparison test.

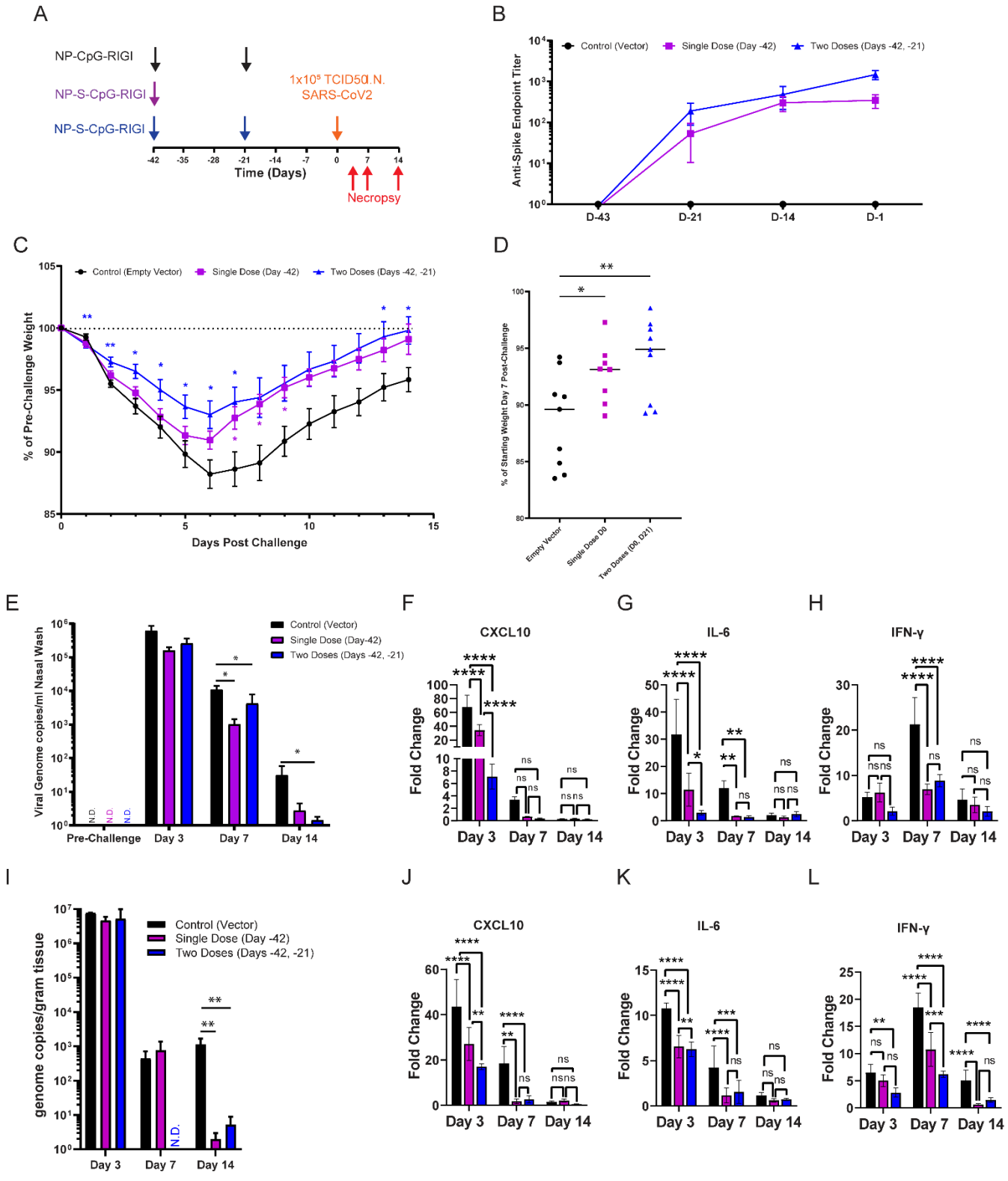
A
NP-CpG-RIGI
NP-S-CpG-RIGI
NP-S-CpG-RIGI
1x10⁵ TCID50I.N.
SARS-CoV2
-42 -35 -28 -21 -14 -7 0 7 14
Time (Days)
Necropsy
B
Control (Vector)
Single Dose (Day -42)
Two Doses (Days -42, -21)
Anti-Spike Endpoint Titer
D-43
D-21
D-14
D-1
C
Control (Empty Vector)
Single Dose (Day -42)
Two Doses (Days -42, -21)
% of Pre-Challenge Weight
Days Post Challenge
D
% of Starting Weight Day 7 Post-Challenge
Empty Vector
Single Dose D0
Two Doses (D0, D21)
E
Control (Vector)
Single Dose (Day-42)
Two Doses (Days -42, -21)
Viral Genome copies/ml Nasal Wash
N.D.
Pre-Challenge
Day 3
Day 7
Day 14
F
CXCL10
Fold Change
G
IL-6
H
IFN-γ
I
Control (Vector)
Single Dose (Day -42)
Two Doses (Days -42, -21)
genome copies/gram tissue
J
CXCL10
K
IL-6
L
IFN-γ

**Figure 3.7. NP-S-CpG-RIGI Protects Hamsters from SARS-CoV-2 Infection in a Challenge Model.**

A) Timeline of hamster immunizations on Day -42 for all groups, or Day -21 for control and two dose groups. Animals were challenged with 1x10^5 $TCID_{50}$ units i.n. on day 0. Tissues were harvested on Day3, Day7 and Day14 post challenge.

B) Pre-Challenge anti-Spike antibody titers as measured by endpoint ELISA, mean endpoint titer ±SEM at each time point measured is depicted (n=12 animals per group).

C) Body weight changes post challenge, mean % of pre-challenge weight ± SEM is depicted * denotes $P<0.05$, **denotes $P<0.01$ compared to control treated animals by two-way ANNOVA and Dunnett's post test.

D) Percent of starting weight at peak weight loss (Day 7) is depicted, each point represents one animal, median values are marked with a horizontal line. * Denotes $P<0.05$, **denotes $P<0.01$ compared to control treated animals by one-way ANNOVA and Dunnett's post test.

E) Viral genome copies present in nasal washes at the indicated timepoints. Mean viral genome copies/ml of nasal wash ± SEM is depicted, n=12 animals per group pre-challenge and Day 3, n= 9 animals per group on Day 7 and n= 6 animals per group on Day 14. N.D. denotes not detected, * denotes $P<0.05$, by Mann-Whitney test.

F) CXCL10 expression in nasal turbinates as determined by qRT-PCR. Fold change versus uninfected control is depicted ±SEM. n=3 or 6 animals per group on days 3/7 and 14, respectively. **** denotes P<0.0001, *** denotes P<0.001, ** denotes P<0.01, * denotes P<0.05, ns denotes P>0.05 by two-way ANNOVA and Tukey's multiple comparison test.

G) IL6 expression in nasal turbinates as in (F).

H) IFNγ expression in nasal turbinates as in (F).

I) Viral genome copies present in lung tissue at the indicated timepoints. Mean viral genome copies/g of tissue ± SEM is depicted, n=3 or 6 animals per group on days 3/7 and 14, respectively. N.D. denotes not detected, ** denotes $P<0.01$, by Mann-Whitney test.

J) CXCL10 expression in lung as determined by qRT-PCR. Fold change versus uninfected control is depicted ±SEM. n=3 or 6 animals per group on days 3/7 and 14, respectively. **** denotes P<0.0001, *** denotes P<0.001, ** denotes P<0.01, * denotes P<0.05, ns denotes P>0.05 by two-way ANNOVA and Tukey's multiple comparison test.

K) IL6 expression in lung as in (J).

L) IFNγ expression in lung as in (J).

## 3.6. Supplementary Material

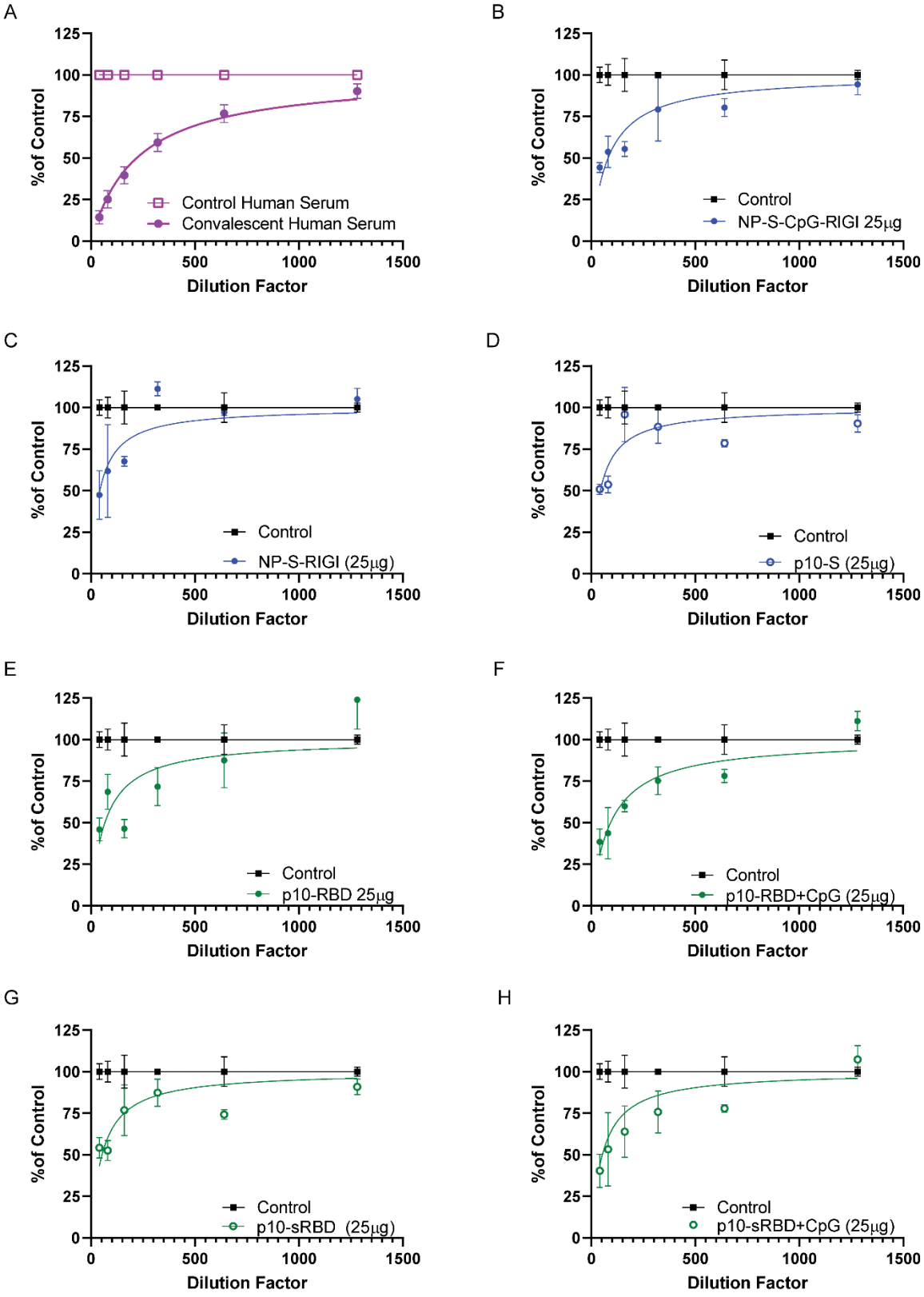

**Supplementary Figure 3.1 Neutralizing Antibody Dilution Curves.**
Neutralizing antibody dilution curves. Mean relative luciferase counts compared to control serum ±SEM.
A) Control human serum (n=1) and Convalescent Human Serum (N=19), B) Naïve mouse control (n=3), NPS-CpG-RIGI (n=3), C) NP-S-RIGI (n=3). D) p10-S (n=3), E) p10-RBD (n=3), F) p10-RBD+CpG, G) p10-sRBD, H) p10-sRBD+CpG.

A

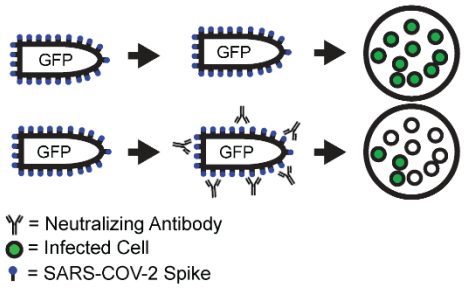
GFP
GFP
GFP
GFP
= Neutralizing Antibody
= Infected Cell
= SARS-COV-2 Spike

B

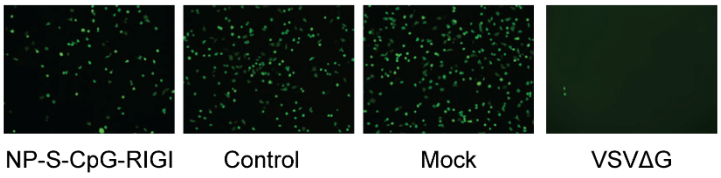
NP-S-CpG-RIGI
Control
Mock
VSVΔG

C

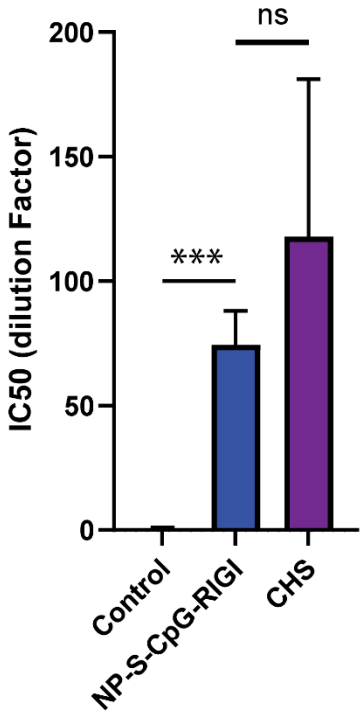
ns
***
200
150
100
50
0
IC50 (dilution Factor)
Control
NP-S-CpG-RIGI
CHS

D

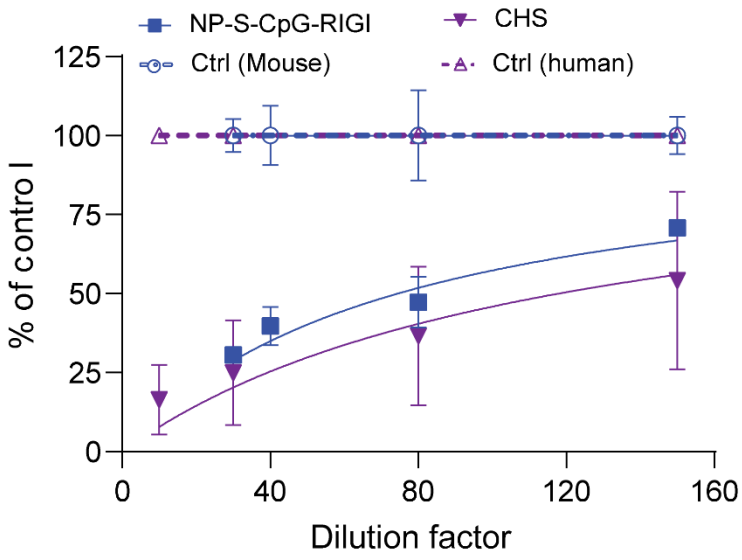
NP-S-CpG-RIGI
CHS
Ctrl (Mouse)
Ctrl (human)
125
100
75
50
25
0
% of contro l
0
40
80
120
160
Dilution factor

**Supplementary Figure 3.2 Validation of neutralizing titers using a Pseudotyped VSV Assay.**
A) Neutralizing antibody titer was determined by incubating sera from immunized animals with recombinant VSV, expressing GFP, pseudotyped with SARS-CoV-2 Spike protein. VSV infects permissive 293T-ACE2 cells, GFP positive cells are enumerated by counting GFP positive cells.
B) Representative images of permissive cells infected with recombinant, pseudotyped VSV, note ΔG VSV requires Spike pseudotyping to infect 293T-ACE2 cells.
C) IC50 for NP-S-CpG-RIGI and control vaccinated animals compared to CHS. Data are represented as mean ± SEM, one-way ANOVA and Dunnet's multiple comparisons test, **P*<0.001 relative to control, NS denotes *P*>0.05 compared to CHS.
D) The mean relative number of GFP+ cells per field at each dilution compared to naïve controls ±SEM is depicted.

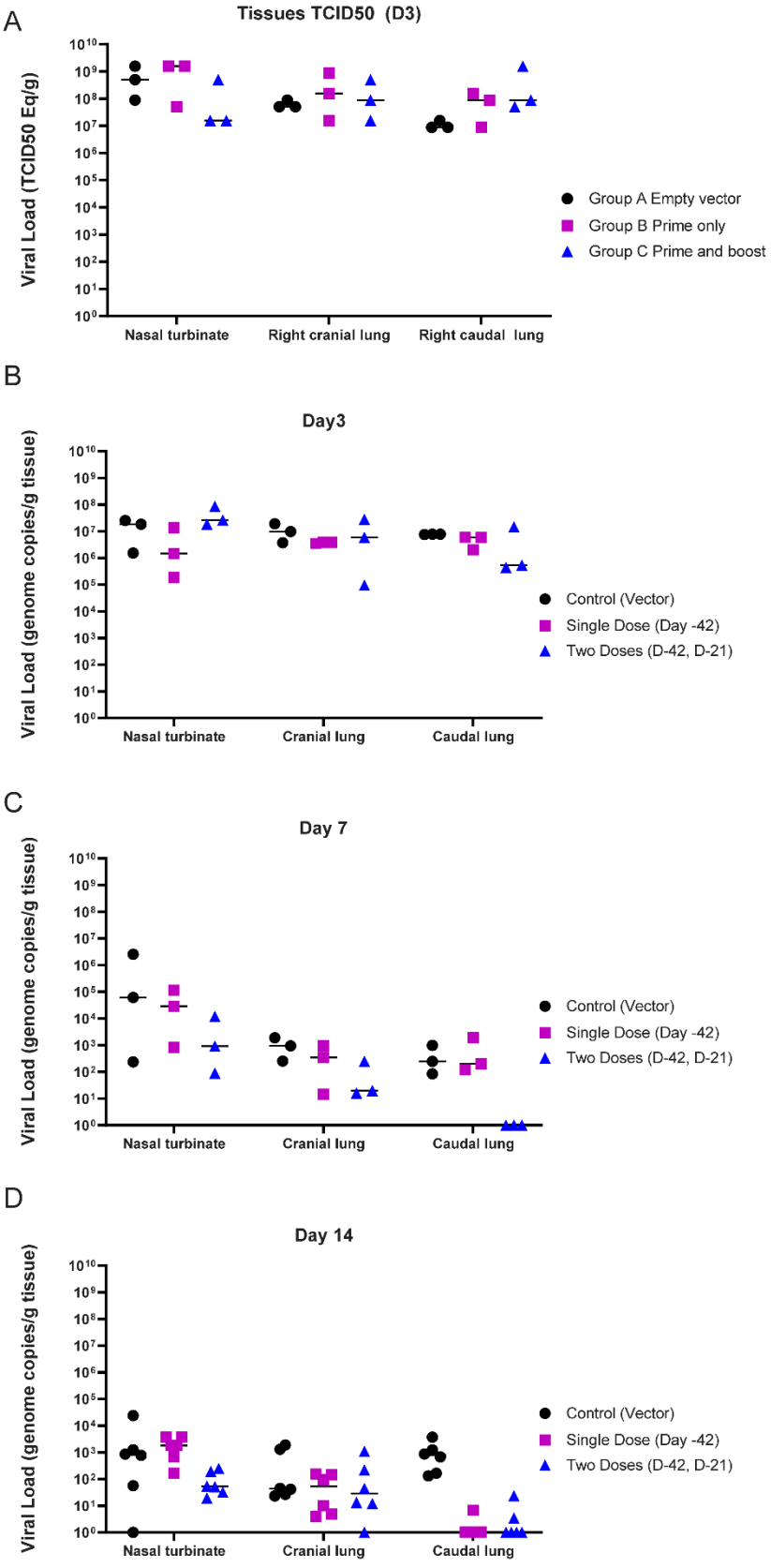
A
Tissues TCID50 (D3)
Viral Load (TCID50 Eq/g)
Nasal turbinate
Right cranial lung
Right caudal lung
Group A Empty vector
Group B Prime only
Group C Prime and boost
B
Day3
Viral Load (genome copies/g tissue)
Nasal turbinate
Cranial lung
Caudal lung
Control (Vector)
Single Dose (Day -42)
Two Doses (D-42, D-21)
C
Day 7
Viral Load (genome copies/g tissue)
Nasal turbinate
Cranial lung
Caudal lung
Control (Vector)
Single Dose (Day -42)
Two Doses (D-42, D-21)
D
Day 14
Viral Load (genome copies/g tissue)
Nasal turbinate
Cranial lung
Caudal lung
Control (Vector)
Single Dose (Day -42)
Two Doses (D-42, D-21)

**Supplementary Figure 3.3 Extended Viral Load Data Following Hamster Challenge.**
Each point represents an individual animal, lines are present at the median for each group.
A) Viral load in the indicated tissues 3 days post challenge as determined by $TCID_{50}$ assay, expressed as $TCID_{50}$ equivalents per gram of tissue.
B) As in A measured by RT-qPCR and expressed as genome copies/gram of tissue.
C) Viral load in the indicated tissues 7 days post challenge.
D) As in C, 14 days post challenge.

# **Chapter 4:** Selective Ablation of Solid Tumors with Dysfunctional P53 Signaling using a Suicide Gene Delivered via Fusogenix Proteolipid Vehicles

# Selective Ablation of Solid Tumors with Dysfunctional P53 Signaling using a Suicide Gene Delivered via Fusogenix Proteolipid Vehicles

Douglas W. Brown[1], Arun Raturi[1,2], Prakash Bhandari[2], Ping Wee[2], Deborah Sosnowski[1], Liliya Grin[2], Manoj Parmar[2], Hector Vega[2], Maryam Hejazi[1], Jennifer Gyoba[2], Paola Solis Ares[2], Jitendra Kumar[2], Suellen Lamb[1], Jailal Ablack[3], Desmond Pink[1], Perrin H. Beatty[2], Henry Garcia[5], Matthew Scholz[5], Roy Duncan[2,4], and John D. Lewis[1,2,3,5,6]*

[1] Department of Oncology, University of Alberta, Edmonton, Alberta, Canada, T6G 2E1.
[2] Entos Pharmaceuticals, 10230 Jasper Avenue, Suite 4550, Edmonton, Alberta, Canada, T5J 4P6
[3] OncoSenX, 701 Fifth Ave, Suite 4200, Seattle, Washington 98104
[4] Department of Microbiology & Immunology, Dalhousie University, Halifax, Nova Scotia, Canada, B3H 4R2
[5] Oisin Biotechnologies, 701 Fifth Ave, Suite 4200, Seattle, Washington 98104
[6] Lead Contact: John D. Lewis.
*Correspondence to: John D. Lewis, University of Alberta, Katz Group Centre, 5-142, Edmonton, Canada. Phone: 780.492.6113, Email: jdlewis@ualberta.ca

Figures (5) and Tables (1)

In Brief:
We developed a novel DNA-based suicide gene therapy that requires upregulated p53 transcriptional activation to be expressed. This restricts suicide gene expression to cancer cells, offering a highly efficacious alternative to current genotoxic therapies.

**Abstract**

While chemotherapy is a key treatment strategy for many solid tumors, it is rarely curative as patients will eventually become resistant. In this study, we sought to develop an effective suicide gene therapy approach for solid tumors that specifically exploits the unique transcriptional activation state of the tumor suppressor, p53. We have developed a Fusogenix proteolipid vehicle (PLV) formulation to deliver a plasmid DNA vector where the p53 promoter is included upstream of the inducible suicide gene, iCasp9. Addition of the small molecule dimerizer agent, rapamycin (RAPA), facilitates cleavage and activation of iCasp9 leading to caspase-mediated apoptosis in cells with elevated p53 promoter activity. We observed a high degree of apoptotic cell death, as measured by live-cell imaging, as well as Annexin V and TUNEL flow cytometry. No cell death was observed in cells with intact p53 such as the fibroblast cell line IMR-90. Systemic delivery of the p53-iCasp9 vector to subcutaneous PC3 or H1299 tumors results in robust apoptosis induction upon activation with RAPA that effectively controls tumor growth overtime. When p53-iCasp9 was combined with the anti-CTLA-4 (α-CTLA4) checkpoint inhibitor, treatment was able to reduce total metastatic burden in the poorly immunogenic B16F10 melanoma lung metastasis model. Treatment correlated with an increase in activated CD4 T lymphocytes and a reduction in suppressive CD4 $T_{reg}$ cells – leading to improved recognition and elimination of B16F10 cells *ex vivo*. In conclusion, we describe a novel PLV based suicide gene therapy approach for the treatment of cancer with high selectivity for tumors with dysregulated p53 transcriptional activation.

Keywords: Cancer, Gene therapy, Nucleic acid delivery, Proteolipid Vehicle, PLV, Inducible Caspase 9, iCasp9, Rapamycin, Suicide Gene Therapy.

## 4.1. Introduction

Nearly two decades after the first p53 gene therapy was introduced in China, p53 remains one of the most elusive targets in cancer therapy[214]. With the discovery that p53 is mutated in the majority of cancers a significant amount of research has been directed towards understanding the importance of p53 in tumorigenesis[169,475–477]. P53 has an essential role in multiple tumor suppressive pathways, and inhibiting its activity leads to extensive cellular dysfunction that is crucial for maintaining tumor growth[478,479]. Because of its vital role as a tumor suppressor, many gene therapies have been designed to restore p53 function. Unfortunately, most of these treatments did not demonstrate high efficacy as a monotherapy, and in the case of ovarian cancer, actually increased morbidity[480,481]. Despite these limitations, the promise of targeting p53 for cancer treatment remains intact.

The primary focus of cancer gene therapy has been achieving ectopic expression of genes that facilitate tumor regression, as was anticipated for p53 gene therapy. Suicide gene therapy offers a means to achieve this, whereby the selective introduction of an exogenous gene that when expressed can convert a non-toxic compound into a lethal agent[482]. One of the most promising suicide genes, inducible caspase 9 (iCasp9), demonstrates exquisite control over apoptosis induction, displaying minimal activity in the absence of a small molecule chemical inducer of dimerization (CID)[483,484]. When CID is added, two molecules of iCasp9 are dimerized and undergo a cleavage that exposes the active site of caspase 9, which in turn results in robust apoptosis induction[483–486]. However, the most widely used CID, AP1903, is not a licensed therapeutic; therefore, a recently designed iCasp9 activated by low dose rapamycin (RAPA) is a cheaper and more widely accessible means to implement this technology[487]. Contrary to AP1903, which is a bifunctional molecule that forms a homodimer of two iCasp9 proteins, RAPA addition

heterodimerizes two iCasp9 proteins by binding to the FKBP12-rapamycin binding (FRB) domain of one protein and the FKBP12 domain of the other[488]. This heterodimer then undergoes proximity induced cleavage and activation resulting in apoptosis induction. Though a promising genetic medicine, iCasp9 based gene therapy is limited by a lack of a safe and effective nucleic acid delivery platform[3,489,490].

Viral vectors have dominated gene therapy clinical trials[3], though, the recent approval of three RNA encapsulating lipid nanoparticles (LNPs) has set the stage for more non-viral gene therapy delivery vectors to enter the clinic in the near future[34,491]. Despite growing popularity, systemically delivered LNPs have significant limitations, such as poor extrahepatic delivery, dose-limiting toxicity, and immune stimulation[41,42,492,493]. We have recently described the design of a novel non-viral nucleic acid delivery platform called Fusogenix proteolipid vehicles (PLVs). These PLVs incorporate the positive aspects from both viral and non-viral delivery vehicles, by incorporating a chimeric fusion-associated small transmembrane (FAST) protein isolated from orthoreoviruses into a well-tolerated lipid formulation. PLVs encapsulating DNA demonstrated significantly improved tolerability over conventional LNP formulations and the ability to reach extrahepatic targets, making them an ideal candidate for a cancer targeted gene therapy approach[472]. Here, we examine the transcriptional activation state of the p53 promoter in cancer cells and use this promoter to design an iCasp9-based suicide gene DNA vector capable of being delivered systemically to cancer cells via encapsulation within Fusogenix PLVs.

## 4.2. Results

### *4.2.1. P53 Promoter Upregulation*

The p53 network is the most perturbed pathway in cancer, with some estimates predicting 80% of tumors have dysregulated p53 function[176,177]. Despite an unprecedented research

investment directed towards understanding the role of p53 in tumor biology[143,144,155,169,494,495], little is known about its transcriptional regulation[170]. Using the Gene Expression Profiling Interactive Analysis (GEPIA) database[496], we compared the p53 transcript level in multiple tumor subtypes relative to their corresponding normal tissues. All tumor types displayed some degree of upregulated p53 transcription, except for kidney chromophobe, pheochromocytoma/paraganglioma, and head and neck squamous cell carcinoma. On average, tumor tissue presented with a 1.5-fold increase in p53 transcript levels. Of the 31 tumor subtypes analyzed, 14 had significantly higher p53 transcript levels than their corresponding normal tissue counterpart (**Figure 4.1A, Supplementary Figure 4.1A**). Interestingly, p53 transcription was significantly upregulated in 3 out of 4 of the tumor subtypes with the highest frequency of p53 mutations (ovarian serous carcinoma, lung squamous cell carcinoma, and glioblastoma)[497,498]. These results implicate mutant p53 and dysfunctional p53 signaling as key players in the transcriptional activation state of p53 in cancer.

Approximately 10% of all p53 mutations result in a complete loss of p53 protein that would not be detected by standard RNA sequencing methods[499] and therefore the GEPIA analysis may be under-representing the full scope of p53 transcriptional upregulation. To understand the effect that loss of p53 protein would have on p53 transcription, we examined p53 promoter activity in HCT116 cells with wildtype p53 and p53 knocked out by homologous recombination[500]. Knockout of p53 resulted in approximately a 6-fold increase in p53 promoter activity (**Figure 4.1B**). Next, we assessed the p53 promoter activity in 30 cancer cell lines and 3 normal cell lines. All 3 normal cell lines had the lowest p53 promoter activity, with cancer cell lines presenting with a wide range of p53 promoter activities (**Figure 4.1C, Table 4.1**). Interestingly, even with p53 transcription upregulated in cancerous tissue (**Figure 4.1A**), we found that p53 transcript level[501] in each of

these cell lines had no correlation to p53 promoter activity (**Figure 4.1D**). These results indicate that additional pathways outside of the immediate p53 autoregulatory network[502,503] are likely responsible for the increase in p53 transcription and the corresponding increase in p53 promoter activity. We therefore looked for other possible explanations for upregulated p53 promoter activity in cancer. Despite only constituting ~27% of the cells selected for screening, 40% of the cell lines with top ten p53 promoter activity had some form of p53 deletion mutation, whereas only 21% of cells with p53 point mutations had top ten p53 promoter activity, and surprisingly, 30% of cells with wild type p53 had top ten p53 promoter activity. Next, we analyzed Depmap RNA expression data[501] to try and identify a gene signature that correlated with upregulated p53 promoter activity. TP53 target 3 family member E (TP53TG3E) was highly correlated with p53 promoter activity, giving a Pearson correlation coefficient of 0.941 and a p-value < 0.0001 (**Supplementary Figure 4.1B**). However, only 20% of the cell lines analyzed had any measurable TP53TG3E expression and therefore, we ran an additional Pearson correlation with the top expressor, H1299, removed from analysis as we assumed it was potentially skewing the results. This analysis gave two prospective targets both with p-values < 0.001, Zinc Finger Protein 223 (ZNF223) and Phosphatase and Tensin Homolog (PTEN), with Pearson correlation coefficients of -0.623 and -0.605, respectively (**Supplementary Figure 4.1C, D**). Adding H1299 back into the analysis resulted in the elimination of PTEN as a prospective target as its p-value become > 0.05, ZNF223 on the other hand, still had a p-value < 0.01 and gave a Pearson correlation coefficient of -0.543 (**Supplementary Figure 4.1E**). We therefore propose a potential gene signature predictive of high p53 promoter activity: TP53TG3E $\log_2$(TPM+1) expression greater than 0.2 and/or ZNF223 $\log_2$(TPM+1) expression less than 1.2. Of course, this signature needs to be validated further in

more cell lines and clinical samples, but it offers an excellent starting point for predicting p53 transcriptional activation.

### *4.2.2. Design of a Programmable Apoptotic Gene Therapy*

Given its role in nearly all aspects of cancer biology, p53 represents an enticing target for future therapeutic strategies[498,504]. Research has predominately been directed towards restoring wild type p53 function in cancer cells with the hopes it will induce apoptosis[479]. Instead of attempting to restore endogenous p53 activity, we sought to develop a therapeutic that exploits existing perturbations in the p53 signaling network. With p53 promoter activity being orders of magnitude higher in cancer cells compared to normal cells (**Figure 4.1C**), we hypothesize a gene therapy approach that relies on the increased transcriptional activation state of p53 to become active offers a mechanism to selectively target cancer cells in a highly efficacious manner. To accomplish this, we generated a plasmid DNA vector where the p53 promoter is driving the expression of the suicide gene, iCasp9. This DNA vector is delivered systemically to cancer cells by encapsulating it within a Fusogenix proteolipid vehicle (PLV), which enables safe and effective extrahepatic DNA delivery[472]. iCasp9 is then expressed in cancer cells displaying elevated p53 promoter activity. Adding the CID, RAPA, causes the expressed iCasp9 to become active and selectively facilitates apoptosis induction in cancer cells (**Figure 4.2**).

### *4.2.3. P53 Promoter is Effective at Facilitating iCasp9 Expression in Cancer Cells*

The human p53 promoter and iCasp9 sequence was cloned into the p10 plasmid DNA expression vector (herein described as p53-iCasp9) developed by Entos pharmaceuticals[472]. PLVs were added to H1299 cells *in vitro* and western blot was conducted to confirm full length iCasp9 expression. Addition of increasing concentrations of RAPA for two hours resulted in cleavage of the full length iCasp9 band and the appearance of two cleaved caspase 9 bands as well as a cleaved

caspase 3 band (**Figure 4.3A**). Densiometric analysis of these bands indicates a reciprocal relationship between full length iCasp9 and cleaved caspase 9 with RAPA giving a cleavage IC50 value between 0.3-0.4nM (**Figure 4.3B**). To confirm that the expressed iCasp9 was functional following RAPA addition, an LEHD cleavage activity assay was conducted[505]. Caspase 9 activity was significantly increased following RAPA addition (**Supplementary Figure 4.2A**). These results confirm that the elevated p53 promoter activity in cancer cells can be hijacked with an exogenously delivered DNA vector and used to produce a functional suicide gene.

### *4.2.4. Suicide Gene Therapy Facilitates Robust Apoptosis Induction in Cancer Cells*

To enable the evaluation of treatment efficacy via fluorescent methods, a bicistronic DNA vector was constructed with green fluorescent protein (GFP) included downstream of the p53-iCasp9 sequence. The iCasp9 and GFP sequences are connected via a T2A linker that enables equimolar amounts of both proteins to be produced without being connected to one another[506,507]. Cells expressing GFP are therefore assumed to also be expressing iCasp9. Addition of PLVs encapsulating p53-iCasp9-GFP to H1299 cells resulted in a large population of GFP expressing cells visible with a fluorescent microscope, 36 hours after addition. A 12-hour incubation with RAPA resulted in significant cell death with a corresponding loss of GFP expressing cells, indicating dual expression of iCasp9 and GFP (**Figure 4.3C**).

Using an imaging cytometer, the presence of cleaved caspase 3 was evaluated in H1299 cells following addition of PLVs encapsulating p53-iCasp9-GFP. RAPA caused a significant increase in the intensity of cleaved caspase 3 staining in the entire cell population (**Supplementary Figure 4.2B-D**). Additionally, the proportion of cells positive for both cleaved caspase 3 and p53-GFP was significantly increased following RAPA addition (**Supplementary Figure 4.2C, E**). The phenotypic changes that characterize apoptosis, plasma membrane blebbing and nuclear

fragmentation, were also observed in cells receiving RAPA (**Supplementary Figure 4.2B**). These changes were quantified in the cleaved caspase 3+ GFP+ population, demonstrating a significant increase in apoptosis (**Supplementary Figure 4.2C, F**). Next, we evaluated the selectivity of treatment for cancer cells. H1299 were cocultured with normal human IMR90 fibroblasts and had PLVs encapsulating p53-iCasp9-GFP added. Cells were visualized using time lapse confocal microscopy. GFP expression was restricted to H1299 cells, which are smaller and rounder than the elongated IMR90 fibroblasts. Addition of RAPA caused a rapid apoptosis induction – visible within 10 minutes of RAPA addition, with all $GFP^+$ H1299 cells being eliminated by 145 minutes (**Figure 4.3D**). In line with this, we observed a time dependent increase in the Annexin $V^+$ fraction of cells expressing the p53-iCasp9 vector after RAPA addition (**Supplementary Figure 4.2G**).

To rule out any possibility that cell death was being caused by RAPA addition in combination with exogenous gene expression, we generated an expression control DNA vector. This construct still has the p53 promoter driving the expression of an iCasp9 molecule, however, the iCasp9 was made catalytically inactive by generating a point mutation (C386A) in its active site (p53-inactive) – akin to the endogenous caspase 9 C287A inactivating mutation[508,509]. This control DNA vector enables us to determine if cell death is simply brought on by RAPAs other cellular effects in combination with transcription/translation stress or the presence of intracellular plasmid DNA. Annexin V/Zombie-UV staining was conducted on H1299 cells expressing the p53-iCasp9 construct or the p53-inactive construct following RAPA administration. RAPA addition had no effect on cells expressing the p53-inactive construct, however, it facilitated a significant increase in all apoptotic cell populations (early, late, and necrotic/dead) as well as Annexin V stain intensity in cells expressing the functional p53-iCasp9. We also observed a slight increase in the apoptotic population of cells expressing the function p53-iCasp9 in the absence of RAPA,

indicating that iCasp9 likely undergoes some auto-activation (**Figure 4.3E-G**). We next conducted Annexin V/Zombie-UV staining on p53-iCasp9 expressing PC3 and C33A cells, as they were second and third overall in p53 promoter activity, respectively (**Table 4.1**). RAPA addition caused a significant increase in all apoptotic cell populations (early, late, and necrotic/dead) in both PC3 and C33A cells (**Supplementary Figure 4.2H**). Next, we conducted terminal deoxynucleotidyl transferase dUTP nick end labeling (TUNEL) staining in treated H1299 cells to identify fragmented nuclear DNA due to apoptosis. PLVs encapsulating p53-iCasp9-GFP were added to H1299 cells, following which, RAPA was administered for 12-hours before cells were assessed for TUNEL staining via imaging cytometry. RAPA administration caused a significant increase in the $TUNEL^{+}$ population as well as TUNEL staining intensity (**Figure 4.3H-K**). Phenotypic changes associated with apoptosis (plasma membrane blebbing and nuclear fragmentation) were also observed in the cells receiving RAPA (**Figure 4.3H**).

### *4.2.5. P53 Promoter Drives Tumor Specific Expression*

Large barriers exist that hinder nanoparticle-based drug delivery to tumors in patients, including off-target effects, poor tumor vascularization, tumor heterogeneity, and presence of a necrotic core. To first validate whether DNA delivery and expression was possible in tumors growing *in vivo*, we generated a bicistronic DNA vector with firefly luciferase (FLuc) downstream of the p53-iCasp9 sequence with a T2A linker included between these two sequences (p53-iCasp9-FLuc). Encapsulation of this p53-iCasp9-FLuc vector within Fusogenix PLVs lead to particles with a mean size of 70.9nm, a polydispersity index of 0.1880, and a zeta potential of -2.59mV. PLVs encapsulating this p53-iCasp9-FLuc construct were injected intratumorally into mice bearing subcutaneous H1299 tumors. We detected a strong bioluminescent signal radiating

selectively from the tumor during whole-body imaging (**Supplementary Figure 4.3A**). Like the *in vitro* data demonstrating that $GFP^+$ cells undergo apoptosis following RAPA addition due to co-expression of iCasp9, it is expected that $FLuc^+$ cells expressing the p53-iCasp9-FLuc construct would also be co-expressing iCasp9. Therefore, RAPA addition will facilitate cell death in $FLuc^+$ cells, thus resulting in a loss of luminescent signal. To test this and determine what dose of RAPA would be required *in vivo*, mice bearing subcutaneous H1299 tumors were injected intratumorally with PLVs encapsulating the p53-iCasp9-FLuc construct and had 0.1 mg/kg RAPA administered via intraperitoneal (IP) injection 24 hours later. Whole-body bioluminescent imaging confirmed tumor specific FLuc expression rapidly decreased ~70% over the next two days (**Supplementary Figure 4.3B, C**). We anticipate that the kinetics of FLuc removal from a tumor *in vivo* is substantially different than *in vitro*, consequently resulting in the FLuc signal remaining after cells have died.

Next, we evaluated the ability of systemically delivered PLVs to reach and facilitate iCasp9 expression in tumors. Mice bearing subcutaneous H1299 tumors were injected intravenously (IV) with 6 mg/kg p53-iCasp9-FLuc encapsulated in PLVs and whole-body bioluminescent imaging confirmed tumor specific FLuc expression (**Figure 4.4A**). 8 hours after PLV injection mice received an IP injection of 0.1mg/kg RAPA or vehicle control and were sacrificed 16 hours later. *Ex vivo* bioluminescent imaging established tumor specific FLuc expression that was absent in mice receiving RAPA. Additionally, FLuc was not detected in the major PLV uptake organs; lungs, liver, spleen, or kidney (**Figure 4.4B**). Compared to a plasmid DNA vector with the ubiquitous cytomegalovirus promoter (CMV) driving FLuc expression, the tumor selectivity of the p53 promoter becomes more apparent. Though we detected high FLuc activity in subcutaneous H1299 tumors following IV injection with PLVs encapsulating the CMV-FLuc DNA vector,

whole-body bioluminescent imaging indicated a wide distribution of expression extending far beyond the tumor (**Supplementary Figure 3D**), as we have previously shown for systemically delivered DNA utilizing the CMV promoter[472].

### *4.2.6. Selective Ablation of Subcutaneous Prostate Tumors*

Prostate cancer represents an ideal candidate for suicide gene therapy because apoptosis induction mediated by iCasp9 is independent of the cell cycle and therefore slow growing cancers like prostate cancer are still susceptible to treatment[483]. We first examined the ability of treatment to control PC3 tumor growth *in vivo*. To limit potential off-target effects, mice bearing subcutaneous PC3 tumors received an intratumoral (IT) injection of 100μg p53-iCasp9 when tumors reached ~150mm$^3$. Four days after injection, mice received a single IP injection of 0.1 mg/kg RAPA. We observed a rapid and sustainable decrease in tumor volume in the days following RAPA injection, with one mouse achieving a 90% decrease in tumor volume (**Supplementary Figure 4.4A, B**). In total, the group demonstrated ~40% decrease in tumor volume in the first 24 hours following RAPA injection (**Supplementary Figure 4.4C**). Next, we tested the anti-tumor efficacy of IV delivered PLVs encapsulating p53-iCasp9. Mice received four daily IV injections of 3 mg/kg p53-iCasp9, with 0.1 mg/kg RAPA being administered on the fifth day. Again, we observed a rapid decrease in tumor volume ranging from 60-80%, with one mouse not responding to treatment (**Supplementary Figure 4.4D-F**). Regardless of administration route, a single treatment cycle of PLVs encapsulating the p53-iCasp9 vector extended median survival by 200%, relative to untreated PC3 tumor bearing animals (**Supplementary Figure 4.4G**). Overall, our results indicate promise for the treatment of prostate cancer, either by local or systemic PLV p53-iCasp9 administration.

### *4.2.7. Attenuation of Subcutaneous Lung Tumor Growth*

The results of our initial cell line screen (**Figure 4.1C, Table 4.1**) identified the non-small cell lung cancer cell line, H1299, as having the highest level of p53 promoter activity; approximately 4-fold higher than PC3 cells, therefore making H1299 an exciting candidate for treatment. Because H1299 tumors grow faster than PC3 tumors *in vivo*, with the latter taking up to 80 days to reach end point in some cases, treatment commenced once H1299 tumors reached 25mm$^3$ (palpable). All animals received IV injections of PLVs encapsulating 6 mg/kg p53-iCasp9. 24 and 48 hours after PLV injection, control animals received an IP injection of vehicle buffer and treated animals received an IP injection of 0.1 mg/kg RAPA. This treatment cycle was repeated twice a week for three weeks. We observed a potent suppression of tumor growth in mice receiving RAPA injections (**Figure 4.4C**). Moreover, mice receiving RAPA also had significantly smaller and lighter tumors than their vehicle control counterparts (**Figure 4.4D, E**). TUNEL staining of tumor sections isolated from control and treated animals demonstrated a significant increase in TUNEL$^+$ cells in mice receiving the combination of p53-iCasp9 and RAPA, confirming apoptotic cell death as a mechanism for tumor control (**Figure 4.4F, G**). To rule out the possibility that this effect was due solely to RAPA administration, a long-term treatment/survival assay was conducted in H1299 subcutaneous tumor bearing mice. The treatment schedule was that same as described above, with mice receiving an IV PLV injection followed by two daily 0.1 mg/kg RAPA IP injections, repeated twice a week until the tumors reached 1500mm$^3$. Treated animals received a slightly lower dose of 3 mg/kg p53-iCasp9 encapsulated in PLVs to prevent toxicity development. However, control mice were treated with PLVs encapsulating 3 mg/kg of the p53-inactive (catalytically inactive iCasp9) control DNA vector. Tumor growth was significantly reduced in mice receiving the active p53-iCasp9 construct (**Supplementary Figure 4.3E**). Additionally, median survival was increased by 120% in treated animals (**Supplementary Figure 4.3F**). Thus,

when administered systemically in a rapidly growing subcutaneous tumor model with high p53 promoter activity we demonstrate that treatment with p53-iCasp9 offers an effective means to control tumor growth and prolong survival.

#### *4.2.8. Reduced Metastatic Burden When Combined with Immune Checkpoint Inhibitor*

Anti-cancer immunotherapy has rapidly become one of the most important clinical breakthroughs in controlling cancer growth and progression[510]. Cancer cells can avoid immune recognition by expressing programmed death ligand 1 (PD-L1), which in turn binds to PD-1 on T cells thereby blocking the anti-tumor T cell response. Additionally, T cells present with a negative regulatory system where activated T cells in the lymph node will increase surface levels of cytotoxic T lymphocyte antigen-4 (CTLA-4), which facilitates inhibition of T cell activation[511]. Monoclonal antibodies targeting PD-1 and CTLA-4 have demonstrated clinical success, particularly for the treatment of advanced melanoma[512,513], with the combination of these therapies significantly increasing survival compared to either as a monotherapy[514]. Clearly, the importance of anti-tumor immunity cannot be overlooked when it comes achieving durable clinical responses. Therefore, we decided to investigate the ability of suicide gene therapy in combination with an anti-CTLA-4 (α-CTLA4) checkpoint inhibitor to achieve an anti-tumor response in the poorly immunogenic B16F10 mouse model of metastatic melanoma[515]. Simpson *et al*.[516] demonstrated that α-CTLA4 monotherapy is ineffective against subcutaneous B16F10 tumors in the absence of additional immune stimulation, making it an ideal candidate to examine treatment synergy. We have previously demonstrated high (mouse) p53 promoter activity in B16F10 cells and therefore chose to examine the efficacy of treatment in this lung metastasis model. 100,000 B16F10 cells were injected IV into 8-week-old female C57BL6 mice. One day after tumor cell injection, mice were injected IV with PLVs encapsulating 5 mg/kg of either p53-iCasp9 DNA or p53-inactive

DNA (Ctrl PLV). 24 hours after PLV injection, mice receiving p53-iCasp9 PLVs one of three treatment options. They were either injected IP with vehicle, 0.1 mg/kg RAPA, or 0.1 mg/kg RAPA + 5 mg/kg α-CTLA4. Mice receiving Ctrl PLV injections were injected with 0.1 mg/kg RAPA + 5 mg/kg α-CTLA4. An additional RAPA (or vehicle) injection was given IP 24 hours later. This treatment cycle was repeated twice a week for three weeks until mice were sacrificed 22 days after B16F10 injection. Treatment was well tolerated across all treatment groups. Lungs were removed and bleached to enable quantification of metastatic colonies. Diameter of each metastatic colony was calculated in ImageJ and used to determine surface area, which was summed together for each animal and used to evaluate total metastatic burden (surface area of the lungs occupied by tumor). We observed a significant reduction of total metastatic burden in mice receiving the immunotherapy + suicide gene combination treatment – p53-iCasp9 PLVs + RAPA + α-CTLA4 (**Figure 4.5A, B**). Histological analysis confirmed these results, with the lungs of dual therapy mice displaying smaller metastatic colonies (**Figure 4.5A**). Monotherapy with p53-iCasp9 and RAPA slightly decreased metastatic burden, however, these results were not significant (**Figure 4.5A, B**). As treatment with inactive Ctrl PLVs combined with RAPA and α-CTLA4 was not sufficient for controlling metastatic burden, these results indicate that cell death induced by p53-iCasp9 and RAPA likely generates an immunogenic response that is augmented by addition the α-CTLA4 checkpoint inhibitor.

To elucidate the mechanism by which α-CTLA4 potentiates p53-iCasp9 mediated cell death we conducted immunophenotyping on splenocytes isolated from treated animals. Treatment with p53-iCasp9 in addition to α-CTLA4 significantly increased the frequency of activated $CD25^+$ CD4 T cells (**Figure 4.5C**) but had no effect on the frequency of activated $CD69^+$ CD8 T cells (data not shown). The frequency of $CD25^+$ $FOXP3^+$ CD4 T regulatory cells (CD4 $T_{reg}$) was

significantly reduced in immunotherapy + suicide gene therapy treatment group (**Figure 4.5D**). These results indicate combination treatment increased the activation and proliferation of the CD4 T cell population, indicated by increased surface expression of CD25 [517], while simultaneously decreasing the frequency of the suppressive CD4 $T_{reg}$ population required for immunological tolerance[518,519]. Next, we examined the ability of isolated splenocytes to identify and target B16F10 cells *in vitro*. When splenocytes isolated from mice treated with p53-iCasp9 and α-CTLA4 were co-cultured with B16F10 cells we detected a significant increase in the frequency of dead B16F10 cells relative to mice treated with Ctrl PLVs and α-CTLA4 (**Figure 4.5E**). These results indicate that the addition of α-CTLA4 on its own is not sufficient to increase T cell activation, whereas p53-iCasp9 mediated apoptosis in combination with α-CTLA4 results in a potent anti-tumor response presumably mediated by increased tumor cell antigen processing[520] with an increase in CD4 T cell activation and a reduction in CD4 $T_{reg}$ mediated suppression.

## 4.3. Discussion

P53 has represented an intriguing target for cancer therapy since its critical role as a tumor suppressor was uncovered over 30 years ago[164–168]. With altered functionality present in nearly all tumor types, a significant research effort has been directed towards restoring endogenous p53 activity; in fact, the first ever approved gene therapy approved was an adenoviral vector delivering wild type p53 to tumors[213,214]. Additionally, a number of small molecules have been designed to prevent negative regulation of wild type p53 [521] as well as some that have been developed to reverse the effects of the oncogenic gain-of-function p53 mutants[522]. Despite the interest in restoring wild type p53 function, most of these treatments have seen little clinical success and largely exert their effect by sensitizing cancer cells to other cytotoxic therapies. As p53 dysfunction is essential for maintaining tumor growth[478,479], we decided to capitalize on this dysfunctional state by designing

a suicide gene therapy that selectively targets cancer on the basis of upregulated p53 promoter activity.

Alteration of p53 function represents an important event in tumorigenesis, with mutant p53 characterizing triple negative and HER2 overexpressing breast cancer[188,523], progression of prostate cancer to an androgen-independent metastatic state[189,190,524,525], as well as poor survival and metastasis in lung cancer patients[526,527]. Despite cancerous tissue having upregulated transcription of p53, we found no correlation between transcript level and p53 promoter activity. However, loss of wild type p53 resulted in an upregulation in p53 promoter activity. As transcriptional regulation of p53 is a relatively overlooked topic in tumor biology[170], the mechanism for this upregulation requires some speculation. Perhaps one of the most interesting possibilities is cooperative regulation by c-Myc and RAS; both of which are frequently mutated and activate in many cancers[173,528]. RAS and c-Myc are intricately linked, with aberrant RAS signaling resulting in increased c-Myc protein stability[529,530]. c-Myc functioning as a transcription factor, has been found to directly bind to and positively regulate the p53 promoter[171]. Conversely, p53 can bind to the c-Myc promoter and inhibits its expression[531] and the p53 target, miR-145, can silence c-Myc[269]. It is possible that a loss of p53 can directly increase c-Myc activity, therefore resulting in upregulation of p53 promoter activity. This has been partially demonstrated before, as p53 loss was found to increase c-Myc expression and the expression of c-Myc regulated genes in breast cancer stem cells[532]. RAS and p53 also share a link, but it is far less direct than connection between p53 and c-Myc. Wild-type p53 has been demonstrated to facilitate expression of B-cell translocation gene 2 (BTG2), which functions as an inhibitor of aberrantly activate RAS[533]. Therefore, a loss of p53 could result in BTG2 loss, which causes RAS activity to increase, leading to increased stability of c-Myc and transcriptional activation of c-Myc regulated genes, including

p53. RAS has also been demonstrated to activate NF-κB, which in addition to increasing c-Myc expression[529], also directly binds to the p53 promoter and induces its expression (**Supplementary Figure 4.5**) [268]. Of course, validating if these pathways are responsible for upregulated p53 promoter activity will require work in the future.

Selectively targeting treatment to cancer remains one of the most difficult hurdles to overcome in oncology. Genetic medicines designed using DNA have an intrinsic ability to restrict gene expression to specific organs by using tissue-specific promoters. Uncovering cancer specific promoters with minimal activity in normal cells and high enough activity in cancer cells to facilitate meaningful gene expression has resulted in nearly 30 promoters being examined for cancer specific gene therapy[534]. Xie *et al.*[535] were one of the first groups to demonstrate the feasibility of tailoring selective suicide gene expression to prostate cancer cells by including the probasin promoter as well as two androgen responsive elements upstream of the iCasp9 sequence and utilizing an adenoviral vector to deliver the construct via intratumoral injection. Though effective at controlling subcutaneous prostate cancer tumor growth, the authors noted an important limitation being that progression to androgen-independent prostate cancer would hinder the efficacy of iCasp9 expression. Additionally, suicide gene therapy approaches are often restricted to intratumoral injections, which limits their clinical utility. Early suicide gene iterations have previously made their way into the clinic. Delivery of an adenoviral vector carrying the enzymatic suicide gene, cytosine deaminase/herpes simplex virus-1 thymidine kinase, to prostate cancer via intraprostatic injection demonstrated the ability to decrease circulating levels of prostate specific antigen[536,537]. However, the clinical success of this approach is limited due to low anti-tumor efficacy caused by insufficient expression of the enzymatic suicide gene[538]. Indeed, this could be overcome with multiple injections, however, as mentioned previously, host immune responses to

viral vectors prevents repeat administration. Conversely, we have previously shown that Fusogenix PLVs can be administered multiple times without significantly reducing efficacy, thus enabling meaningful gene expression overtime[472]. Our results indicate that the p53 promoter enables selective expression in tumors following systemic PLV delivery, enabling treatment of disseminated cancer. Additionally, the p53 promoter drives high enough expression levels of iCasp9 to achieve therapeutic responses.

The importance of the immune system in regulating tumor growth and progression cannot be overlooked when evaluating the efficacy of new treatments. This is especially relevant for gene therapy approaches, where viral vectors can have their efficacy limited by host immune responses and pre-existing antibodies. To overcome this limitation, non-viral delivery vectors, mainly LNPs, have recently increased in popularity primarily due to their improved safety, easier manufacturing, and lower immunogenicity. However, interactions between LNPs and the immune system can have detrimental systemic effects and lead to secretion of proinflammatory cytokines like TNF-α, IFN-γ, and IL-6 [43,44]. Furthermore, LNPs can stimulate complement activation-related pseudoallergy (CARPA), a hypersensitivity reaction that may result in death in severe circumstances[45–47]. We recently demonstrated that the PLV platform does not stimulate significant immune responses when compared to conventional LNPs, making them an ideal candidate for genetic medicines targeting cancer[472]. With gene therapy efficacy and tumor progression being intimately linked to immune regulation, we examined the efficacy of p53-iCasp9 treatment in the immune competent B16F10 melanoma lung metastasis model. Treatment efficacy is therefore evaluated in an advanced metastatic disease model with a fully functional immune system. Though monotherapy with the p53-iCasp9 system did not significantly reduce metastatic burden, the addition of the immune checkpoint inhibitor, α-CTLA4, significantly decreased metastatic burden presumably

due to a decrease in the suppressive CD4 $T_{reg}$ population and a consequential increase in T cell activation. Similar to what others have found, α-CTLA4 on its own had no anti-tumor effect in this model[516]. Dendritic cells have previously been demonstrated to acquire antigens from influenza-infected apoptotic monocytes resulting in a cytotoxic T lymphocyte response[539]. In the context of cancer, chemotherapy has been demonstrated to result in uptake of apoptotic bodies into dendritic cells and illicit potent anti-tumor immune responses[540,541]. We postulate that apoptosis induction via p53-iCasp9 activation may lead to the generation of immunogenic apoptotic bodies and the addition of α-CTLA4 prevents T cell exhaustion thereby increasing recognition of cancer cells by the immune system.

In conclusion, we demonstrated here that the p53 promoter is upregulated in many subtypes of cancer and this upregulation can be utilized to facilitate tumor selective gene expression when the p53 promoter is incorporated into a DNA vector. Administration of the dimerizing agent, RAPA, to iCasp9 expressing cells promotes rapid apoptosis induction mediated by iCasp9 cleavage/activation and the subsequent cleavage caspase 3 cleavage. This translates to effective control of subcutaneous prostate cancer and lung cancer growth *in vivo* following local or systemic administration of PLVs encapsulating the suicide gene. Furthermore, combination therapy with the immune checkpoint inhibitor, α-CTLA4, decreases metastatic burden in the B16F10 mouse melanoma model presumably due to a decrease in the suppressive CD4 $T_{reg}$ population and the generation of immunogenic apoptotic bodies. This novel gene therapy approach has the potential to provide a highly efficacious alternative to current therapies for local and advanced solid tumors with dysregulated p53 transcriptional activation.

## 4.4. Methods

*Materials*

Rapamycin was purchased from Fisher Scientific (Cat# BP29631) and dissolved in DMSO (Millipore Sigma, Cat# D8418) to a concentration of 40mg/ml. For in vivo injection, rapamycin was diluted in a solution of 5% PEG-400 (Fisher Scientific, Cat#P167-1) and 5% Tween-80 (Millipore Sigma, Cat# P4780) dissolved in $H_2O$. The following lipids were purchased from NOF Co. (Tokyo, Japan): 1,2-dioleoyl-3-dimethylammonium-propane (DODAP), 1,2-dimyristoyl-*sn*-glycero-3-methoxypolyethylene glycol-2000 (DMG-PEG). 2-dioleoyl-*sn*-glycero-3-phosphoethanolamine (DOPE) and 1,2-dioleoyl-3-trimethylammonium-propane (DOTAP) were purchased from Avanti Polar Lipids (Alabaster, United States). Anti-mouse CTLA4 (CD152) In Vivo antibody was purchased from BioXCell (Clone 9D9, Cat# BP0164). Rabbit anti-caspase 9 (Cat# 9502) and rabbit anti-cleaved caspase 3 antibodies (Cat# 9661) were purchased from Cell Signaling Technologies, mouse anti-GAPDH antibody was purchased from Abcam (Clone 6C5, ab8245). Goat anti-rabbit Alexa Fluor 680 (Cat# A27042) and goat anti-mouse Alexa Fluor 750 (Cat# A-21084) were purchased from Thermo Scientific. Annexin V APC (Cat# 640941) and Zombie-UV dye (Cat# 423108) were purchased from BioLegend. All flow cytometry antibodies were purchased from BioLegend: Brilliant Violet 421 CD25 (Clone PC61, Cat# 102043), Alexa Fluor 488 CD3 (Clone 17A2, Cat# 100212), APC-Fire 750 CD4 (Clone RM4-4, Cat# 116019), Brilliant Violet 510 CD44 (Clone IM7, Cat# 103043), APC CD45 (Clone 30-F11, Cat# 103112), PE-Cy7 CD8α (Clone 53-6.7, Cat# 100721), PE FoxP3 (Clone MF-14, Cat# 126403). MitoTracker Red was purchased from Invitrogen (Cat# M7512). TUNEL assay kit was purchased from Abcam (Cat# ab66110). All plasmid DNA cloning was done into the p10 plasmid vector produced by

Entos Pharmaceuticals. Plasmid DNA preps were expanded and purified by Precision Bio Laboratories (Edmonton, Alberta).

*Cells and Culturing*

Quail fibrosarcoma (QM5) cells were cultured in Medium 199 with 3% fetal bovine serum (FBS; Sigma) and 0.5% penicillin/streptomycin (Thermo Fisher Scientific, Edmonton, Canada). All cell lines used in this study were purchased from ATCC (Manassas, VA) and cultured in accordance with recommended guidelines. HCT-116 $p53^{+/+}$ and HCT-116 $p53^{-/-}$ were a gift from Dr. Vogelstein[500]. Human umbilical vein endothelial cells (HUVEC) were a gift from Dr. Allan Murray (University of Alberta) and were cultured in EGM-2 BulletKit (Lonza, Cat No. CC-3162). Cells were grown in tissue-culture treated 75 cm2 flasks (VWR 10062-860) until cells were 80% confluent or nutrients in the media are depleted in a 37°C incubator with humidified atmosphere of 5% CO2 (Nuaire NU-5510). Spodoptera frugiperda pupal ovarian tissue (Sf9) cells used to produce FAST protein were stepwise cultured at 25C to $2x10^6$ – $4x10^6$ cells/mL from 25 mL to 100 mL and finally into a 2 L wave bioreactor. The Trypan Blue assay was used to check for cell viability.

*Purification of FAST Proteins*

FAST proteins were purified and had activity checked as described previously[472]. Briefly, Sf9 cells were lysed, and supernatant was clarified by 0.2 μm filtration. The FAST proteins were purified from the supernatant using an AKTA affinity purification column, followed by dialysis and cationic exchange purification (AKTA). Protein samples were quality control analyzed by SDS-PAGE and Western blot; functional validation was done via syncytia formation assay.

*FAST-PLV Manufacturing and Validation*

Lipid formulation composition, manufacturing, and validation was described previously[472]. Briefly, individual lipids were heated in a 37°C water bath for 1 min, vortexed for 10 seconds each, then combined and vortexed for 10 seconds. The combined lipid mixture was dehydrated in a rotavapor at 60 rpm for 2 hours, under vacuum, then rehydrated with 14 mL 100% ethanol, and sonicated (Branson 2510 Sonicator) at 37°C, set to sonication of 60. The lipid formulation was aliquoted in 500 µL batches and stored at -20°C. The NanoAssemblr Benchtop microfluidics mixing instrument (Precision NanoSystems, Vancouver, BC, NIT0013, and NA-1.5-88, respectively) was used to mix the organic and aqueous solutions and make the PLVs. The organic solution consisted of lipid formulation in EtOH. The aqueous solution consisted of pDNA, 5 nM FAST protein, and 10 mM acetate buffer (pH 4.0). NanoAssemblr was run at a total flow rate of 12 mL/min and a 3:1 aqueous to organic flow rate ratio. PLVs were dialyzed in 8000 MWCO dialysis tubing (BioDesign, D102). The loaded tubing was rinsed with 5 mL of double distilled water and dialyzed in 500 mL of Dialysis Buffer (ENT1844) with gentle stirring (60 rpm) at ambient temperature for 1 hour and was repeated twice with fresh Dialysis Buffer. PLVs were concentrated using a 100 kDa Ultra filter (Amicon, UFC810096) according to the manufacturer's instructions. PLVs were filter sterilized through 0.2 µm Acrodisc Supor filters (Amicon, UFC910008). Particle size, polydispersity index (PDI), and zeta potential was measured on final samples using the Malvern Zetasizer Range and a Universal 'Dip' Cell Kit (Malvern, ZEN1002) following the manufacturer's instructions. The nucleic acid encapsulation efficiency and concentration was calculated using a modified Quant-IT PicoGreen dsDNA assay (Thermo Fisher Scientific, Edmonton, Canada).

*In Vitro Transfection and Cell Line Screen*

All cells were counted using a hemocytometer prior to plating. All pDNA constructs were prepared with Entos pharmaceuticals *in vitro* transfection reagent (formulation 37N as described previously[472], with slight modifications to the formulation to increase *in vitro* transfection efficiency, stability, and tolerability). Lipid and pDNA were prepared in separate 1.5 ml tubes. pDNA was added to 10 mM acetate buffer (pH 4.0) to reach a final concentration of 100 ng/uL, and modified lipid formulation 37N was added to 10 mM acetate buffer (pH 4.0) at a 5:1 molar ratio of ionizable lipid:pDNA. The pDNA tube was added dropwise to the lipid tube, gently mixed by inverting, and left at room temperature before adding to cells. For the cell line screen, 5,000 cells were seeded into 96-well plates (250µL) and immediately transfected with a 2-fold dilution series from 1000-31.25 ng pDNA (6 total DNA amounts). Plates were incubated for 72 hours, following which, a luciferase reporter assay was used to measure expression levels of FLuc produced by the CMV or p53 promoters. Cell culture media was removed from cells growing in a 96-well plate, and cells washed with 1x PBS. A 50-microliter aliquot of reporter lysis buffer (Promega, Cat# E397A) was added to the cells. The cells were mixed and incubated at room temperature for 15 mins on an orbital shaker. D-luciferin (150µg/mL, GOLDBIO, LUCK-100) was dissolved in 100 mM Tris-HCl (pH 7.8), 5 mM $MgCl_2$, 2 mM EDTA, 4 mM DTT, 250 µM acetyl-CoA, and 150 µM ATP. The luciferin substrate (100 µL) of was added via auto-injector to each well immediately before measurement (1-2 second settling time). Luminescence was measured via the FLUOstar Omega plate reader (BMG Labtech, 415-1147) using the MARS data analysis software for analysis. The amount of pDNA that gave the highest level of p53-Luc readings is presented (Figure 1C and Table 1). Cells being transfected for cell death assays or western blotting were seeded at 500,000 cells/well in a 6-well plate and immediately transfected with 10 µg pDNA (p53-iCasp9, p53-iCasp9-GFP, or p53-inactive).

*Caspase 9 Activity Assay*

Caspase-Glo 9 LEHD cleavage activation assay was purchased from Promega (Cat# G8211) and conducted according to manufactures instructions. 100nM RAPA was added to p53-iCasp9 transfected cells 48 hours after transfection for 2 hours before cleavage assay was conducted.

*Western Blot*

Cells were lysed in ice-cold Pierce RIPA buffer (Thermo Scientific, Cat. No. 89900) 48 hours after transfection with p53-iCasp9. Protein amount was determined using Pierce BCA protein assay (Thermo Scientific, Cat. No. 23225). Equal amounts of total protein from each lysate were loaded onto Mini-PROTEAN 4-20% Gradient TGX precast gels (BIO-RAD, Cat. No. 456-1095). Separated protein was transferred to nitrocellulose membranes (BIO-RAD, Cat. No. 1620112). Membranes were blocked with fluorescent western blocking buffer (Rockland, Cat. No. MB-070) for 1 hour at room temperature. Rabbit anti-caspase 9 (Cell Signaling Technologies, Cat# 9502), rabbit anti-cleaved caspase 3 (Cell Signaling Technologies, Cat# 9661), and mouse anti-β-Tubulin (Clone AA2, Sigma Aldrich, Cat# T8328) primary antibodies were diluted 1:1000 in blocking buffer and added to the membranes overnight at 4˚C with shaking. Goat anti-rabbit Alexa Fluor 680 (Thermo Scientific, Cat. No. A27042), or goat anti-mouse Alexa Fluor 750 (Thermo Scientific, Cat. No. A-21084) were diluted 1:10000 in blocking buffer and added for 1 hour at room temperature in the dark. Membranes were visualized on the LI-COR Odyssey.

*Cleaved Caspase 3 Imaging Cytometry*

44 hours after transfection with p53-iCasp9-GFP, H1299 cells have 5 nM RAPA added for 4 hours before staining. Cells are lifted, washed, and fixed/permeabilized using eBioscience Intracellular Fixation and Permeabilization Kit (Invitrogen, Cat# 88-8824-00). Cells are fixed for 30 minutes

at room temperature and then washed twice with permeabilization buffer. Cleaved caspase-3 primary antibody (Cell Signaling Technology, Cat# 9661) was diluted 1:200 in permeabilization buffer and incubated overnight at 4˚C with constant rotation. Cells are then washed with flow cytometry buffer (PBS with 2% FBS and 0.09% $NaN_3$) and have goat anti-rabbit Alexa Fluor 647 secondary antibody (Invitrogen, Cat# A-21244) diluted 1:400 added for one hour are room temperature. Cells were washed and resuspended in 50 µL of flow cytometry buffer and run on the Amnis ImageStream Mark II imaging flow cytometrer. Cells were gated based on their Area vs Aspect Ratio to identify single cells, then based on a positive nuclear stain. At least 10,000 events were captured before data was analyzed on the IDEAS imaging software

*Annexin V/Zombie-UV Flow Cytometry*

24 hours after transfection with p53-iCasp9 or p53-inactive, cells have 100 nM RAPA added for 16 hours before staining. Annexin V APC and Zombie UV were purchased from BioLegend (Cat# 640941 and Cat# 423108, respectively) and cells were stained according to manufactures specifications. Briefly, cells were lifted with trypsin and spun down at 300g. Cells were washed with PBS once, before 100 µL of 1:100 diluted Zombie UV (in PBS) was added for 20-30 minutes. Cells were washed twice with flow cytometry buffer (PBS with 2% FBS and 0.09% $NaN_3$) and once with Annexin V binding buffer (BioLegend, Cat# 422201). 5 µL of Annexin V APC was added to ~100,000 cells in 100 µL Annexin V binding buffer for 20-30 minutes, before 400 µL of Annexin V binding buffer was added and cells were analyzed on a BD LSRFortessa X20 SORP.

*Live Cell Apoptosis Imaging*

175,000 of H1299 cells and 175,000 of IMR-90 cells were seeded into a 6-well plate and immediately transfected with 10 µg of p53-iCasp9-GFP. 48 hours later, cells were stained with

400nM MitoTracker Red (Invitrogen, Cat# M7512) diluted in media for 15 minutes at 37˚C before cells were visualized on the Nikon A1r MP microscope with a 25X magnification lens and the imaging chamber set at 37°C. Once cells were in focus, 100 nM RAPA was added to growth media and 250 µL mineral oil was added on top to prevent evaporation. Capture was started immediately, and images were taken at a 5-minute frequency for 4 hours total or until all $GFP^+$ transfected cells had been eliminated.

*TUNEL Imagining Cytometry*

24 hours after transfection with p53-iCasp9-GFP cells, 100 nM RAPA was added for 16 hours before staining. Cells were stained with TUNEL according to manufactures recommendations (Abcam, Cat# ab66110). Briefly, cells were lifted and fixed with 4% paraformaldehyde and permeabilized with 70% ethanol. Terminal 3' ends of fragmented DNA are then labelled with Br-dUTP using TdT enzyme for 30 minutes at 37˚C. Cells are then stained with an anti-BrdU-Red antibody and 7-AAD is used to label nuclei. Cells were resuspended in 50 µL of flow cytometry buffer and run on the Amnis ImageStream Mark II imaging flow cytometer. Cells were gated based on their Area vs Aspect Ratio to identify single cells, then based on a positive nuclear stain. At least 10,000 events were captured before data was analyzed on the IDEAS imaging software.

*Mouse Studies*

All animal studies were carried out according to the guidelines of the Canadian Council on Animal Care (CCAC) and approved by the University of Alberta Animal Care and Use Committee. Mice were group-housed in IVCs under SPF conditions, with constant temperature and humidity with lighting on a fixed light/dark cycle (12-hours/12-hours). Human tumor xenograft studies were conducted in male NSG mice (30 to 35 g body weight, 6-8 weeks old) housed under animal biocontainment level 2 (JAX Laboratories). 5 million H1299 or PC3 cells were diluted in 25 µL

of PBS and added to 25 µL of Matrigel. The 50 µL cell suspension is injected subcutaneously into the right flank of NSG mice and allowed to grow until tumors are 25mm3 (H1299) or 150mm3 (PC3) before treatment is started. FAST-PLVs delivered via intravenous injection occurred via the lateral tail vein with a max volume of 200 µL. For intratumoral injection, mice were anaesthetized with isoflurane and a 31-gauge syringe is inserted near the bottom of the tumor until it is roughly in the middle of the tumor. 50 µL of FAST-PLVs are slowly injected while gently moving the syringe within the tumor. Once all the test article is injected, the syringe is held in place for 30-60 seconds before being slowly removed. RAPA is dissolved in 5%PEG400/5%Tween-80 (in $H_2O$) to give an amount equivalent to 0.1 mg/kg per 100µL and is administered via intraperitoneal injection. Mice are sacrificed via CO2 asphyxiation with cervical dislocation to confirm euthanasia. B16F10 studies were conducted using female C57BL/6j mice (JAX Laboratories) 6–8-weeks-old and 20 to 30 g body weight. Animals were injected intravenously with 100,000 B16F10 cells diluted in 100 µL PBS. The next day treatment was initiated, with FAST-PLVs being injected intravenously. 24 hours after FAST-PLV injection, RAPA and α-CTLA4 were injected via intraperitoneal injection, and 24 hours after that RAPA was administered again. Treatment cycle was repeated once a week for 3 weeks before animals are sacrificed via $CO_2$ asphyxiation. Lungs were bleached using Fekete's solution overnight (580mL 95% Ethanol, 200mL H2O, 80mL 37% Formaldehyde, 40mL Glacial acetic acid).

*Whole Body and Ex Vivo Bioluminescence*

At indicated time points after the injection of the FAST-PLVs, mice were injected intraperitoneally with 0.25 mL D-luciferin (30 mg/mL in PBS) and allowed to recover for 5 minutes. The mice were then anesthetized in a ventilated anesthesia chamber with 2% isoflurane in oxygen and imaged ~10 min after D-luciferin injection with an *in vivo* imaging system (In Vivo Xtreme, Bruker,

Montreal, Canada). All images are taken with a non-injected control mouse to serve as a reference point to determine the lower threshold of each image. Grouped experiments are presented with the upper threshold being held consistent between time points; however, the lower threshold is set based on the signal of the non-injected control mouse at the point when it no longer shows any signal. For *ex vivo* images, major organs were paired with those from a non-injected control mouse. 30 mg/ml D-Luciferin was mixed at a 1:1 ratio with the *in vitro* 150µg/mL D-Luciferin described above and added to the organs immediately before imaging. Non-injected control mouse organs were included with each set as a reference point to determine the lower threshold.

*Histology*

Lungs and tumors were formalin fixed, and paraffin embedded. 4-6 µm sections were generated. Sections were dewaxed in xylene and rehydrated using graded ethanol to water washes. Sections were stained in Harris Modified Hematoxylin (SH30-4D, Fisher Chemical) for 8 minutes, briefly differentiated in acid alcohol and blued with Scott's Tap Water (pH 8). Slides were then stained in acidified eosin for 30 seconds and dehydrated, cleared, and then mounted.

*TUNEL Staining Tumor Sections*

Tumor sections were stained following manufactures recommended guidelines (Abcam, Cat# ab66110). Briefly, sections were dewaxed in xylene and rehydrated using graded ethanol to water washes. Antigen retrieval done using 20µg/mL Proteinase K solution (2 µL Proteinase K 10 mg/mL + 998 µL Tris-HCl pH 8.0 + 50 mM EDTA) for 5 minutes at room temperature and then cells are fixed in 4% formaldehyde. Sections are labeled with Br-dUTP for one hour at 37˚C, following which, the anti-BrdU-Red secondary antibody is added. Nuclei are labeled with Hoechst 33342 and immediately imaged on the Nikon A1r MP microscope.

*Flow Cytometry for Immune Phenotyping and B16F10 Killing*

Spleen were isolated and dispersed into single-cell suspensions using mechanical dispersion and filtered through a 70 μm wire mesh. Red blood cells were lysed using ammonium chloride buffer, followed by a wash with PBS with 2% FBS/PBS. Splenocytes were co-cultured at a 5:1 ratio with B16F10 cells for 18hrs at 37°C, 5% CO2 in Dulbecco's Modified Eagle's Medium (DMEM) (Corning, Cat# 10-013-CV) supplemented with 10% fetal bovine serum (Gibco, Cat# 12484028), 100 units/mL of Penicillin (Hyclone, Cat# 16777-164), 100μg/mL of Streptomycin (Hyclone, Cat# 16777-164), and 10 ng/ml of both IL-2 and IL-4. Splenocytes and B16F10 cells were lifted and stained with Zombie-UV as described above. CD45 was added to improve gating. For immune phenotyping experiments, splenocytes were stained with the following antibodies all purchased from Biolegend: Brilliant Violet 421 CD25 (Clone PC61, Cat# 102043), Alexa Fluor 488 CD3 (Clone 17A2, Cat# 100212), APC-Fire 750 CD4 (Clone RM4-4, Cat# 116019), Brilliant Violet 510 CD44 (Clone IM7, Cat# 103043), APC CD45 (Clone 30-F11, Cat# 103112), PE-Cy7 CD8α (Clone 53-6.7, Cat# 100721), PE FoxP3 (Clone MF-14, Cat# 126403). Zombie-UV was used to identify live splenocytes.

*Statistical analysis*

A two-tailed Student's *t*-test or a one-way analysis of variance (ANOVA) was performed when comparing two groups or more than two groups, respectively. Statistical analysis was performed using Microsoft Excel and Prism 7.0 (GraphPad). Data are expressed as means ± s.d. The difference was considered significant if $P < 0.05$ ($*P < 0.05$, $**P < 0.01$, $***P < 0.001$, $****P < 0.0001$ unless otherwise indicated).

**Acknowledgments**

This research was supported by an operating grant to John D. Lewis from the Canadian Institutes of Health Research (CIHR), in partnership with the Institute of Aging: Research Nova Scotia, reference number VR1-172710. Dr. Lewis holds the Frank and Carla Sojonky Chair in Prostate Cancer Research funded by the Alberta Cancer Foundation. Roy Duncan's laboratory was funded by the CIHR and the Natural Sciences and Engineering Research Council of Canada (NSERC). Douglas W. Brown was funded by fellowships from Prostate Cancer Canada and Mitacs. We thank Abul Kalam Azad for isolating and sub-culturing HUVEC and Katia Carmine-Simmen for her technical support.

**Author Contributions**

DWB, AR, and JDL designed the study. RD developed the FAST protein. AR, PW, PB, MP, HV, LG, JG and PSA optimized the PLV system. PB performed DNA cloning. DWB performed in vitro work. DWB, DS, MH, and SL performed the mice studies. DWB, AR, and JDL wrote the manuscript with input from all authors.

**Table 4.1. P53 promoter activity and p53 transcript levels in multiple cancer and normal cell lines**

| Cell Line | Type | p53 Status | p53 Transcript Level (TCM) | p53 Promoter (RLU) |
|---|---|---|---|---|
| **NCI-H1299** | Lung Large Cell Carcinoma | Deletion - Homozygous | 4.651 | 62861 ± 35481 |
| **PC-3** | Prostate Adenocarcinoma | Deletion - Frameshift | 1.782 | 15455 ± 6633 |
| **C-33A** | Cervical Carcinoma | Mutant - R273C | 5.583 | 15191 ± 1275 |
| **HT1080** | Fibrosarcoma | Wild Type | 5.353 | 10383 ± 2154 |
| **NCI-H661** | Lung Large Cell Carcinoma | Mutant - R158L, S215I | 5.675 | 8267 ± 404 |
| **KATO III** | Gastric Adenocarcinoma | Deletion - Homozygous | 0.422 | 7696 ± 565 |
| **A2058** | Malignant Melanoma | Mutant - V274F | 6.010 | 7243 ± 2047 |
| **DMS-114** | Lung Small Cell Carcinoma | Truncation - R213* | 3.400 | 6000 ± 300 |
| **U-87MG** | Glioblastoma | Wild Type | 4.093 | 5529 ± 1457 |
| **HCT116** | Colon Adenocarcinoma | Wild Type | 5.256 | 5115 ± 1206 |
| **SW480** | Colon Adenocarcinoma | Mutant - R273H, P309S | 5.293 | 4783 ± 2517 |
| **MCF-7** | Breat Adenocarcinoma | Wild Type | 6.637 | 4064 ± 1291 |
| **SW620** | Colon Adenocarcinoma | Mutant - R273H | 6.111 | 3645 ± 1297 |
| **SW1353** | Chondrosarcoma | Mutant - V203L | 5.183 | 3521 ± 860 |
| **NCI-H1693** | Non-Small Cell Lung Adenocarcinoma | Deletion - Splice Mutation | 4.180 | 3284 ± 819 |
| **LNCaP** | Prostate Carcinoma | Silent Mutation - P152P | 6.355 | 2904 ± 1339 |
| **SW-13** | Adrenal Carcinoma | Mutant - H193Y | 5.047 | 2701 ± 230 |
| **LN-229** | Glioblastoma | Mutant - K164G | 5.590 | 2476 ± 399 |
| **MDA-MB-231** | Breast Adenocarcinoma | Mutant - R280K | 5.583 | 2471 ± 221 |
| **Hep3B** | Hepatocellular Carcinoma | Deletion | 4.578 | 2258 ± 926 |
| **A549** | Non-Small Cell Lung Carcinoma | Wild Type | 5.295 | 1595 ± 251 |
| **G-402** | Renal Leiomyoblastoma | Wild Type | 5.740 | 1530 ± 219 |
| **KM12** | Colon Adenocarcinoma | Deletion - Frameshift | 4.971 | 1223 ± 27 |
| **NCI-H2110** | Non-Small Cell Lung Carcinoma | Mutant - R158P | 6.090 | 1033 ± 80 |
| **OVCAR-8** | Ovarian Adenocarcinoma | Deletion - Splice Mutation | 5.876 | 854 ± 360 |
| **T47D** | Breast Ductal Carcinoma | Mutant - L194F | 5.827 | 851 ± 169 |
| **MDA-MB-468** | Breast Adenocarcinoma | Mutant - R273H | 6.754 | 809 ± 490 |
| **DU-145** | Prostate Adenocarcinoma | Mutant - P223L, V274F | N/A | 696 ± 60 |
| **MDA-MB-436** | Breat Adenocarcinoma | Deletion - Frameshift | 5.116 | 619 ± 95 |
| **U-118-MG** | Glioblastoma | Mutant - R213Q | 5.224 | 274 ± 96 |
| **IMR90** | Normal Fibroblast | Wild Type | N/A | 161 ± 12 |
| **HUVEC** | Umbillical Vein Endothelial Cells | Wild Type | N/A | 80 ± 40 |
| **WI38** | Normal Fibroblast | Wild Type | N/A | 26 ± 9 |

## 4.5. Figures

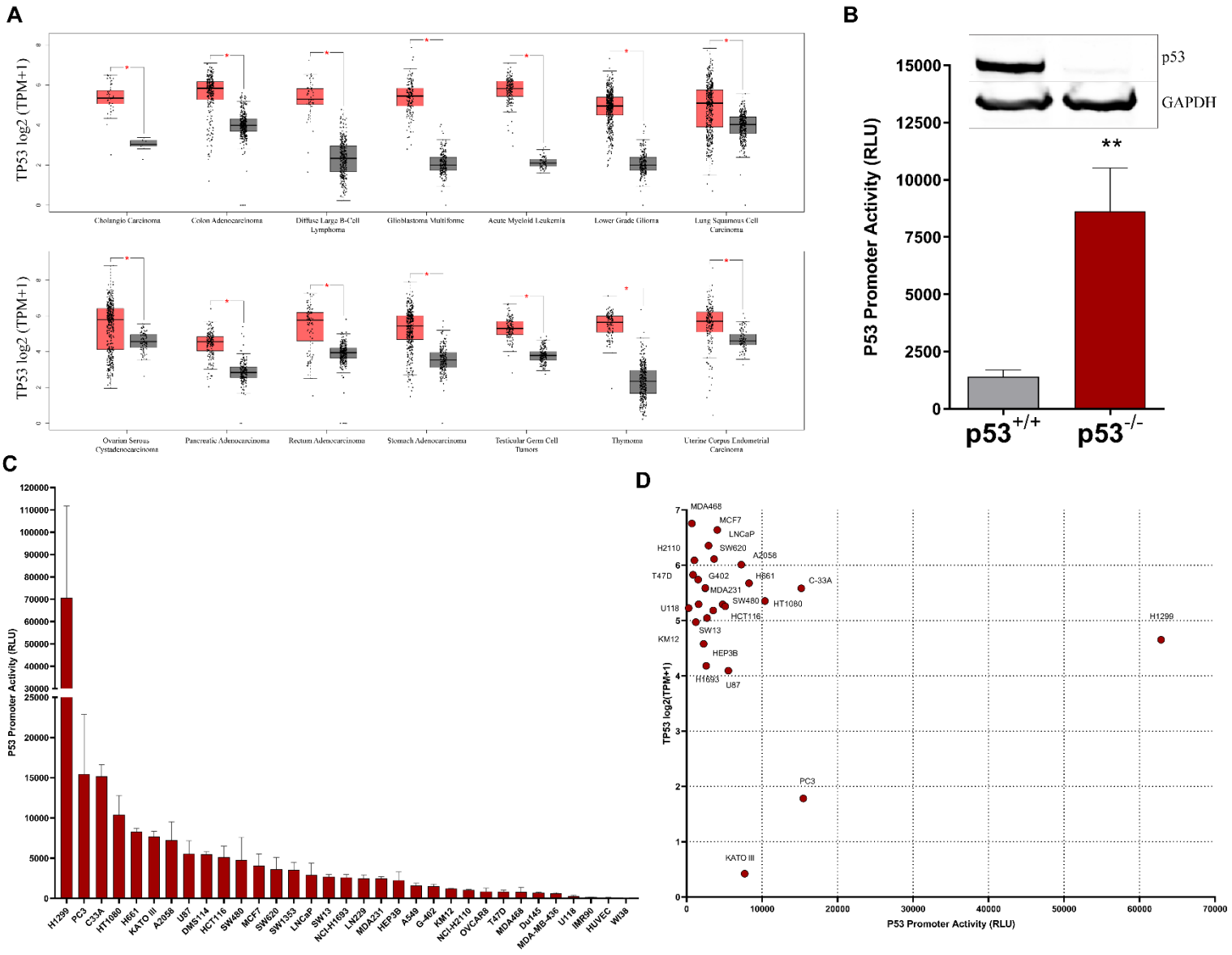


**Figure 4.1 – P53 transcription and promoter activity is upregulated in cancer cells.**

(A) Gene Expression Profiling Interactive Analysis (GEPIA) database was utilized to compare p53 transcript levels in cancerous tissue (red) and its corresponding normal tissue counterpart (grey). The remaining cancer subtypes are presented in Supplementary Figure 1.

(B) Luminescence of a p53 promoter reporter construct 72 hours after transfection into HCT-116 $p53^{+/+}$ or HCT-116 $p53^{-/-}$ cells

(C) Luminescence of a p53 promoter reporter construct 72 hours after transfection into multiple normal and cancer cell lines.

(D) P53 transcript level as a function of p53 promoter activity showing no correlation between the two variables.

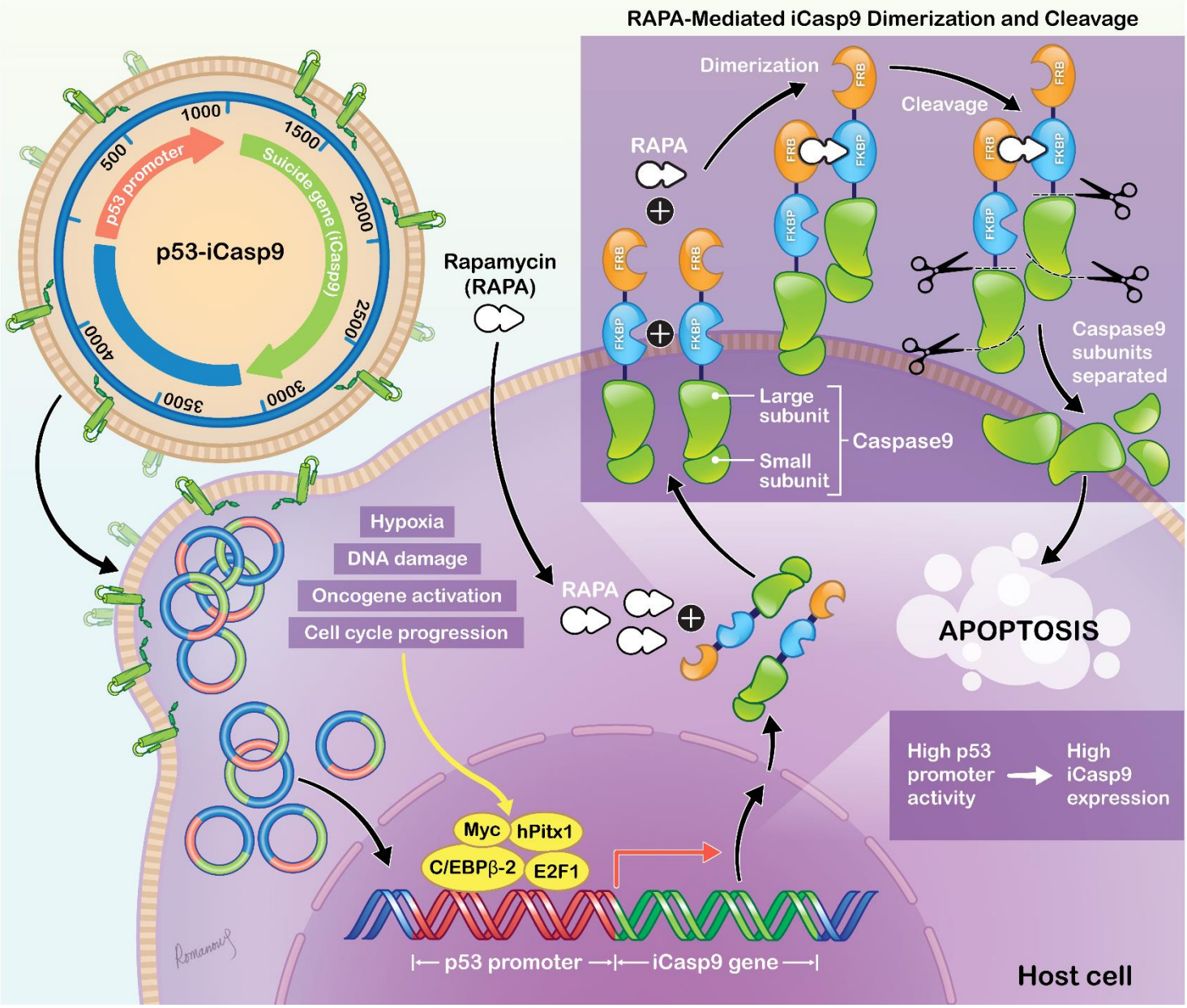


**Figure 4.2 – Mechanism of action for the p53 promoter driven suicide gene construct.** The p53-iCasp9 pDNA construct is encapsulated within Fusogenix FAST-PLVs. The FAST protein facilitates fusion between the PLV membrane and the target cancer cell membrane, resulting in delivery of the encapsulated p53-iCasp9 construct directly into the cytosol. The p53-iCasp9 is translocated to the nucleus, where transcription factors activated by tumorigenic pathways can bind to the p53 promoter and stimulate iCasp9 transcription. Addition of the CID, RAPA, enables two iCasp9 molecules to be dimerized and undergo proximity-induced cleavage and activation, generating active caspase 9 fragments that can stimulate apoptosis induction. Cells with higher p53 promoter activity (cancer cells) will produce higher amounts of iCasp9, leading to robust apoptosis induction. Normal cells with low p53 promoter activity will not produce enough iCasp9 to facilitate apoptosis induction.

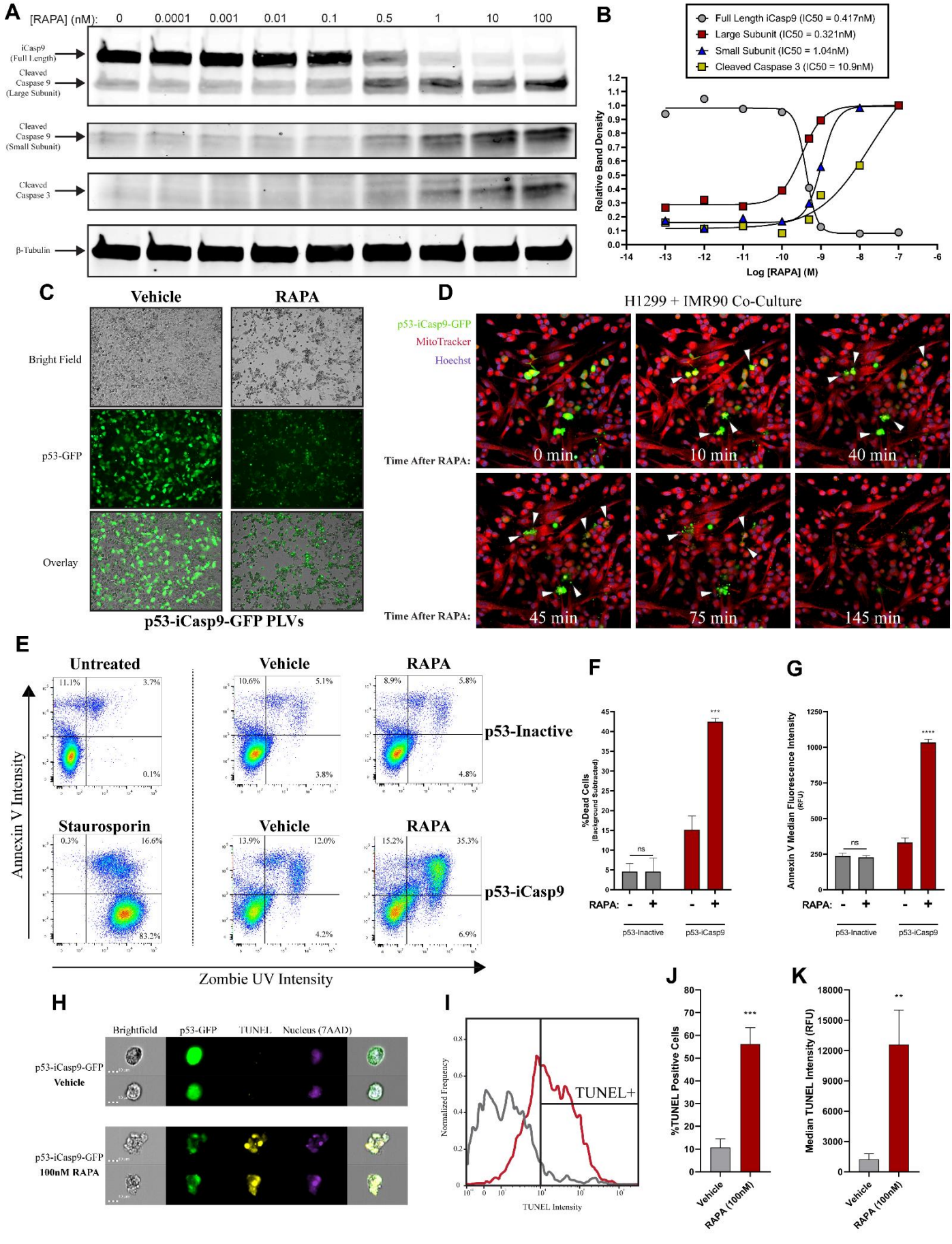
A
[RAPA] (nM): 0 0.0001 0.001 0.01 0.1 0.5 1 10 100
iCasp9 (Full Length)
Cleaved Caspase 9 (Large Subunit)
Cleaved Caspase 9 (Small Subunit)
Cleaved Caspase 3
β-Tubulin
B
Full Length iCasp9 (IC50 = 0.417nM)
Large Subunit (IC50 = 0.321nM)
Small Subunit (IC50 = 1.04nM)
Cleaved Caspase 3 (IC50 = 10.9nM)
Relative Band Density
Log [RAPA] (M)
C
Vehicle
RAPA
Bright Field
p53-GFP
Overlay
p53-iCasp9-GFP PLVs
D
H1299 + IMR90 Co-Culture
p53-iCasp9-GFP
MitoTracker
Hoechst
Time After RAPA:
0 min
10 min
40 min
45 min
75 min
145 min
E
Untreated
Vehicle
RAPA
Staurosporin
p53-Inactive
p53-iCasp9
Annexin V Intensity
Zombie UV Intensity
F
%Dead Cells (Background Subtracted)
RAPA:
p53-Inactive
p53-iCasp9
G
Annexin V Median Fluorescence Intensity (RFU)
H
Brightfield
p53-GFP
TUNEL
Nucleus (7AAD)
p53-iCasp9-GFP Vehicle
p53-iCasp9-GFP 100nM RAPA
I
TUNEL+
Normalized Frequency
TUNEL Intensity
J
%TUNEL Positive Cells
Vehicle
RAPA (100nM)
K
Median TUNEL Intensity (RFU)
Vehicle
RAPA (100nM)

**Figure 4.3 – In vitro expression of the p53-iCasp9 construct leads to robust apoptosis induction.**

(A) Western blot of H1299 cells following addition of PLVs encapsulating p53-iCasp9. 48 hours after p53-iCasp9 addition, increasing concentrations of RAPA was added for 2 hours.

(B) Densiometric analysis of the full length iCasp9, cleaved caspase 9 (large and small subunit), and cleaved caspase 3 bands. All values normalized to β-Tubulin, with the highest band intensity being set as '1.0.'

(C) Bright field and fluorescent images H1299 48 hours after p53-iCasp9 transfection with 100nM RAPA added for the final 12 hours before image collection.

(D) H1299 cells were co-cultured with normal human IMR-90 fibroblasts and had PLVs encapsulating p53-iCasp9-GFP added for 48 hours. Cells are counterstained with MitoTracker Red and Hoechst 33342. 100nM RAPA was added to cells and they were immediately imaged under a Nikon A1r MP confocal microscope every 5 minutes to track apoptosis induction

(E) Annexin V/Zombie UV flow cytometry on H1299 cells transfected with p53-iCasp9 or p53-inactive for 48 hours, with 100nM RAPA being added for the final 12 hours of transfection. Untreated H1299 cells and H1299 cells exposed to 1μM staurosporin for 12 hours included as controls

(F) Percentage dead cells based on Annexin V/Zombie UV staining. The early apoptosis (Annexin V+, Zombie–), late apoptosis (Annexin V+, Zombie+), and dead/necrotic (Annexin V–, Zombie+) cell populations were added together to give an indication of total cell death induced by treatment. Values obtained by untreated H1299 cells are subtracted from each treatment to normalize for background staining. Unpaired t-test, ***P<0.001.

(G) Median Annexin V intensity of treated cells. Unpaired t-test, ****P<0.001.

(H) Representative imaging cytometry images on TUNEL stained H1299 cells following 48-hour transfection with p53-iCasp9-GFP with 100nM RAPA being added for the final 12 hours.

(I) Histogram of TUNEL intensity in p53-iCasp9-GFP transfected H1299 cells treated with vehicle (grey) or 100nM RAPA (red).

(J) Percentage of TUNEL positive H1299 cells transfected with p53-iCasp9-GFP treated with vehicle (grey) or 100nM RAPA (red). Unpaired t-test, ***P<0.001.

(K) Median TUNEL intensity of vehicle and RAPA treated H1299 cells transfected with p53-iCasp9-GFP. Unpaired t-test, **P<0.01.

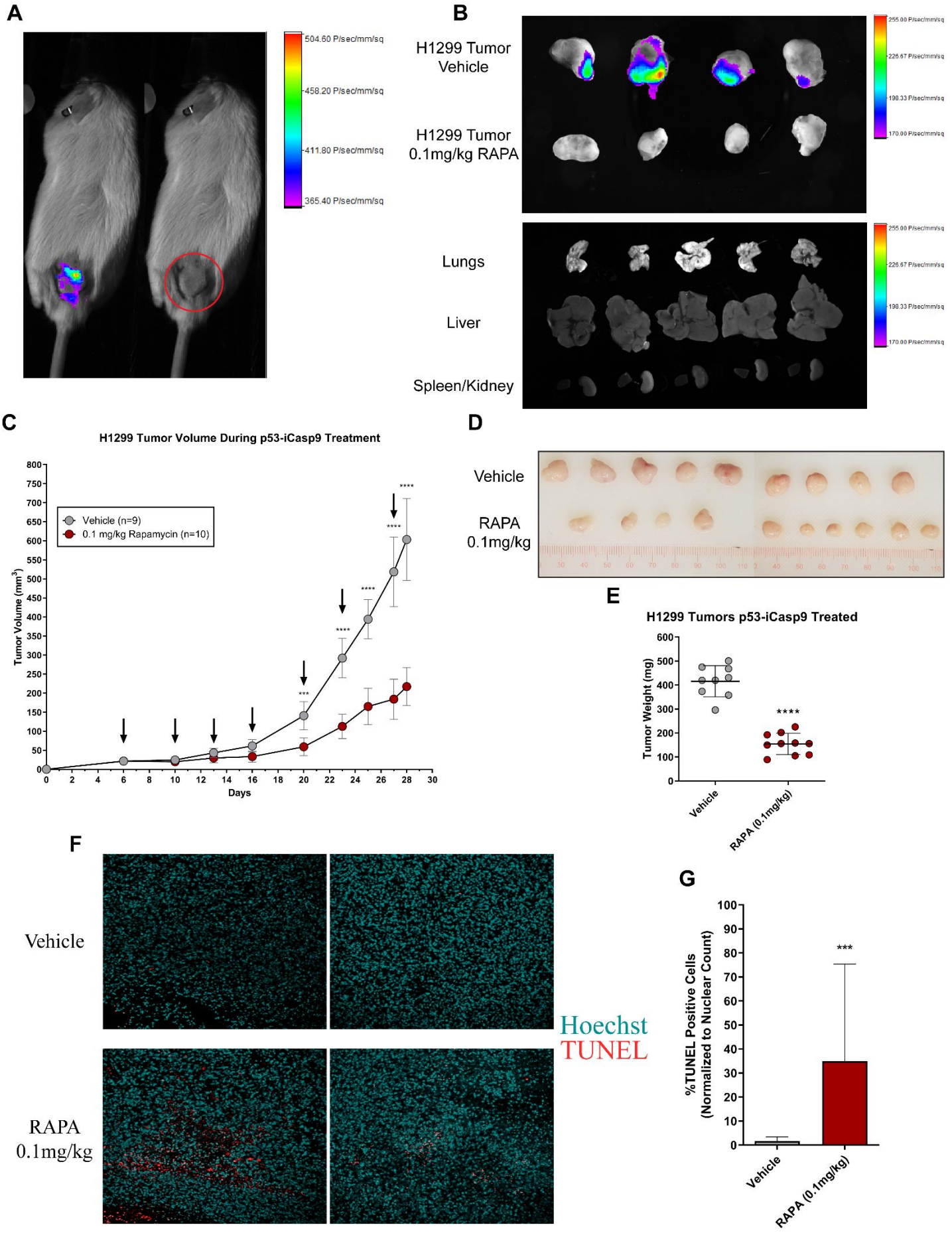
A
504.60 P/sec/mm/sq
458.20 P/sec/mm/sq
411.80 P/sec/mm/sq
365.40 P/sec/mm/sq
B
H1299 Tumor
Vehicle
H1299 Tumor
0.1mg/kg RAPA
255.00 P/sec/mm/sq
226.67 P/sec/mm/sq
198.33 P/sec/mm/sq
170.00 P/sec/mm/sq
Lungs
Liver
Spleen/Kidney
C
H1299 Tumor Volume During p53-iCasp9 Treatment
Vehicle (n=9)
0.1 mg/kg Rapamycin (n=10)
Tumor Volume (mm3)
Days
D
Vehicle
RAPA
0.1mg/kg
E
H1299 Tumors p53-iCasp9 Treated
Tumor Weight (mg)
Vehicle
RAPA (0.1mg/kg)
F
Vehicle
RAPA
0.1mg/kg
Hoechst
TUNEL
G
%TUNEL Positive Cells
(Normalized to Nuclear Count)
Vehicle
RAPA (0.1mg/kg)

**Figure 4.4 – Systemic administration of the p53-iCasp9 vector encapsulated within PLVs leads to tumor selective expression and attenuation of H1299 tumor growth.**

(A) H1299 tumor bearing mice were injected intravenously with 6 mg/kg p53-iCasp9-FLuc encapsulated within PLVs and whole-body luminescence was measured indicated tumor localized signal

(B) Ex vivo imaging organ imaging of vehicle and RAPA treated mice 24 hours after systemic p53-iCasp9-FLuc administration.

(C) Effect of systemic treatment on H1299 tumor growth. H1299 tumor bearing mice were injected IV with PLVs encapsulating 6 mg/kg p53-iCasp9 twice a week for three weeks (indicated by black arrows), with vehicle or 0.1 mg/kg RAPA being administer 24 and 48 hours after PLV injection. Two-way ANOVA and Sidak's multiple comparisons test, ***P<0.001, ****P<0.0001.

(D) Size comparison of excised H1299 tumors from p53-iCasp9 treated mice that were administered vehicle of RAPA.

(E) Weight of excised H1299 tumors from vehicle of RAPA treated mice. Unpaired t-test, ****P<0.0001.

(F) Representative TUNEL stained H1299 sections isolated from p53-iCasp9 treated mice that were administered vehicle or RAPA. Nuclei are stained blue with Hoechst and TUNEL positive spots are stained red.

(G) TUNEL positive cells in H1299 sections isolated from p53-iCasp9 treated mice that were administered vehicle or RAPA. Unpaired t-test, ***P<0.001.

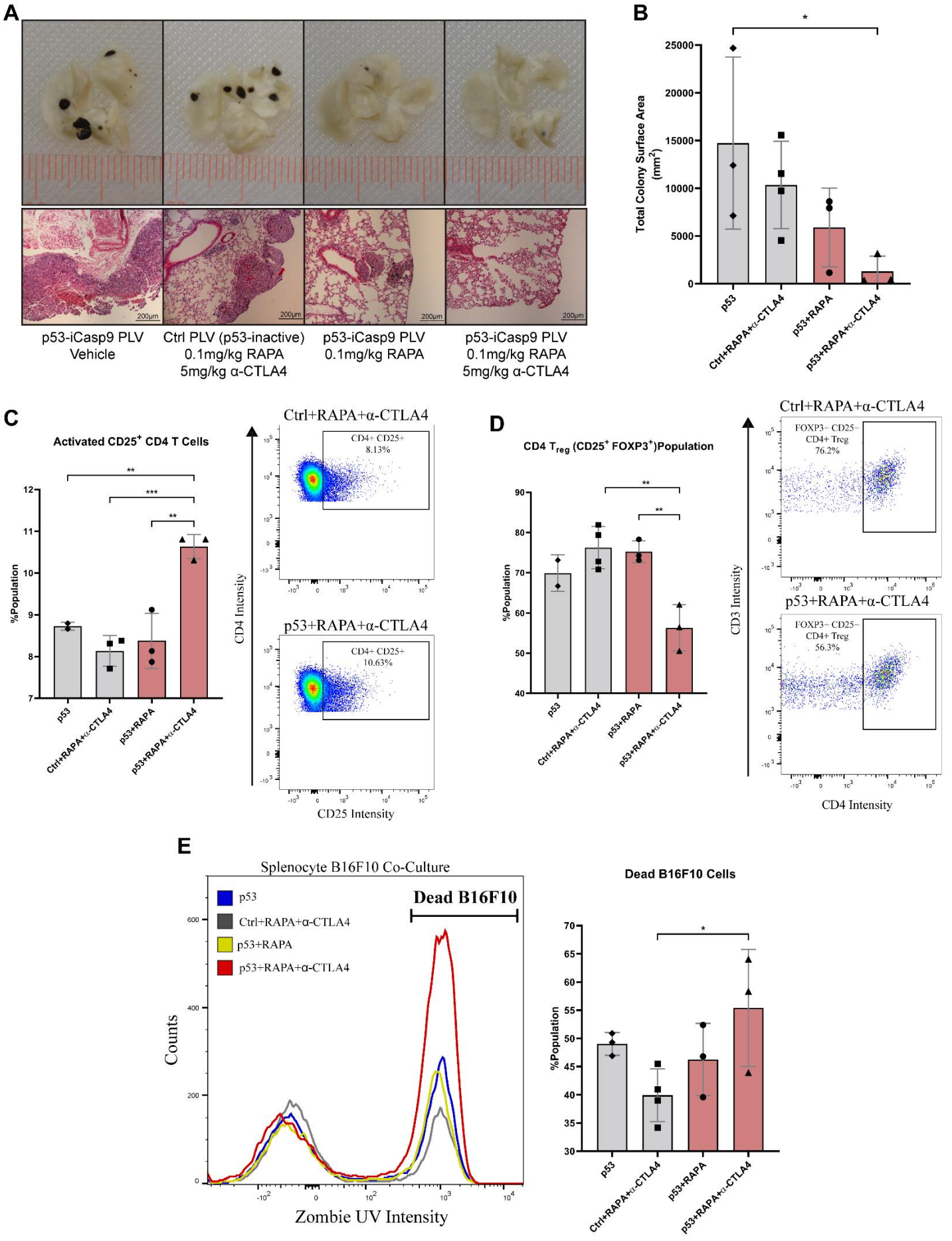
A
p53-iCasp9 PLV
Vehicle
Ctrl PLV (p53-inactive)
0.1mg/kg RAPA
5mg/kg α-CTLA4
p53-iCasp9 PLV
0.1mg/kg RAPA
p53-iCasp9 PLV
0.1mg/kg RAPA
5mg/kg α-CTLA4
200μm
B
Total Colony Surface Area (mm²)
p53
Ctrl+RAPA+α-CTLA4
p53+RAPA
p53+RAPA+α-CTLA4
C
Activated CD25⁺ CD4 T Cells
%Population
Ctrl+RAPA+α-CTLA4
CD4+ CD25+
8.13%
p53+RAPA+α-CTLA4
CD4+ CD25+
10.63%
CD4 Intensity
CD25 Intensity
D
CD4 Treg (CD25⁺ FOXP3⁺)Population
%Population
Ctrl+RAPA+α-CTLA4
FOXP3− CD25−
CD4+ Treg
76.2%
p53+RAPA+α-CTLA4
FOXP3− CD25−
CD4+ Treg
56.3%
CD3 Intensity
CD4 Intensity
E
Splenocyte B16F10 Co-Culture
p53
Ctrl+RAPA+α-CTLA4
p53+RAPA
p53+RAPA+α-CTLA4
Dead B16F10
Counts
Zombie UV Intensity
Dead B16F10 Cells
%Population

**Figure 4.5 – Combining systemic p53-iCasp9 treatment with α-CTLA4 immune checkpoint inhibitor reduces metastatic burden of B16F10 tumor bearing mice.**

(A) Representative whole bleached lung and H&E-stained lung sections isolated from treated and control animals with disseminated B16F10 tumors.

(B) Total metastatic colony surface area was calculated by adding the surface area occupied by all B16F10 colonies for each mouse. One-way ANOVA and Dunnett's multiple comparisons test, *P<0.05.

(C) Activation of CD4+ T lymphocytes was determined via flow cytometry analysis on the CD25+ population in freshly isolated splenocytes. One-way ANOVA and Tukey's multiple comparisons test, **P<0.01, ***P<0.001.

(D) CD4 $T_{reg}$ population was determined via flow cytometry analysis on freshly isolated splenocytes. The FOXP3+ CD25+ population was gated on the $CD45^{+}$ CD3+ population. The CD4+ CD3+ (CD4 Treg) was then determined on this FOXP3+ CD25+ population. One-way ANOVA and Tukey's multiple comparisons test, **P<0.01.

(E) Splenocytes isolated from treated and control animals were co-cultured with B16F10 cells for 24 hours, following which, Zombie UV staining was done to identify dead cells. CD45- B16F10 cells are gated on FSC vs SSC as they form a distinct population separate from splenocytes. One-way ANOVA and Tukey's multiple comparisons test, *P<0.05.

# 4.6. Supplementary Material

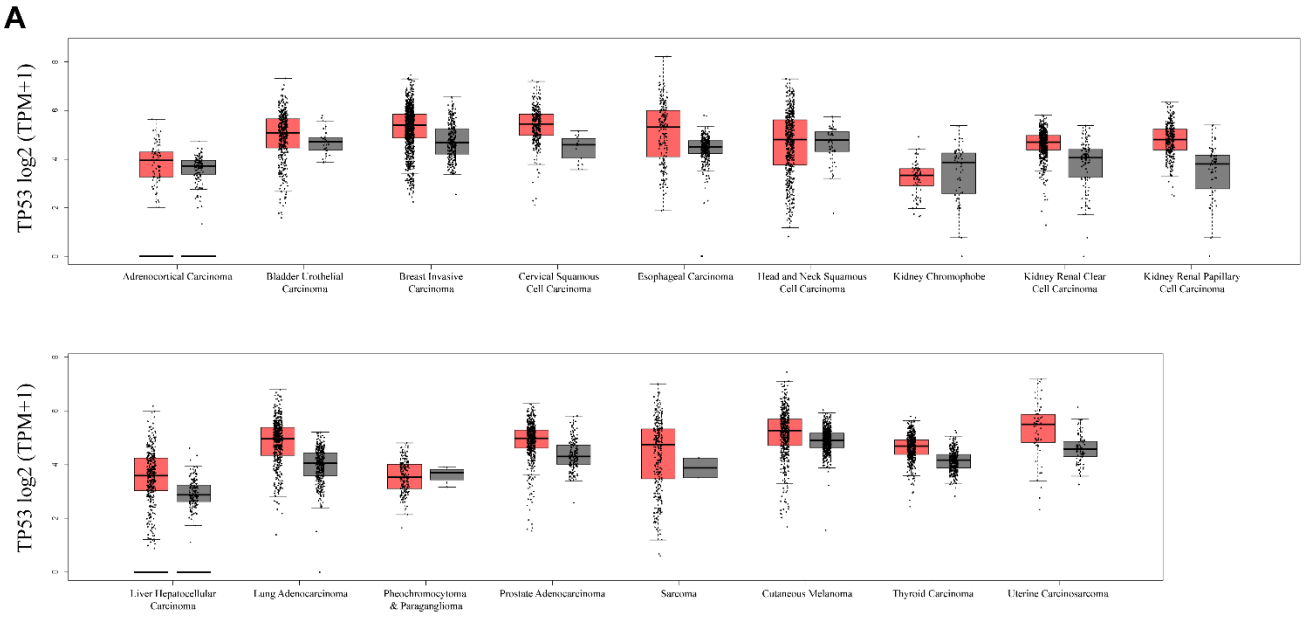


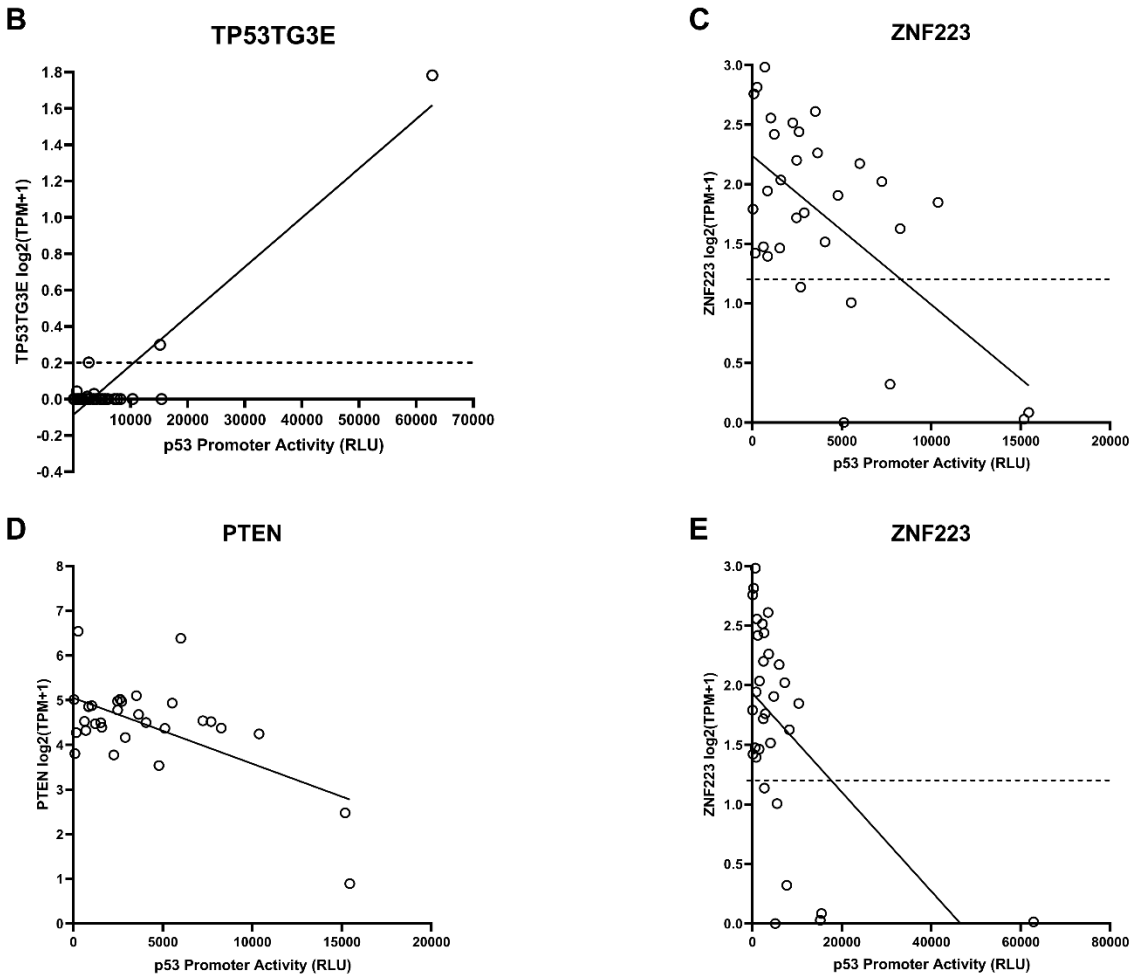

**Supplementary Figure 4.1 – P53 promoter activity is predicted by TP53TG3E and ZNF223 expression.**

(A) Remaining cancer subtypes from the Gene Expression Profiling Interactive Analysis (GEPIA) on p53 transcription
(B) TP53TG3E expression as a function of p53 promoter activity
(C) ZNF223 expression as a function of p53 promoter activity (H1299 removed from analysis)
(D) PTEN expression as a function of p53 promoter activity (H1299 removed from analysis)
(E) ZNF223 expression as a function of p53 promoter activity with H1299 included in analysis

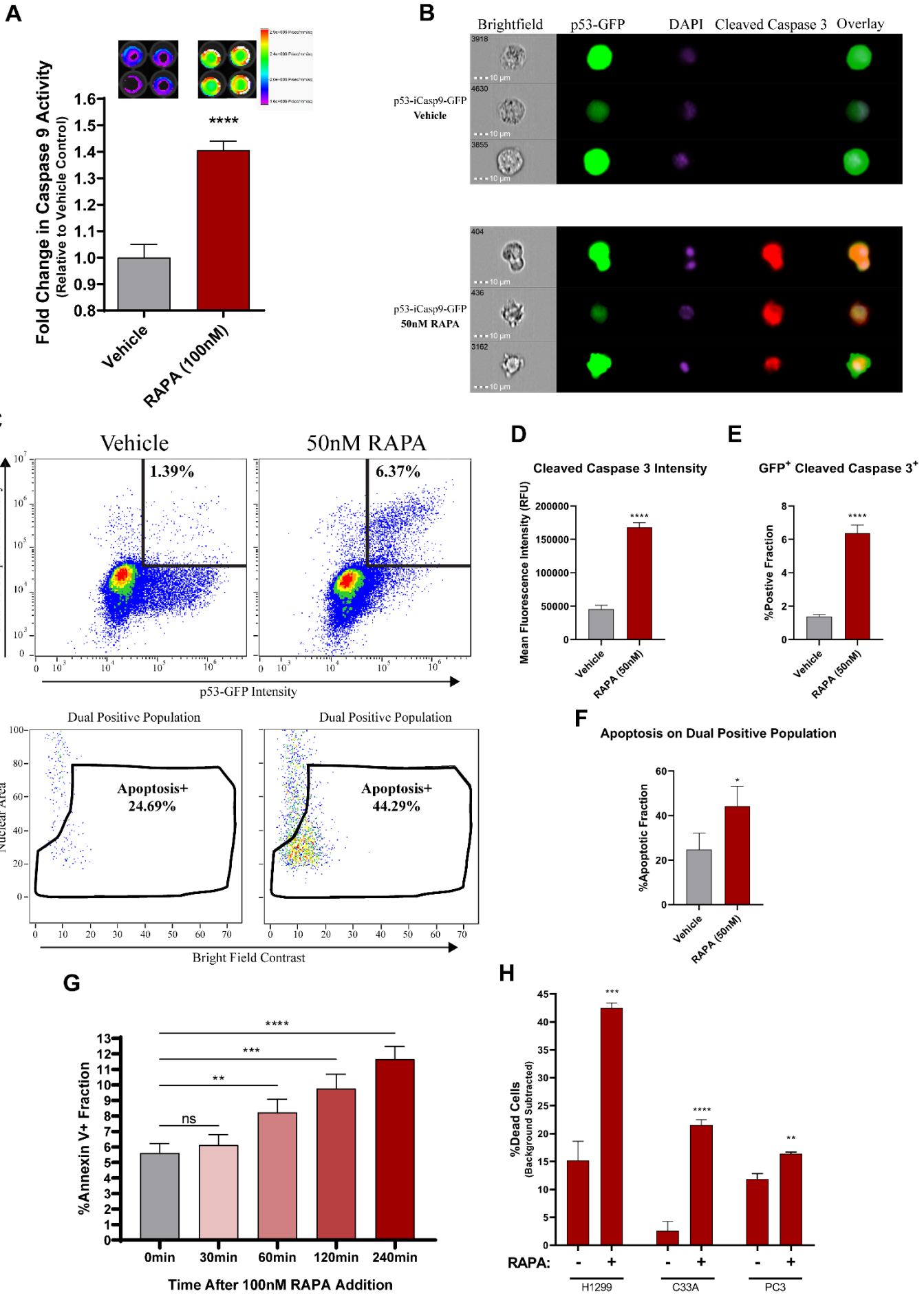
A
Fold Change in Caspase 9 Activity
(Relative to Vehicle Control)
****
Vehicle
RAPA (100nM)
B
Brightfield
p53-GFP
DAPI
Cleaved Caspase 3
Overlay
p53-iCasp9-GFP
Vehicle
p53-iCasp9-GFP
50nM RAPA
C
Vehicle
50nM RAPA
1.39%
6.37%
Cleaved Caspase 3 Intensity
p53-GFP Intensity
Dual Positive Population
Dual Positive Population
Apoptosis+
24.69%
Apoptosis+
44.29%
Nuclear Area
Bright Field Contrast
D
Cleaved Caspase 3 Intensity
Mean Fluorescence Intensity (RFU)
Vehicle
RAPA (50nM)
E
GFP+ Cleaved Caspase 3+
%Postive Fraction
F
Apoptosis on Dual Positive Population
%Apoptotic Fraction
G
%Annexin V+ Fraction
ns
0min
30min
60min
120min
240min
Time After 100nM RAPA Addition
H
%Dead Cells
(Background Subtracted)
RAPA:
H1299
C33A
PC3

**Supplementary Figure 4.2 – RAPA mediated cleavage of iCasp9 leads to apoptosis induction in transfected cells.**

(A) LEHD caspase 9 cleavage assay in BPH-1 cells transfected with p53-iCasp9 for 48 hours, with 100nM RAPA being administered for 2 hours before assay is conducted. Unpaired t-test, ****P<0.0001.

(B) Representative imaging cytometry images on cleaved caspase 3 stained H1299 cells following 48-hour transfection with p53-iCasp9-GFP with 50nM RAPA being added for the final 4 hours.

(C) P53-GFP Intensity vs Cleaved Caspase 3 intensity plots with gating drawn on the dual positive population. Imaging cytometry apoptosis wizard was done on the dual positive population, which estimates apoptosis induction on the basis of high bright field contrast (plasma membrane blebbing) and/or low nuclear area (nuclear fragmentation).

(D) Intensity of cleaved caspase 3 staining on the entire population of H1299 cells. Unpaired t-test, ****P<0.0001.

(E) Percentage of population positive for both p53-GFP and cleaved caspase 3. Unpaired t-test, ****P<0.0001.

(F) Imaging cytometry apoptosis wizard conducted on the p53-GFP and cleaved caspase 3 dual positive population. Unpaired t-test, *P<0.05.

(G) Precent of p53-iCasp9 transfected H1299 cells positive for Annexin V at indicated time points following 100nM RAPA administration. One-way ANOVA and Dunnett's multiple comparisons test, **P<0.01, ***P<0.001, ****P<0.0001.

(H) Percentage of total dead cells following Annexin V/Zombie UV flow cytometry conducted on H1299 (presented in Figure 4.3), C33A, and PC3. Percentage dead cells based on Annexin V/Zombie UV staining. The early apoptosis (Annexin V+, Zombie–), late apoptosis (Annexin V+, Zombie+), and dead/necrotic (Annexin V–, Zombie+) cell populations were added together to give an indication of total cell death induced by treatment. Values obtained by untreated cells are subtracted from each treatment to normalize for background staining. Unpaired t-test, **P<0.01, ***P<0.001, ****P<0.0001.

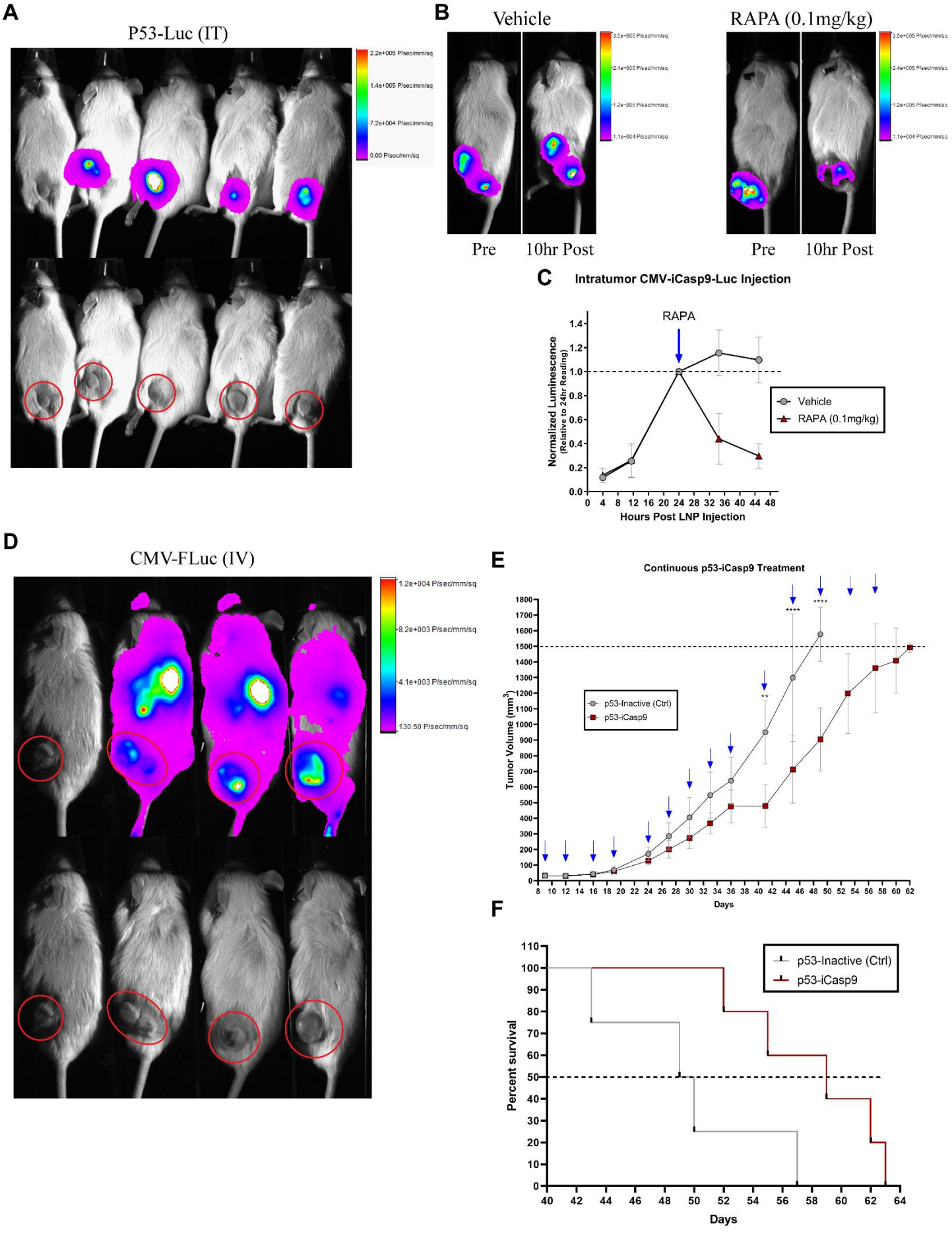
A
P53-Luc (IT)
2.2e+005 P/sec/mm/sq
1.4e+005 P/sec/mm/sq
7.2e+004 P/sec/mm/sq
0.00 P/sec/mm/sq
B
Vehicle
RAPA (0.1mg/kg)
Pre
10hr Post
Pre
10hr Post
C
Intratumor CMV-iCasp9-Luc Injection
RAPA
Normalized Luminescence (Relative to 24hr Reading)
Vehicle
RAPA (0.1mg/kg)
Hours Post LNP Injection
D
CMV-FLuc (IV)
1.2e+004 P/sec/mm/sq
8.2e+003 P/sec/mm/sq
4.1e+003 P/sec/mm/sq
130.50 P/sec/mm/sq
E
Continuous p53-iCasp9 Treatment
p53-Inactive (Ctrl)
p53-iCasp9
Tumor Volume (mm3)
Days
F
p53-Inactive (Ctrl)
p53-iCasp9
Percent survival
Days

**Supplementary Figure 4.3 – Characterization of PLV p53-iCasp9 expression kinetics *in vivo* and efficacy of continuous treatment.**

(A) H1299 tumor bearing mice are injected intratumorally with PLVs encapsulating 100µg of p53-iCasp9. Image taken 24 hours after injection.

(B) Intraperitoneal injection of 0.1 mg/kg RAPA is sufficient to facilitate dimerization of iCasp9 *in vivo*. H1299 tumor bearing mice are injected intratumorally with p53-iCasp9-FLuc, 24 hours after injection whole-body bioluminescence imaging is conducted and 0.1 mg/kg RAPA is administered via intraperitoneal injection. Whole-body bioluminescence imaging is conducted 10 hours after RAPA administration

(C) Quantification of tumor bioluminescence signal for 24 hours after RAPA administration

(D) Whole-body bioluminescence imaging following intravenous injection with PLVs encapsulating CMV-FLuc in H1299 tumor bearing mice

(E) H1299 tumor bearing mice were injected intravenously with PLVs encapsulating 3 mg/kg of either p53-iCasp9 or the control p53-inactive (catalytically inactive iCasp9) vector twice a week until tumors reached 1500mm$^3$, with 0.1 mg/kg RAPA being administered intraperitoneally 24 and 48 hours. Two-way ANOVA and Sidak's multiple comparisons test, **P<0.01, ****P<0.0001.

(F) Survival (time until endpoint of 1500mm$^3$ tumor volume) of H1299 tumor bearing mice treated with p53-iCasp9 or p53-inactive.

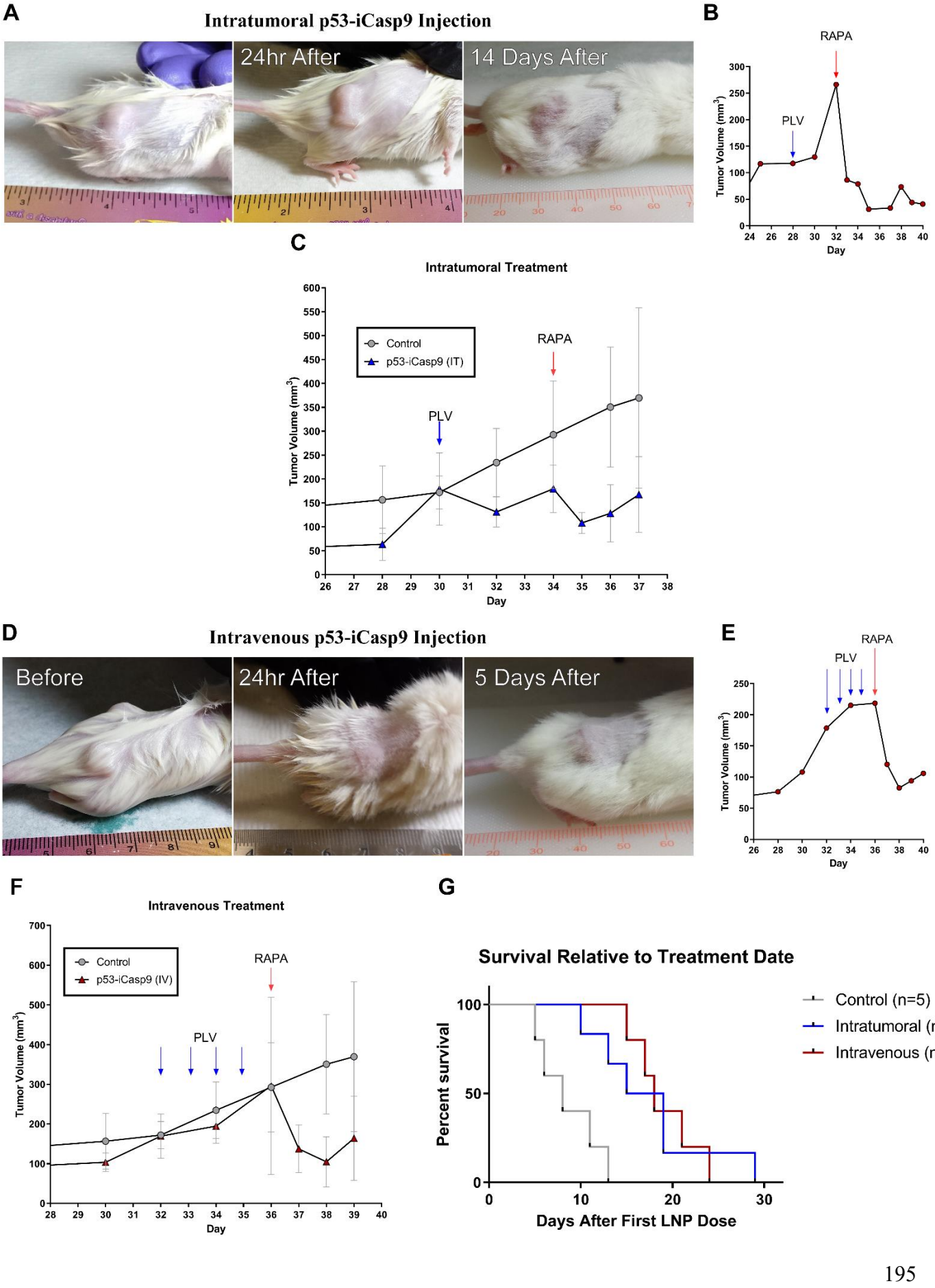
A
Intratumoral p53-iCasp9 Injection
24hr After
14 Days After
B
RAPA
PLV
Tumor Volume (mm3)
Day
C
Intratumoral Treatment
Control
p53-iCasp9 (IT)
RAPA
PLV
Tumor Volume (mm3)
Day
D
Intravenous p53-iCasp9 Injection
Before
24hr After
5 Days After
E
RAPA
PLV
Tumor Volume (mm3)
Day
F
Intravenous Treatment
Control
p53-iCasp9 (IV)
RAPA
PLV
Tumor Volume (mm3)
Day
G
Survival Relative to Treatment Date
Control (n=5)
Intratumoral (n=6)
Intravenous (n=5)
Percent survival
Days After First LNP Dose

**Supplementary Figure 4.4 – Control of subcutaneous PC3 tumor growth.**

(A) Representative images of PC3 tumor bearing mouse that received 100μg intratumoral injection of PLVs encapsulating p53-iCasp9, pre- and post-RAPA administration.
(B) Tumor volume overtime in a single mouse receiving intratumoral p53-iCasp9 injections
(C) Tumor volume overtime in the entire cohort of intratumorally injected mice.
(D) Representative images of PC3 tumor bearing mouse that received four daily intravenous injections of PLVs encapsulating 3 mg/kg p53-iCasp9, pre- and post-RAPA administration.
(E) Tumor volume overtime in a single mouse receiving intravenous p53-iCasp9 injections
(F) Tumor volume overtime in the entire cohort of intravenously injected mice
(G) Survival of PC3 tumor bearing mice treated intratumorally or intravenously with PLVs encapsulating p53-iCasp9, relative to untreated control mice.

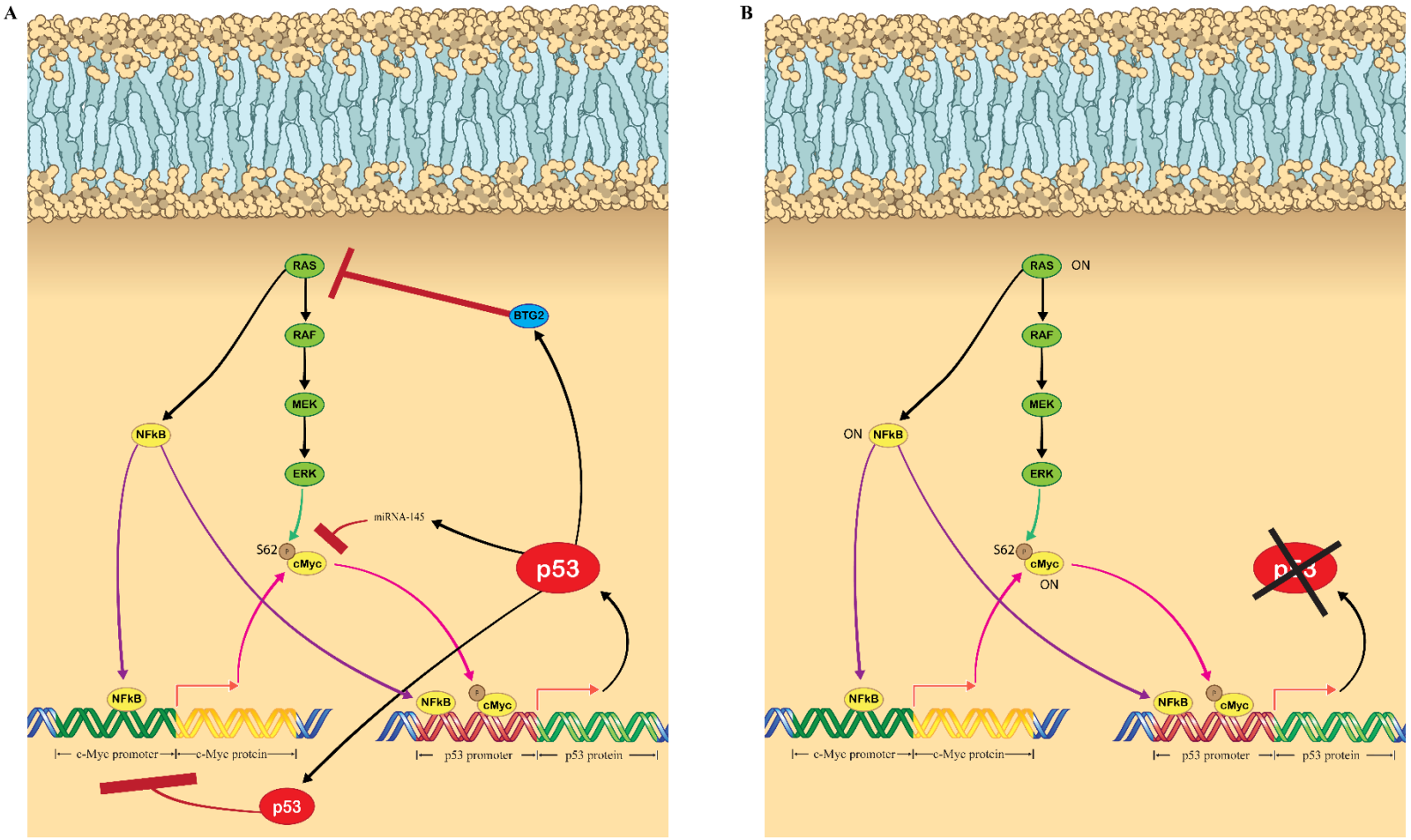


**Supplementary Figure 4.5 – Proposed mechanism for p53 promoter upregulation in cancer cells**

(A) Regulation of p53 expression in normal cells. RAS signaling leads to the activation of NF-κB as well as c-Myc, both of which directly bind to the p53 promoter and facilitate its expression. NF-kB also binds to the c-Myc promoter and induces its expression. P53 protein then regulates these pathways, by stimulating the production of BTG2 and miRNA-145, which inhibit RAS and c-Myc function, respectively. Additionally, p53 protein can directly repress the c-Myc transcription.

(B) Effect of p53 loss on promoter regulation. Loss of p53 function results in persistent RAS signaling through NF-κB and c-Myc, both of which will stimulate the p53 promoter. In cells with constitutively active RAS and c-Myc, this pathway may be active in the absence of p53 mutation/silencing.

# **Chapter 5:** Systemic Senolysis in Naturally Aged Mice using Fusogenix Proteolipid Vehicle Gene Therapy Approach

# Systemic Senolysis in Naturally Aged Mice using Fusogenix Proteolipid Vehicle Gene Therapy Approach

Douglas W. Brown[1], Arun Raturi[1,2], Prakash Bhandari[2], Ping Wee[2], Deborah Sosnowski[1], Liliya Grin[2], Manoj Parmar[2], Hector Vega[2], Maryam Hejazi[1], Jennifer Gyoba[2], Paola Solis Ares[2], Jitendra Kumar[2], Suellen Lamb[1], Jailal Ablack[3], Perrin H. Beatty[2], Henry Garcia[5], Gary Hudson[5], Matthew Scholz[5], Roy Duncan[2,4], Marco Demaria[6], and John D. Lewis[1,2,3,5,7]*

[1] Department of Oncology, University of Alberta, Edmonton, Alberta, Canada, T6G 2E1.
[2] Entos Pharmaceuticals, 10230 Jasper Avenue, Suite 4550, Edmonton, Alberta, Canada, T5J 4P6
[3] OncoSenX, 701 Fifth Ave, Suite 4200, Seattle, Washington 98104
[4] Department of Microbiology & Immunology, Dalhousie University, Halifax, Nova Scotia, Canada, B3H 4R2
[5] Oisin Biotechnologies, 701 Fifth Ave, Suite 4200, Seattle, Washington 98104
[6] European Research Institute for the Biology of Ageing (ERIBA), University Medical Center Groningen, Groningen, 9713 AV, the Netherlands
[7] Lead Contact: John D. Lewis.
*Correspondence to: John D. Lewis, University of Alberta, Katz Group Centre, 5-142, Edmonton, Canada. Phone: 780.492.6113, Email: jdlewis@ualberta.ca

Figures (4) and Tables (0)

In Brief:
We developed a novel DNA-based suicide gene therapy that requires upregulated p53 and/or p16 transcriptional activation to be expressed. This restricts suicide gene expression to cells undergoing senescence and offers a pharmacological method to achieve senolysis similar to the original transgenic models.

**Abstract**

Therapeutic approaches to eliminate senescent cells *in vivo* using transgenic mouse models have demonstrated significant improvements in lifespan, reduction of cancer and amelioration of age-related degeneration. Unfortunately, this approach requires that the organism be genetically engineered from the embryo and thus cannot be implemented in humans. Furthermore, previous studies have shown the need for repetitive dosing over the course of the organism's lifespan, which means that a gene delivery approach using viruses will be ineffective over time. To overcome these limitations, we developed a senolytic gene therapy that attempts to replicates the original transgenic mouse models using a senescent DNA promoter to drive expression of a suicide gene. This senolytic gene therapy consists of a plasmid DNA (pDNA) vector where the suicide gene, inducible caspase 9 (iCasp9), is under control of the early senescence p53 promoter or the late senescence $p16^{Ink4a}$ promoter. These genetic senolytics are encapsulated withing Fusogenix proteolipid vehicles (PLVs), which enable highly tolerable systemic delivery of nucleic acids. *In vitro*, these promoters are highly stimulated by senescence inducing DNA damage and senolytic treatment can facilitate apoptosis in senescent cells. When administered systemically to aged mice, a combination treatment using both senolytic agents lead to a significant increase in median lifespan. Furthermore, treatment resulted in a decreased $p19^{ARF}$ and senescence associated β-galactosidase (SA-β-Gal) staining in the renal cortex. In summary, this approach represents a first-in-class therapeutic that targets senescent cells based on transcriptional activity similar to what was done in original transgenic models

Keywords: Senescence, Aging, Senolytic, Senolysis, Gene therapy, Nucleic Acid Delivery, Proteolipid Vehicle, PLV, Inducible Caspase 9, iCasp9, Rapamycin, Suicide Gene Therapy.

## 5.1. Introduction

With significant medical advances in the modern era, life expectancy has seen a steady increase, contributing to an aging population[542]. With this, substantial challenges are on the horizon. As age progressively increases, so too does the incidence of chronic diseases[543]. Cellular senescence, irreversible growth arrest, represents one of the most important hallmarks of aging. Accumulation of senescent cells overtime contributes to age-related decline in organ function and ultimately disease development[271,544]. Senescence functions primarily to prevent malignant transformation and is induced by a myriad of stresses, such as genotoxic damage, telomere shortening, and oncogene activation. When these stresses occur, the cell responds by activating p53, which in turn facilitates p21 expression[275]. P21 inhibits cell cycle progression by inhibiting the activity of cyclin dependent kinase (CDK) 2 [276]. The expression of p21 gradually increases as cells begin losing growth potential but declines as cells reach senescence with a reciprocal increase in $p16^{Ink4a}$ expression. $P16^{Ink4a}$ functions as an inhibitor of CDK4 and CDK6, therefore resulting hypophosphorylation of the retinoblastoma protein (pRb), which can now facilitate cell cycle arrest. These findings implicate the p53/p21 axis in initiation of senescence and the $p16^{Ink4a}$/pRb axis in maintaining senescence[291–294]. Expression of $p16^{Ink4a}$ has been demonstrated to increase with age, therefore connecting p16-mediated cell cycle arrest and senescence to aging[295]. Elimination of $p16^{Ink4a}$ expressing cells via genetic means has been demonstrated to increase lifespan, prevent age-related organ function decline, reduce cancer incidence, and reduce the incidence of multiple markers of aging and senescence across multiple tissue types in both naturally aged and rapidly aging mouse models[323,324]. These experiments demonstrated a critical role for $p16^{Ink4a}$ expressing senescent cells in facilitating organ decline and ultimately aging. Contrary to quiescent cells, senescent cells influence the area around them by secreting a variety

of proinflammatory factors, growth factors, and proteases. This senescence-associated secretory phenotype (SASP) promotes immune cell recruitment, proliferation, angiogenesis, and disrupts surrounding tissue architecture therefore leading to increased incidence of cancer and a decline in organ function associated with aging[296–300].

Clearly, senescent cells represent an exciting therapeutic target as they are implicated in numerous age-related disorders, ranging from cancer to arthritis to neurodegenerative disease[545–548]. Senolytics are a relatively new class of drugs that function to selectively eliminate senescent cells. A combination treatment with dasatinib and quercetin was the first identified senolytic therapy and by eliminating senescent cells the drug cocktail was able to improve physical function, health span, and lifespan in aged mice[325,326]. Dasatinib and quercetin have demonstrated some clinical success, decreasing circulating SASP levels and several senescent cell markers in patients with diabetic kidney disease[327], as well as improving physical function in patients with idiopathic pulmonary fibrosis[328]. Other senolytic agents have been identified like ABT-737 and ABT-263, which target the B-cell lymphoma 2 (BCL-2) family of proteins that are upregulated in senescent cells and serve to resist apoptotic stimuli[331,332]. Additionally, a synthetic FOXO4 D-Retro Inverso (FOXO4-DRI) peptide that competes with endogenous FOXO4 for binding to p53 in senescent cells was found to selectively induce apoptosis in senescent cells and ameliorate frailty and kidney dysfunction in aged mice[335].

Dasatinib, quercetin, and ABT-737/ABT-263 senolytics were the product of drug repurposing and though they displayed selectivity for senescent cells, at higher concentrations they all impacted normal cells[325,331,332]. BCL-2 inhibitors have a well-documented history of myelosuppression and have recently been reported to facilitate loss of bone density in aged animals[549–552]. Evidently, there is a significant amount of research that must be done prior to

senolytics becoming a pillar of modern medicine. To overcome the limitations surrounding current senolytics, we propose utilizing a genetic medicine approach to tailor therapeutic gene expression to senescent cells. Contrary to small molecule drugs that interact with all cells in the body, genetic approaches can target specific gene signatures present in senescent cells. In fact, the senolytic properties of dasatinib and quercetin were identified by analyzing the gene expression patterns of senescent cells and honing in pharmacological agents targeting these pathways[325]. Given that p53 and $p16^{Ink4a}$ transcription are active in the early and late stages of senescence induction, respectively, we hypothesize that a senolytic that requires the activation of one or both genes would offer a means to selectively target senescent cells. Herein, we describe the development of plasmid DNA (pDNA) based senolytic with the expression of a late-stage apoptotic protein dependent on transcriptional activation of p53 or $p16^{Ink4a}$.

## 5.2. Results

### *5.2.1. P53 and P16 Promoter Induction*

P53 protein is known to be activated by multiple stresses, resulting in the accumulation of p53 protein and subsequent expression of p53 regulated genes. Though most of these changes have been found to effect p53 at the protein level[144], a number of research groups have found an important role for increased transcription of p53 in response to genotoxic stress[150,151,154]. Activation of p53 and the sequential expression of p21 in response to these DNA damaging stressors results in an immediate cell cycle arrest necessary for initiating senescence, following which, $p16^{Ink4a}$ becomes activated in order to maintain senescence[293,553]. Induction of the $p16^{Ink4a}$ promoter occurs via similar mechanisms to the p53 promoter with DNA damage and oncogene activation leading to $p16^{Ink4a}$ transcription[548]. To confirm that exogenously delivered pDNA with the p53 or p16 promoter was responsive to stresses, we first exposed the BPH-1 cell line to

increasing concentrations of the senescence inducing chemotherapeutic, doxorubicin (DOX)[151,554], following transfection with a p53-promoter or p16-promoter firefly luciferase (FLuc) reporter pDNA construct. As expected, increasing concentrations of DOX resulted in an accumulation of p53 protein (**Figure 5.1A**) that was mirrored by an increase in p53 promoter activity. Cells were also transfected with a control cytomegalovirus (CMV) promoter FLuc reporter construct, which showed consistently decreased activity at higher DOX concentrations (**Figure 5.1B**). P16 protein accumulation and promoter activation were unaffected by DOX treatment (data not shown). Next, we examined the ability of 10 Gray (Gy) ionizing radiation to induce the p53 and p16 promoters[154,555]. P53 protein demonstrated a time dependent increase in accumulation, with 48 hours producing a maximal response (**Figure 5.1C**). We then transfected BPH-1 cells with a p53-promoter driven green fluorescent protein (GFP) reporter pDNA construct to enable assessment of the p53 promoter in individual cells. Transfected cells were exposed to 10Gy ionizing radiation and GFP expression was assessed 48 hours later. At a cellular level, we observed increased intensity of GFP signal in transfected cells, however, overall transfection efficiency remained unchanged (**Figure 5.1D**). 10Gy ionizing radiation resulted in an immediate increase in $p16^{Ink4a}$ protein accumulation 24 hours after irradiation that remained stable for 5 days (**Figure 5.1E**). Relative to unirradiated cells transfected with the p16 promoter FLuc reporter construct, cells exposed to 10Gy showed a dramatic increase in p16 promoter activity at all time points, with maximal p16 promoter activity occurring 72 hours after irradiation, greater than 10-fold higher than control (**Figure 5.1F**).

### *5.2.2. Effect of Ionizing Radiation on Common Senescence Markers*

Uncovering reliable markers of senescence is an active and constantly changing field, with senescence associated β galactosidase (SA-β-Gal), $p16^{Ink4a}$, and the p53 target, p21, representing

the most widely used markers[295,556–561]. We examined the presence of these markers in cells one week after exposure to 10Gy ionizing radiation, except p53 was analyzed instead of p21 as p53 represents a more favorable therapeutic target for gene therapy approaches. Using the method of SA-β-Gal analysis developed by Biran *et al.*[562], imaging flow cytometry was conducted to quantitatively assess these markers following senescence-inducing DNA damage. Senescent cells often undergo characteristic morphological changes, with cells becoming larger and in the case of adherent cells, adopting a flattened shape[563,564]. We observed a significant increase in cell surface area in cells exposed to ionizing radiation (**Supplementary Figure 5.1A**). As expected, the $p16^{Ink4a}$ and p53 positive populations were significantly increased in irradiated cells (**Supplementary Figure 5.1B, C**). Additionally, nearly 30% of irradiated cells stained positively for both $p16^{Ink4a}$ and p53 (**Supplementary Figure 5.1D**). Using the mean pixel intensity of the bright field channel, we detected 35% of irradiated cells staining positively for SA-β-Gal (**Supplementary Figure 5.1E**). The SA-β-$Gal^+$ and SA-β-$Gal^-$ populations in irradiated cells were then separated for individual analysis (**Supplementary Figure 5.1F**). We detected an increase in cell surface area in SA-β-$Gal^+$ cells (**Supplementary Figure 5.1G**). 50% of SA-β-$Gal^+$ cells stained positively for $p16^{Ink4a}$, whereas only 20% of SA-β-$Gal^-$ cells were positive for $p16^{Ink4a}$ (**Supplementary Figure 5.1H**). Interestingly, p53 was elevated in both SA-β-$Gal^+$ and SA-β-$Gal^-$ populations, with positive fractions of 77% and 70%, respectively (**Supplementary Figure 5.1I**). It is likely that ionizing radiation led to an activation of p53 pathways independent of senescence induction, such as DNA repair and apoptosis[144]. Finally, the SA-β-$Gal^+$ population displayed a p53/$p16^{Ink4a}$ dual positive population of 44%, whereas only 18% of SA-β-$Gal^-$ cells were positive for both markers (**Supplementary Figure 5.1J**). Taken together, these results indicate that

analysis of the SA-β-Gal$^{+}$ population on an imaging cytometer represents a viable option to study senescent cells, as most cells are positive for multiple markers of senescence.

### *5.2.3. Development of a Transcriptionally Active Senolytic Therapy*

In the landmark study on senescent cell elimination, Baker *et al.*[323] generated a genetic mouse model where the expression of the inducible caspase 8 suicide gene was under control of the p16$^{Ink4a}$ promoter. This restricted suicide gene expression to senescent cells therefore enabling selective elimination of this cell population following the addition of a small molecule chemical inducer of dimerization (CID). We used this mouse model as a framework to design a genetic medicine capable of eliminating senescent cells following systemic administration. A pDNA vector was developed where the expression of the suicide gene, inducible caspase 9 (iCasp9), is under the control of either the p53 promoter or the p16$^{Ink4a}$ promoter. Like the mouse model, these senescent-associated promoters would therefore restrict suicide gene expression to pre-senescent or senescent cells, respectively. iCasp9 represents an ideal suicide gene to eliminate senescent cells as apoptosis induction is independent of the cell cycle and can bypass upstream abnormalities, such as upregulation of BCL-2 family proteins[565]. The iCasp9 molecule is non-functional until a CID is added, which binds to two molecules of iCasp9 and facilitates proximity induced cleavage and activation[483,484]. We chose to utilize a recently developed iCasp9 molecule that is activated by low dose rapamycin (RAPA), as it is the most cost-effective CID, which increases the accessibility of this therapy[487]. To enable visualization of cell populations expressing the pDNA vector, these constructs also have a green fluorescent protein (GFP) sequence downstream of the iCasp9 sequence, with a T2A linker between the two sequences (p53-iCasp9-GFP and p16-iCasp9-GFP)[506,507].

Though gene therapy gives an opportunity to selectively target cells throughout all stages of senescence induction, it also comes with a unique set of challenges that need to be overcome to become clinically viable. The primary concern being sufficient transgene expression to effectively eliminate senescent cells. The nuclear envelope acts as a significant barrier that impedes the delivery and expression of DNA in non-dividing cells, with initial *in vitro* transfection studies demonstrating that DNA could only be expressed when the nuclear envelop dissolves during mitosis[566–570]. However, DNA expression has been observed in non-dividing cells, albeit with a lower efficiency of gene expression, presumably due to DNA transport through nuclear pore complexes[571–573]. We therefore first examined if expression of pDNA in growth arrested senescent cells was possible using a non-viral nucleic acid delivery vehicle. Fusogenix proteolipid vehicles (PLVs) represent an ideal gene therapy delivery platform, as the use of a fusion-associated small transmembrane (FAST) protein limits the use of toxic components, making Fusogenix FAST-PLVs one of the most well tolerated non-viral delivery vehicles[472]. Normal diploid IMR-90 fibroblasts were exposed to 10Gy ionizing radiation to induce senescence. Seven days after irradiation, FAST-PLVs encapsulating a pDNA vector where GFP expression was under the control of the ubiquitous CMV promoter (pDNA-CMV-GFP) were added for 96 hours, following which SA-β-Gal staining and imaging cytometry was conducted. Irradiation resulted in ~70% of cells staining positively for SA-β-Gal (**Figure 5.1G**), with both the SA-β-Gal$^+$ and the SA-β-Gal$^-$ populations showing GFP expression (**Figure 5.1H**). These results indicate that it is possible to achieve transgene expression from cytosolically delivered pDNA in growth arrested senescent cells using the Fusogenix FAST-PLV platform.

Next, we tested the efficacy of senescent cell elimination using the p53-iCasp9-GFP and p16-iCasp9-GFP constructs *in vitro*. BPH-1 cells were irradiated with 10Gy and had FAST-PLVs

encapsulating either of the constructs added for two days. Cells were then exposed to 100 nM RAPA for 24 hours and stained for SA-β-Gal before analyzing cells via imaging cytometry. The total SA-β-Gal$^+$ population was unaffected by either treatment (**Figure 5.2A and Supplementary Figure 5.2A**). However, cells receiving the p53-iCasp9-GFP construct in combination with RAPA displayed a significantly reduced GFP$^+$ fraction, indicative of loss of cells co-expressing iCasp9 and GFP (**Figure 5.2C, D**). Cells receiving the p16-iCasp9-GFP had a reduction in the GFP$^+$ fraction, although this was not significant (**Supplementary Figure 5.2B**). Next, we examined the significance of the loss of GFP$^+$ cells. When the SA-β-Gal$^+$ population was examined in cells receiving the suicide gene vector in combination with RAPA, we observed some of the characteristic phenotypical changes of apoptosis, such as plasma membrane blebbing and nuclear fragmentation (**Figure 5.2C**). Using the built-in apoptosis wizard in the ImageStream® Image Data Exploration and Analysis Software that identifies apoptotic cells based on high bright field contrast (blebbing) and low nuclear area (fragmentation), we identified that p53-iCasp9-GFP in combination with RAPA results in a significant increase in apoptotic SA-β-Gal$^+$ cells relative to cells treated with vehicle control (**Figure 5.2E, F**). Cells treated with the p16-iCasp9-GFP construct in combination with RAPA had an increase in apoptotic SA-β-Gal$^+$ cells, although this was not significant (**Supplementary Figure 5.2C**). Taken together, these results indicate that the p53 and p16 promoters can drive expression of the iCasp9 in SA-β-Gal$^+$ cells, and in the case of the p53 promoter, the amount produced is sufficient to facilitate significant apoptosis induction *in vitro*.

### *5.2.4. Treatment of Naturally Aged Mice Prolongs Survival*

Significant steps have been taken in recent years to achieve senescent cell clearance with the use of senolytic compounds[325,327,335,574,575]. However, with the exception of Xu *et al.*[326], none

of these studies examined the ability of senolytic treatment to improve lifespan in naturally aged animals. Therefore, we examined the ability of systemic treatment with our genetic senolytic to prolong survival in naturally aged C57BL/6 mice. Starting when animals were over two years of age (average starting age of 105 weeks), mice were injected intravenously with PBS, or PLVs encapsulating 5 mg/kg p53-iCasp9, 5 mg/kg p16-iCasp9, or 2.5 mg/kg of both p53-iCasp9 and p16-iCasp9 (for 5 mg/kg total DNA). 24 hours after PLV or PBS injection, mice received an intraperitoneal injection of 0.1 mg/kg RAPA. This treatment cycle was repeated once a month for one year, or until mice died of natural causes or displayed significant clinical morbidity warranting veterinarian directed euthanasia. Relative to PBS injected control mice with a median survival of 122.5 weeks, p53-iCasp9 monotherapy increased median survival to 132 weeks (+7.6%), p16-iCasp9 monotherapy increased median survival to 142 weeks (+15.9%), and the combination of p53-iCasp9 and p16-iCasp9 increased median survival to 144 weeks (+17.6%), with one animal in this group reaching the endpoint of 1 year post treatment (**Figure 5.3**). These values are particularly interesting because they are in agreeance with the median survival obtained by Xu *et al.*[326], where they found that treating 80-week-old C57BL/6 mice biweekly with dasatinib and quercetin increased median survival from 133.9 weeks in control mice to 142.3 weeks. Surprisingly, we also found that the p16-iCasp9 construct outperformed the p53-iCasp9 construct, contradicting what was found *in vitro*. However, the only treatment group with a statistically significant increase in survival was the combination p53-iCasp9 + p16-iCasp9 group. This indicates that these two promoters are somewhat synergistic, likely targeting at least two distinct populations of senescent or pre-senescent cells. Next, we examined the incidence rate of various medical conditions between treatment groups identified during post-mortem analysis, including cancer, liver disease, and splenomegaly. We found no difference in the rates of each condition

between groups, apart from mice euthanized for non-urgent medical conditions (anal prolapse, dermatitis, and cataracts) in the p16-iCasp9 monotherapy group. However, these conditions were censored in survival analysis (**Supplementary Table 5.1**). Taken together our results indicate that targeting senescent cells *in vivo* based on the transcriptional activity of p53 and p16 offers an effective means to improve longevity.

### *5.2.5. Treatment Reduces the Abundance of Senescence Markers in the Kidney*

To uncover a potential mechanism responsible for the increased longevity in treated animals we conducted a one-month high dose treatment cycle. Mice 108 weeks of age were injected intravenously with PBS or PLVs encapsulating 10 mg/kg p53-iCasp9, 10 mg/kg p16-iCasp9, or 5 mg/kg of both p53-iCasp9 and p16-iCasp9 (for 10 mg/kg total pDNA). 24 hours after PLV or PBS injection, mice received an intraperitoneal injection of 0.1 mg/kg RAPA. This treatment cycle was repeated once a week for three weeks, with animals being sacrificed one week after the final RAPA injection. Circulating levels of proinflammatory SASP markers were unchanged between treatment groups (**Supplementary Table 5.2**). Next, we examined immunohistochemical staining of the senescence marker, $p19^{ARF}$ (mouse homolog to $p14^{ARF}$ in humans). Relative to PBS injected control animals, all mice receiving PLVs displayed significantly reduced $p19^{ARF}$ staining in the kidney cortex (**Figure 5.4A**). Staining in the kidney medulla was highly variable with substantial background staining and was therefore excluded from analysis. Surprisingly, monotherapy with p53-iCasp9 or p16-iCasp9 resulted in lower $p19^{ARF}$ kidney staining than the combination therapy (**Figure 5.4B**). This is possibly due to the lower dose of both constructs in the combination group indicating a potential minimum effective dose around 5 mg/kg for each construct. Because the combination group had the greatest effect on longevity, we examined the impact of p53-iCasp9 + p16-iCasp9 treatment on kidney SA-β-Gal staining.

Following dissociation into single cell suspensions, kidney cells were stained for SA-β-Gal and analyzed by imaging flow cytometry. Kidneys from mice receiving the combination treatment of both p53-iCasp9 and p16-iCasp9 vectors had a significantly lower SA-β-Gal+ population than control mice receiving PBS (**Figure 5.4C-E**). These results were confirmed in frozen kidney sections, where mice receiving the combination treatment had less SA-β-Gal staining than mice injected with PLVs encapsulating a control pDNA construct where the p53 promoter drives the expression of a catalytically inactive iCasp9 (p53-inactive) (**Figure 5.4F**). We therefore postulate that a potential mechanism for increased longevity is via decreased senescent cell burden in the kidneys leading to improved organ function and overall fitness.

### 5.3. Discussion

Here, we describe the development of two senolytic genetic medicines that can be used as a monotherapy or in combination to improve lifespan and reduce multiple markers of senescence in the kidney. As cellular senescence is primarily dependent on the expression of two proteins, p53 and $p16^{Ink4a}$, we sought to develop a transcriptionally active gene therapy dependent on one or both of these factors[291–294]. We developed two pDNA vectors where the p16 or p53 promoter regions are upstream of the iCasp9 suicide gene sequence. As demonstrated by Baker *et al.*[323], only senescent cells or pre-senescent cells[291,293] would achieve iCasp9 expression following systemic delivery of the genetic senolytic. Following the administration of the CID, RAPA, cells expressing the iCasp9 suicide gene undergo selective apoptosis induction[483,484,487]. Our *in vitro* results indicate that irradiated SA-β-$Gal^{+}$ cells treated with the p53-iCasp9 construct (and to a lesser extend the p16-iCasp9 construct) undergo a selective apoptosis induction following RAPA administration.

Gene therapy holds great promise to treat a myriad of age-related diseases, with more than 2600 clinical trials being initiated worldwide[3,576]. Despite this, most potential gene therapies reach

a bottleneck, as safety and efficacy concerns prevent most treatments from reaching the clinic[15–17]. The recent success of lipid nanoparticles (LNPs) as delivery vehicles for mRNA-based vaccines has revitalized the gene therapy landscape[577]. However, LNPs present with their own challenges and safety concerns, which limit tolerability following systemic delivery[41,42]. Given that aging is a complex process that typically results in frailty even in the absence of disease, senolytics must be designed with particular attention being paid to safety. By restricting gene expression to senescent cells, our senescent promoter-based approach eliminates off-target expression resulting in clearance of healthy cells. To prevent toxicity stemming from the nucleic acid delivery vehicle, we utilized Fusogenix FAST-PLVs. By combining the beneficial aspects of both viral and non-viral delivery vehicles, FAST-PLVs are able to achieve a high degree of transgene expression without an accompanying increase in toxicity, therefore making it the ideal platform to deliver a genetic senolytic[472]. Furthermore, FAST-PLVs can be administered multiple times without generating humoral responses that imped gene transfer overtime, a significant barrier with viral nucleic acid delivery platforms[19,21–24,578].

Monthly systemic injections of FAST-PLVs encapsulating the p53-iCasp9 and p16-iCasp9 constructs resulted in an increase in median lifespan relative to PBS injected mice. These results not only demonstrate the senolytic capacity of these DNA constructs, but also further validate the tolerability of the FAST-PLV platform. We found that combination of both the p53-iCasp9 and p16-iCasp9 constructs resulted in better survival than either construct administered as a monotherapy, even at half the dose. This is indicative of two separate senescent cell populations that are targeted by each promoter, resulting in a synergistic effect when they are combined. Alcorta *et al.*[292] found that the p53 target, p21, was elevated as cells neared senescence and once senescent, cells displayed increased $p16^{Ink4a}$ expression. It is likely that the p53-iCasp9 construct

targets cells that are in the early stage of senescence or cells that are responding to DNA damage[275]. On the other hand, the p16-iCasp9 construct is likely targeting cells that have entered a growth arrested senescent state and require sustained $p16^{Ink4a}$ expression[293].

A potential mechanism for the improved survival following treatment still requires some clarification. We found that the kidney cortex of treated mice displayed lower levels of $p19^{ARF}$ and SA-β-Gal. The kidney represents an interesting target for senolytic treatments as senescent renal cells accumulate with age and have been implicated in renal fibrosis following injury and reduced renal function[579–581]. However, the role of $p19^{ARF}$ in cellular senescence and in the kidney is still not entirely clear. $P19^{ARF}$ (mouse homolog to $p14^{ARF}$ in humans) regulates p53 stability by binding to MDM2 and promoting its degradation, thus enabling p53 to facilitate cell cycle arrest[162,582,583]. Krishnamurthy *et al.*[295] found expression of both $p16^{Ink4a}$ and $p19^{ARF}$ was increased in organs from aged rodents. Baker *et al.*[584] elucidated the role of $p19^{ARF}$ further in a rapidly aging mouse model ($BubR1^{H/H}$) and found that although $p19^{ARF}$ was elevated in tissues that expressed high levels of $p16^{Ink4a}$, $p19^{ARF}$ loss resulted in an accelerated aging and increased $p16^{Ink4a}$ expression. These results lead them to the conclusion that $p19^{ARF}$ functions as an attenuator of senescence and $p19^{ARF}$ expression is dependent on high $p16^{Ink4a}$ expression as it may exert some of its effects via negative regulation of $p16^{Ink4a}$. On the other hand, $p19^{ARF}$ expression has been found to contribute to age-related decline in lung function. Elimination of $p19^{ARF}$ expressing pulmonary cells in C57BL/6j mice resulted in improved lung function as well as a decrease in the expression of $p16^{Ink4a}$, p21, and other senescence-related genes[585]. Furthermore, $p19^{ARF}$ expression has also been implicated in pulmonary emphysema and elimination of $p19^{ARF}$ expressing cells with senolytic treatment (ABT-263) improved lung function[586]. The conflicting results for $p19^{ARF}$ involvement in senescence could potentially be explained by the use of the rapidly aging $BubR1^{H/H}$ mice by Baker *et al.*[584]

and the use of C57BL/6j mice by Hashimoto *et al.*[585] and Mikawa *et al.*[586]. In kidneys, ischemic injury was found to induce $p19^{ARF}$ and p53 expression while having no effect on $p16^{Ink4a}$ expression. Additionally, $p19^{ARF}$ overexpression in Madin-Darby Canine Kidney (MDCK) cells was found to facilitate cell cycle arrest[587]. Taking these results into consideration, the loss of renal $p19^{ARF}$ expression in our study was either directly related to treatment and $p19^{ARF}$ expressing cells are directly eliminated[585–587], or the reduced $p19^{ARF}$ expression was secondary to loss of high $p16^{Ink4a}$ expressing cells as the result of a compensatory feedback mechanism[584]. Regardless, $p19^{ARF}$ represents a marker of aging and treatment with p53-iCasp9 or p16-iCasp9 resulted in a decreased proportion of $p19^{ARF}$ expressing cells in the kidney.

Arguably one of the most detrimental aspects of cellular senescence is the SASP[296]. In an acute setting, the SASP plays an important role in tumor suppression. In oncogene-induced senescent cells, the SASP functions to increase secretion of IL-6, IL-8, and GROα, which functions to reinforce growth arrest via autocrine signaling[303,304]. In hepatocytes that have undergone oncogene-induced senescence, the SASP serves to recruit immune cells to eliminate oncogene expressing cells and prevent malignant transformation[306]. However, as we age it is likely that the immune system's ability to recognize and remove senescent cells declines, therefore leading to an accumulation of senescent cells and unregulated SASP. This promotes local inflammation, decreased organ function, and increased tumorigenicity of cells in the vicinity of the SASP[275]. One of the primary goals of senolytic therapy is to eliminate cells exhibiting the SASP. The FOXO4-DRI was found to preferentially induce apoptosis in SASP expressing senescent cells. Decreased renal expression of IL-6 following treatment was associated with improved overall kidney function and mouse fitness[335]. Additionally, Dasatinib and Quercetin combination therapy was found to decrease mRNA expression of IL-6, MCP1, and CXCL1 in the adipose tissue of aged mice that

also demonstrated improved physical function[326]. In our study, we examined the circulating levels of SASP markers, but failed to see any difference between treatment groups. A possible explanation for this is a relatively low proportion of senescent cells located throughout the body[588,589]. Therefore, elimination of this small collection of cells would not result in a significant decrease in circulating SASP levels. We have not yet analyzed the tissue specific expression of common SASP markers following treatment. It is possible that we will see changes in SASP expression at this level, which may correlate with improvements in organ function.

In conclusion, we have developed a novel genetic senolytic treatment that relies on the transcriptional activity of senescent cells. By generating a pDNA vector where the p53 or p16 promoter region drives the expression of the suicide gene, iCasp9, we can selectively induce apoptosis in senescent cells with active transcription of either marker. Utilizing FAST-PLV to encapsulate these pDNA vectors enables systemic administration without tolerability concerns that have plagued other non-viral nucleic acid delivery platforms. Treatment with the combination of p53-iCasp9 and p16-iCasp9 resulted in increased median survival. The mechanism for this improvement is still yet to be fully delineated, but our results indicate a decrease of some common senescent markers in the kidneys of treated animals, which can result in improved organ function and lifespan.

## 5.4. Methods

*Materials*

Rapamycin was purchased from Fisher Scientific (Cat# BP29631) and dissolved in DMSO (Millipore Sigma, Cat# D8418) to a concentration of 40mg/ml. For in vivo injection, rapamycin

was diluted in a solution of 5% PEG-400 (Fisher Scientific, Cat#P167-1) and 5% Tween-80 (Millipore Sigma, Cat# P4780) dissolved in $H_2O$. The following lipids were purchased from NOF Co. (Tokyo, Japan): 1,2-dioleoyl-3-dimethylammonium-propane (DODAP), 1,2-dimyristoyl-*sn*-glycero-3-methoxypolyethylene glycol-2000 (DMG-PEG). 2-dioleoyl-*sn*-glycero-3-phosphoethanolamine (DOPE) and 1,2-dioleoyl-3-trimethylammonium-propane (DOTAP) were purchased from Avanti Polar Lipids (Alabaster, United States). All plasmid DNA cloning was done into the p10 plasmid vector produced by Entos Pharmaceuticals. Plasmid DNA preps were expanded and purified by Precision Bio Laboratories (Edmonton, Alberta).

*Cells and Culturing*

Quail fibrosarcoma (QM5) cells were cultured in Medium 199 with 3% fetal bovine serum (FBS; Sigma) and 0.5% penicillin/streptomycin (Thermo Fisher Scientific, Edmonton, Canada). BPH-1 and IMR-90 cell lines used in this study were purchased from ATCC (Manassas, VA) and cultured in accordance with recommended guidelines. Cells were grown in tissue-culture treated 75 cm2 flasks (VWR 10062-860) until cells were 80% confluent or nutrients in the media are depleted in a 37°C incubator with humidified atmosphere of 5% CO2 (Nuaire NU-5510). Spodoptera frugiperda pupal ovarian tissue (Sf9) cells used to produce FAST protein were stepwise cultured at 25C to $2x10^6$ – $4x10^6$ cells/mL from 25 mL to 100 mL and finally into a 2 L wave bioreactor. The Trypan Blue assay was used to check for cell viability.

*Purification of FAST Proteins*

FAST proteins were purified and had activity checked as described previously[472]. Briefly, Sf9 cells were lysed, and supernatant was clarified by 0.2 μm filtration. The FAST proteins were purified from the supernatant using an AKTA affinity purification column, followed by dialysis and

cationic exchange purification (AKTA). Protein samples were quality control analyzed by SDS-PAGE and Western blot; functional validation was done via syncytia formation assay.

*FAST-PLV Manufacturing and Validation*

Lipid formulation composition, manufacturing, and validation was described previously[472]. Briefly, individual lipids were heated in a 37°C water bath for 1 min, vortexed for 10 seconds each, then combined and vortexed for 10 seconds. The combined lipid mixture was dehydrated in a rotavapor at 60 rpm for 2 hours, under vacuum, then rehydrated with 14 mL 100% ethanol, and sonicated (Branson 2510 Sonicator) at 37°C, set to sonication of 60. The lipid formulation was aliquoted in 500 µL batches and stored at -20°C. The NanoAssemblr Benchtop microfluidics mixing instrument (Precision NanoSystems, Vancouver, BC, NIT0013, and NA-1.5-88, respectively) was used to mix the organic and aqueous solutions and make the PLVs. The organic solution consisted of lipid formulation in EtOH. The aqueous solution consisted of pDNA, 5 nM FAST protein, and 10 mM acetate buffer (pH 4.0). NanoAssemblr was run at a total flow rate of 12 mL/min and a 3:1 aqueous to organic flow rate ratio. PLVs were dialyzed in 8000 MWCO dialysis tubing (BioDesign, D102). The loaded tubing was rinsed with 5 mL of double distilled water and dialyzed in 500 mL of Dialysis Buffer (ENT1844) with gentle stirring (60 rpm) at ambient temperature for 1 hour and was repeated twice with fresh Dialysis Buffer. PLVs were concentrated using a 100 kDa Ultra filter (Amicon, UFC810096) according to the manufacturer's instructions. PLVs were filter sterilized through 0.2 µm Acrodisc Supor filters (Amicon, UFC910008). Particle size, polydispersity index (PDI), and zeta potential was measured on final samples using the Malvern Zetasizer Range and a Universal 'Dip' Cell Kit (Malvern, ZEN1002) following the manufacturer's instructions. The nucleic acid encapsulation efficiency and

concentration was calculated using a modified Quant-IT PicoGreen dsDNA assay (Thermo Fisher Scientific, Edmonton, Canada).

*In Vitro Transfection*

All cells were counted using a hemocytometer prior to plating. All pDNA constructs were prepared with Entos pharmaceuticals *in vitro* transfection reagent (formulation 41N as described previously[472], with slight modifications to the formulation to increase *in vitro* transfection efficiency, stability, and tolerability). BPH-1 and IMR-90 cells were transfected with pDNA encapsulating FAST-PLVs for 48-96 hours. For luciferase assays, cell culture media was removed, and cells were washed with once with PBS. A 50-microliter aliquot of reporter lysis buffer (Promega, Cat# E397A) was added to the cells. The cells were mixed and incubated at room temperature for 15 mins on an orbital shaker. D-luciferin (150µg/mL, GOLDBIO, LUCK-100) was dissolved in 100 mM Tris-HCl (pH 7.8), 5 mM $MgCl_2$, 2 mM EDTA, 4 mM DTT, 250 µM acetyl-CoA, and 150 µM ATP. The luciferin substrate (100 µL) was added via auto-injector to each well immediately before measurement (1-2 second settling time). Luminescence was measured via the FLUOstar Omega plate reader (BMG Labtech, 415-1147) using the MARS data analysis software for analysis. Green fluorescent protein (GFP) expressing cells were processed for flow cytometry analysis. The cells were trypsinized and resuspended in 400 µL (per well of 48 well plate) of FACS buffer, then transferred to a 5 mL flow cytometry tube (SARSTEDT 75X 12 mm PS Cat. no. 55.1579) and analyzed with a BD LSRFortessa X20 SORP.

*Western Blot*

Cells were lysed in ice-cold Pierce RIPA buffer (Thermo Scientific, Cat. No. 89900). Protein amount was determined using Pierce BCA protein assay (Thermo Scientific, Cat. No. 23225).

Equal amounts of total protein from each lysate were loaded onto Mini-PROTEAN 4-20% Gradient TGX precast gels (BIO-RAD, Cat. No. 456-1095). Separated protein was transferred to nitrocellulose membranes (BIO-RAD, Cat. No. 1620112). Membranes were blocked with fluorescent western blocking buffer (Rockland, Cat. No. MB-070) for 1 hour at room temperature. Anti-p53 antibody (Clone DO-1, Santa Cruz Biotechnology, Cat# sc-126), anti-$p16^{Ink4a}$ antibody (Clone EPR1473, Abcam, Cat# ab108349), rabbit anti-GAPDH (Clone 0411, Santa Cruz Biotechnology, Cat# sc-47724), and mouse anti-β-Tubulin (Clone AA2, Sigma Aldrich, Cat# T8328) primary antibodies were diluted 1:1000 in blocking buffer and added to the membranes overnight at 4˚C with shaking. Goat anti-rabbit Alexa Fluor 680 (Thermo Scientific, Cat. No. A27042), or goat anti-mouse Alexa Fluor 750 (Thermo Scientific, Cat. No. A-21084) were diluted 1:10000 in blocking buffer and added for 1 hour at room temperature in the dark. Membranes were visualized on the LI-COR Odyssey.

*Mouse Studies*

All animal studies were carried out according to the guidelines of the Canadian Council on Animal Care (CCAC) and approved by the University of Alberta Animal Care and Use Committee. *In vivo* studies were done using 24-month-old male and female C57BL/6 (Charles River Laboratories, Saint-Constant, Canada). Animals were group-housed in IVCs under SPF conditions, with constant temperature and humidity with lighting on a fixed light/dark cycle (12-hours/12-hours). Intravenous injection occurred via the lateral tail vein with 200 μL of the test agent. Blood was collected via the lateral tail vein or terminal cardiac puncture at indicated time points into serum collection tubes (Sarstedt, Montreal, Canada).

*Meso Scale Discovery*

The Mesoscale Discovery QuickPlex SQ 120 (MSD, Rockville, MD) was used with mouse serum samples as per the manufacturer's instructions. The data was analyzed with MSD Workbench 4.0 software, following the software protocol. The Meso Scale Discovery V-PLEX Proinflammatory Panel 1 mouse kit was used to quantitatively determine serum concentrations of 10 proinflammatory cytokines: IFN-γ, IL-1β, IL-2, IL-4, IL-5, IL-6, IL-10, IL-12p70, CXCL1 (KC/GRO), and TNF-α.

*Histology*

Major organs, including the heart, liver, spleen, lungs, and kidneys, were collected, formalin-fixed, and paraffin-embedded. 4-6 μm sections were generated. Sections were dewaxed in xylene and rehydrated using graded ethanol to water washes. Samples for H&E staining were stained in hematoxylin for 8 minutes, briefly differentiated in acid alcohol, and blued with Scott's Tap Water (pH 8). Slides were then stained in acidified eosin for 30 seconds, and dehydrated, cleared, and then mounted. Heat-induced antigen retrieval for IHC samples was conducted by immersing rehydrated slides in 10mM sodium citrate (pH 6) and heating until boiling occurred. Slides were blocked in 10% normal rabbit serum (Cat. No. 869019-M, Sigma, Oakville, Canada) with 1% bovine serum albumin (BSA, Cat. No. A9418, Sigma, Oakville, Canada) in TBS with 0.1% Tween-20 for one hour at ambient temperature. Anti-$p19^{ARF}$ antibody (Invitrogen, Cat# PA1-30670) was diluted 1:250 in blocking buffer and incubated on sections overnight. Endogenous peroxidase was blocked with 3% $H_2O_2$ in PBS. Goat anti-rabbit HRP (Agilent Dako, Cat# P044801-2) was added to slides for 1 hour. Slides were stained with EnVision FLEX DAB + Chromogen (Agilent Dako, Cat# GV82511-2). Kidneys for SA-β-Gal staining were flash-frozen in O.C.T. Compound (Fisher Scientific, Cat# 23-730-571) and sectioned using a cryostat. 10 μm sections were warmed to room temperature and fixed with 3.7% formaldehyde for 15 minutes.

SA-β-Gal staining was performed using a staining kit (Sigma-Aldrich, Cat# K146501), according to the manufacturer's instructions. Nuclei were counterstained with Nuclear Fast Red (Sigma-Aldrich, Cat# N3020) and images were acquired using a Zeiss AxioCam HRc mounted on a Leitz Laborlux S light microscope. The percentage of senescent cells was determined by counting of total and SA-β-Gal positive cells with the positive cell selection tool available in QuPath v. 0.2.3[590].

*Imaging Flow Cytometry: SA-β-Gal Staining and p53/p16$^{Ink4a}$ Staining*

Using the method for SA-β-Gal staining developed by Biran *et al.*[562] with slight modifications. Cells are lifted, washed, and fixed with 2% paraformaldehyde for 5 minutes. Cells are then washed with 1mM $MgCl_2$/PBS (pH 6 for human cells, pH 5.5 for mouse cells) twice, before resuspending in SA-β-Gal staining buffer: 1mg/ml X-Gal (Sigma Aldrich, Cat# B4252), 5mM $K_3[Fe(CN)_6]$ (Sigma Aldrich, Cat# 244023), 5mM $K_4[Fe(CN)_6]\cdot 3H_2O$ (Sigma Aldrich, Cat# 455989) in 1mM $MgCl_2$/PBS (pH 6 for human cells, pH 5.5 for mouse cells). Cells are incubated for 12 hours in a 37˚C incubator with no $CO_2$ in the dark. Cells are washed twice with flow cytometry buffer and stained with Hoechst 33342 if analysis is to be done immediately. If intracellular staining is required, washed cells are fixed/permeabilized using eBioscience Intracellular Fixation and Permeabilization Kit (Invitrogen, Cat# 88-8824-00). Cells are fixed for 30 minutes at room temperature and then washed twice with permeabilization buffer. Anti-p53 antibody (Clone DO-1, Santa Cruz Biotechnology, Cat# sc-126) and anti-p16$^{Ink4a}$ antibody (Clone EPR1473, Abcam, Cat# ab108349) were both diluted 1:100 in permeabilization buffer and incubated overnight at 4˚C with constant rotation. Cells are then washed with flow cytometry buffer (PBS with 2% FBS and 0.09% $NaN_3$) and have goat anti-mouse Alexa Fluor 647 secondary antibody (Invitrogen, Cat# A-21235) and goat anti-rabbit Alexa Fluor 488 secondary antibody (Invitrogen, Cat# A-11008) were

diluted 1:400 added for one hour are room temperature. Cells were washed and resuspended in 50 µL of flow cytometry buffer and run on the Amnis ImageStream Mark II imaging flow cytometrer. Cells were gated based on their Area vs Aspect Ratio to identify single cells, then captured based on a positive nuclear stain. SA-β-Gal staining intensity is determined via the mean pixel intensity of the bright field channel (lower values = higher stain intensity), typically a value of -100 to -150 represents the upper cut-off for senescent cells. At least 10,000 events were captured before data was analyzed on the IDEAS imaging software. For SA-β-Gal kidney single cell suspensions, due to a high degree of debris impacting the analysis a mask recapitulating the area occupied by the nuclear stain is generated. This mask is then applied to the bright field channel and expanded 20% to ensure only nucleated cells are included in SA-β-Gal analysis. Cell area is calculated from pixel area with the conversion: $1\mu m^2 = 4$ pixels.

*Statistical analysis*

A two-tailed Student's *t*-test or a one-way analysis of variance (ANOVA) was performed when comparing two groups or more than two groups, respectively. Statistical analysis was performed using Microsoft Excel and Prism 7.0 (GraphPad). Data are expressed as means ± s.d. The difference was considered significant if $P < 0.05$ ($*P < 0.05$, $**P < 0.01$, $***P < 0.001$, $****P < 0.0001$ unless otherwise indicated).

**Acknowledgments**

This research was supported by an operating grant to John D. Lewis from the Canadian Institutes of Health Research (CIHR), in partnership with the Institute of Aging: Research Nova Scotia, reference number VR1-172710. Dr. Lewis holds the Frank and Carla Sojonky Chair in Prostate Cancer Research funded by the Alberta Cancer Foundation. Roy Duncan's laboratory was funded by the CIHR and the Natural Sciences and Engineering Research Council of Canada (NSERC). Douglas W. Brown was funded by fellowships from Prostate Cancer Canada and Mitacs. We thank Abul Kalam Azad for isolating and sub-culturing HUVEC and Katia Carmine-Simmen for her technical support.

**Author Contributions**

DWB, AR, and JDL designed the study. RD developed the FAST protein. AR, PW, PB, MP, HV, LG, JG and PSA optimized the PLV system. HG, GH, and MS conceived the DNA constructs. PB performed DNA cloning. DWB performed in vitro work. DWB, DS, MH, SL, and MD performed the mice studies. DWB, AR, and JDL wrote the manuscript with input from all authors.

## 5.5. Figures

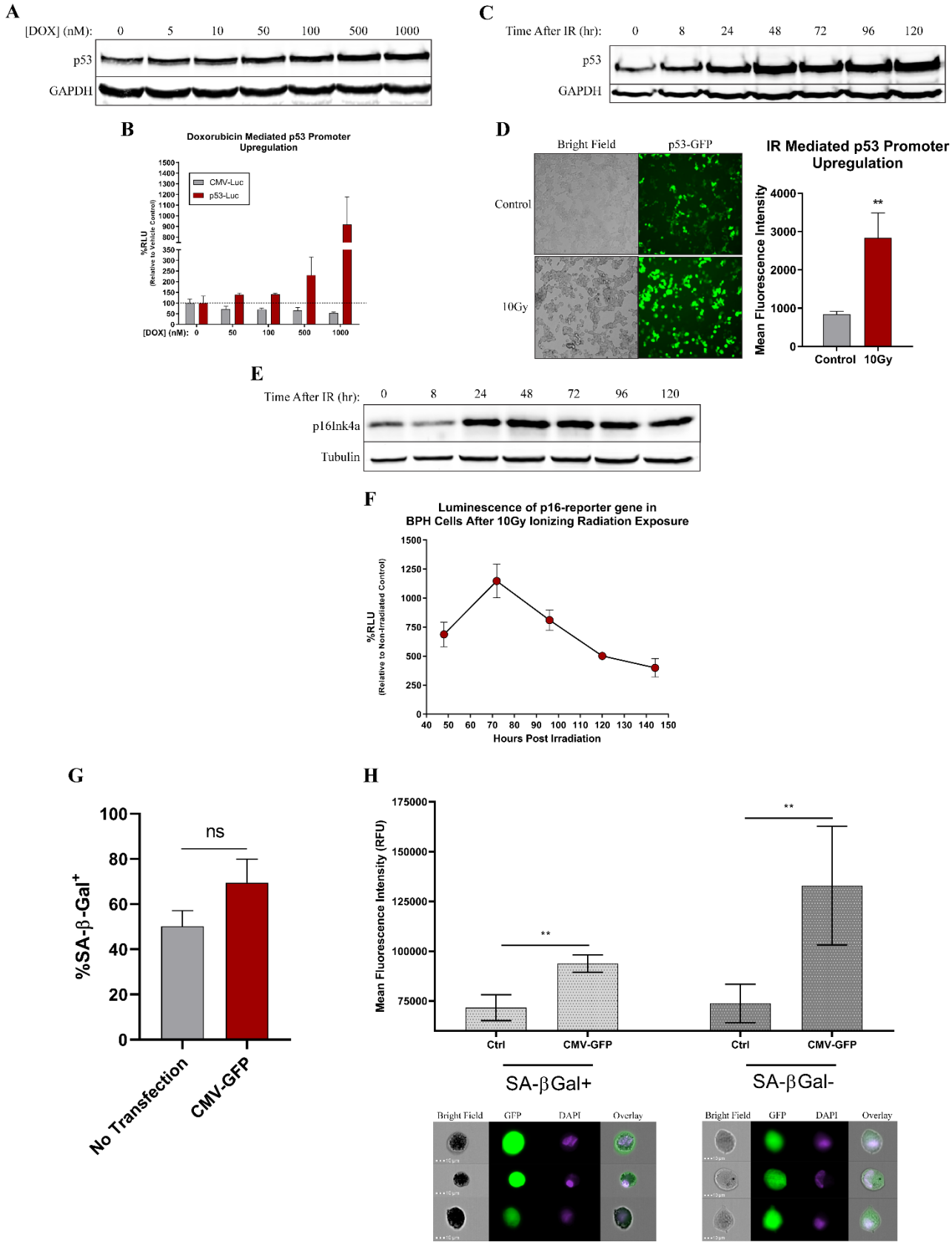
A
[DOX] (nM): 0 5 10 50 100 500 1000
p53
GAPDH
C
Time After IR (hr): 0 8 24 48 72 96 120
p53
GAPDH
B
Doxorubicin Mediated p53 Promoter Upregulation
CMV-Luc
p53-Luc
%RLU (Relative to Vehicle Control)
[DOX] (nM): 0 50 100 500 1000
D
Bright Field
p53-GFP
Control
10Gy
IR Mediated p53 Promoter Upregulation
Mean Fluorescence Intensity
Control 10Gy
E
Time After IR (hr): 0 8 24 48 72 96 120
p16Ink4a
Tubulin
F
Luminescence of p16-reporter gene in BPH Cells After 10Gy Ionizing Radiation Exposure
%RLU (Relative to Non-Irradiated Control)
Hours Post Irradiation
G
%SA-β-Gal+
ns
No Transfection
CMV-GFP
H
Mean Fluorescence Intensity (RFU)
Ctrl
CMV-GFP
SA-βGal+
SA-βGal-
Bright Field
GFP
DAPI
Overlay

**Figure 5.1 – Exogenously delivered pDNA with the p53 or p16$^{Ink4a}$ promoter is responsive to DNA damaging stress.**

(A) Effect of increasing DOX concentrations on p53 protein accumulation in BPH-1 cells.

(B) BPH-1 cells were transfected with a p53-promoter driven FLuc reporter pDNA construct or a CMV-promoter driven FLuc pDNA construct and exposed to increasing concentrations of DOX. Values are normalized to the 0nM DOX control treatment.

(C) Effect of ionizing radiation of p53 protein accumulation in BPH-1 cells.

(D) BPH-1 cells were transfected with a p53-promoter GFP reporter pDNA construct and exposed to 10Gy ionizing radiation 24 hours later. Fluorescence imaging and flow cytometry are conducted 48 hours after radiation exposure. Mean fluorescence intensity presented on the GFP+ population. Unpaired t-test, **P<0.01.

(E) Effect of ionizing radiation of p16$^{Ink4a}$ protein accumulation in BPH-1 cells.

(F) BPH-1 cells were transfected with a p16-promoter driven FLuc reporter pDNA construct and have luminescence determined at indicated time points. Data is normalized to unirradiated transfected cells at the same time points.

(G) Normal human IMR-90 fibroblasts are irradiated with 10Gy and 7 days later have FAST-PLVs encapsulating pDNA-CMV-GFP added for 96 hours before cells are stained with SA-β-Gal and analyzed on the imaging flow cytometer. Transfection has no effect on the SA-β-Gal+ population. Unpaired t-test, ns = not significant (P>0.05).

(H) SA-β-Gal+ and SA-β-Gal– populations have GFP mean fluorescence intensity assessed to demonstrate pDNA expression in senescent cells. Unpaired t-test, **P<0.01.

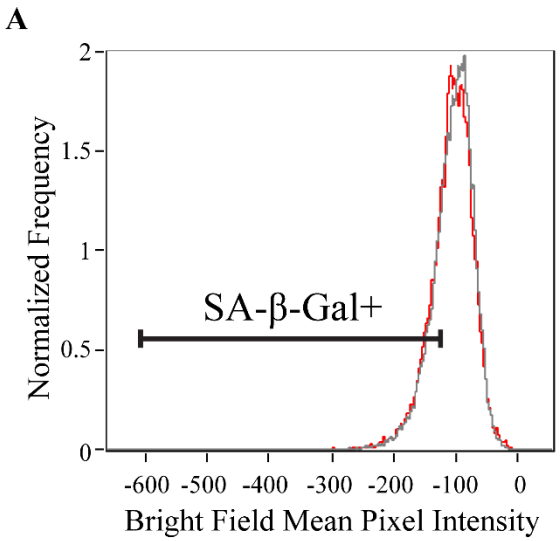
A
Normalized Frequency
SA-β-Gal+
Bright Field Mean Pixel Intensity

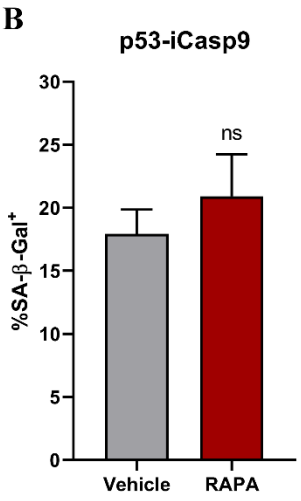
B
p53-iCasp9
%SA-β-Gal+
ns
Vehicle
RAPA

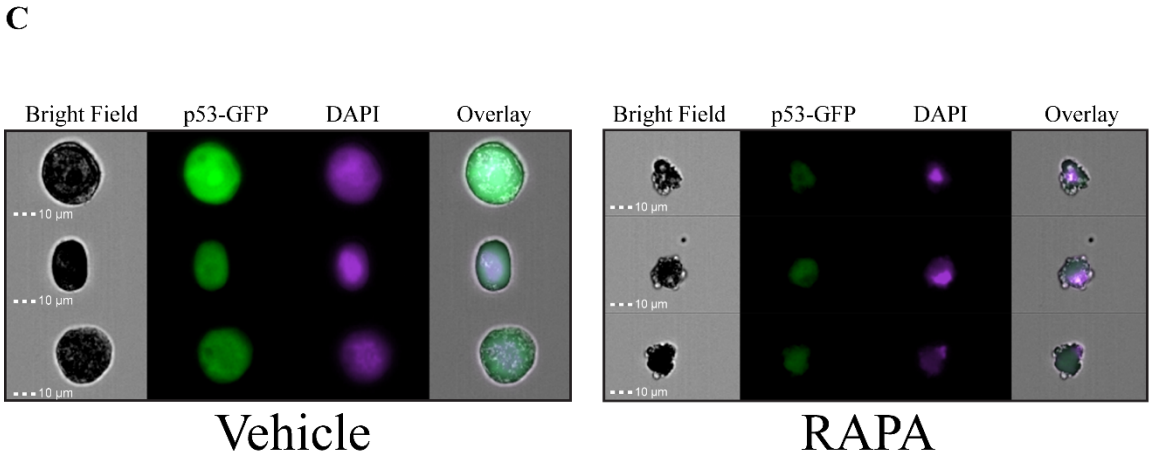
C
Bright Field
p53-GFP
DAPI
Overlay
Vehicle
RAPA

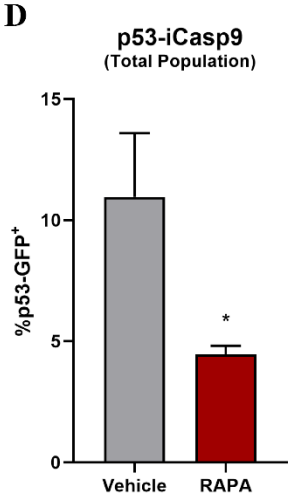
D
p53-iCasp9
(Total Population)
%p53-GFP+
Vehicle
RAPA

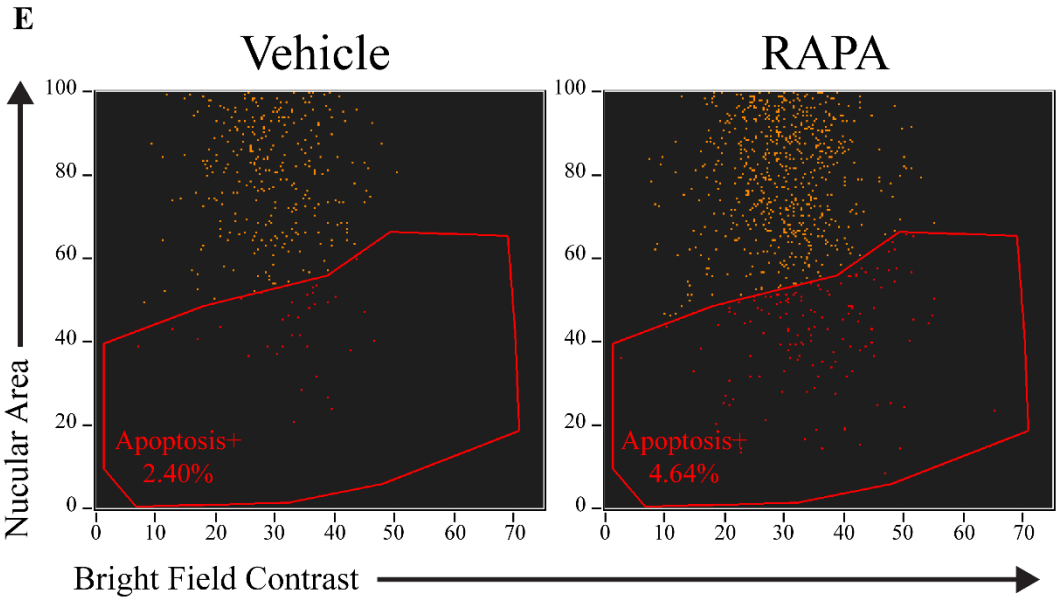
E
Vehicle
RAPA
Nucular Area
Apoptosis+
2.40%
Apoptosis+
4.64%
Bright Field Contrast

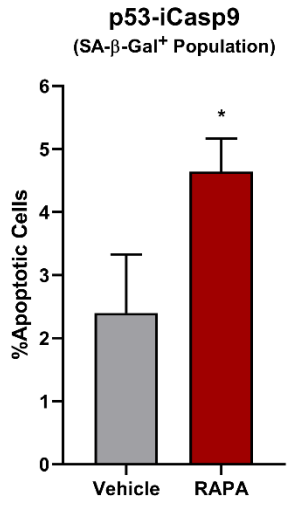
F
p53-iCasp9
(SA-β-Gal+ Population)
%Apoptotic Cells
Vehicle
RAPA

**Figure 5.2 – Treatment of senescent BPH-1 cells with p53-iCasp9-GFP results in apoptosis induction.**

(A) BPH-1 cells were irradiated with 10Gy and had FAST-PLVs encapsulating p53-iCasp9-GFP added for 48 hours, following which, cells were exposed to 100nM RAPA for 24 hours. Cells are then stained for SA-β-Gal and analyzed on the Imaging Cytometer. Treatment had no effect on SA-β-Gal+ population. Unpaired t-test, ns = not significant ($P>0.05$).

(B) Treatment has no significant effect on SA-β-Gal staining.

(C) Representative imaging cytometer images from SA-β-Gal stained irradiated BPH-1 cells transfected with p53-iCasp9-GFP and treated with vehicle or RAPA.

(D) Percentage of the total population that is positive for p53-GFP following treatment with vehicle or RAPA. Unpaired t-test, *$P<0.05$.

(E) BPH-1 cells are gated on the SA-β-Gal positive population and the built-in apoptosis wizard in the ImageStream® analysis software analyzed the incidence of apoptosis induction in transfected cells treated with vehicle or 100nM RAPA.

(F) In the SA-β-Gal positive population of p53-iCasp9-GFP transfected BPH-1 cells, RAPA administration increases the apoptotic positive population. Unpaired t-test, *$P<0.05$.

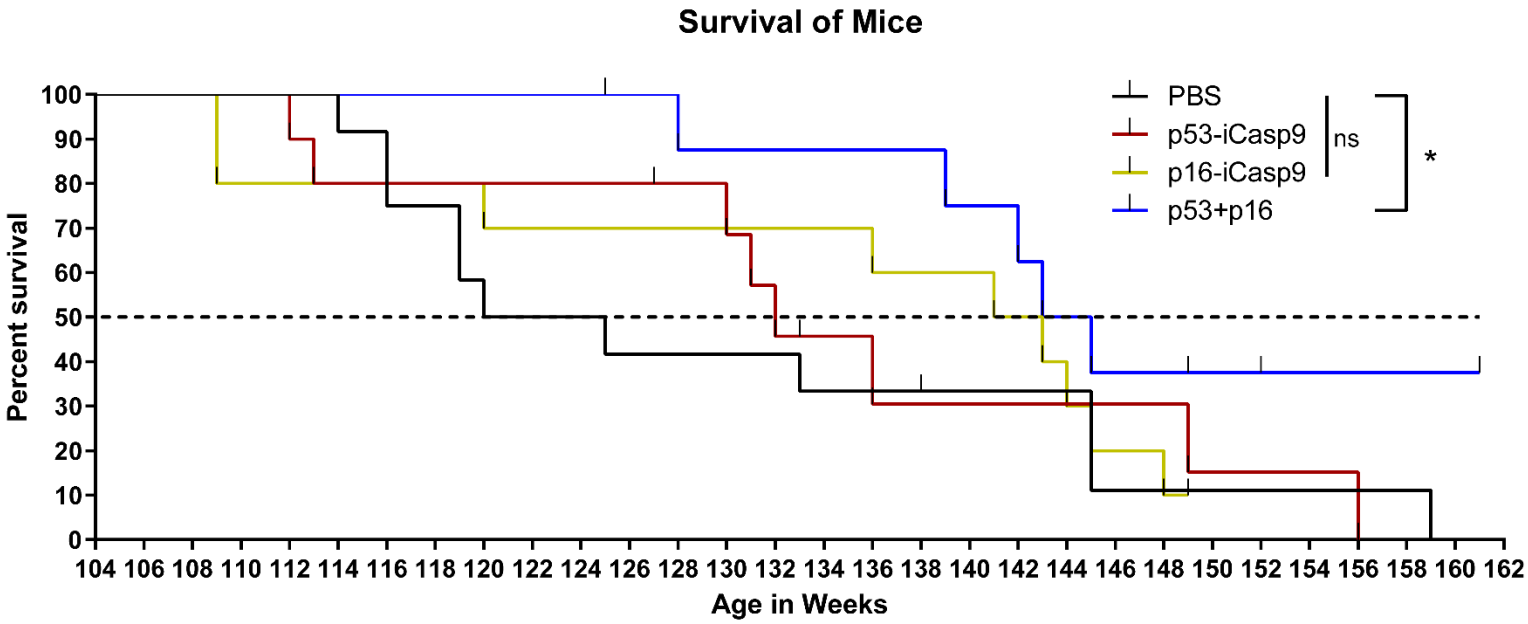


**Figure 5.3 – Systemic treatment of naturally aged mice prolongs survival**

(A) Naturally aged C57BL/6j (105-weeks-old) received intravenous injections with PBS or PLVs encapsulating: 5 mg/kg p53-iCasp9, 5 mg/kg p16-iCasp9, or 2.5 mg/kg of both p53-iCasp9 and p16-iCasp9 (for 5 mg/kg total DNA). 24 hours after PLV or PBS injection, mice received an intraperitoneal injection of 0.1 mg/kg RAPA. This treatment cycle was repeated once a month for one year, or until mice died of natural causes or displayed significant clinical morbidity warranting veterinarian directed euthanasia. Censored cases represent veterinarian directed euthanasia for non-urgent medical conditions (cataracts, dermatitis, anal prolapse). Logrank test for trend, *P<0.05.

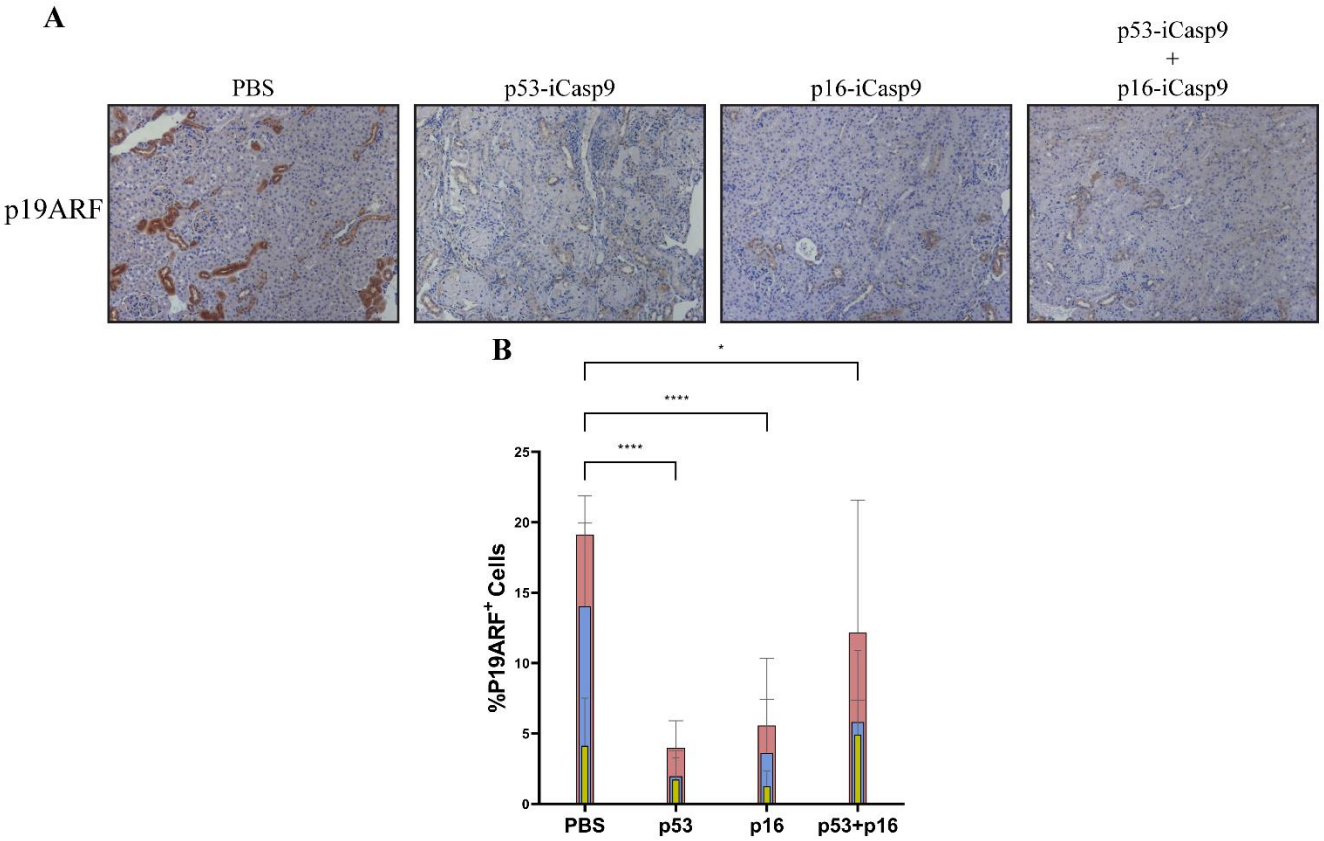
A
PBS
p53-iCasp9
p16-iCasp9
p53-iCasp9
+
p16-iCasp9
p19ARF
B
%P19ARF+ Cells
PBS
p53
p16
p53+p16
C
Bright Field
SSC
DAPI
PBS
p53-iCasp9
+
p16-iCasp9
10 µm
D
Normalized Frequency
SA-β-Gal+
Bright Field Mean Pixel Intensity
E
Kidney
%SA-β-Gal+
PBS
p53+p16
F
p53-inactive
p53-iCasp9
+
p16-iCasp9

**Figure 5.4 – Systemic treatment decreases the incidence rate of senescence markers in the kidney.**

(A) $P19^{ARF}$ staining conducted in the kidney cortex of treated mice. Mice 108 weeks of age were injected intravenously with PBS or PLVs encapsulating 10 mg/kg p53-iCasp9, 10 mg/kg p16-iCasp9, or 5 mg/kg of both p53-iCasp9 and p16-iCasp9 (for 10 mg/kg total pDNA). 24 hours after PLV or PBS injection, mice received an intraperitoneal injection of 0.1 mg/kg RAPA. This treatment cycle was repeated once a week for three weeks.

(B) QuPath was utilized to quantify $p19^{ARF}$ staining in the kidneys of treated and control animals. *n*=3 biologically independent mice per group with five images taken at random per mouse. Two-way ANOVA and Dunnett's multiple comparisons test, *P<0.05, ****P<0.0001.

(C) Representative imaging flow cytometry images of SA-β-Gal-stained kidney single cell suspensions following treatment.

(D) Histogram of the bright field mean pixel intensity (SA-β-Gal stain intensity) in PBS and p53-iCasp9 + p16-iCasp9 combination treated mice.

(E) Quantification of the SA-β-Gal positive population in the kidneys of control and treated mice. Unpaired t-test, *P<0.05.

(F) Representative SA-β-Gal-stained kidney sections. Blue dots represent SA-β-Gal positive staining. Control is a pDNA vector where the p53 promoter is driving the expression of a catalytically inactive iCasp9, encapsulated within FAST-PLVs.

## 5.6. Supplementary Material

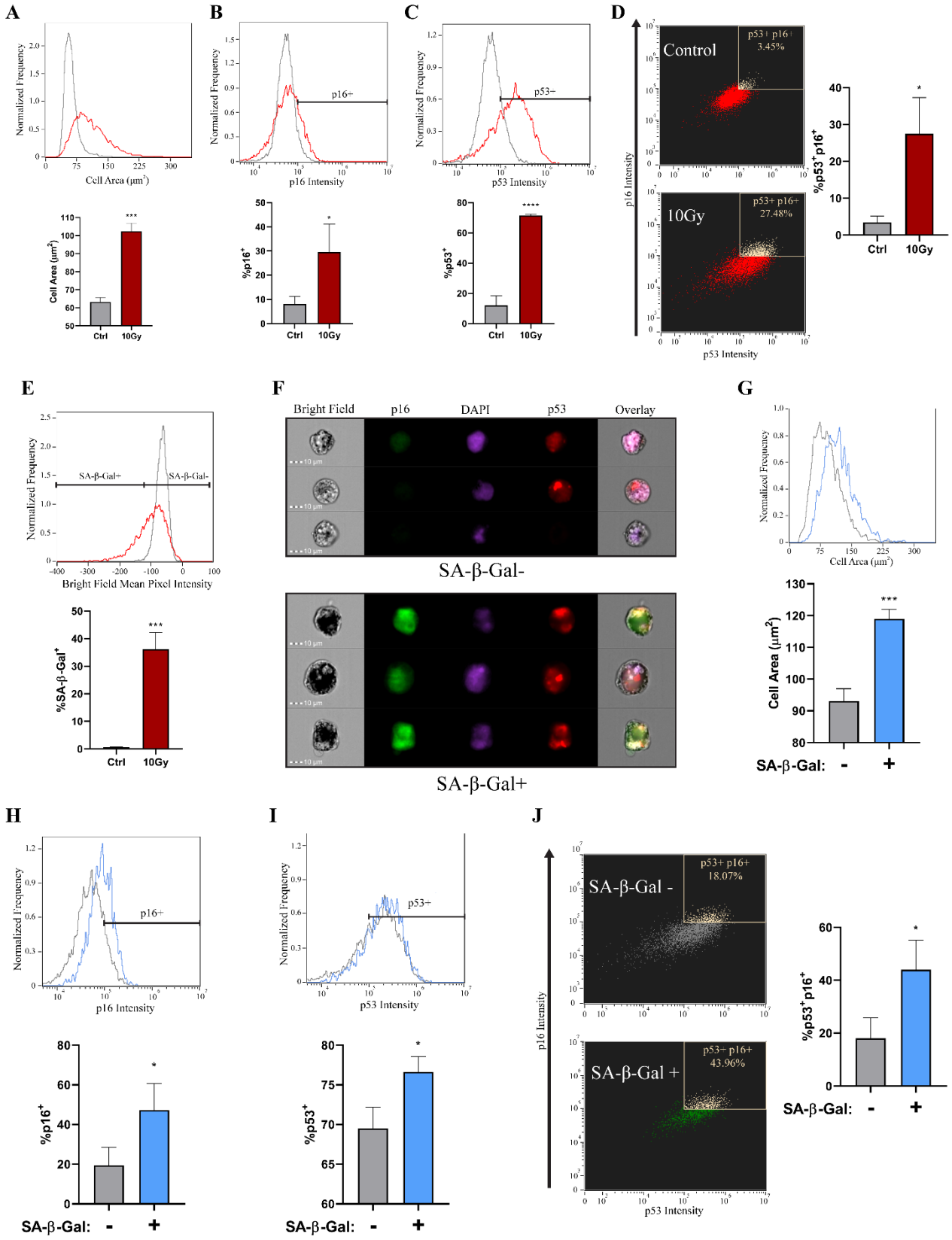

**Supplementary Figure 5.1 – SA-β-Gal analysis on imaging cytometer enables identification of multiple senescence markers.**

(A) Cell area of irradiated BPH-1 cells. Unpaired t-test, ***P<0.001.
(B) $P16^{Ink4a}$ positive population in irradiated and control BPH-1 cells. Unpaired t-test, *P<0.05.
(C) P53 positive population in irradiated and control BPH-1 cells. Unpaired t-test, ****P<0.0001.
(D) P53 and p16Ink4a dual positive population in irradiated and control BPH-1 cells. Unpaired t-test, *P<0.05.
(E) SA-β-Gal positive population in irradiated and control BPH-1 cells. Unpaired t-test, ***P<0.001.
(F) Representative imaging flow cytometry images of SA-β-Gal+ and SA-β-Gal- irradiated BPH-1 cells
(G) Cell area of SA-β-Gal+ and SA-β-Gal- irradiated BPH-1 cells. Unpaired t-test, ***P<0.001.
(H) $P16^{Ink4a}$ positive population in SA-β-Gal+ and SA-β-Gal- irradiated BPH-1 cells. Unpaired t-test, *P<0.05.
(I) P53 positive population in SA-β-Gal+ and SA-β-Gal- irradiated BPH-1 cells. Unpaired t-test, *P<0.05.
(J) $P16^{Ink4a}$ + p53 dual positive population in SA-β-Gal+ and SA-β-Gal- irradiated BPH-1 cells. Unpaired t-test, *P<0.05.

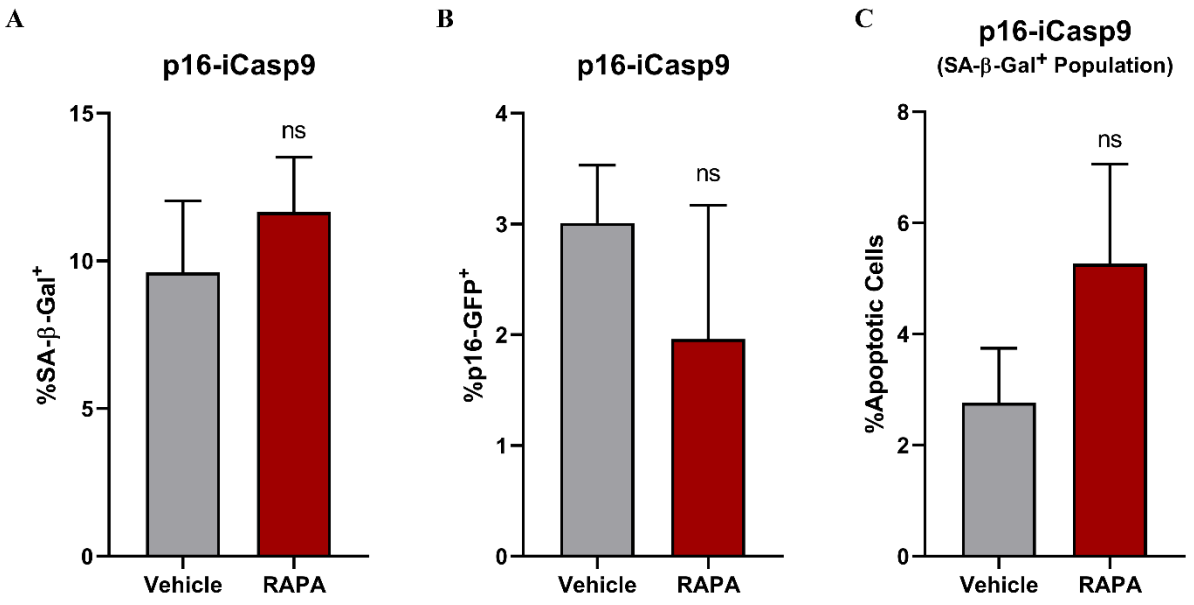


**Supplementary Figure 5.2 – Treatment of senescent BPH-1 cells with p16-iCasp9-GFP.**

(A) SA-β-Gal positive irradiated BPH-1 cells transfected with p16-iCasp9-GFP.

(B) Percentage of the total population that is positive for p16-GFP following treatment with vehicle or RAPA.

(C) BPH-1 cells are gated on the SA-β-Gal positive population and the built-in apoptosis wizard in the ImageStream® analysis software analyzed the incidence of apoptosis induction in p16-iCasp9-GFP transfected cells treated with vehicle or 100nM RAPA.

**Supplementary Table 5.1: Cause of death in longevity study.** Non-urgent medical conditions define: cataracts, anal prolapse, and dermatitis – these morbidities were censored from survival analysis.

| Group: | PBS | | p53 | | p16 | | p53+p16 | |
|---|---|---|---|---|---|---|---|---|
| Total Mice: | 12 | | 10 | | 10 | | 9 | |
| [redacted] | Count | Percentage | Count | Percentage | Count | Percentage | Count | Percentage |
| Cancer | 3 | 25 | 3 | 30 | 4 | 40 | 3 | 33.3 |
| Infection | 1 | 8.3 | 0 | 0 | 1 | 10 | 0 | 0 |
| Liver disease | 3 | 25 | 3 | 30 | 2 | 20 | 1 | 11.1 |
| Internal bleeding | 0 | 0 | 1 | 10 | 1 | 10 | 0 | 0 |
| Non-Urgent | 2 | 16.7 | 2 | 20 | 0 | 0 | 3 | 33.3 |
| Urogenital | 1 | 8.3 | 1 | 10 | 0 | 0 | 0 | 0 |
| Splenomegaly | 1 | 8.3 | 2 | 20 | 1 | 10 | 1 | 11.1 |

**Supplementary Table 5.2: Circulating levels of pro-inflammatory cytokines**

| Cytokine | Treatment Group | Time Post Injection (Days) | | |
|---|---|---|---|---|
| (pg/ml) | | 0 | 12 | 24 |
| IFNγ | PBS | 0.13 ± 0.08 | 0.17 ± 0.11 | 0.21 ± 0.09 |
| | p53 | 0.23 ± 0.08 | 0.86 ± 0.5 | 0.48 ± 0.09 |
| | p16 | 0.40 ± 0.39 | 0.91 ± 0.08 | 0.48 ± 0.14 |
| | p53+p16 | 0.30 ± 0.16 | 3.94 ± 4.62 | 0.49 ± 0.16 |
| IL-10 | PBS | 2.03 ± 2.03 | 5.68 ± 2.30 | 20.83 ± 16.58 |
| | p53 | 8.94 ± 1.71 | 28.20 ± 10.79 | 50.51 ± 47.40 |
| | p16 | 8.96 ± 2.80 | 33.53 ± 8.75 | 22.72 ± 4.76 |
| | p53+p16 | 31.11 ± 25.25 | 71.79 ± 22.44 | 49.26 ± 37.29 |
| IL-1β | PBS | 0.41 ± 0.34 | 4.37 ± 3.80 | 0.67 ± 0.49 |
| | p53 | 0.88 ± 0.32 | 0.92 ± 0.37 | 2.64 ± 2.83 |
| | p16 | 0.05 ± 0.07 | 7.69 ± 10.31 | 0.41 ± 0.48 |
| | p53+p16 | 0.04 ± 0.06 | 1.19 ± 0.76 | 0.72 ± 0.06 |
| IL-2 | PBS | N/A | N/A | 0.22 ± 0.09 |
| | p53 | 0.12 ± 0.14 | 0.57 ± 0.54 | 1.10 ± 0.52 |
| | p16 | N/A | 0.31 ± 0.44 | 0.75 ± 0.22 |
| | p53+p16 | 0.06 ± 0.10 | 0.61 ± 0.46 | 0.59 ± 0.17 |
| IL-5 | PBS | 1.89 ± 0.22 | 1.94 ± 0.84 | 1.60 ± 0.93 |
| | p53 | 0.93 ± 0.68 | 6.92 ± 6.07 | 1.74 ± 0.77 |
| | p16 | 2.25 ± 0.76 | 4.09 ± 0.49 | 1.07 ± 0.85 |
| | p53+p16 | 1.11 ± 0.61 | 2.33 ± 0.65 | 0.29 ± 0.18 |
| IL-6 | PBS | 40.09 ± 9.23 | 91.03 ± 10.22 | 17.42 ± 6.98 |
| | p53 | 23.63 ± 10.23 | 37.69 ± 7.52 | 100.46 ± 40.48 |
| | p16 | 75.79 ± 29.03 | 104.46 ± 19.93 | 73.52 ± 69.22 |
| | p53+p16 | 54.26 ± 17.44 | 151.77 ± 192.42 | 28.01 ± 23.20 |
| CXCL1 | PBS | 98.94 ± 36.74 | 140.89 ± 17.49 | 89.83 ± 3.95 |
| | p53 | 105.12 ± 49.07 | 73.20 ± 15.09 | 102.25 ± 27.31 |
| | p16 | 157.12 ± 65.40 | 103.30 ± 4.46 | 51.47 ± 29.69 |
| | p53+p16 | 118.19 ± 33.54 | 82.88 ± 12.69 | 102.10 ± 20.75 |
| TNF-α | PBS | 7.34 ± 0.94 | 9.59 ± 2.60 | 7.41 ± 0.14 |

| | | | | |
|---|---|---|---|---|
| | p53 | 8.89 ± 2.37 | 15.83 ± 4.53 | 17.11 ± 5.02 |
| | p16 | 20.86 ± 20.51 | 18.87 ± 6.36 | 12.87 ± 1.18 |
| | p53+p16 | 10.46 ± 4.80 | 27.11 ± 9.83 | 15.57 ± 4.80 |

## 6. Summary and Future Directions

Gene therapy is one of the most rapidly growing fields in modern medicine. The goal of this thesis was to present a novel gene therapy delivery platform as well as examine several potential genetic treatment modalities. Development of Fusogenix proteolipid vehicles (FAST-PLVs) as described here stems from our hypothesis that a nucleic acid delivery platform that combines the positive aspects of both non-viral and viral platforms would be able to achieve a high degree of transgene expression, while maintaining an excellent safety profile required for the treatment of patients in poor health. The challenge with this method is deciding what viral proteins would be valuable and how to incorporate them into a non-viral platform. A common theme throughout this thesis has been immunogenicity: repetitive dosing is not feasible with a highly immunogenic platform. Therefore, care most be taken when incorporating a potentially immunogenic protein. As discussed previously, CPPs represent one of the first viral peptides utilized for enhancing drug delivery. Conjugation of CPPs to nanoparticles has been extensively examined to improve drug delivery, however, to the best of our knowledge these techniques have seen little clinical success[591,592]. CPPs are highly charged molecules that are heavily influenced by the immune system and serum proteins, which impacts their efficacy [63,593].

Targeting is one of the most extensively studied areas in nanoparticle-mediated drug delivery. This is especially true with small molecule cytotoxic compounds like chemotherapy, where uptake into healthy tissues can lead to adverse events. Many methods of nanoparticle targeting have been developed and include antibody or ligand attachment, or incorporation of activatable CPPs that can only function when in the presence of enzymes released in the tumor microenvironment. However, the problem with all these strategies is selectivity. Targeting nanoparticles does not make them selective for the target tissue, rather it increases the efficacy of uptake. Therefore, non-

target cells will still take up and be affected by the encapsulated cargo. Indeed, targeting does increase efficacy and consequently enables lower doses, however, the goal of any targeting strategy is to increase efficacy while simultaneously decreasing off-target effects, not to compromise the dose to limit adverse events[594,595]. FAST proteins show no target selectively, they function as bona fide fusogens able to fuse and mediate delivery to all cell types. How then are we able to ensure off-target effects are limited with the FAST-PLV platform? We propose utilizing the intrinsic ability of DNA to have expression regulated by tissue specific promoters. Though this method is far from perfect and off-target transgene expression is to be expected, the results presented here illustrate the feasibility of this strategy. In chapter two of this thesis, I demonstrate that expression of the therapeutic protein, FST, can be improved by including the liver specific TTR promoter to the pDNA vector. Though the circulating levels of FST between the ubiquitous CMV promoter and the TTR promoter were not substantially different, we found the TTR promoter resulted in greater functional responses (grip strength and body weight) when compared to the CMV promoter. FST is primarily produced by the liver, this effect could simply be due to the intrinsic protein production and secretion capacity of hepatocytes[596]. Of course, these experiments were conducted using a therapeutic protein and therefore expression in other tissues would not be detrimental and may be beneficial, as was observed with intramuscular FST injection.

This strategy of targeting becomes even more pertinent to cancer therapy, where off-target gene expression can cause substantial toxicity. As including targeting ligands on the surface of nanoparticles has been demonstrated to lack the appropriate selectivity required for systemic treatment[594], we chose to make the encapsulated cargo rather than the nanoparticle selective for cancer. The problem then becomes selecting a DNA promoter that will provide the desired expression profile required for therapeutic effect. In chapter four of this thesis, I examine the

consequences that loss of p53 protein function has on the p53 promoter. I found that p53 loss significantly increases p53 promoter activity and this trend maintains when compared to normal cells, as cancer cells on average have p53 promoter activity orders of magnitude higher than healthy cells. This was exploited by designing a pDNA vector, where the expression of the suicide gene iCasp9 was dependent on p53 promoter activity. This limits suicide gene expression to cancer cells and enables treatment to be administered systemically to target localized and disseminated cancer. We also took this approach to generate a senolytic therapy where the senescent promoters, $p16^{Ink4a}$ and p53, drive the expression of iCasp9, as described in chapter 5. As demonstrated previously, the $p16^{Ink4a}$ promoter is active mainly in senescent cells and can be utilized to target gene expression selectively to this cell population[597,598] . The p53 promoter also has a role in senescence, however, it is mainly functional during the initial stages of senescence induction primarily in response to DNA damage[292]. We therefore postulated that including one or both promoters would offer a means to selectively target suicide gene expression to senescent cells. Though these experiments are still in the preliminary stages, we found that when both promoters were utilized, systemic PLV administration in naturally aged mice increased median lifespan by 17.6% relative to PBS injected controls. A definitive mechanism for this improvement is yet to be determined, but our results indicate there may be decreased senescent cell burden in the kidney, which would lead to improved functionality and overall health.

In chapter 3 of this thesis, I describe the development of a FAST-PLV based DNA SARS-CoV-2 vaccine. An overarching theme of this thesis has been that immunogenicity is detrimental to gene therapy, however, vaccinology is likely an important exception. This is partially the reason adenoviral vectors have substantial clinical utility as vaccine delivery platforms because host immune responses can amplify responses to the encoded antigen[26]. However, this comes with its

own problems as well because the adenoviral vector will have its delivery efficacy decreased substantially with each subsequent administration, therefore limiting it to one or two vaccine doses. This can come as a problem for a virus as widespread and diverse as SARS-CoV-2 and its variants as there is a great possibility that multiple booster doses will be required over the years[599,600]. For this reason, we opted to maintain the FAST-PLV platform in its low immunogenic state and instead focused on increasing the immunogenicity of encapsulated cargo. To achieve this, we included the genetic adjuvants, CpG motifs and eRNA41H (RIG-I agonist), to enhance the adaptive immune response via activation of the innate immune response (TLRs and RIG-I). We anticipate that this DNA SARS-CoV-2 vaccine can overcome the stability issues that have hindered the deployment of the mRNA vaccines in developed nations [423]. Also, given the low immunogenicity of the platform and ease of manufacturing, we expect that the FAST-PLV platform can be utilized for multiple booster doses dealing with any future variants that arise.

We demonstrated here the ability of FAST-PLVs to deliver therapeutic DNA cargo. In the future, we intend to examine the clinical utility of this in relevant disease models. FST has been investigated clinically as a treatment for muscular dystrophy[404,601]. The Duchenne muscular dystrophy (DMD) *mdx* mouse model[602] will be an excellent opportunity to evaluate the clinical utility of this FAST-PLV treatment modality. As for our COVID-19 vaccine, it has completed phase I clinical trials in Canada and is currently undergoing phase II testing in South Africa, where COVID-19 cases are soaring, and vaccine deployment has been limited. Of course, the outcomes of these trials are paramount to determining the clinical utility of our vaccine platform. Additionally, as new strains of SARS-CoV-2 are emerging at an alarming rate, we have also begun testing new variant DNA vaccines that will soon be essential in the fight against COVID-19.

Perhaps the most important unanswered question surrounding our p53 promoter driven suicide gene is the mechanism responsible for p53 promoter activity. We speculate that a complex interplay between RAS, c-Myc, NF-κB, and p53 may facilitate p53 promoter upregulation, however, this is not based on any direct experimental evidence, rather it is speculation given the importance of these proteins in tumor progression and p53 function. Experiments are currently underway to determine the impact p53 loss has on the transcriptional activity of c-Myc and NF-κB. Additionally, uncovering a gene signature that predicts p53 promoter activity will be instrumental in ensuring clinical success of this treatment. One of the major flaws of clinical studies examining p53 targeted therapies described in Section 1.3 is they often lack an inclusion criterion centered around p53 status. Uncovering a predictive gene signature will ensure only patients that are likely to benefit from treatment will be enrolled.

The results described in chapter 5 serve as a steppingstone to future studies. More *in vitro* work is required to characterize cell death following senolytic treatment. Though we did see an improvement in median survival of treated animals, the mechanisms for this improvement are still largely unknown. Our preliminary results indicate that reduced senescent cell burden in the kidneys may be a factor, however, functional readouts must be examined in addition to more senescent markers before any conclusions can be made. We found that treatment was not associated with a reduction in the circulating levels of any SASP markers, however, we are yet to examine the expression of these markers at a tissue specific level. It is possible that SASP was reduced locally in the area surrounding senescent cells and the amount was too low to detect systemically. In a collaboration with Dr. Jahroudi we are examining the impact that treatment will have on senescent endothelial cells. Though this research is still in the early stages, they have

demonstrated that treatment is associated with a reduction platelet aggregation, which may result in improved organ function.

This thesis describes the development of a safe and redosable gene therapy delivery platform that can be utilized multiple treatment indications. To the best of our knowledge, these FAST-PLVs are the only non-viral nucleic acid delivery platform that has reported successful systemic delivery of pDNA. The impact that this could have on the medical field is tremendous. With the ability to alter promoters to achieve tissue specific gene expression this enables protein expression to be tailored to the treatment indication, thus limiting side effects. Furthermore, given the safety of the platform, it is likely that FAST-PLV mediated gene delivery to delicate tissues such as the brain may be possible in the future. As gene delivery is not limited by host immune responses, FAST-PLVs can be utilized to treat chronic diseases that cannot be cured with a single dose. This opens the door to treat numerous diseases in the future that were previously deemed to be untreatable.

# 7. References


1. Ma, C.-C., Wang, Z.-L., Xu, T., He, Z.-Y. & Wei, Y.-Q. The approved gene therapy drugs worldwide: from 1998 to 2019. *Biotechnology Advances* **40**, 107502 (2020).

2. Stein, C. A. & Castanotto, D. FDA-Approved Oligonucleotide Therapies in 2017. *Molecular Therapy* **25**, 1069–1075 (2017).

3. Ginn, S. L., Amaya, A. K., Alexander, I. E., Edelstein, M. & Abedi, M. R. Gene therapy clinical trials worldwide to 2017: An update. *The Journal of Gene Medicine* **20**, e3015 (2018).

4. Rosenberg, S. A. *et al.* Gene Transfer into Humans — Immunotherapy of Patients with Advanced Melanoma, Using Tumor-Infiltrating Lymphocytes Modified by Retroviral Gene Transduction. *New England Journal of Medicine* **323**, 570–578 (1990).

5. Blaese, R. M. *et al.* T Lymphocyte-Directed Gene Therapy for ADA−SCID: Initial Trial Results After 4 Years. *Science* **270**, 475 LP – 480 (1995).

6. Aiuti, A., Roncarolo, M. G. & Naldini, L. Gene therapy for ADA-SCID, the first marketing approval of an ex vivo gene therapy in Europe: paving the road for the next generation of advanced therapy medicinal products. *EMBO molecular medicine* **9**, 737–740 (2017).

7. Yin, H. *et al.* Non-viral vectors for gene-based therapy. *Nature Reviews Genetics* **15**, 541–555 (2014).

8. Milone, M. C. & O'Doherty, U. Clinical use of lentiviral vectors. *Leukemia* **32**, 1529–1541 (2018).

9. Ferrua, F. *et al.* Lentiviral haemopoietic stem/progenitor cell gene therapy for treatment of Wiskott-Aldrich syndrome: interim results of a non-randomised, open-label, phase 1/2 clinical study. *The Lancet Haematology* **6**, e239–e253 (2019).

10. De Ravin, S. S. *et al.* Lentiviral hematopoietic stem cell gene therapy for X-linked severe combined immunodeficiency. *Science Translational Medicine* **8**, 335ra57 LP-335ra57 (2016).

11. Maude, S. L. *et al.* Chimeric antigen receptor T cells for sustained remissions in leukemia. *The New England journal of medicine* **371**, 1507–1517 (2014).

12. Roex, G. *et al.* Safety and clinical efficacy of BCMA CAR-T-cell therapy in multiple myeloma. *Journal of Hematology & Oncology* **13**, 164 (2020).

13. Milone, M. C. & O'Doherty, U. Clinical use of lentiviral vectors. *Leukemia* **32**, 1529–1541 (2018).

14. Bulcha, J. T., Wang, Y., Ma, H., Tai, P. W. L. & Gao, G. Viral vector platforms within the gene therapy landscape. *Signal Transduction and Targeted Therapy* **6**, 53 (2021).

15. Raper, S. E. *et al.* Fatal systemic inflammatory response syndrome in a ornithine transcarbamylase deficient patient following adenoviral gene transfer. *Molecular Genetics and Metabolism* **80**, 148–158 (2003).

16. Thomas, C. E., Ehrhardt, A. & Kay, M. A. Progress and problems with the use of viral vectors for gene therapy. *Nature Reviews Genetics* **4**, 346–358 (2003).

17. Wang, D., Tai, P. W. L. & Gao, G. Adeno-associated virus vector as a platform for gene therapy delivery. *Nature Reviews Drug Discovery* **18**, 358–378 (2019).

18. Scott, L. J. Alipogene Tiparvovec: A Review of Its Use in Adults with Familial Lipoprotein Lipase Deficiency. *Drugs* **75**, 175–182 (2015).

19. Masat, E., Pavani, G. & Mingozzi, F. Humoral immunity to AAV vectors in gene therapy: challenges and potential solutions. *Discovery medicine* **15**, 379–389 (2013).

20. Bessis, N., GarciaCozar, F. J. & Boissier, M.-C. Immune responses to gene therapy vectors: influence on vector function and effector mechanisms. *Gene Therapy* **11**, S10–S17 (2004).

21. Halbert, C. L., Rutledge, E. A., Allen, J. M., Russell, D. W. & Miller, A. D. Repeat Transduction in the Mouse Lung by Using Adeno-Associated Virus Vectors with Different Serotypes. *Journal of Virology* **74**, 1524 LP – 1532 (2000).

22. Boutin, S. *et al.* Prevalence of serum IgG and neutralizing factors against adeno-associated virus (AAV) types 1, 2, 5, 6, 8, and 9 in the healthy population: implications for gene therapy using AAV vectors. *Human gene therapy* **21**, 704–712 (2010).

23. Nayak, S. & Herzog, R. W. Progress and prospects: immune responses to viral vectors. *Gene therapy* **17**, 295–304 (2010).

24. Ferreira, V. *et al.* Immune responses to intramuscular administration of alipogene tiparvovec (AAV1-LPL(S447X)) in a phase II clinical trial of lipoprotein lipase deficiency gene therapy. *Human gene therapy* **25**, 180–188 (2014).

25. Masat, E., Pavani, G. & Mingozzi, F. Humoral immunity to AAV vectors in gene therapy: challenges and potential solutions. *Discovery medicine* **15**, 379–389 (2013).

26. Tatsis, N. & Ertl, H. C. J. Adenoviruses as vaccine vectors. *Molecular Therapy* **10**, 616–629 (2004).

27. Manno, C. S. *et al.* Successful transduction of liver in hemophilia by AAV-Factor IX and limitations imposed by the host immune response. *Nature Medicine* **12**, 342–347 (2006).

28. Mingozzi, F. *et al.* CD8+ T-cell responses to adeno-associated virus capsid in humans. *Nature Medicine* **13**, 419–422 (2007).

29. Mendell, J. R. *et al.* Single-Dose Gene-Replacement Therapy for Spinal Muscular Atrophy. *New England Journal of Medicine* **377**, 1713–1722 (2017).

30. Yin, H. *et al.* Non-viral vectors for gene-based therapy. *Nature Reviews Genetics* **15**, 541–555 (2014).

31. Miao, L. *et al.* Delivery of mRNA vaccines with heterocyclic lipids increases anti-tumor efficacy by STING-mediated immune cell activation. *Nature Biotechnology* **37**, 1174–1185 (2019).

32. Kauffman, K. J. *et al.* Optimization of Lipid Nanoparticle Formulations for mRNA Delivery in Vivo with Fractional Factorial and Definitive Screening Designs. *Nano Letters* **15**, 7300–7306 (2015).

33. Cullis, P. R. & Hope, M. J. Lipid Nanoparticle Systems for Enabling Gene Therapies. *Molecular therapy : the journal of the American Society of Gene Therapy* **25**, 1467–1475 (2017).

34. Akinc, A. *et al.* The Onpattro story and the clinical translation of nanomedicines containing nucleic acid-based drugs. *Nature Nanotechnology* **14**, 1084–1087 (2019).

35. Polack, F. P. *et al.* Safety and Efficacy of the BNT162b2 mRNA Covid-19 Vaccine. *The New England journal of medicine* **383**, 2603–2615 (2020).

36. Baden, L. R. *et al.* Efficacy and Safety of the mRNA-1273 SARS-CoV-2 Vaccine. *The New England journal of medicine* **384**, 403–416 (2021).

37. Reichmuth, A. M., Oberli, M. A., Jaklenec, A., Langer, R. & Blankschtein, D. mRNA vaccine delivery using lipid nanoparticles. *Therapeutic Delivery* **7**, 319–334 (2016).

38. Kulkarni, J. A., Cullis, P. R. & van der Meel, R. Lipid Nanoparticles Enabling Gene Therapies: From Concepts to Clinical Utility. *Nucleic Acid Therapeutics* **28**, 146–157 (2018).

39. Wan, C., Allen, T. M. & Cullis, P. R. Lipid nanoparticle delivery systems for siRNA-based therapeutics. *Drug Delivery and Translational Research* **4**, 74–83 (2014).

40. Hassett, K. J. *et al.* Optimization of Lipid Nanoparticles for Intramuscular Administration of mRNA Vaccines. *Molecular Therapy - Nucleic Acids* **15**, 1–11 (2019).

41. Xue, H. Y., Liu, S. & Wong, H. L. Nanotoxicity: a key obstacle to clinical translation of siRNA-based nanomedicine. *Nanomedicine (London, England)* **9**, 295–312 (2014).

42. Sedic, M. *et al.* Safety Evaluation of Lipid Nanoparticle–Formulated Modified mRNA in the Sprague-Dawley Rat and Cynomolgus Monkey. *Veterinary Pathology* **55**, 341–354 (2017).

43. Zolnik, B. S., González-Fernández, A., Sadrieh, N. & Dobrovolskaia, M. A. Nanoparticles and the immune system. *Endocrinology* **151**, 458–465 (2010).

44. Zhang, J.-S., Liu, F. & Huang, L. Implications of pharmacokinetic behavior of lipoplex for its inflammatory toxicity. *Advanced Drug Delivery Reviews* **57**, 689–698 (2005).

45. Goncalves, G. A. R. & Paiva, R. de M. A. Gene therapy: advances, challenges and perspectives. *Einstein (Sao Paulo, Brazil)* **15**, 369–375 (2017).

46. Szebeni, J. *et al.* Liposome-induced complement activation and related cardiopulmonary distress in pigs: factors promoting reactogenicity of Doxil and AmBisome. *Nanomedicine: Nanotechnology, Biology and Medicine* **8**, 176–184 (2012).

47. Szebeni, J. Complement activation-related pseudoallergy: A stress reaction in blood triggered by nanomedicines and biologicals. *Molecular Immunology* **61**, 163–173 (2014).

48. Yin, W., Xiang, P. & Li, Q. Investigations of the effect of DNA size in transient transfection assay using dual luciferase system. *Analytical Biochemistry* **346**, 289–294 (2005).

49. Kreiss, P. *et al.* Plasmid DNA size does not affect the physicochemical properties of lipoplexes but modulates gene transfer efficiency. *Nucleic acids research* **27**, 3792–3798 (1999).

50. Kulkarni, J. A. *et al.* Design of lipid nanoparticles for in vitro and in vivo delivery of plasmid DNA. *Nanomedicine: Nanotechnology, Biology and Medicine* **13**, 1377–1387 (2017).

51. White, J. M., Delos, S. E., Brecher, M. & Schornberg, K. Structures and mechanisms of viral membrane fusion proteins: multiple variations on a common theme. *Critical reviews in biochemistry and molecular biology* **43**, 189–219 (2008).

52. Copolovici, D. M., Langel, K., Eriste, E. & Langel, Ü. Cell-Penetrating Peptides: Design, Synthesis, and Applications. *ACS Nano* **8**, 1972–1994 (2014).

53. Frankel, A. D. & Pabo, C. O. Cellular uptake of the tat protein from human immunodeficiency virus. *Cell* **55**, 1189–1193 (1988).

54. Mitchell, D. J., Steinman, L., Kim, D. T., Fathman, C. G. & Rothbard, J. B. Polyarginine enters cells more efficiently than other polycationic homopolymers. *The Journal of Peptide Research* **56**, 318–325 (2000).

55. Staecker, H. *et al.* Efficacy and Safety of AM-111 in the Treatment of Acute Unilateral Sudden Deafness-A Double-blind, Randomized, Placebo-controlled Phase 3 Study. *Otology & neurotology : official publication of the American Otological Society, American Neurotology Society [and] European Academy of Otology and Neurotology* **40**, 584–594 (2019).

56. Capron, M. *et al.* Safety of P28GST, a Protein Derived from a Schistosome Helminth Parasite, in Patients with Crohn's Disease: A Pilot Study (ACROHNEM). *Journal of clinical medicine* **9**, 41 (2019).

57. Chiquet, C. *et al.* Postoperative Ocular Inflammation: A Single Subconjunctival Injection of XG-102 Compared to Dexamethasone Drops in a Randomized Trial. *American Journal of Ophthalmology* **174**, 76–84 (2017).

58. Lulla, R. R. *et al.* Phase I trial of p28 (NSC745104), a non-HDM2-mediated peptide inhibitor of p53 ubiquitination in pediatric patients with recurrent or progressive central nervous system tumors: A Pediatric Brain Tumor Consortium Study. *Neuro-oncology* **18**, 1319–1325 (2016).

59. Futaki, S. *et al.* Stearylated Arginine-Rich Peptides: A New Class of Transfection Systems. *Bioconjugate Chemistry* **12**, 1005–1011 (2001).

60. Saleh, T., Bolhassani, A., Shojaosadati, S. A. & Aghasadeghi, M. R. MPG-based nanoparticle: An efficient delivery system for enhancing the potency of DNA vaccine expressing HPV16E7. *Vaccine* **33**, 3164–3170 (2015).

61. Xiang, B. *et al.* PSA-responsive and PSMA-mediated multifunctional liposomes for targeted therapy of prostate cancer. *Biomaterials* **34**, 6976–6991 (2013).

62. Palm, C., Jayamanne, M., Kjellander, M. & Hällbrink, M. Peptide degradation is a critical determinant for cell-penetrating peptide uptake. *Biochimica et Biophysica Acta (BBA) - Biomembranes* **1768**, 1769–1776 (2007).

63. Ritz, S. *et al.* Protein Corona of Nanoparticles: Distinct Proteins Regulate the Cellular Uptake. *Biomacromolecules* **16**, 1311–1321 (2015).

64. Moschos, S. A. *et al.* Lung Delivery Studies Using siRNA Conjugated to TAT(48−60) and Penetratin Reveal Peptide Induced Reduction in Gene Expression and Induction of Innate Immunity. *Bioconjugate Chemistry* **18**, 1450–1459 (2007).

65. Ciechonska, M. & Duncan, R. Reovirus FAST proteins: virus-encoded cellular fusogens. *Trends in Microbiology* **22**, 715–724 (2014).

66. Duncan, R. Fusogenic Reoviruses and Their Fusion-Associated Small Transmembrane (FAST) Proteins. *Annual review of virology* **6**, 341–363 (2019).

67. Dawe, S., Corcoran, J. A., Clancy, E. K., Salsman, J. & Duncan, R. Unusual Topological Arrangement of Structural Motifs in the Baboon Reovirus Fusion-Associated Small Transmembrane Protein. *Journal of Virology* **79**, 6216 LP – 6226 (2005).

68. Jayme, S., Deniz, T., Julie, B. & Roy, D. Extensive Syncytium Formation Mediated by the Reovirus FAST Proteins Triggers Apoptosis-Induced Membrane Instability. *Journal of Virology* **79**, 8090–8100 (2005).

69. Corcoran, J. A. *et al.* Myristoylation, a protruding loop, and structural plasticity are essential features of a nonenveloped virus fusion peptide motif. *The Journal of biological chemistry* **279**, 51386–51394 (2004).

70. Barry, C. & Duncan, R. Multifaceted sequence-dependent and -independent roles for reovirus FAST protein cytoplasmic tails in fusion pore formation and syncytiogenesis. *Journal of virology* **83**, 12185–12195 (2009).

71. Read, J. *et al.* Reovirus FAST Proteins Drive Pore Formation and Syncytiogenesis Using a Novel Helix-Loop-Helix Fusion-Inducing Lipid Packing Sensor. *PLoS pathogens* **11**, e1004962 (2015).

72. Top, D., Read, J. A., Dawe, S. J., Syvitski, R. T. & Duncan, R. Cell-cell membrane fusion induced by p15 fusion-associated small transmembrane (FAST) protein requires a novel fusion peptide motif containing a myristoylated polyproline type II helix. *The Journal of biological chemistry* **287**, 3403–3414 (2012).

73. Top, D. *et al.* Liposome reconstitution of a minimal protein-mediated membrane fusion machine. *The EMBO journal* **24**, 2980–2988 (2005).

74. Kawasaki, T. & Kawai, T. Toll-Like Receptor Signaling Pathways . *Frontiers in Immunology* vol. 5 461 (2014).

75. Hemmi, H. *et al.* A Toll-like receptor recognizes bacterial DNA. *Nature* **408**, 740–745 (2000).

76. Heil, F. *et al.* Species-specific recognition of single-stranded RNA via toll-like receptor 7 and 8. *Science (New York, N.Y.)* **303**, 1526–1529 (2004).

77. Diebold, S. S., Kaisho, T., Hemmi, H., Akira, S. & Reis e Sousa, C. Innate antiviral responses by means of TLR7-mediated recognition of single-stranded RNA. *Science (New York, N.Y.)* **303**, 1529–1531 (2004).

78. Alexopoulou, L., Holt, A. C., Medzhitov, R. & Flavell, R. A. Recognition of double-stranded RNA and activation of NF-κB by Toll-like receptor 3. *Nature* **413**, 732–738 (2001).

79. Kawai, T. & Akira, S. TLR signaling. *Cell Death & Differentiation* **13**, 816–825 (2006).

80. Iwasaki, A. & Medzhitov, R. Toll-like receptor control of the adaptive immune responses. *Nature Immunology* **5**, 987–995 (2004).

81. Loo, Y.-M. & Gale Jr, M. Immune signaling by RIG-I-like receptors. *Immunity* **34**, 680–692 (2011).

82. Hornung, V. *et al.* 5'-Triphosphate RNA is the ligand for RIG-I. *Science (New York, N.Y.)* **314**, 994–997 (2006).

83. Goubau, D. *et al.* Antiviral immunity via RIG-I-mediated recognition of RNA bearing 5'-diphosphates. *Nature* **514**, 372–375 (2014).

84. Chiang, J. J. *et al.* Viral unmasking of cellular 5S rRNA pseudogene transcripts induces RIG-I-mediated immunity. *Nature immunology* **19**, 53–62 (2018).

85. Zhao, Y., Ye, X., Dunker, W., Song, Y. & Karijolich, J. RIG-I like receptor sensing of host RNAs facilitates the cell-intrinsic immune response to KSHV infection. *Nature communications* **9**, 4841 (2018).

86. Sun, L., Wu, J., Du, F., Chen, X. & Chen, Z. J. Cyclic GMP-AMP synthase is a cytosolic DNA sensor that activates the type I interferon pathway. *Science (New York, N.Y.)* **339**, 786–791 (2013).

87. Bowie, A. G. & Unterholzner, L. Viral evasion and subversion of pattern-recognition receptor signalling. *Nature reviews. Immunology* **8**, 911–922 (2008).

88. Chaplin, D. D. Overview of the immune response. *The Journal of allergy and clinical immunology* **125**, S3–S23 (2010).

89. Schmidlin, H., Diehl, S. A. & Blom, B. New insights into the regulation of human B-cell differentiation. *Trends in immunology* **30**, 277–285 (2009).

90. Zhu, N. *et al.* A Novel Coronavirus from Patients with Pneumonia in China, 2019. *New England Journal of Medicine* **382**, 727–733 (2020).

91. Chen, N. *et al.* Epidemiological and clinical characteristics of 99 cases of 2019 novel coronavirus pneumonia in Wuhan, China: a descriptive study. *The Lancet* **395**, 507–513 (2020).

92. Huang, C. *et al.* Clinical features of patients infected with 2019 novel coronavirus in Wuhan, China. *The Lancet* **395**, 497–506 (2020).

93. Zhou, P. *et al.* A pneumonia outbreak associated with a new coronavirus of probable bat origin. *Nature* **579**, 270–273 (2020).

94. Ge, X.-Y. *et al.* Isolation and characterization of a bat SARS-like coronavirus that uses the ACE2 receptor. *Nature* **503**, 535–538 (2013).

95. Li, F., Li, W., Farzan, M. & Harrison, S. C. Structure of SARS coronavirus spike receptor-binding domain complexed with receptor. *Science (New York, N.Y.)* **309**, 1864–1868 (2005).

96. Lan, J. *et al.* Structure of the SARS-CoV-2 spike receptor-binding domain bound to the ACE2 receptor. *Nature* **581**, 215–220 (2020).

97. Hoffmann, M. *et al.* SARS-CoV-2 Cell Entry Depends on ACE2 and TMPRSS2 and Is Blocked by a Clinically Proven Protease Inhibitor. *Cell* **181**, 271-280.e8 (2020).

98. Xiaojie, S., Yu, L., lei, Y., Guang, Y. & Min, Q. Neutralizing antibodies targeting SARS-CoV-2 spike protein. *Stem Cell Research* **50**, 102125 (2021).

99. Walls, A. C. *et al.* Structure, Function, and Antigenicity of the SARS-CoV-2 Spike Glycoprotein. *Cell* **181**, 281-292.e6 (2020).

100. Jafarzadeh, A., Chauhan, P., Saha, B., Jafarzadeh, S. & Nemati, M. Contribution of monocytes and macrophages to the local tissue inflammation and cytokine storm in COVID-19: Lessons from SARS and MERS, and potential therapeutic interventions. *Life sciences* **257**, 118102 (2020).

101. Blanco-Melo, D. *et al.* Imbalanced Host Response to SARS-CoV-2 Drives Development of COVID-19. *Cell* **181**, 1036-1045.e9 (2020).

102. Fu, Y., Cheng, Y. & Wu, Y. Understanding SARS-CoV-2-Mediated Inflammatory Responses: From Mechanisms to Potential Therapeutic Tools. *Virologica Sinica* **35**, 266–271 (2020).

103. Zhou, F. *et al.* Clinical course and risk factors for mortality of adult inpatients with COVID-19 in Wuhan, China: a retrospective cohort study. *Lancet (London, England)* **395**, 1054–1062 (2020).

104. Jamilloux, Y. *et al.* Should we stimulate or suppress immune responses in COVID-19? Cytokine and anti-cytokine interventions. *Autoimmunity reviews* **19**, 102567 (2020).

105. Chen, G. *et al.* Clinical and immunological features of severe and moderate coronavirus disease 2019. *The Journal of Clinical Investigation* **130**, 2620–2629 (2020).

106. Liu, P. P., Blet, A., Smyth, D. & Li, H. The Science Underlying COVID-19. *Circulation* **142**, 68–78 (2020).

107. Ng, O.-W. *et al.* Memory T cell responses targeting the SARS coronavirus persist up to 11 years post-infection. *Vaccine* **34**, 2008–2014 (2016).

108. Cao, W.-C., Liu, W., Zhang, P.-H., Zhang, F. & Richardus, J. H. Disappearance of Antibodies to SARS-Associated Coronavirus after Recovery. *New England Journal of Medicine* **357**, 1162–1163 (2007).

109. Le Bert, N. *et al.* SARS-CoV-2-specific T cell immunity in cases of COVID-19 and SARS, and uninfected controls. *Nature* **584**, 457–462 (2020).

110. Bachmann, M. F., Mohsen, M. O., Zha, L., Vogel, M. & Speiser, D. E. SARS-CoV-2 structural features may explain limited neutralizing-antibody responses. *npj Vaccines* **6**, 2 (2021).

111. Sekine, T. *et al.* Robust T Cell Immunity in Convalescent Individuals with Asymptomatic or Mild COVID-19. *Cell* **183**, 158-168.e14 (2020).

112. National Research Council (US) Division of Health Promotion and Disease Prevention. Vaccine Supply and Innovation. in *Vaccine Supply and Innovation* (1985).

113. Pollard, A. J. & Bijker, E. M. A guide to vaccinology: from basic principles to new developments. *Nature Reviews Immunology* **21**, 83–100 (2021).

114. Abu Abed, O. S. Gene therapy avenues and COVID-19 vaccines. *Genes & Immunity* **22**, 120–124 (2021).

115. Mendonça, S. A., Lorincz, R., Boucher, P. & Curiel, D. T. Adenoviral vector vaccine platforms in the SARS-CoV-2 pandemic. *npj Vaccines* **6**, 97 (2021).

116. Jeyanathan, M. *et al.* Immunological considerations for COVID-19 vaccine strategies. *Nature Reviews Immunology* **20**, 615–632 (2020).

117. Corbett, K. S. *et al.* SARS-CoV-2 mRNA vaccine design enabled by prototype pathogen preparedness. *Nature* **586**, 567–571 (2020).

118. Mulligan, M. J. *et al.* Phase I/II study of COVID-19 RNA vaccine BNT162b1 in adults. *Nature* **586**, 589–593 (2020).

119. Walsh, E. E. *et al.* Safety and Immunogenicity of Two RNA-Based Covid-19 Vaccine Candidates. *New England Journal of Medicine* **383**, 2439–2450 (2020).

120. Liu, Y. *et al.* Neutralizing Activity of BNT162b2-Elicited Serum. *New England Journal of Medicine* **384**, 1466–1468 (2021).

121. Wu, K. *et al.* Serum Neutralizing Activity Elicited by mRNA-1273 Vaccine. *New England Journal of Medicine* **384**, 1468–1470 (2021).

122. van Doremalen, N. *et al.* ChAdOx1 nCoV-19 vaccine prevents SARS-CoV-2 pneumonia in rhesus macaques. *Nature* **586**, 578–582 (2020).

123. Alharbi, N. K. *et al.* ChAdOx1 and MVA based vaccine candidates against MERS-CoV elicit neutralising antibodies and cellular immune responses in mice. *Vaccine* **35**, 3780–3788 (2017).

124. Voysey, M. *et al.* Safety and efficacy of the ChAdOx1 nCoV-19 vaccine (AZD1222) against SARS-CoV-2: an interim analysis of four randomised controlled trials in Brazil, South Africa, and the UK. *The Lancet* **397**, 99–111 (2021).

125. Emary, K. R. W. *et al.* Efficacy of ChAdOx1 nCoV-19 (AZD1222) vaccine against SARS-CoV-2 variant of concern 202012/01 (B.1.1.7): an exploratory analysis of a randomised controlled trial. *Lancet (London, England)* **397**, 1351–1362 (2021).

126. Bolles, M. *et al.* A double-inactivated severe acute respiratory syndrome coronavirus vaccine provides incomplete protection in mice and induces increased eosinophilic proinflammatory pulmonary response upon challenge. *Journal of virology* **85**, 12201–12215 (2011).

127. Tseng, C.-T. *et al.* Immunization with SARS coronavirus vaccines leads to pulmonary immunopathology on challenge with the SARS virus. *PloS one* **7**, e35421–e35421 (2012).

128. Grifoni, A. *et al.* Targets of T Cell Responses to SARS-CoV-2 Coronavirus in Humans with COVID-19 Disease and Unexposed Individuals. *Cell* **181**, 1489-1501.e15 (2020).

129. Sahin, U. *et al.* COVID-19 vaccine BNT162b1 elicits human antibody and TH1 T cell responses. *Nature* **586**, 594–599 (2020).

130. Bray, F., Laversanne, M., Weiderpass, E. & Soerjomataram, I. The ever-increasing importance of cancer as a leading cause of premature death worldwide. *Cancer* **127**, 3029–3030 (2021).

131. Sung, H. *et al.* Global Cancer Statistics 2020: GLOBOCAN Estimates of Incidence and Mortality Worldwide for 36 Cancers in 185 Countries. *CA: A Cancer Journal for Clinicians* **71**, 209–249 (2021).

132. Knudson, A. G. Mutation and Cancer: Statistical Study of Retinoblastoma. *Proceedings of the National Academy of Sciences* **68**, 820 LP – 823 (1971).

133. Kennedy, S. R., Loeb, L. A. & Herr, A. J. Somatic mutations in aging, cancer and neurodegeneration. *Mechanisms of Ageing and Development* **133**, 118–126 (2012).

134. Hanahan, D. & Weinberg, R. A. The Hallmarks of Cancer. *Cell* **100**, 57–70 (2000).

135. Hanahan, D. & Weinberg, R. A. Hallmarks of Cancer: The Next Generation. *Cell* **144**, 646–674 (2011).

136. Fortunato, A. *et al.* Natural Selection in Cancer Biology: From Molecular Snowflakes to Trait Hallmarks. *Cold Spring Harbor perspectives in medicine* **7**, a029652 (2017).

137. Shah, S. P. *et al.* Mutational evolution in a lobular breast tumour profiled at single nucleotide resolution. *Nature* **461**, 809–813 (2009).

138. Mansoori, B., Mohammadi, A., Davudian, S., Shirjang, S. & Baradaran, B. The Different Mechanisms of Cancer Drug Resistance: A Brief Review. *Advanced pharmaceutical bulletin* **7**, 339–348 (2017).

139. Shaw, A. T. *et al.* Resensitization to Crizotinib by the Lorlatinib ALK Resistance Mutation L1198F. *The New England journal of medicine* **374**, 54–61 (2016).

140. Alfarouk, K. O. *et al.* Resistance to cancer chemotherapy: failure in drug response from ADME to P-gp. *Cancer cell international* **15**, 71 (2015).

141. Zugazagoitia, J. *et al.* Current Challenges in Cancer Treatment. *Clinical Therapeutics* **38**, 1551–1566 (2016).

142. Arnedos, M., Soria, J.-C., Andre, F. & Tursz, T. Personalized treatments of cancer patients: A reality in daily practice, a costly dream or a shared vision of the future from the oncology community? *Cancer Treatment Reviews* **40**, 1192–1198 (2014).

143. Lane, D. P. Cancer. p53, guardian of the genome. *Nature* **358**, 15–16 (1992).

144. Vogelstein, B., Lane, D. & Levine, A. J. Surfing the p53 network. *Nature* **408**, 307–310 (2000).

145. Haupt, Y., Maya, R., Kazaz, A. & Oren, M. Mdm2 promotes the rapid degradation of p53. *Nature* **387**, 296–299 (1997).

146. Kubbutat, M. H., Jones, S. N. & Vousden, K. H. Regulation of p53 stability by Mdm2. *Nature* **387**, 299–303 (1997).

147. Shvarts, A. *et al.* MDMX: a novel p53-binding protein with some functional properties of MDM2. *The EMBO Journal* **15**, 5349–5357 (1996).

148. Jackson, M. W. & Berberich, S. J. MdmX protects p53 from Mdm2-mediated degradation. *Molecular and cellular biology* **20**, 1001–1007 (2000).

149. Wade, M. & Wahl, G. M. Targeting Mdm2 and Mdmx in Cancer Therapy: Better Living through Medicinal Chemistry? *Molecular Cancer Research* **7**, 1 LP – 11 (2009).

150. Wang, S. & El-Deiry, W. S. p73 or p53 directly regulates human p53 transcription to maintain cell cycle checkpoints. *Cancer Res* **66**, 6982–6989 (2006).

151. Bug, M. & Dobbelstein, M. Anthracyclines induce the accumulation of mutant p53 through E2F1-dependent and -independent mechanisms. *Oncogene* **30**, 3612–3624 (2011).

152. Kogan-Sakin, I. *et al.* Mutant p53(R175H) upregulates Twist1 expression and promotes epithelial-mesenchymal transition in immortalized prostate cells. *Cell Death Differ* **18**, 271–281 (2011).

153. Fei, P. & El-Deiry, W. S. P53 and radiation responses. *Oncogene* **22**, 5774 (2003).

154. Shirley, S. H. *et al.* Transcriptional Regulation of Estrogen Receptor-α by p53 in Human Breast Cancer Cells. *Cancer research* **69**, 3405–3414 (2009).

155. Bieging, K. T., Mello, S. S. & Attardi, L. D. Unravelling mechanisms of p53-mediated tumour suppression. *Nature Reviews Cancer* **14**, 359 (2014).

156. Shieh, S. Y., Ikeda, M., Taya, Y. & Prives, C. DNA damage-induced phosphorylation of p53 alleviates inhibition by MDM2. *Cell* **91**, 325–334 (1997).

157. Chehab, N. H., Malikzay, A., Stavridi, E. S. & Halazonetis, T. D. Phosphorylation of Ser-20 mediates stabilization of human p53 in response to DNA damage. *Proc Natl Acad Sci U S A* **96**, 13777–13782 (1999).

158. Pereg, Y. *et al.* Phosphorylation of Hdmx mediates its Hdm2- and ATM-dependent degradation in response to DNA damage. *Proceedings of the National Academy of Sciences of the United States of America* **102**, 5056 LP – 5061 (2005).

159. Kawai, H. *et al.* DNA Damage-induced MDMX Degradation Is Mediated by MDM2*. *Journal of Biological Chemistry* **278**, 45946–45953 (2003).

160. Jin, Y. *et al.* 14-3-3γ binds to MDMX that is phosphorylated by UV-activated Chk1, resulting in p53 activation. *The EMBO Journal* **25**, 1207–1218 (2006).

161. Komori, H., Enomoto, M., Nakamura, M., Iwanaga, R. & Ohtani, K. Distinct E2F-mediated transcriptional program regulates p14ARF gene expression. *The EMBO journal* **24**, 3724–3736 (2005).

162. Pomerantz, J. *et al.* The Ink4a Tumor Suppressor Gene Product, p19ARF, Interacts with MDM2 and Neutralizes MDM2's Inhibition of p53. *Cell* **92**, 713–723 (1998).

163. Fogal, V., Hsieh, J.-K., Royer, C., Zhong, S. & Lu, X. Cell cycle-dependent nuclear retention of p53 by E2F1 requires phosphorylation of p53 at Ser315. *The EMBO journal* **24**, 2768–2782 (2005).

164. Mercer, W. E. *et al.* Negative growth regulation in a glioblastoma tumor cell line that conditionally expresses human wild-type p53. *Proceedings of the National Academy of Sciences* **87**, 6166 LP – 6170 (1990).

165. Baker, S. J., Markowitz, S., Fearon, E. R., Willson, J. K. & Vogelstein, B. Suppression of human colorectal carcinoma cell growth by wild-type p53. *Science* **249**, 912 LP – 915 (1990).

166. Donehower, L. A. *et al.* Mice deficient for p53 are developmentally normal but susceptible to spontaneous tumours. *Nature* **356**, 215–221 (1992).

167. Nigro, J. M. *et al.* Mutations in the p53 gene occur in diverse human tumour types. *Nature* **342**, 705–708 (1989).

168. Baker, S. J. *et al.* Chromosome 17 deletions and p53 gene mutations in colorectal carcinomas. *Science* **244**, 217 LP – 221 (1989).

169. Vousden, K. H. & Prives, C. Blinded by the Light: The Growing Complexity of p53. *Cell* **137**, 413–431 (2009).

170. Saldana-Meyer, R. & Recillas-Targa, F. Transcriptional and epigenetic regulation of the p53 tumor suppressor gene. *Epigenetics* **6**, 1068–1077 (2011).

171. Roy, B., Beamon, J., Balint, E. & Reisman, D. Transactivation of the human p53 tumor suppressor gene by c-Myc/Max contributes to elevated mutant p53 expression in some tumors. *Molecular and Cellular Biology* **14**, 7805–7815 (1994).

172. Raman, V. *et al.* Compromised HOXA5 function can limit p53 expression in human breast tumours. *Nature* **405**, 974–978 (2000).

173. Gabay, M., Li, Y. & Felsher, D. W. MYC activation is a hallmark of cancer initiation and maintenance. *Cold Spring Harbor perspectives in medicine* **4**, a014241 (2014).

174. Ordonez-Moran, P., Dafflon, C., Imajo, M., Nishida, E. & Huelsken, J. HOXA5 Counteracts Stem Cell Traits by Inhibiting Wnt Signaling in Colorectal Cancer. *Cancer Cell* **28**, 815–829 (2015).

175. Teo, W. W. *et al.* HOXA5 determines cell fate transition and impedes tumor initiation and progression in breast cancer through regulation of E-cadherin and CD24. *Oncogene* **35**, 5539 (2016).

176. Freed-Pastor, W. A. & Prives, C. Mutant p53: one name, many proteins. *Genes Dev* **26**, 1268–1286 (2012).

177. Liu, J., Zhang, C. & Feng, Z. Tumor suppressor p53 and its gain-of-function mutants in cancer. *Acta Biochim Biophys Sin (Shanghai)* **46**, 170–179 (2014).

178. Baliou, E. *et al.* Deregulation of p53-MDM2 auto-regulatory pathway in breast carcinoma. *Journal of B.U.ON. : official journal of the Balkan Union of Oncology* **21**, 1099–1103 (2016).

179. Oren, M. & Rotter, V. Mutant p53 gain-of-function in cancer. *Cold Spring Harb Perspect Biol* **2**, a001107 (2010).

180. Mello, S. S. & Attardi, L. D. Not all p53 gain-of-function mutants are created equal. *Cell Death and Differentiation* **20**, 855–857 (2013).

181. Gaiddon, C., Lokshin, M., Ahn, J., Zhang, T. & Prives, C. A subset of tumor-derived mutant forms of p53 down-regulate p63 and p73 through a direct interaction with the p53 core domain. *Molecular and cellular biology* **21**, 1874–1887 (2001).

182. Dötsch, V., Bernassola, F., Coutandin, D., Candi, E. & Melino, G. p63 and p73, the ancestors of p53. *Cold Spring Harbor perspectives in biology* **2**, a004887–a004887 (2010).

183. Liu, G. *et al.* solo,mHigh metastatic potential in mice inheriting a targeted p53 missense mutation. *Proc Natl Acad Sci U S A* **97**, 4174–4179 (2000).

184. Olive, K. P. *et al.* Mutant p53 gain of function in two mouse models of Li-Fraumeni syndrome. *Cell* **119**, 847–860 (2004).

185. Lang, G. A. *et al.* Gain of function of a p53 hot spot mutation in a mouse model of Li-Fraumeni syndrome. *Cell* **119**, 861–872 (2004).

186. Solomon, H. *et al.* Mutant p53 gain of function underlies high expression levels of colorectal cancer stem cells markers. *Oncogene* **37**, 1669–1684 (2018).

187. Roman-Rosales, A. A., Garcia-Villa, E., Herrera, L. A., Gariglio, P. & Diaz-Chavez, J. Mutant p53 gain of function induces HER2 over-expression in cancer cells. *BMC Cancer* **18**, 709 (2018).

188. Wilson, J. R. F. *et al.* A novel HER2-positive breast cancer phenotype arising from germline TP53 mutations. *Journal of Medical Genetics* **47**, 771 LP – 774 (2010).

189. Eastham, J. A. *et al.* Association of p53 mutations with metastatic prostate cancer. *Clinical Cancer Research* **1**, 1111 LP – 1118 (1995).

190. Grignon, D. J. *et al.* p53 Status and Prognosis of Locally Advanced Prostatic Adenocarcinoma: a Study Based on RTOG 8610. *JNCI: Journal of the National Cancer Institute* **89**, 158–165 (1997).

191. Schwartzenberg-Bar-Yoseph, F., Armoni, M. & Karnieli, E. The Tumor Suppressor p53 Down-Regulates Glucose Transporters GLUT1and GLUT4 Gene Expression. *Cancer Research* **64**, 2627 LP – 2633 (2004).

192. Bensaad, K. *et al.* TIGAR, a p53-Inducible Regulator of Glycolysis and Apoptosis. *Cell* **126**, 107–120 (2006).

193. Chang, C.-J. *et al.* p53 regulates epithelial–mesenchymal transition and stem cell properties through modulating miRNAs. *Nature Cell Biology* **13**, 317–323 (2011).

194. Ren, D. *et al.* Wild-type p53 suppresses the epithelial-mesenchymal transition and stemness in PC-3 prostate cancer cells by modulating miR-145. *Int J Oncol* **42**, 1473–1481 (2013).

195. Coussens, L. M. & Werb, Z. Inflammation and cancer. *Nature* **420**, 860–867 (2002).

196. Schoppmann, S. F. *et al.* Tumor-associated macrophages express lymphatic endothelial growth factors and are related to peritumoral lymphangiogenesis. *The American journal of pathology* **161**, 947–956 (2002).

197. Tsung, K., Dolan, J. P., Tsung, Y. L. & Norton, J. A. Macrophages as Effector Cells in Interleukin 12-induced T Cell-dependent Tumor Rejection. *Cancer Research* **62**, 5069 LP – 5075 (2002).

198. Brighenti, E. *et al.* Interleukin 6 downregulates p53 expression and activity by stimulating ribosome biogenesis: a new pathway connecting inflammation to cancer. *Oncogene* **33**, 4396–4406 (2014).

199. Pastor, D. M., Irby, R. B. & Poritz, L. S. Tumor Necrosis Factor α Induces p53 Up-regulated Modulator of Apoptosis Expression in Colorectal Cancer Cell Lines. *Diseases of the Colon & Rectum* **53**, (2010).

200. Liu, T., Zhang, L., Joo, D. & Sun, S.-C. NF-κB signaling in inflammation. *Signal transduction and targeted therapy* **2**, 17023 (2017).

201. Lu, T. *et al.* Secreted transforming growth factor beta2 activates NF-kappaB, blocks apoptosis, and is essential for the survival of some tumor cells. *Proceedings of the National Academy of Sciences of the United States of America* **101**, 7112–7117 (2004).

202. Kirch, H. C., Flaswinkel, S., Rumpf, H., Brockmann, D. & Esche, H. Expression of human p53 requires synergistic activation of transcription from the p53 promoter by AP-1, NF-kappaB and Myc/Max. *Oncogene* **18**, 2728–2738 (1999).

203. Fujiwara, T. *et al.* A Retroviral Wild-type p53 Expression Vector Penetrates Human Lung Cancer Spheroids and Inhibits Growth by Inducing Apoptosis. *Cancer Research* **53**, 4129 LP – 4133 (1993).

204. Shaw, P. *et al.* Induction of apoptosis by wild-type p53 in a human colon tumor-derived cell line. *Proceedings of the National Academy of Sciences of the United States of America* **89**, 4495–4499 (1992).

205. Fujiwara, T. *et al.* Therapeutic Effect of a Retroviral Wild-Type p53 Expression Vector in an Orthotopic Lung Cancer Model. *JNCI: Journal of the National Cancer Institute* **86**, 1458–1462 (1994).

206. Roth, J. A. *et al.* Retrovirus–mediated wild–type P53 gene transfer to tumors of patients with lung cancer. *Nature Medicine* **2**, 985–991 (1996).

207. Zhang, W. W. *et al.* High-efficiency gene transfer and high-level expression of wild-type p53 in human lung cancer cells mediated by recombinant adenovirus. *Cancer gene therapy* **1**, 5–13 (1994).

208. Spitz, F. R. *et al.* Adenoviral-mediated wild-type p53 gene expression sensitizes colorectal cancer cells to ionizing radiation. *Clinical Cancer Research* **2**, 1665 LP – 1671 (1996).

209. Nielsen, L. L. *et al.* Efficacy of p53 adenovirus-mediated gene therapy against human breast cancer xenografts. *Cancer gene therapy* **4**, 129–138 (1997).

210. Swisher, S. G. *et al.* Adenovirus-Mediated p53 Gene Transfer in Advanced Non-Small-Cell Lung Cancer. *JNCI: Journal of the National Cancer Institute* **91**, 763–771 (1999).

211. Clayman, G. L. *et al.* Adenovirus-mediated p53 gene transfer in patients with advanced recurrent head and neck squamous cell carcinoma. *Journal of Clinical Oncology* **16**, 2221–2232 (1998).

212. Peng, Z. *et al.* Clinical Evaluation of Safety and Efficacy of Intratumoral Administration of a Recombinant Adenoviral-p53 Anticancer Agent (Genkaxin). *Molecular Therapy* **7**, S422–S423 (2003).

213. Swisher, S. G. *et al.* Induction of p53-regulated Genes and Tumor Regression in Lung Cancer Patients after Intratumoral Delivery of Adenoviral p53 (INGN 201) and Radiation Therapy. *Clinical Cancer Research* **9**, 93 LP – 101 (2003).

214. Zhang, W.-W. *et al.* The First Approved Gene Therapy Product for Cancer Ad-p53 (Gendicine): 12 Years in the Clinic. *Human Gene Therapy* **29**, 160–179 (2018).

215. Chen, G.-X. *et al.* Clinical utility of recombinant adenoviral human p53 gene therapy: current perspectives. *OncoTargets and therapy* **7**, 1901–1909 (2014).

216. Wang, Y. *et al.* Restoring expression of wild-type p53 suppresses tumor growth but does not cause tumor regression in mice with a p53 missense mutation. *The Journal of Clinical Investigation* **121**, 893–904 (2011).

217. Clayman, G. L. *et al.* In Vivo Molecular Therapy with p53 Adenovirus for Microscopic Residual Head and Neck Squamous Carcinoma. *Cancer Research* **55**, 1 LP – 6 (1995).

218. Zhang, W.-W. *et al.* Safety Evaluation of Ad5CMY-p53 In Vitro and In Vivo. *Human Gene Therapy* **6**, 155–164 (1995).

219. Vassilev, L. T. *et al.* In Vivo Activation of the p53 Pathway by Small-Molecule Antagonists of MDM2. *Science* **303**, 844 LP – 848 (2004).

220. Vu, B. *et al.* Discovery of RG7112: A Small-Molecule MDM2 Inhibitor in Clinical Development. *ACS Medicinal Chemistry Letters* **4**, 466–469 (2013).

221. Ding, K. *et al.* Structure-Based Design of Potent Non-Peptide MDM2 Inhibitors. *Journal of the American Chemical Society* **127**, 10130–10131 (2005).

222. Wang, S. *et al.* SAR405838: An Optimized Inhibitor of MDM2–p53 Interaction That Induces Complete and Durable Tumor Regression. *Cancer Research* **74**, 5855 LP – 5865 (2014).

223. Zhao, Y. *et al.* Diastereomeric Spirooxindoles as Highly Potent and Efficacious MDM2 Inhibitors. *Journal of the American Chemical Society* **135**, 7223–7234 (2013).

224. Sun, D. *et al.* Discovery of AMG 232, a Potent, Selective, and Orally Bioavailable MDM2–p53 Inhibitor in Clinical Development. *Journal of Medicinal Chemistry* **57**, 1454–1472 (2014).

225. Ray-Coquard, I. *et al.* Effect of the MDM2 antagonist RG7112 on the P53 pathway in patients with MDM2-amplified, well-differentiated or dedifferentiated liposarcoma: an exploratory proof-of-mechanism study. *The Lancet Oncology* **13**, 1133–1140 (2012).

226. Mahfoudhi, E. *et al.* P53 activation inhibits all types of hematopoietic progenitors and all stages of megakaryopoiesis. *Oncotarget* **7**, 31980–31992 (2016).

227. Wagner, A. J. *et al.* Phase I Trial of the Human Double Minute 2 Inhibitor MK-8242 in Patients With Advanced Solid Tumors. *Journal of clinical oncology : official journal of the American Society of Clinical Oncology* **35**, 1304–1311 (2017).

228. Garcia, D. *et al.* Validation of MdmX as a therapeutic target for reactivating p53 in tumors. *Genes & development* **25**, 1746–1757 (2011).

229. Yu, D.-H. *et al.* Targeting MDMX for Cancer Therapy: Rationale, Strategies, and Challenges . *Frontiers in Oncology* vol. 10 1389 (2020).

230. Dewaele, M. *et al.* Antisense oligonucleotide-mediated MDM4 exon 6 skipping impairs tumor growth. *The Journal of clinical investigation* **126**, 68–84 (2016).

231. Bykov, V. J. N. *et al.* Restoration of the tumor suppressor function to mutant p53 by a low-molecular-weight compound. *Nature Medicine* **8**, 282–288 (2002).

232. Lambert, J. M. R. *et al.* PRIMA-1 Reactivates Mutant p53 by Covalent Binding to the Core Domain. *Cancer Cell* **15**, 376–388 (2009).

233. Cluzeau, T. *et al.* Eprenetapopt Plus Azacitidine in TP53-Mutated Myelodysplastic Syndromes and Acute Myeloid Leukemia: A Phase II Study by the Groupe Francophone des Myélodysplasies (GFM). *Journal of Clinical Oncology* **39**, 1575–1583 (2021).

234. Boeckler, F. M. *et al.* Targeted rescue of a destabilized mutant of p53 by an in silico screened drug. *Proceedings of the National Academy of Sciences of the United States of America* **105**, 10360–10365 (2008).

235. Hiraki, M. *et al.* Small-Molecule Reactivation of Mutant p53 to Wild-Type-like p53 through the p53-Hsp40 Regulatory Axis. *Chemistry & biology* **22**, 1206–1216 (2015).

236. Nguyen, D., Liao, W., Zeng, S. X. & Lu, H. Reviving the guardian of the genome: Small molecule activators of p53. *Pharmacology & therapeutics* **178**, 92–108 (2017).

237. Schulz-Heddergott, R. *et al.* Therapeutic Ablation of Gain-of-Function Mutant p53 in Colorectal Cancer Inhibits Stat3-Mediated Tumor Growth and Invasion. *Cancer cell* **34**, 298-314.e7 (2018).

238. Bossi, G. *et al.* Mutant p53 gain of function: reduction of tumor malignancy of human cancer cell lines through abrogation of mutant p53 expression. *Oncogene* **25**, 304–309 (2006).

239. Yan, W., Liu, G., Scoumanne, A. & Chen, X. Suppression of inhibitor of differentiation 2, a target of mutant p53, is required for gain-of-function mutations. *Cancer Res* **68**, 6789–6796 (2008).

240. Alexandrova, E. M. *et al.* Improving survival by exploiting tumour dependence on stabilized mutant p53 for treatment. *Nature* **523**, 352–356 (2015).

241. Li, D., Marchenko, N. D. & Moll, U. M. SAHA shows preferential cytotoxicity in mutant p53 cancer cells by destabilizing mutant p53 through inhibition of the HDAC6-Hsp90 chaperone axis. *Cell death and differentiation* **18**, 1904–1913 (2011).

242. Pillai, R. N. *et al.* Randomized Phase III Study of Ganetespib, a Heat Shock Protein 90 Inhibitor, With Docetaxel Versus Docetaxel in Advanced Non–Small-Cell Lung Cancer (GALAXY-2). *Journal of Clinical Oncology* **38**, 613–622 (2019).

243. Blumenschein, G. R. *et al.* Phase II trial of the histone deacetylase inhibitor vorinostat (Zolinza™, suberoylanilide hydroxamic acid, SAHA) in patients with recurrent and/or metastatic head and neck cancer. *Investigational New Drugs* **26**, 81–87 (2008).

244. Martinez, L. A. *et al.* Synthetic small inhibiting RNAs: Efficient tools to inactivate oncogenic mutations and restore p53 pathways. *Proceedings of the National Academy of Sciences* **99**, 14849 LP – 14854 (2002).

245. Ubby, I. *et al.* Cancer therapeutic targeting using mutant–p53-specific siRNAs. *Oncogene* **38**, 3415–3427 (2019).

246. Debbas, M. & White, E. Wild-type p53 mediates apoptosis by E1A, which is inhibited by E1B. *Genes & Development* **7**, 546–554 (1993).

247. Bischoff, J. R. *et al.* An adenovirus mutant that replicates selectively in p53-deficient human tumor cells. *Science (New York, N.Y.)* **274**, 373–376 (1996).

248. Heise, C. *et al.* ONYX-015, an E1B gene-attenuated adenovirus, causes tumor-specific cytolysis and antitumoral efficacy that can be augmented by standard chemotherapeutic agents. *Nature Medicine* **3**, 639–645 (1997).

249. D., G. F. & A., O. D. p53 Status Does Not Determine Outcome of E1B 55-Kilodalton Mutant Adenovirus Lytic Infection. *Journal of Virology* **72**, 9479–9490 (1998).

250. Thomas, R., Arnd, H., J., W. N., Martin, S. & Harald, zur H. Replication of ONYX-015, a Potential Anticancer Adenovirus, Is Independent of p53 Status in Tumor Cells. *Journal of Virology* **72**, 9470–9478 (1998).

251. Rogulski, K. R. *et al.* In Vivo Antitumor Activity of ONYX-015 Is Influenced by p53 Status and Is Augmented by Radiotherapy. *Cancer Research* **60**, 1193 LP – 1196 (2000).

252. Nemunaitis, J. *et al.* Phase II Trial of Intratumoral Administration of ONYX-015, a Replication-Selective Adenovirus, in Patients With Refractory Head and Neck Cancer. *Journal of Clinical Oncology* **19**, 289–298 (2001).

253. Kirn, D. Clinical research results with dl1520 (Onyx-015), a replication-selective adenovirus for the treatment of cancer: what have we learned? *Gene Therapy* **8**, 89–98 (2001).

254. Reid, T. *et al.* Hepatic Arterial Infusion of a Replication-selective Oncolytic Adenovirus (dl1520). *Cancer Research* **62**, 6070 LP – 6079 (2002).

255. Khuri, F. R. *et al.* a controlled trial of intratumoral ONYX-015, a selectively-replicating adenovirus, in combination with cisplatin and 5-fluorouracil in patients with recurrent head and neck cancer. *Nature medicine* **6**, 879–885 (2000).

256. Garber, K. China Approves World's First Oncolytic Virus Therapy For Cancer Treatment. *JNCI: Journal of the National Cancer Institute* **98**, 298–300 (2006).

257. Weissmueller, S. *et al.* Mutant p53 drives pancreatic cancer metastasis through cell-autonomous PDGF receptor β signaling. *Cell* **157**, 382–394 (2014).

258. Di Agostino, S. *et al.* Gain of function of mutant p53: The mutant p53/NF-Y protein complex reveals an aberrant transcriptional mechanism of cell cycle regulation. *Cancer Cell* **10**, 191–202 (2006).

259. Welti, J. *et al.* Targeting the p300/CBP Axis in Lethal Prostate Cancer. *Cancer Discovery* **11**, 1118 LP – 1137 (2021).

260. Lasko, L. M. *et al.* Discovery of a selective catalytic p300/CBP inhibitor that targets lineage-specific tumours. *Nature* **550**, 128–132 (2017).

261. Yang, Y. *et al.* Discovery of Highly Potent, Selective, and Orally Efficacious p300/CBP Histone Acetyltransferases Inhibitors. *Journal of Medicinal Chemistry* **63**, 1337–1360 (2020).

262. Capaci, V., Mantovani, F. & Del Sal, G. Amplifying Tumor–Stroma Communication: An Emerging Oncogenic Function of Mutant p53 . *Frontiers in Oncology* vol. 10 2869 (2021).

263. Dong, Z.-Y. *et al.* Potential Predictive Value of TP53 and KRAS Mutation Status for Response to PD-1 Blockade Immunotherapy in Lung Adenocarcinoma. *Clinical Cancer Research* **23**, 3012 LP – 3024 (2017).

264. Sun, H. *et al.* Specific TP53 subtype as biomarker for immune checkpoint inhibitors in lung adenocarcinoma. *EBioMedicine* **60**, (2020).

265. Bartek, J. & Lukas, J. Chk1 and Chk2 kinases in checkpoint control and cancer. *Cancer Cell* **3**, 421–429 (2003).

266. Urist, M., Tanaka, T., Poyurovsky, M. V & Prives, C. p73 induction after DNA damage is regulated by checkpoint kinases Chk1 and Chk2. *Genes & Development* **18**, 3041–3054 (2004).

267. Gottifredi, V., Karni-Schmidt, O., Shieh, S. S. & Prives, C. p53 down-regulates CHK1 through p21 and the retinoblastoma protein. *Molecular and cellular biology* **21**, 1066–1076 (2001).

268. Kirch, H. C., Flaswinkel, S., Rumpf, H., Brockmann, D. & Esche, H. Expression of human p53 requires synergistic activation of transcription from the p53 promoter by AP-1, NF-kappaB and Myc/Max. *Oncogene* **18**, 2728–2738 (1999).

269. Sachdeva, M. *et al.* p53 represses c-Myc through induction of the tumor suppressor miR-145. *Proceedings of the National Academy of Sciences of the United States of America* **106**, 3207–3212 (2009).

270. Shao, J. *et al.* Overexpression of the wild-type p53 gene inhibits NF-κB activity and synergizes with aspirin to induce apoptosis in human colon cancer cells. *Oncogene* **19**, 726–736 (2000).

271. de Keizer, P. L. J. The Fountain of Youth by Targeting Senescent Cells? *Trends in Molecular Medicine* **23**, 6–17 (2017).

272. van Deursen, J. M. The role of senescent cells in ageing. *Nature* **509**, 439–446 (2014).

273. Hayflick, L. THE LIMITED IN VITRO LIFETIME OF HUMAN DIPLOID CELL STRAINS. *Exp Cell Res* **37**, 614–636 (1965).

274. Shay, J. W. & Wright, W. E. Hayflick, his limit, and cellular ageing. *Nature Reviews Molecular Cell Biology* **1**, 72–76 (2000).

275. Campisi, J. Aging, cellular senescence, and cancer. *Annual review of physiology* **75**, 685–705 (2013).

276. Abbas, T. & Dutta, A. p21 in cancer: intricate networks and multiple activities. *Nature Reviews Cancer* **9**, 400–414 (2009).

277. Xiong, Y. *et al.* p21 is a universal inhibitor of cyclin kinases. *Nature* **366**, 701–704 (1993).

278. Victorelli, S. & Passos, J. F. Telomeres and Cell Senescence - Size Matters Not. *EBioMedicine* **21**, 14–20 (2017).

279. Ogrunc, M. *et al.* Oncogene-induced reactive oxygen species fuel hyperproliferation and DNA damage response activation. *Cell death and differentiation* **21**, 998–1012 (2014).

280. Yamakoshi, K. *et al.* Real-time in vivo imaging of p16Ink4a reveals cross talk with p53. *The Journal of cell biology* **186**, 393–407 (2009).

281. Passos, J. F. *et al.* Feedback between p21 and reactive oxygen production is necessary for cell senescence. *Molecular systems biology* **6**, 347 (2010).

282. Konishi, H. *et al.* Activation of protein kinase C by tyrosine phosphorylation in response to H2O2. *Proceedings of the National Academy of Sciences* **94**, 11233 LP – 11237 (1997).

283. Takahashi, A. *et al.* Mitogenic signalling and the p16INK4a–Rb pathway cooperate to enforce irreversible cellular senescence. *Nature Cell Biology* **8**, 1291–1297 (2006).

284. Graves, B. J. & Petersen, J. M. Specificity within the ets Family of Transcription Factors. in (eds. vande Woude, G. F. & Klein, G. B. T.-A. in C. R.) vol. 75 1–57 (Academic Press, 1998).

285. Ohtani, N. *et al.* Opposing effects of Ets and Id proteins on p16INK4a expression during cellular senescence. *Nature* **409**, 1067–1070 (2001).

286. Zhang, X. *et al.* The HBP1 transcriptional repressor participates in RAS-induced premature senescence. *Molecular and cellular biology* **26**, 8252–8266 (2006).

287. Li, H. *et al.* Transcriptional factor HBP1 targets P16INK4A, upregulating its expression and consequently is involved in Ras-induced premature senescence. *Oncogene* **29**, 5083–5094 (2010).

288. Kotake, Y., Zeng, Y. & Xiong, Y. DDB1-CUL4 and MLL1 Mediate Oncogene-Induced p16INK4a Activation. *Cancer Research* **69**, 1809 LP – 1814 (2009).

289. Sun, D. *et al.* Epigenomic profiling of young and aged HSCs reveals concerted changes during aging that reinforce self-renewal. *Cell stem cell* **14**, 673–688 (2014).

290. Bracken, A. P. *et al.* The Polycomb group proteins bind throughout the INK4A-ARF locus and are disassociated in senescent cells. *Genes & Development* **21**, 525–530 (2007).

291. Vjekoslav, D., Georges-Edouard, B., Guillaume, F., F., D. L. & H., S. G. Uncoupling between Phenotypic Senescence and Cell Cycle Arrest in Aging p21-Deficient Fibroblasts. *Molecular and Cellular Biology* **20**, 6741–6754 (2000).

292. Alcorta, D. A. *et al.* Involvement of the cyclin-dependent kinase inhibitor p16 (INK4a) in replicative senescence of normal human fibroblasts. *Proceedings of the National Academy of Sciences* **93**, 13742 LP – 13747 (1996).

293. Beauséjour, C. M. *et al.* Reversal of human cellular senescence: roles of the p53 and p16 pathways. *The EMBO journal* **22**, 4212–4222 (2003).

294. Takeuchi, S. *et al.* Intrinsic Cooperation between p16INK4a and p21Waf1/Cip1 in the Onset of Cellular Senescence and Tumor Suppression In vivo. *Cancer Research* **70**, 9381 LP – 9390 (2010).

295. Krishnamurthy, J. *et al.* Ink4a/Arf expression is a biomarker of aging. *The Journal of Clinical Investigation* **114**, 1299–1307 (2004).

296. Coppé, J.-P., Desprez, P.-Y., Krtolica, A. & Campisi, J. The senescence-associated secretory phenotype: the dark side of tumor suppression. *Annual review of pathology* **5**, 99–118 (2010).

297. Coppé, J.-P. *et al.* A Human-Like Senescence-Associated Secretory Phenotype Is Conserved in Mouse Cells Dependent on Physiological Oxygen. *PLOS ONE* **5**, e9188 (2010).

298. Coppe, J. P. *et al.* Senescence-associated secretory phenotypes reveal cell-nonautonomous functions of oncogenic RAS and the p53 tumor suppressor. *PLoS Biol* **6**, 2853–2868 (2008).

299. Coppé, J.-P., Kauser, K., Campisi, J. & Beauséjour, C. M. Secretion of Vascular Endothelial Growth Factor by Primary Human Fibroblasts at Senescence. *Journal of Biological Chemistry* **281**, 29568–29574 (2006).

300. Krtolica, A., Parrinello, S., Lockett, S., Desprez, P.-Y. & Campisi, J. Senescent fibroblasts promote epithelial cell growth and tumorigenesis: A link between cancer and aging. *Proceedings of the National Academy of Sciences* **98**, 12072 LP – 12077 (2001).

301. Coppé, J.-P. *et al.* Senescence-Associated Secretory Phenotypes Reveal Cell-Nonautonomous Functions of Oncogenic RAS and the p53 Tumor Suppressor. *PLOS Biology* **6**, e301 (2008).

302. Rodier, F. *et al.* Persistent DNA damage signalling triggers senescence-associated inflammatory cytokine secretion. *Nature cell biology* **11**, 973–979 (2009).

303. Kuilman, T. *et al.* Oncogene-Induced Senescence Relayed by an Interleukin-Dependent Inflammatory Network. *Cell* **133**, 1019–1031 (2008).

304. Acosta, J. C. *et al.* Chemokine Signaling via the CXCR2 Receptor Reinforces Senescence. *Cell* **133**, 1006–1018 (2008).

305. Acosta, J. C. *et al.* A complex secretory program orchestrated by the inflammasome controls paracrine senescence. *Nature cell biology* **15**, 978–990 (2013).

306. Kang, T.-W. *et al.* Senescence surveillance of pre-malignant hepatocytes limits liver cancer development. *Nature* **479**, 547–551 (2011).

307. Wilkinson, H. N. & Hardman, M. J. Senescence in Wound Repair: Emerging Strategies to Target Chronic Healing Wounds. *Frontiers in cell and developmental biology* **8**, 773 (2020).

308. Demaria, M. *et al.* An essential role for senescent cells in optimal wound healing through secretion of PDGF-AA. *Developmental Cell* **31**, 722–733 (2014).

309. Jun, J.-I. & Lau, L. F. The matricellular protein CCN1 induces fibroblast senescence and restricts fibrosis in cutaneous wound healing. *Nature cell biology* **12**, 676–685 (2010).

310. Krizhanovsky, V. *et al.* Senescence of activated stellate cells limits liver fibrosis. *Cell* **134**, 657–667 (2008).

311. Nelson, G. *et al.* A senescent cell bystander effect: senescence-induced senescence. *Aging cell* **11**, 345–349 (2012).

312. Kuwano, K. *et al.* P21Waf1/Cip1/Sdi1 and p53 expression in association with DNA strand breaks in idiopathic pulmonary fibrosis. *American Journal of Respiratory and Critical Care Medicine* **154**, 477–483 (1996).

313. Minagawa, S. *et al.* Accelerated epithelial cell senescence in IPF and the inhibitory role of SIRT6 in TGF-β-induced senescence of human bronchial epithelial cells. *American Journal of Physiology-Lung Cellular and Molecular Physiology* **300**, L391–L401 (2010).

314. Chilosi, M., Carloni, A., Rossi, A. & Poletti, V. Premature lung aging and cellular senescence in the pathogenesis of idiopathic pulmonary fibrosis and COPD/emphysema. *Translational Research* **162**, 156–173 (2013).

315. Gardner, J. P. *et al.* Rise in Insulin Resistance Is Associated With Escalated Telomere Attrition. *Circulation* **111**, 2171–2177 (2005).

316. Gregor, M. F. & Hotamisligil, G. S. Inflammatory Mechanisms in Obesity. *Annual Review of Immunology* **29**, 415–445 (2011).

317. Minamino, T. *et al.* A crucial role for adipose tissue p53 in the regulation of insulin resistance. *Nature Medicine* **15**, 1082–1087 (2009).

318. Sone, H. & Kagawa, Y. Pancreatic beta cell senescence contributes to the pathogenesis of type 2 diabetes in high-fat diet-induced diabetic mice. *Diabetologia* **48**, 58–67 (2005).

319. Cosgrove, B. D. *et al.* Rejuvenation of the muscle stem cell population restores strength to injured aged muscles. *Nature medicine* **20**, 255–264 (2014).

320. Bernet, J. D. *et al.* p38 MAPK signaling underlies a cell-autonomous loss of stem cell self-renewal in skeletal muscle of aged mice. *Nature medicine* **20**, 265–271 (2014).

321. Du, J. *et al.* Aging increases CCN1 expression leading to muscle senescence. *American journal of physiology. Cell physiology* **306**, C28–C36 (2014).

322. Sousa-Victor, P. *et al.* Geriatric muscle stem cells switch reversible quiescence into senescence. *Nature* **506**, 316–321 (2014).

323. Baker, D. J. *et al.* Clearance of p16 Ink4a-positive senescent cells delays ageing-associated disorders. *Nature* **479**, 232–236 (2011).

324. Baker, D. J. *et al.* Naturally occurring p16(Ink4a)-positive cells shorten healthy lifespan. *Nature* **530**, 184–189 (2016).

325. Zhu, Y. *et al.* The Achilles' heel of senescent cells: from transcriptome to senolytic drugs. *Aging cell* **14**, 644–658 (2015).

326. Xu, M. *et al.* Senolytics improve physical function and increase lifespan in old age. *Nature medicine* **24**, 1246–1256 (2018).

327. Hickson, L. J. *et al.* Senolytics decrease senescent cells in humans: Preliminary report from a clinical trial of Dasatinib plus Quercetin in individuals with diabetic kidney disease. *EBioMedicine* **47**, 446–456 (2019).

328. Justice, J. N. *et al.* Senolytics in idiopathic pulmonary fibrosis: Results from a first-in-human, open-label, pilot study. *EBioMedicine* **40**, 554–563 (2019).

329. Bruncko, M. *et al.* Studies Leading to Potent, Dual Inhibitors of Bcl-2 and Bcl-xL. *Journal of Medicinal Chemistry* **50**, 641–662 (2007).

330. Tse, C. *et al.* ABT-263: A Potent and Orally Bioavailable Bcl-2 Family Inhibitor. *Cancer Research* **68**, 3421 LP – 3428 (2008).

331. Zhu, Y. *et al.* Identification of a novel senolytic agent, navitoclax, targeting the Bcl-2 family of anti-apoptotic factors. *Aging cell* **15**, 428–435 (2016).

332. Yosef, R. *et al.* Directed elimination of senescent cells by inhibition of BCL-W and BCL-XL. *Nature communications* **7**, 11190 (2016).

333. Chang, J. *et al.* Clearance of senescent cells by ABT263 rejuvenates aged hematopoietic stem cells in mice. *Nature Medicine* **22**, 78–83 (2016).

334. Wiley, C. D. *et al.* Small-molecule MDM2 antagonists attenuate the senescence-associated secretory phenotype. *Scientific Reports* **8**, 2410 (2018).

335. Baar, M. P. *et al.* Targeted Apoptosis of Senescent Cells Restores Tissue Homeostasis in Response to Chemotoxicity and Aging. *Cell* **169**, 132-147.e16 (2017).

336. Roberts, T. C., Langer, R. & Wood, M. J. A. Advances in oligonucleotide drug delivery. *Nature Reviews Drug Discovery* (2020) doi:10.1038/s41573-020-0075-7.

337. He, X., Urip, B. A., Zhang, Z., Ngan, C. C. & Feng, B. Evolving AAV-delivered therapeutics towards ultimate cures. *Journal of molecular medicine (Berlin, Germany)* **99**, 593–617 (2021).

338. Thomas, C. E., Ehrhardt, A. & Kay, M. A. Progress and problems with the use of viral vectors for gene therapy. *Nature Reviews Genetics* **4**, 346–358 (2003).

339. Ginn, S. L., Amaya, A. K., Alexander, I. E., Edelstein, M. & Abedi, M. R. Gene therapy clinical trials worldwide to 2017: An update. *The Journal of Gene Medicine* **20**, e3015–e3015 (2018).

340. Boutin, S. *et al.* Prevalence of serum IgG and neutralizing factors against adeno-associated virus (AAV) types 1, 2, 5, 6, 8, and 9 in the healthy population: implications for gene therapy using AAV vectors. *Human gene therapy* **21**, 704–712 (2010).

341. Nayak, S. & Herzog, R. W. Progress and prospects: immune responses to viral vectors. *Gene therapy* **17**, 295–304 (2010).

342. Masat, E., Pavani, G. & Mingozzi, F. Humoral immunity to AAV vectors in gene therapy: challenges and potential solutions. *Discovery medicine* **15**, 379–389 (2013).

343. Ferreira, V. *et al.* Immune responses to intramuscular administration of alipogene tiparvovec (AAV1-LPL(S447X)) in a phase II clinical trial of lipoprotein lipase deficiency gene therapy. *Human gene therapy* **25**, 180–188 (2014).

344. Halbert, C. L., Rutledge, E. A., Allen, J. M., Russell, D. W. & Miller, A. D. Repeat Transduction in the Mouse Lung by Using Adeno-Associated Virus Vectors with Different Serotypes. *Journal of Virology* **74**, 1524 LP – 1532 (2000).

345. Jayaraman, M. *et al.* Maximizing the potency of siRNA lipid nanoparticles for hepatic gene silencing in vivo. *Angewandte Chemie (International ed. in English)* **51**, 8529–8533 (2012).

346. Miao, L. *et al.* Delivery of mRNA vaccines with heterocyclic lipids increases anti-tumor efficacy by STING-mediated immune cell activation. *Nature Biotechnology* **37**, 1174–1185 (2019).

347. Kauffman, K. J. *et al.* Optimization of Lipid Nanoparticle Formulations for mRNA Delivery in Vivo with Fractional Factorial and Definitive Screening Designs. *Nano Letters* **15**, 7300–7306 (2015).

348. Semple, S. C. *et al.* Rational design of cationic lipids for siRNA delivery. *Nature Biotechnology* **28**, 172–176 (2010).

349. Gu, F. *et al.* Precise engineering of targeted nanoparticles by using self-assembled biointegrated block copolymers. *Proceedings of the National Academy of Sciences* **105**, 2586 LP – 2591 (2008).

350. Akinc, A. *et al.* A combinatorial library of lipid-like materials for delivery of RNAi therapeutics. *Nature biotechnology* **26**, 561–569 (2008).

351. Sabnis, S. *et al.* A Novel Amino Lipid Series for mRNA Delivery: Improved Endosomal Escape and Sustained Pharmacology and Safety in Non-human Primates. *Molecular therapy : the journal of the American Society of Gene Therapy* **26**, 1509–1519 (2018).

352. Akinc, A. *et al.* The Onpattro story and the clinical translation of nanomedicines containing nucleic acid-based drugs. *Nature Nanotechnology* **14**, 1084–1087 (2019).

353. Wan, C., Allen, T. M. & Cullis, P. R. Lipid nanoparticle delivery systems for siRNA-based therapeutics. *Drug Delivery and Translational Research* **4**, 74–83 (2014).

354. Cullis, P. R. & Hope, M. J. Lipid Nanoparticle Systems for Enabling Gene Therapies. *Molecular therapy : the journal of the American Society of Gene Therapy* **25**, 1467–1475 (2017).

355. Reichmuth, A. M., Oberli, M. A., Jaklenec, A., Langer, R. & Blankschtein, D. mRNA vaccine delivery using lipid nanoparticles. *Therapeutic Delivery* **7**, 319–334 (2016).

356. Kulkarni, J. A., Cullis, P. R. & van der Meel, R. Lipid Nanoparticles Enabling Gene Therapies: From Concepts to Clinical Utility. *Nucleic Acid Therapeutics* **28**, 146–157 (2018).

357. Hassett, K. J. *et al.* Optimization of Lipid Nanoparticles for Intramuscular Administration of mRNA Vaccines. *Molecular Therapy - Nucleic Acids* **15**, 1–11 (2019).

358. Xue, H. Y., Liu, S. & Wong, H. L. Nanotoxicity: a key obstacle to clinical translation of siRNA-based nanomedicine. *Nanomedicine (London, England)* **9**, 295–312 (2014).

359. Sedic, M. *et al.* Safety Evaluation of Lipid Nanoparticle–Formulated Modified mRNA in the Sprague-Dawley Rat and Cynomolgus Monkey. *Veterinary Pathology* **55**, 341–354 (2017).

360. White, J. M., Delos, S. E., Brecher, M. & Schornberg, K. Structures and mechanisms of viral membrane fusion proteins: multiple variations on a common theme. *Critical reviews in biochemistry and molecular biology* **43**, 189–219 (2008).

361. Ciechonska, M. & Duncan, R. Reovirus FAST proteins: virus-encoded cellular fusogens. *Trends in Microbiology* **22**, 715–724 (2014).

362. Duncan, R. Fusogenic Reoviruses and Their Fusion-Associated Small Transmembrane (FAST) Proteins. *Annual review of virology* **6**, 341–363 (2019).

363. Top, D. *et al.* Liposome reconstitution of a minimal protein-mediated membrane fusion machine. *The EMBO journal* **24**, 2980–2988 (2005).

364. Dawe, S., Corcoran, J. A., Clancy, E. K., Salsman, J. & Duncan, R. Unusual Topological Arrangement of Structural Motifs in the Baboon Reovirus Fusion-Associated Small Transmembrane Protein. *Journal of Virology* **79**, 6216 LP – 6226 (2005).

365. Salsman, J., Top, D., Boutilier, J. & Duncan, R. Extensive syncytium formation mediated by the reovirus FAST proteins triggers apoptosis-induced membrane instability. *J Virol* **79**, 8090–8100 (2005).

366. Corcoran, J. A. *et al.* Myristoylation, a protruding loop, and structural plasticity are essential features of a nonenveloped virus fusion peptide motif. *The Journal of biological chemistry* **279**, 51386–51394 (2004).

367. Top, D., Read, J. A., Dawe, S. J., Syvitski, R. T. & Duncan, R. Cell-cell membrane fusion induced by p15 fusion-associated small transmembrane (FAST) protein requires a novel fusion peptide motif containing a myristoylated polyproline type II helix. *The Journal of biological chemistry* **287**, 3403–3414 (2012).

368. Parmar, H. B., Barry, C., Kai, F. & Duncan, R. Golgi complex–plasma membrane trafficking directed by an autonomous, tribasic Golgi export signal. *Molecular Biology of the Cell* **25**, 866–878 (2014).

369. Read, J. *et al.* Reovirus FAST Proteins Drive Pore Formation and Syncytiogenesis Using a Novel Helix-Loop-Helix Fusion-Inducing Lipid Packing Sensor. *PLoS pathogens* **11**, e1004962–e1004962 (2015).

370. Clancy, E. K. & Duncan, R. Reovirus FAST Protein Transmembrane Domains Function in a Modular, Primary Sequence-Independent Manner To Mediate Cell-Cell Membrane Fusion. *Journal of Virology* **83**, 2941 LP – 2950 (2009).

371. Clancy, E. K. & Duncan, R. Helix-Destabilizing, β-Branched, and Polar Residues in the Baboon Reovirus p15 Transmembrane Domain Influence the Modularity of FAST Proteins. *Journal of Virology* **85**, 4707 LP – 4719 (2011).

372. Richardson, A., de Antueno, R., Duncan, R. & Hoskin, D. W. Intracellular delivery of bovine lactoferricin's antimicrobial core (RRWQWR) kills T-leukemia cells. *Biochemical and Biophysical Research Communications* **388**, 736–741 (2009).

373. Yin, H. *et al.* Non-viral vectors for gene-based therapy. *Nature Reviews Genetics* **15**, 541–555 (2014).

374. Belliveau, N. M. *et al.* Microfluidic Synthesis of Highly Potent Limit-size Lipid Nanoparticles for In Vivo Delivery of siRNA. *Molecular therapy. Nucleic acids* **1**, e37–e37 (2012).

375. Leung, A. K. K., Tam, Y. Y. C., Chen, S., Hafez, I. M. & Cullis, P. R. Microfluidic Mixing: A General Method for Encapsulating Macromolecules in Lipid Nanoparticle Systems. *The Journal of Physical Chemistry B* **119**, 8698–8706 (2015).

376. Chen, G., Xu, S., Renko, K. & Derwahl, M. 71 - Metformin inhibits growth of thyroid carcinoma cells, suppresses self-renewal of derived cancer stem cells, and potentiates the effect of chemotherapeutic agents. *J Clin Endocrinol Metab* **97**, E510-20 (2012).

377. Elsabahy, M. & Wooley, K. L. Cytokines as biomarkers of nanoparticle immunotoxicity. *Chemical Society reviews* **42**, 5552–5576 (2013).

378. Lv, H., Zhang, S., Wang, B., Cui, S. & Yan, J. Toxicity of cationic lipids and cationic polymers in gene delivery. *Journal of Controlled Release* **114**, 100–109 (2006).

379. Goswami, R. *et al.* Gene therapy leaves a vicious cycle. *Frontiers in Oncology* **9**, 1–25 (2019).

380. Arteta, M. Y. *et al.* Successful reprogramming of cellular protein production through mRNA delivered by functionalized lipid nanoparticles. *Proceedings of the National Academy of Sciences* **115**, E3351–E3360 (2018).

381. Bessis, N., GarciaCozar, F. J. & Boissier, M.-C. Immune responses to gene therapy vectors: influence on vector function and effector mechanisms. *Gene Therapy* **11**, S10–S17 (2004).

382. Lowenstine, L. J. A primer of primate pathology: lesions and nonlesions. *Toxicologic Pathology* **31**, 92–102 (2003).

383. Ward, K. W. *et al.* Exploration of the African green monkey as a preclinical pharmacokinetic model: intravenous pharmacokinetic parameters. *Drug Metab Dispos* **36**, 715–720 (2008).

384. Szebeni, J. Complement activation-related pseudoallergy: A stress reaction in blood triggered by nanomedicines and biologicals. *Molecular Immunology* **61**, 163–173 (2014).

385. Szebeni, J. *et al.* Liposome-induced complement activation and related cardiopulmonary distress in pigs: factors promoting reactogenicity of Doxil and AmBisome. *Nanomedicine: Nanotechnology, Biology and Medicine* **8**, 176–184 (2012).

386. Lee, S.-J. & McPherron, A. C. Regulation of myostatin activity and muscle growth. *Proceedings of the National Academy of Sciences* **98**, 9306 LP – 9311 (2001).

387. Al-Zaidy, S. A., Sahenk, Z., Rodino-Klapac, L. R., Kaspar, B. & Mendell, J. R. Follistatin Gene Therapy Improves Ambulation in Becker Muscular Dystrophy. *Journal of neuromuscular diseases* **2**, 185–192 (2015).

388. Mendell, J. R. *et al.* Single-Dose Gene-Replacement Therapy for Spinal Muscular Atrophy. *New England Journal of Medicine* **377**, 1713–1722 (2017).

389. Winbanks, C. E. *et al.* Follistatin-mediated skeletal muscle hypertrophy is regulated by Smad3 and mTOR independently of myostatin. *The Journal of cell biology* **197**, 997–1008 (2012).

390. Hansen, J. S. *et al.* Circulating Follistatin Is Liver-Derived and Regulated by the Glucagon-to-Insulin Ratio. *The Journal of Clinical Endocrinology & Metabolism* **101**, 550–560 (2016).

391. Fitzgerald, K. *et al.* A Highly Durable RNAi Therapeutic Inhibitor of PCSK9. *New England Journal of Medicine* **376**, 41–51 (2016).

392. Fitzgerald, K. *et al.* A Highly Durable RNAi Therapeutic Inhibitor of PCSK9. *N Engl J Med* **376**, 41–51 (2017).

393. Nathwani, A. C. *et al.* Long-term safety and efficacy of factor IX gene therapy in hemophilia B. *The New England journal of medicine* **371**, 1994–2004 (2014).

394. Mendell, J. R. *et al.* Follistatin Gene Therapy for Sporadic Inclusion Body Myositis Improves Functional Outcomes. *Molecular therapy : the journal of the American Society of Gene Therapy* **25**, 870–879 (2017).

395. Keeler, A. M. & Flotte, T. R. Recombinant adeno-associated virus gene therapy in light of Luxturna (and Zolgensma and Glybera): where are we, and how did we get here? *Annual review of virology* **6**, 601–621 (2019).

396. Mingozzi, F. *et al.* CD8+ T-cell responses to adeno-associated virus capsid in humans. *Nature Medicine* **13**, 419–422 (2007).

397. Manno, C. S. *et al.* Successful transduction of liver in hemophilia by AAV-Factor IX and limitations imposed by the host immune response. *Nature Medicine* **12**, 342–347 (2006).

398. Flotte, T. R. *et al.* Phase I Trial of Intranasal and Endobronchial Administration of a Recombinant Adeno-Associated Virus Serotype 2 (rAAV2)-CFTR Vector in Adult Cystic Fibrosis Patients: A Two-Part Clinical Study. *Human Gene Therapy* **14**, 1079–1088 (2003).

399. Flotte, T. R., Schwiebert, E. M., Zeitlin, P. L., Carter, B. J. & Guggino, W. B. Correlation between DNA transfer and cystic fibrosis airway epithelial cell correction after recombinant adeno-associated virus serotype 2 gene therapy. *Human gene therapy* **16**, 921–928 (2005).

400. Ambegia, E. *et al.* Stabilized plasmid–lipid particles containing PEG-diacylglycerols exhibit extended circulation lifetimes and tumor selective gene expression. *Biochimica et Biophysica Acta (BBA) - Biomembranes* **1669**, 155–163 (2005).

401. Paunovska, K. *et al.* Analyzing 2000 in vivo drug delivery data points reveals cholesterol structure impacts nanoparticle delivery. *ACS nano* **12**, 8341–8349 (2018).

402. Haidet, A. M. *et al.* Long-term enhancement of skeletal muscle mass and strength by single gene administration of myostatin inhibitors. *Proceedings of the National Academy of Sciences of the United States of America* **105**, 4318–4322 (2008).

403. Kota, J. *et al.* Follistatin gene delivery enhances muscle growth and strength in nonhuman primates. *Science translational medicine* **1**, 6ra15-6ra15 (2009).

404. Mendell, J. R. *et al.* A phase 1/2a follistatin gene therapy trial for becker muscular dystrophy. *Molecular therapy : the journal of the American Society of Gene Therapy* **23**, 192–201 (2015).

405. Raper, S. E. *et al.* Fatal systemic inflammatory response syndrome in a ornithine transcarbamylase deficient patient following adenoviral gene transfer. *Molecular Genetics and Metabolism* **80**, 148–158 (2003).

406. Wang, D., Tai, P. W. L. & Gao, G. Adeno-associated virus vector as a platform for gene therapy delivery. *Nature Reviews Drug Discovery* **18**, 358–378 (2019).

407. Mali, P. *et al.* RNA-Guided Human Genome Engineering via Cas9. *Science* **339**, 823 LP – 826 (2013).

408. Chew, W. L. *et al.* A multifunctional AAV–CRISPR–Cas9 and its host response. *Nature Methods* **13**, 868–874 (2016).

409. Sander, J. D. & Joung, J. K. CRISPR-Cas systems for editing, regulating and targeting genomes. *Nature Biotechnology* **32**, 347–355 (2014).

410. Colella, P., Ronzitti, G. & Mingozzi, F. Emerging Issues in AAV-Mediated In Vivo Gene Therapy. *Molecular therapy. Methods & clinical development* **8**, 87–104 (2017).

411. Long, C. *et al.* Postnatal genome editing partially restores dystrophin expression in a mouse model of muscular dystrophy. *Science* **351**, 400–403 (2016).

412. Yin, H. *et al.* Therapeutic genome editing by combined viral and non-viral delivery of CRISPR system components in vivo. *Nature Biotechnology* **34**, 328–333 (2016).

413. Baden, L. R. *et al.* Efficacy and Safety of the mRNA-1273 SARS-CoV-2 Vaccine. *The New England journal of medicine* **384**, 403–416 (2021).

414. Wu, K. *et al.* Serum Neutralizing Activity Elicited by mRNA-1273 Vaccine. *New England Journal of Medicine* **384**, 1468–1470 (2021).

415. Sahin, U. *et al.* COVID-19 vaccine BNT162b1 elicits human antibody and TH1 T cell responses. *Nature* **586**, 594–599 (2020).

416. Corbett, K. S. *et al.* SARS-CoV-2 mRNA vaccine design enabled by prototype pathogen preparedness. *Nature* **586**, 567–571 (2020).

417. Anderson, E. J. *et al.* Safety and Immunogenicity of SARS-CoV-2 mRNA-1273 Vaccine in Older Adults. *New England Journal of Medicine* (2020) doi:10.1056/NEJMoa2028436.

418. Jorritsma, S. H. T., Gowans, E. J., Grubor-Bauk, B. & Wijesundara, D. K. Delivery methods to increase cellular uptake and immunogenicity of DNA vaccines. *Vaccine* **34**, 5488–5494 (2016).

419. Hannaman, D., Dupuy, L. C., Ellefsen, B. & Schmaljohn, C. S. A Phase 1 clinical trial of a DNA vaccine for Venezuelan equine encephalitis delivered by intramuscular or intradermal electroporation. *Vaccine* **34**, 3607–3612 (2016).

420. Houser, K. v *et al.* DNA vaccine priming for seasonal influenza vaccine in children and adolescents 6 to 17 years of age: A phase 1 randomized clinical trial. *PLOS ONE* **13**, e0206837–e0206837 (2018).

421. Modjarrad, K. *et al.* Safety and immunogenicity of an anti-Middle East respiratory syndrome coronavirus DNA vaccine: a phase 1, open-label, single-arm, dose-escalation trial. *The Lancet Infectious Diseases* **19**, 1013–1022 (2019).

422. Tebas, P. *et al.* Intradermal SynCon® Ebola GP DNA Vaccine Is Temperature Stable and Safely Demonstrates Cellular and Humoral Immunogenicity Advantages in Healthy Volunteers. *The Journal of Infectious Diseases* **220**, 400–410 (2019).

423. Pardi, N., Hogan, M. J., Porter, F. W. & Weissman, D. mRNA vaccines — a new era in vaccinology. *Nature Reviews Drug Discovery* **17**, 261–279 (2018).

424. Jackson, L. A. *et al.* An mRNA Vaccine against SARS-CoV-2 — Preliminary Report. *New England Journal of Medicine* (2020) doi:10.1056/NEJMoa2022483.

425. Roche, J. A. *et al.* Physiological and histological changes in skeletal muscle following in vivo gene transfer by electroporation. *American journal of physiology. Cell physiology* **301**, C1239–C1250 (2011).

426. Basu, A. & Chakraborty, S. Faculty Opinions recommendation of Zika virus protection by a single low-dose nucleoside-modified mRNA vaccination. (2017) doi:10.3410/f.727261558.793533376.

427. Oba, Y., Ojika, M. & Inouye, S. Firefly luciferase is a bifunctional enzyme: ATP-dependent monooxygenase and a long chain fatty acyl-CoA synthetase. *FEBS letters* **540**, 251–254 (2003).

428. Wen, Y. *et al.* MyoVision: software for automated high-content analysis of skeletal muscle immunohistochemistry. *Journal of applied physiology (Bethesda, Md. : 1985)* **124**, 40–51 (2018).

429. Mulligan, M. J. *et al.* Phase I/II study of COVID-19 RNA vaccine BNT162b1 in adults. *Nature* **586**, 589–593 (2020).

430. Walsh, E. E. *et al.* Safety and Immunogenicity of Two RNA-Based Covid-19 Vaccine Candidates. *New England Journal of Medicine* **383**, 2439–2450 (2020).

431. Yu, D.-H. *et al.* Targeting MDMX for Cancer Therapy: Rationale, Strategies, and Challenges. *Frontiers in Oncology* **10**, 1389 (2020).

432. Smith, T. R. F. *et al.* Immunogenicity of a DNA vaccine candidate for COVID-19. *Nature Communications* **11**, 2601 (2020).

433. de Groot, A. S. *et al.* Better Epitope Discovery, Precision Immune Engineering, and Accelerated Vaccine Design Using Immunoinformatics Tools. *Frontiers in Immunology* **11**, (2020).

434. Shin, M. D. *et al.* COVID-19 vaccine development and a potential nanomaterial path forward. *Nature Nanotechnology* **15**, 646–655 (2020).

435. Jahanafrooz, Z. *et al.* Comparison of DNA and mRNA vaccines against cancer. *Drug Discov Today* **25**, 552–560 (2020).

436. Corrales, L. *et al.* Antagonism of the STING Pathway via Activation of the AIM2 Inflammasome by Intracellular DNA. *Journal of immunology (Baltimore, Md. : 1950)* **196**, 3191–3198 (2016).

437. Suschak, J. J., Wang, S., Fitzgerald, K. A. & Lu, S. A cGAS-Independent STING/IRF7 Pathway Mediates the Immunogenicity of DNA Vaccines. *The Journal of Immunology* **196**, 310 (2016).

438. Jazayeri, S. D. & Poh, C. L. Development of Universal Influenza Vaccines Targeting Conserved Viral Proteins. *Vaccines* **7**, (2019).

439. Koday, M. T. *et al.* Multigenic DNA vaccine induces protective cross-reactive T cell responses against heterologous influenza virus in nonhuman primates. *PLOS ONE* **12**, e0189780–e0189780 (2017).

440. Hobernik, D. & Bros, M. DNA Vaccines-How Far From Clinical Use? *International journal of molecular sciences* **19**, (2018).

441. le Bert, N. *et al.* SARS-CoV-2-specific T cell immunity in cases of COVID-19 and SARS, and uninfected controls. *Nature* **584**, 457–462 (2020).

442. MacGregor, R. R. *et al.* First Human Trial of a DNA-Based Vaccine for Treatment of Human Immunodeficiency Virus Type 1 Infection: Safety and Host Response. *The Journal of Infectious Diseases* **178**, 92–100 (1998).

443. Kulkarni, J. A. *et al.* Design of lipid nanoparticles for in vitro and in vivo delivery of plasmid DNA. *Nanomedicine: Nanotechnology, Biology and Medicine* **13**, 1377–1387 (2017).

444. Cho, H. *et al.* RapidCaP, a novel GEM model for metastatic prostate cancer analysis and therapy, reveals myc as a driver of Pten-mutant metastasis. *Cancer Discov* **4**, 318–333 (2014).

445. Kutzler, M. A. & Weiner, D. B. DNA vaccines: ready for prime time? *Nature Reviews Genetics* **9**, 776–788 (2008).

446. Mriouah, J. *et al.* Abstract 5143: Fusogenic targeted liposomes: novel nanotherapy for specific treatment of prostate cancer. *Cancer Research* **77**, 5143 (2017).

447. Cho, C.-F. *et al.* Molecular targeted viral nanoparticles as tools for imaging cancer. *Methods in molecular biology (Clifton, N.J.)* **1108**, 211–230 (2014).

448. Pharmajet. PharmaJet Partner Zydus Cadila Seeks EUA on World's First Plasmid DNA COVID-19 Vaccine. (2021).

449. Zhang, J.-S., Liu, F. & Huang, L. Implications of pharmacokinetic behavior of lipoplex for its inflammatory toxicity. *Advanced Drug Delivery Reviews* **57**, 689–698 (2005).

450. Zolnik, B. S., González-Fernández, A., Sadrieh, N. & Dobrovolskaia, M. A. Nanoparticles and the immune system. *Endocrinology* **151**, 458–465 (2010).

451. Brown, D. W. *et al.* Safe and Effective Delivery of Nucleic Acids Using Proteolipid Vehicles Formulated with Fusion-Associated Small Transmembrane Proteins. *Pre-submission* (2021).

452. Top, D., Barry, C., Racine, T., Ellis, C. L. & Duncan, R. Enhanced fusion pore expansion mediated by the trans-acting Endodomain of the reovirus FAST proteins. *PLoS pathogens* **5**, e1000331–e1000331 (2009).

453. Corcoran, J. A. *et al.* The p14 fusion-associated small transmembrane (FAST) protein effects membrane fusion from a subset of membrane microdomains. *J Biol Chem* **281**, 31778–31789 (2006).

454. Wu, F. *et al.* A new coronavirus associated with human respiratory disease in China. *Nature* **579**, 265–269 (2020).

455. Luke, J., Carnes, A. E., Hodgson, C. P. & Williams, J. A. Improved antibiotic-free DNA vaccine vectors utilizing a novel RNA based plasmid selection system. *Vaccine* **27**, 6454–6459 (2009).

456. Suschak, J. J. *et al.* Nanoplasmid Vectors Co-expressing Innate Immune Agonists Enhance DNA Vaccines for Venezuelan Equine Encephalitis Virus and Ebola Virus. *Molecular Therapy - Methods & Clinical Development* **17**, 810–821 (2020).

457. Auletta, C. S. Current in vivo Assays for Cutaneous Toxicity: Local and Systemic Toxicity Testing. *Basic & Clinical Pharmacology & Toxicology* **95**, 201–208 (2004).

458. Ulmer, J. B., Donnelly, J. J. & Liu, M. A. DNA Vaccines: Immunogenicity and Preclinical Efficacy. in *Vaccines* (eds. Perlmann, P. & Wigzell, H.) 43–55 (Springer Berlin Heidelberg, 1999). doi:10.1007/978-3-642-59955-2_3 LB - Ulmer1999.

459. NCT04591184, C. T. I. A Clinical Trial of a Prophylactic Plasmid DNA Vaccine for COVID-19 [Covigenix VAX-001] in Adults. vol. 2021 (2020).

460. le Bert, N. *et al.* SARS-CoV-2-specific T cell immunity in cases of COVID-19 and SARS, and uninfected controls. *Nature* **584**, 457–462 (2020).

461. Sekine, T. *et al.* Robust T Cell Immunity in Convalescent Individuals with Asymptomatic or Mild COVID-19. *Cell* **183**, 158-168.e14 (2020).

462. Jeyanathan, M. *et al.* Immunological considerations for COVID-19 vaccine strategies. *Nature Reviews Immunology* **20**, 615–632 (2020).

463. Mateus, J. *et al.* Selective and cross-reactive SARS-CoV-2 T cell epitopes in unexposed humans. *Science* **370**, 89–94 (2020).

464. Tudor, D. *et al.* TLR9 pathway is involved in adjuvant effects of plasmid DNA-based vaccines. *Vaccine* (2005) doi:10.1016/j.vaccine.2004.09.001.

465. Halperin, S. A. *et al.* A phase I study of the safety and immunogenicity of recombinant hepatitis B surface antigen co-administered with an immunostimulatory phosphorothioate oligonucleotide adjuvant. *Vaccine* **21**, 2461–2467 (2003).

466. Cooper, C. L., Angel, J. B., Seguin, I., Davis, H. L. & Cameron, D. W. CPG 7909 adjuvant plus hepatitis B virus vaccination in HIV-infected adults achieves long-term seroprotection for up to 5 years. *Clinical Infectious Diseases* **46**, 1310–1314 (2008).

467. Cooper, C. L. *et al.* CPG 7909, an immunostimulatory TLR9 agonist oligodeoxynucleotide, as adjuvant to Engerix-B® HBV vaccine in healthy adults: A double-blind phase I/II study. *Journal of clinical immunology* **24**, 693–701 (2004).

468. Bange, E. M. *et al.* CD8+ T cells contribute to survival in patients with COVID-19 and hematologic cancer. *Nature Medicine* (2021) doi:10.1038/s41591-021-01386-7.

469. Xiaojie, S., Yu, L., lei, Y., Guang, Y. & Min, Q. Neutralizing antibodies targeting SARS-CoV-2 spike protein. *Stem Cell Research* **50**, 102125 (2021).

470. van Doremalen, N. *et al.* ChAdOx1 nCoV-19 vaccine prevents SARS-CoV-2 pneumonia in rhesus macaques. *Nature* **586**, 578–582 (2020).

471. McMahan, K. *et al.* Correlates of protection against SARS-CoV-2 in rhesus macaques. *Nature* (2020) doi:10.1038/s41586-020-03041-6.

472. Brown, D. W. *et al.* Safe and Effective Delivery of Nucleic Acids Using Proteolipid Vehicles Formulated with Fusion-Associated Small Transmembrane Proteins. *Pre-submission* (2021).

473. Whitt, M. A. Generation of VSV pseudotypes using recombinant ΔG-VSV for studies on virus entry, identification of entry inhibitors, and immune responses to vaccines. *Journal of virological methods* **169**, 365–374 (2010).

474. Francis, M. E. *et al.* SARS-CoV-2 infection in the Syrian hamster model causes inflammation as well as type I interferon dysregulation in both respiratory and non-respiratory tissues including the heart and kidney. *PLoS Pathog* **17**, e1009705 (2021).

475. Takahashi, T. *et al.* p53: a frequent target for genetic abnormalities in lung cancer. *Science (New York, N.Y.)* **246**, 491–494 (1989).

476. Masuda, H., Miller, C., Koeffler, H. P., Battifora, H. & Cline, M. J. Rearrangement of the p53 gene in human osteogenic sarcomas. *Proceedings of the National Academy of Sciences of the United States of America* **84**, 7716–7719 (1987).

477. Hollstein, M., Sidransky, D., Vogelstein, B. & Harris, C. p53 mutations in human cancers. *Science* **253**, 49–53 (1991).

478. Xue, W. *et al.* Senescence and tumour clearance is triggered by p53 restoration in murine liver carcinomas. *Nature* **445**, 656–660 (2007).

479. Ventura, A. *et al.* Restoration of p53 function leads to tumour regression in vivo. *Nature* **445**, 661–665 (2007).

480. Roth, J. A. Adenovirus p53 gene therapy. *Expert Opinion on Biological Therapy* **6**, 55–61 (2006).

481. Zeimet, A. G. & Marth, C. Why did p53 gene therapy fail in ovarian cancer? *The Lancet Oncology* **4**, 415–422 (2003).

482. Duarte, S., Carle, G., Faneca, H., Lima, M. C. P. de & Pierrefite-Carle, V. Suicide gene therapy in cancer: Where do we stand now? *Cancer Letters* **324**, 160–170 (2012).

483. Fan, L., Freeman, K. W., Khan, T., Pham, E. & Spencer, D. M. Improved artificial death switches based on caspases and FADD. *Hum Gene Ther* **10**, 2273–2285 (1999).

484. Straathof, K. C. *et al.* An inducible caspase 9 safety switch for T-cell therapy. *Blood* **105**, 4247–4254 (2005).

485. Renatus, M., Stennicke, H. R., Scott, F. L., Liddington, R. C. & Salvesen, G. S. Dimer formation drives the activation of the cell death protease caspase 9. *Proceedings of the National Academy of Sciences of the United States of America* **98**, 14250–14255 (2001).

486. Stennicke, H. R. *et al.* Caspase-9 Can Be Activated without Proteolytic Processing. *Journal of Biological Chemistry* **274**, 8359–8362 (1999).

487. Stavrou, M. *et al.* A Rapamycin-Activated Caspase 9-Based Suicide Gene. *Mol Ther* **26**, 1266–1276 (2018).

488. Banaszynski, L. A., Liu, C. W. & Wandless, T. J. Characterization of the FKBP·Rapamycin·FRB Ternary Complex. *Journal of the American Chemical Society* **127**, 4715–4721 (2005).

489. He, X., Urip, B. A., Zhang, Z., Ngan, C. C. & Feng, B. Evolving AAV-delivered therapeutics towards ultimate cures. *Journal of molecular medicine (Berlin, Germany)* **99**, 593–617 (2021).

490. Ramamoorth, M. & Narvekar, A. Non viral vectors in gene therapy- an overview. *Journal of clinical and diagnostic research : JCDR* **9**, GE01-GE6 (2015).

491. Thompson, M. G. *et al.* Prevention and Attenuation of Covid-19 with the BNT162b2 and mRNA-1273 Vaccines. *New England Journal of Medicine* (2021) doi:10.1056/NEJMoa2107058.

492. Dowdy, S. F. Overcoming cellular barriers for RNA therapeutics. *Nature Biotechnology* **35**, 222–229 (2017).

493. Ma, Z. *et al.* Cationic lipids enhance siRNA-mediated interferon response in mice. *Biochemical and Biophysical Research Communications* **330**, 755–759 (2005).

494. Mantovani, F., Collavin, L. & Del Sal, G. Mutant p53 as a guardian of the cancer cell. *Cell Death & Differentiation* **26**, 199–212 (2019).

495. Joerger, A. C. & Fersht, A. R. The p53 Pathway: Origins, Inactivation in Cancer, and Emerging Therapeutic Approaches. *Annual Review of Biochemistry* **85**, 375–404 (2016).

496. Tang, Z. *et al.* GEPIA: a web server for cancer and normal gene expression profiling and interactive analyses. *Nucleic Acids Research* **45**, W98–W102 (2017).

497. Kandoth, C. *et al.* Mutational landscape and significance across 12 major cancer types. *Nature* **502**, 333–339 (2013).

498. Bykov, V. J. N., Eriksson, S. E., Bianchi, J. & Wiman, K. G. Targeting mutant p53 for efficient cancer therapy. *Nature Reviews Cancer* **18**, 89–102 (2018).

499. Baugh, E. H., Ke, H., Levine, A. J., Bonneau, R. A. & Chan, C. S. Why are there hotspot mutations in the TP53 gene in human cancers? *Cell Death & Differentiation* **25**, 154–160 (2018).

500. Bunz, F. *et al.* Requirement for p53 and p21 to sustain G2 arrest after DNA damage. *Science* **282**, 1497–1501 (1998).

501. DepMap, B. DepMap 19Q3 Public. *Figshare. Dataset* (2019) doi:https://doi.org/10.6084/m9.figshare.9201770.v2.

502. Lu, X. Tied up in loops: positive and negative autoregulation of p53. *Cold Spring Harbor perspectives in biology* **2**, a000984–a000984 (2010).

503. Harris, S. L. & Levine, A. J. The p53 pathway: positive and negative feedback loops. *Oncogene* **24**, 2899–2908 (2005).

504. Stegh, A. H. Targeting the p53 signaling pathway in cancer therapy - the promises, challenges and perils. *Expert Opin Ther Targets* **16**, 67–83 (2012).

505. McStay, G. P., Salvesen, G. S. & Green, D. R. Overlapping cleavage motif selectivity of caspases: implications for analysis of apoptotic pathways. *Cell Death & Differentiation* **15**, 322–331 (2008).

506. Kim, J. H. *et al.* High cleavage efficiency of a 2A peptide derived from porcine teschovirus-1 in human cell lines, zebrafish and mice. *PloS one* **6**, e18556–e18556 (2011).

507. Donnelly, M. L. L. *et al.* The “cleavage” activities of foot-and-mouth disease virus 2A site-directed mutants and naturally occurring “2A-like” sequences. *The Journal of general virology* **82**, 1027–1041 (2001).

508. Shiozaki, E. N., Chai, J. & Shi, Y. Oligomerization and activation of caspase-9, induced by Apaf-1 CARD. *Proceedings of the National Academy of Sciences* **99**, 4197 LP – 4202 (2002).

509. Li, P. *et al.* Cytochrome c and dATP-Dependent Formation of Apaf-1/Caspase-9 Complex Initiates an Apoptotic Protease Cascade. *Cell* **91**, 479–489 (1997).

510. Robert, C. A decade of immune-checkpoint inhibitors in cancer therapy. *Nature Communications* **11**, 3801 (2020).

511. Ribas, A. & Wolchok, J. D. Cancer immunotherapy using checkpoint blockade. *Science (New York, N.Y.)* **359**, 1350–1355 (2018).

512. Robert, C. *et al.* Pembrolizumab versus Ipilimumab in Advanced Melanoma. *New England Journal of Medicine* **372**, 2521–2532 (2015).

513. Hodi, F. S. *et al.* Improved Survival with Ipilimumab in Patients with Metastatic Melanoma. *New England Journal of Medicine* **363**, 711–723 (2010).

514. Larkin, J. *et al.* Five-Year Survival with Combined Nivolumab and Ipilimumab in Advanced Melanoma. *New England Journal of Medicine* **381**, 1535–1546 (2019).

515. Lechner, M. G. *et al.* Immunogenicity of murine solid tumor models as a defining feature of in vivo behavior and response to immunotherapy. *Journal of immunotherapy (Hagerstown, Md. : 1997)* **36**, 477–489 (2013).

516. Simpson, T. R. *et al.* Fc-dependent depletion of tumor-infiltrating regulatory T cells co-defines the efficacy of anti–CTLA-4 therapy against melanoma. *Journal of Experimental Medicine* **210**, 1695–1710 (2013).

517. Shipkova, M. & Wieland, E. Surface markers of lymphocyte activation and markers of cell proliferation. *Clinica Chimica Acta* **413**, 1338–1349 (2012).

518. Fontenot, J. D., Gavin, M. A. & Rudensky, A. Y. Foxp3 programs the development and function of CD4+CD25+ regulatory T cells. *Nature Immunology* **4**, 330–336 (2003).

519. Chen, W. *et al.* Conversion of peripheral CD4+CD25- naive T cells to CD4+CD25+ regulatory T cells by TGF-beta induction of transcription factor Foxp3. *The Journal of experimental medicine* **198**, 1875–1886 (2003).

520. Yatim, N., Cullen, S. & Albert, M. L. Dying cells actively regulate adaptive immune responses. *Nature Reviews Immunology* **17**, 262–275 (2017).

521. Ladds, M. J. G. W. & Laín, S. Small molecule activators of the p53 response. *Journal of Molecular Cell Biology* **11**, 245–254 (2019).

522. Parrales, A. & Iwakuma, T. Targeting Oncogenic Mutant p53 for Cancer Therapy . *Frontiers in Oncology* vol. 5 288 (2015).

523. Network, C. G. A. Comprehensive molecular portraits of human breast tumours. *Nature* **490**, 61–70 (2012).

524. Visakorpi, T., Kallioniemi, O.-P., Heikkinen, A., Koivula, T. & Isola, J. Small Subgroup of Aggressive, Highly Proliferative Prostatic Carcinomas Defined by p53 Accumulation. *JNCI: Journal of the National Cancer Institute* **84**, 883–887 (1992).

525. Bookstein, R., MacGrogan, D., Hilsenbeck, S. G., Sharkey, F. & Allred, D. C. p53 Is Mutated in a Subset of Advanced-Stage Prostate Cancers. *Cancer Research* **53**, 3369 LP – 3373 (1993).

526. Chang, Y.-L., Wu, C.-T., Shih, J.-Y. & Lee, Y.-C. Comparison of p53 and Epidermal Growth Factor Receptor Gene Status Between Primary Tumors and Lymph Node Metastases in Non-Small Cell Lung Cancers. *Annals of Surgical Oncology* **18**, 543–550 (2011).

527. Steels, E. *et al.* Role of p53 as a prognostic factor for survival in lung cancer: a systematic review of the literature with a meta-analysis. *European Respiratory Journal* **18**, 705 LP – 719 (2001).

528. Bos, J. L. ras Oncogenes in Human Cancer: A Review. *Cancer Research* **49**, 4682 LP – 4689 (1989).

529. Grzes, M. *et al.* A Driver Never Works Alone-Interplay Networks of Mutant p53, MYC, RAS, and Other Universal Oncogenic Drivers in Human Cancer. *Cancers* **12**, 1532 (2020).

530. Vaseva, A. V *et al.* KRAS Suppression-Induced Degradation of MYC Is Antagonized by a MEK5-ERK5 Compensatory Mechanism. *Cancer cell* **34**, 807-822.e7 (2018).

531. Ho, J. S. L., Ma, W., Mao, D. Y. L. & Benchimol, S. p53-Dependent transcriptional repression of c-myc is required for G1 cell cycle arrest. *Molecular and cellular biology* **25**, 7423–7431 (2005).

532. Santoro, A. *et al.* p53 Loss in Breast Cancer Leads to Myc Activation, Increased Cell Plasticity, and Expression of a Mitotic Signature with Prognostic Value. *Cell Reports* **26**, 624-638.e8 (2019).

533. Buganim, Y. *et al.* p53 Regulates the Ras Circuit to Inhibit the Expression of a Cancer-Related Gene Signature by Various Molecular Pathways. *Cancer Research* **70**, 2274 LP – 2284 (2010).

534. Montaño-Samaniego, M., Bravo-Estupiñan, D. M., Méndez-Guerrero, O., Alarcón-Hernández, E. & Ibáñez-Hernández, M. Strategies for Targeting Gene Therapy in Cancer Cells With Tumor-Specific Promoters . *Frontiers in Oncology* vol. 10 2671 (2020).

535. Xie, X. *et al.* Adenovirus-mediated tissue-targeted expression of a caspase-9-based artificial death switch for the treatment of prostate cancer. *Cancer Res* **61**, 6795–6804 (2001).

536. Freytag, S. O. *et al.* Phase I Trial of Replication-competent Adenovirus-mediated Suicide Gene Therapy Combined with IMRT for Prostate Cancer. *Molecular Therapy* **15**, 1016–1023 (2007).

537. Freytag, S. O. *et al.* Phase I Study of Replication-competent Adenovirus-mediated Double Suicide Gene Therapy for the Treatment of Locally Recurrent Prostate Cancer. *Cancer Research* **62**, 4968 LP – 4976 (2002).

538. Karjoo, Z., Chen, X. & Hatefi, A. Progress and problems with the use of suicide genes for targeted cancer therapy. *Advanced drug delivery reviews* **99**, 113–128 (2016).

539. Albert, M. L., Sauter, B. & Bhardwaj, N. Dendritic cells acquire antigen from apoptotic cells and induce class I-restricted CTLs. *Nature* **392**, 86–89 (1998).

540. Tesniere, A. *et al.* Immunogenic death of colon cancer cells treated with oxaliplatin. *Oncogene* **29**, 482–491 (2010).

541. Casares, N. *et al.* Caspase-dependent immunogenicity of doxorubicin-induced tumor cell death . *Journal of Experimental Medicine* **202**, 1691–1701 (2005).

542. Christensen, K., Doblhammer, G., Rau, R. & Vaupel, J. W. Ageing populations: the challenges ahead. *Lancet (London, England)* **374**, 1196–1208 (2009).

543. World Health. Global health and aging. *NIH Publication* **11–7737**, (2011).

544. López-Otín, C., Blasco, M. A., Partridge, L., Serrano, M. & Kroemer, G. The hallmarks of aging. *Cell* **153**, 1194–1217 (2013).

545. Liu, D. & Hornsby, P. J. Senescent Human Fibroblasts Increase the Early Growth of Xenograft Tumors via Matrix Metalloproteinase Secretion. *Cancer Research* **67**, 3117 LP – 3126 (2007).

546. Jeon, O. H. *et al.* Local clearance of senescent cells attenuates the development of post-traumatic osteoarthritis and creates a pro-regenerative environment. *Nature medicine* **23**, 775–781 (2017).

547. Bussian, T. J. *et al.* Clearance of senescent glial cells prevents tau-dependent pathology and cognitive decline. *Nature* **562**, 578–582 (2018).

548. Muñoz-Espín, D. & Serrano, M. Cellular senescence: from physiology to pathology. *Nature Reviews Molecular Cell Biology* **15**, 482 (2014).

549. von Kobbe, C. Targeting senescent cells: approaches, opportunities, challenges. *Aging* **11**, 12844–12861 (2019).

550. Rudin, C. M. *et al.* Phase II study of single-agent navitoclax (ABT-263) and biomarker correlates in patients with relapsed small cell lung cancer. *Clinical cancer research : an official journal of the American Association for Cancer Research* **18**, 3163–3169 (2012).

551. Sharma, A. K. *et al.* The Senolytic Drug Navitoclax (ABT-263) Causes Trabecular Bone Loss and Impaired Osteoprogenitor Function in Aged Mice . *Frontiers in Cell and Developmental Biology* vol. 8 354 (2020).

552. Schoenwaelder, S. M. *et al.* Bcl-xL–inhibitory BH3 mimetics can induce a transient thrombocytopathy that undermines the hemostatic function of platelets. *Blood* **118**, 1663–1674 (2011).

553. Dulić, V., Beney, G. E., Frebourg, G., Drullinger, L. F. & Stein, G. H. Uncoupling between phenotypic senescence and cell cycle arrest in aging p21-deficient fibroblasts. *Molecular and cellular biology* **20**, 6741–6754 (2000).

554. Demaria, M. *et al.* Cellular Senescence Promotes Adverse Effects of Chemotherapy and Cancer Relapse. *Cancer Discov* **7**, 165–176 (2017).

555. Ju, G. Z., Wang, X. M., Fu, S. B. & Liu, S. Z. Effect of ionizing radiation on the expression of p16, cyclinD1 and CDK4 in mouse thymocytes and splenocytes. *Biomed Environ Sci* **16**, 47–52 (2003).

556. Dimri, G. P. *et al.* A biomarker that identifies senescent human cells in culture and in aging skin in vivo. *Proc Natl Acad Sci U S A* **92**, 9363–9367 (1995).

557. Lee, B. Y. *et al.* Senescence-associated beta-galactosidase is lysosomal beta-galactosidase. *Aging Cell* **5**, 187–195 (2006).

558. Baker, D. J. *et al.* Clearance of p16Ink4a-positive senescent cells delays ageing-associated disorders. *Nature* **479**, 232–236 (2011).

559. Hernandez-Segura, A., Nehme, J. & Demaria, M. Hallmarks of Cellular Senescence. *Trends in Cell Biology* **28**, 436–453 (2018).

560. Waaijer, M. E. C. *et al.* The number of p16INK4a positive cells in human skin reflects biological age. *Aging Cell* **11**, 722–725 (2012).

561. Mokhtarieh, A. A., Cheong, S., Kim, S., Chung, B. H. & Lee, M. K. Asymmetric liposome particles with highly efficient encapsulation of siRNA and without nonspecific cell penetration suitable for target-specific delivery. *Biochim Biophys Acta* **1818**, 1633–1641 (2012).

562. Biran, A. *et al.* Quantitative identification of senescent cells in aging and disease. *Aging cell* **16**, 661–671 (2017).

563. Yang, Y.-H. K., Ogando, C. R., Wang See, C., Chang, T.-Y. & Barabino, G. A. Changes in phenotype and differentiation potential of human mesenchymal stem cells aging in vitro. *Stem Cell Research & Therapy* **9**, 131 (2018).

564. Noren Hooten, N. & Evans, M. K. Techniques to Induce and Quantify Cellular Senescence. *J Vis Exp* (2017) doi:10.3791/55533.

565. Kemper, K., Rodermond, H., Colak, S., Grandela, C. & Medema, J. P. Targeting colorectal cancer stem cells with inducible caspase-9. *Apoptosis* **17**, 528–537 (2012).

566. Fasbender, A., Zabner, J., Zeiher, B. G. & Welsh, M. J. A low rate of cell proliferation and reduced DNA uptake limit cationic lipid-mediated gene transfer to primary cultures of ciliated human airway epithelia. *Gene Therapy* **4**, 1173–1180 (1997).

567. Dean, D. A., Dean, B. S., Muller, S. & Smith, L. C. Sequence requirements for plasmid nuclear import. *Experimental cell research* **253**, 713–722 (1999).

568. Coonrod, A., Li, F.-Q. & Horwitz, M. On the mechanism of DNA transfection: efficient gene transfer without viruses. *Gene Therapy* **4**, 1313–1321 (1997).

569. Capecchi, M. R. High efficiency transformation by direct microinjection of DNA into cultured mammalian cells. *Cell* **22**, 479–488 (1980).

570. Ludtke, J. J., Sebestyén, M. G. & Wolff, J. A. The Effect of Cell Division on the Cellular Dynamics of Microinjected DNA and Dextran. *Molecular Therapy* **5**, 579–588 (2002).

571. Dowty, M. E., Williams, P., Zhang, G., Hagstrom, J. E. & Wolff, J. A. Plasmid DNA entry into postmitotic nuclei of primary rat myotubes. *Proceedings of the National Academy of Sciences of the United States of America* **92**, 4572–4576 (1995).

572. Akita, H., Kurihara, D., Schmeer, M., Schleef, M. & Harashima, H. Effect of the Compaction and the Size of DNA on the Nuclear Transfer Efficiency after Microinjection in Synchronized Cells. *Pharmaceutics* **7**, 64–73 (2015).

573. Hébert, E. Improvement of exogenous DNA nuclear importation by nuclear localization signal-bearing vectors: a promising way for non-viral gene therapy? *Biology of the Cell* **95**, 59–68 (2003).

574. Zhu, Y. *et al.* New agents that target senescent cells: the flavone, fisetin, and the BCL-X(L) inhibitors, A1331852 and A1155463. *Aging* **9**, 955–963 (2017).

575. Cai, Y. *et al.* Elimination of senescent cells by β-galactosidase-targeted prodrug attenuates inflammation and restores physical function in aged mice. *Cell Research* **30**, 574–589 (2020).

576. Roberts, T. C., Langer, R. & Wood, M. J. A. Advances in oligonucleotide drug delivery. *Nature Reviews Drug Discovery* (2020) doi:10.1038/s41573-020-0075-7.

577. Hou, X., Zaks, T., Langer, R. & Dong, Y. Lipid nanoparticles for mRNA delivery. *Nature Reviews Materials* (2021) doi:10.1038/s41578-021-00358-0.

578. Priddy, F. H. *et al.* Adeno-associated virus vectored immunoprophylaxis to prevent HIV in healthy adults: a phase 1 randomised controlled trial. *The Lancet HIV* **6**, e230–e239 (2019).

579. Mylonas, K. *et al.* Cellular senescence inhibits renal regeneration after injury in mice, with senolytic treatment promoting repair. *Science Translational Medicine* **13**, (2021).

580. Melk, A. *et al.* Cell senescence in rat kidneys in vivo increases with growth and age despite lack of telomere shortening. *Kidney International* **63**, 2134–2143 (2003).

581. MELK, A. & HALLORAN, P. F. Cell Senescence and Its Implications for Nephrology. *Journal of the American Society of Nephrology* **12**, 385 LP – 393 (2001).

582. Kurokawa, K., Tanaka, T. & Kato, J. p19ARF prevents G1 cyclin-dependent kinase activation by interacting with MDM2 and activating p53 in mouse fibroblasts. *Oncogene* **18**, 2718–2727 (1999).

583. Zhang, Y., Xiong, Y. & Yarbrough, W. G. ARF Promotes MDM2 Degradation and Stabilizes p53: ARF-Ink4a Locus Deletion Impairs Both the Rb and p53 Tumor Suppression Pathways. *Cell* **92**, 725–734 (1998).

584. Baker, D. J. *et al.* Opposing roles for p16Ink4a and p19Arf in senescence and ageing caused by BubR1 insufficiency. *Nat Cell Biol* **10**, 825–836 (2008).

585. Hashimoto, M. *et al.* Elimination of p19ARF-expressing cells enhances pulmonary function in mice. *JCI Insight* **1**, (2016).

586. Mikawa, R. *et al.* Elimination of p19ARF-expressing cells protects against pulmonary emphysema in mice. *Aging Cell* **17**, e12827 (2018).

587. Tanaka, H. *et al.* Role of the E2F1-p19ARF-p53 Pathway in Ischemic Acute Renal Failure. *Nephron Physiology* **101**, p27–p34 (2005).

588. Hudgins, A. D. *et al.* Age- and Tissue-Specific Expression of Senescence Biomarkers in Mice. *Frontiers in genetics* **9**, 59 (2018).

589. Idda, M. L. *et al.* Survey of senescent cell markers with age in human tissues. *Aging* **12**, 4052–4066 (2020).

590. Bankhead, P. *et al.* QuPath: Open source software for digital pathology image analysis. *Scientific Reports* **7**, 1–7 (2017).

591. Xie, J. *et al.* Cell-Penetrating Peptides in Diagnosis and Treatment of Human Diseases: From Preclinical Research to Clinical Application . *Frontiers in Pharmacology* vol. 11 697 (2020).

592. Gessner, I. & Neundorf, I. Nanoparticles Modified with Cell-Penetrating Peptides: Conjugation Mechanisms, Physicochemical Properties, and Application in Cancer Diagnosis and Therapy. *International journal of molecular sciences* **21**, 2536 (2020).

593. Copolovici, D. M., Langel, K., Eriste, E. & Langel, Ü. Cell-Penetrating Peptides: Design, Synthesis, and Applications. *ACS Nano* **8**, 1972–1994 (2014).

594. Kirpotin, D. B. *et al.* Antibody Targeting of Long-Circulating Lipidic Nanoparticles Does Not Increase Tumor Localization but Does Increase Internalization in Animal Models. *Cancer Research* **66**, 6732 LP – 6740 (2006).

595. Rosenblum, D., Joshi, N., Tao, W., Karp, J. M. & Peer, D. Progress and challenges towards targeted delivery of cancer therapeutics. *Nature Communications* **9**, 1410 (2018).

596. Stanger, B. Z. Cellular homeostasis and repair in the mammalian liver. *Annual review of physiology* **77**, 179–200 (2015).

597. Baker, D. J. *et al.* Clearance of p16 Ink4a-positive senescent cells delays ageing-associated disorders. *Nature* **479**, 232–236 (2011).

598. Baker, D. J. *et al.* Naturally occurring p16(Ink4a)-positive cells shorten healthy lifespan. *Nature* **530**, 184–189 (2016).

599. Wu, K. *et al.* Preliminary Analysis of Safety and Immunogenicity of a SARS-CoV-2 Variant Vaccine Booster. *medRxiv* 2021.05.05.21256716 (2021) doi:10.1101/2021.05.05.21256716.

600. Choi, A. *et al.* Safety and immunogenicity of SARS-CoV-2 variant mRNA vaccine boosters in healthy adults: an interim analysis. *Nature Medicine* (2021) doi:10.1038/s41591-021-01527-y.

601. Al-Zaidy, S. A., Sahenk, Z., Rodino-Klapac, L. R., Kaspar, B. & Mendell, J. R. Follistatin Gene Therapy Improves Ambulation in Becker Muscular Dystrophy. *Journal of neuromuscular diseases* **2**, 185–192 (2015).

602. McGreevy, J. W., Hakim, C. H., McIntosh, M. A. & Duan, D. Animal models of Duchenne muscular dystrophy: from basic mechanisms to gene therapy. *Disease models & mechanisms* **8**, 195–213 (2015).